Advances in point-contact spectroscopy: two-band superconductor MgB₂ (Review)

I. K. Yanson* and Yu.G. Naidyuk

B. Verkin Institute for Low Temperature Physics and Engineering of the National Academy of Sciences of Ukraine, 47 Lenin Ave., Kharkov 61103, Ukraine

Analysis of the point-contact spectroscopy (PCS) data on the dramatic new high-T_c superconductor magnesium diboride MgB₂ reveals quite different behavior of two disconnected σ and π electronic bands, deriving from their anisotropy, different dimensionality, and electron–phonon interaction. PCS allows direct registration of both the superconducting gaps and electron–phonon interaction spectral function of the two-dimensional σ and three-dimensional π band, establishing the correlation between the gap value and the intensity of the high-T_c driving force—the E_{2g} boron vibrational mode. PCS data on some nonsuperconducting transition-metal diborides are surveyed for comparison. © *2004 American Institute of Physics.* [DOI: 10.1063/1.1704612]

1. INTRODUCTION

MgB₂ was discovered to be superconducting only a couple of years ago,[1] and despite that, many of its characteristics have now been investigated and a consensus exists about its outstanding properties. First of all, this refers to its high T_c (≈ 40 K), which is a record-breaking value among the $s-p$ metals and alloys. It appears that this material is a rare example of multiband (at least two bands) electronic structure with weakly interconnected bands. These bands lead to very uncommon properties. For example, T_c is almost independent of elastic scattering, unlike for other two-band superconductors.[2] The maximal upper critical magnetic field can be made much higher than that for a one-band dirty superconductor.[3] The properties of MgB₂ have been comprehensively calculated by modern theoretical methods, which lead to a basic understanding of their behavior in various experiments.
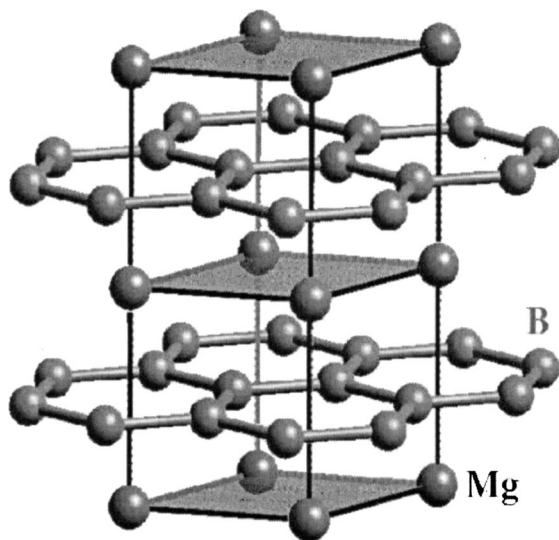
1.1. Crystal structure

Magnesium diboride, like other diborides MeB₂ (Me = Al, Zr, Ta, Nb, Ti, V, etc.), crystalizes in a hexagonal structure, where honeycomb layers of boron are intercalated with hexagonal layers of magnesium located above and below the centers of boron hexagons (Fig. 1). The bonding between boron atoms is much stronger than that between magnesium, and therefore the disordering in the magnesium layers appears to be much easier than in the boron layers. This difference in bonding between boron and magnesium atoms hinders the fabrication of MgB₂ single crystals of appreciable size.

1.2. Electron band structure

The electron band structure of MgB₂ has been calculated using different *ab initio* methods yielding basically the same result.[4–8] The $E(k)$ curves are shown in Fig. 2. The dispersion relations are shown for boron p-character orbitals, which play a major role in transport and thermodynamic
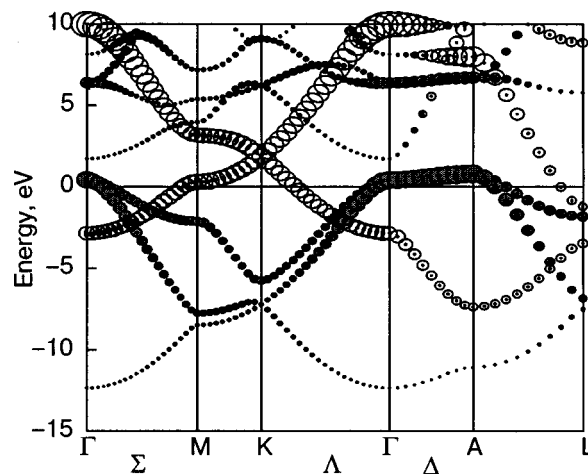

FIG. 1. Crystal structure of MgB₂.

FIG. 2. Band structure of MgB₂ with the B p character. The radii of the hollow (filled) circles are proportional to the π (σ) character and the zero line marks the Fermi energy. After Mazin *et al.*[9]

properties. The radii of the hollow circles are proportional to the π-band character, which is due to p_z boron orbitals, while those of the filled circles are proportional to the σ-band character, due to p_{xy} orbitals. The most important is a quasi-two-dimensional dispersion relation along the $\Gamma A(\Delta)$ direction with a small Fermi energy ≈ 0.6 eV, and accordingly, with a moderate Fermi velocity. The corresponding sheets of the Fermi energy form the cylindrical surfaces along the ΓA direction seen in Fig. 5 below. The corresponding electron transport is very anisotropic $(\rho_c/\rho_{ab}\simeq 3.5)$,[10] with the plasma frequency for the σ band along the c (or z) axis being much smaller than that in the ab (xy) direction.[11] The hole branch along ΓA experiences a huge interaction with the phonon E_{2g} mode for carriers moving along the ab plane (see below), although its manifestation is screened effectively by the much faster hole mobility in the π band.[2]

In a dirty material, with prevailing disorder in the magnesium planes, the π-band conductivity is blocked by defects, and the σ band takes over, implying greater electron–phonon interaction (EPI) than in the clean material. This constitutes a plausible explanation for the violation of the Matthiesen rule, which manifests itself in an increase of the residual resistivity together with an increase of the temperature coefficient at high temperatures.[2]

At the same time, the critical temperature T_c does not decrease substantially in dirty materials,[2] since the superconductivity is induced by EPI in the σ band, whose crystal order is much more robust.

This consideration is very important in understanding the point-contact data, since the disorder at the surface of the native sample depends on the position of the contact spot, and because of the uncontrolled introduction of further disorder while fabricating the contact.

1.3. Critical magnetic field

In a clean material the layered crystal structure dictates strong anisotropy of the upper critical magnetic fields $B_{c2}^{ab} \gg B_{c2}^c$. Their ratio at low temperatures reaches about 6 while B_{c2}^c is as low as 2–3 T.[12] If the magnetic field is not aligned precisely along the ab plane, the B_{c2} value is strongly decreased.

On the other hand, for a dirty material the anisotropy is decreased (to a ratio of about 1.6–2), but both the magnitudes of B_{c2}^{ab} and B_{c2}^c are strongly increased. For strongly disordered sample, it may be[3] as high as 40 T! It is interesting that this high value is achieved at low temperature, where the disordered π band is fully superconducting.

Hence, we may expect that the value of the critical magnetic field at low temperatures is the smaller the cleaner is the part of the MgB$_2$ volume near the contact, provided its $T_c \simeq T_c^{\mathrm{bulk}}$. This observation is important in the classification of contacts with respect to their purity.

1.4. Phonons and electron–phonon interaction

The phonon density of states (PDOS) is depicted in Fig. 3. The upper panel shows the measured PDOS at $T = 8$ K, while the lower ones show the calculated DOS with the partial contribution from boron atoms moving in the ab plane
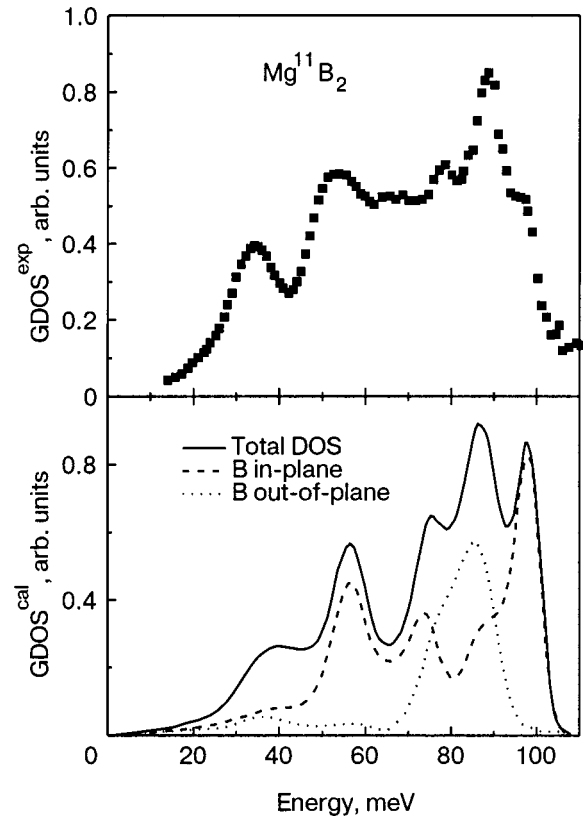

FIG. 3. Upper panel: phonon density of states in MgB$_2$ determined experimentally by neutron scattering. Bottom panel: calculated curve (solid line) with decomposition on boron atoms vibrating out of the ab plane (dotted curve) and parallel to it (dashed curve). After Osborn et al.[13]

and out of it. One can see the peak for boron atoms moving in the ab plane at $\simeq 75$ meV, which plays a very important role in the electron–phonon interaction, as is shown in Fig. 4, measured by inelastic x-ray scattering.[14] This mode gives a weak-dispersion branch between 60 and 70 meV in the ΓA direction with E_{2g} symmetry at the Γ point. The linewidth of this mode is about 20–28 meV along the ΓA direction, while along the ΓM direction it is below the experimental resolution. The same phonon peak is active in Raman scattering.[15–17] It is located at the same energy with the same
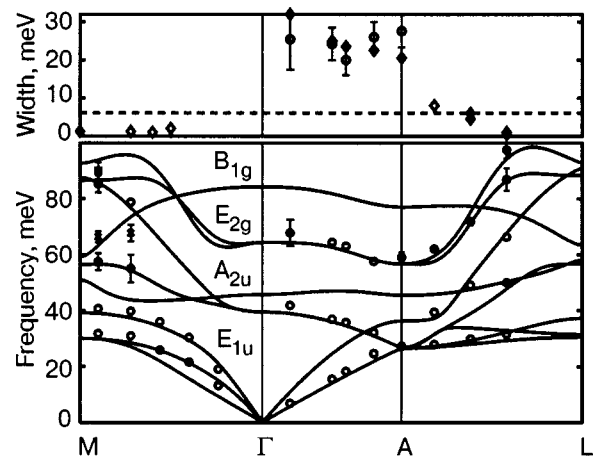

FIG. 4. Dispersion curves of phonons in MgB$_2$ and the width of phonon lines determined by inelastic x-ray scattering (symbols) together with calculations (solid lines). After Shukla et al.[14]
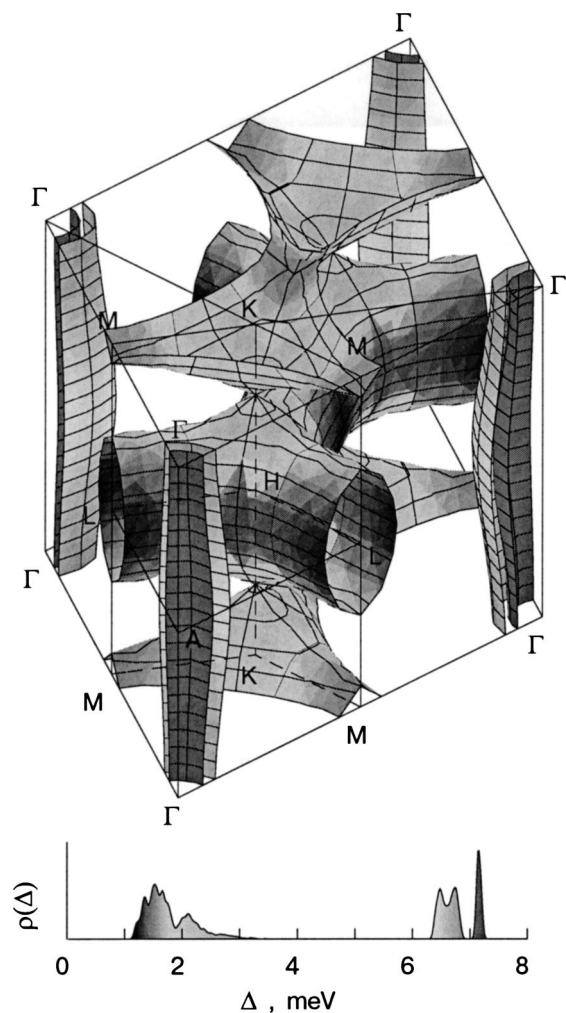
FIG. 5. Superconducting energy gap distribution over the Fermi surface (FS) of MgB_2. The gap value around 7 meV corresponds to cylinderlike sheets of the FS centered at Γ points, while the small gap value around 2 meV corresponds to the tubular FS network. After Choi et al.[18]

linewidth. This points to the very strong EPI for this particular lattice vibration mode. The same result follows from theoretical considerations.

Figure 5 shows the distribution of the superconducting energy gap on the Fermi surface of MgB_2.[18] The maximum gap value is calculated along the ΓA direction due to the very strong EPI. This is the direction in which the 2D σ band is located (the cylinders along the ΓA direction). The 3D π band has a much smaller EPI, and, correspondingly, a smaller energy gap. The EPI parameter λ can be decomposed between different pieces of the Fermi surface. It is shown[19] that the value of λ on the σ band amounts to 2–3. Moreover, λ_σ can be decomposed between different phonon modes, and it appears that only the E_{2g} phonon mode along the ΓA direction plays a major role, with a partial λ_σ value of about $\simeq 25$,[20] though concentrated in a very restricted phase space.

1.5. Mechanism for high T_c in MgB_2

The commonly accepted mechanism for high T_c in MgB_2 is connected with the strong interaction between charge carriers and phonons in the E_{2g} mode. This mode is due to antiparallel vibration of atoms in the boron planes. The key issue is that along the ΓA direction the electron band

structure is such that the Fermi energy of the hole carriers is only 0.5–0.6 eV, which shrinks even more when the borons deviate from the equilibrium positions. Together with the 2D structure of the corresponding sheet of the Fermi surface, this leads to a constant density of states at the Fermi energy and, correspondingly, to a very large EPI with partial λ_σ (the EPI parameter in the σ band) of about ~ 25.[20] Cappelluti et al.[21] point out that the small Fermi velocity for charge carriers along the ΓA direction leads to a large nonadiabatic correction to T_c (about twice as much compared with the adiabatic Migdal–Eliashberg treatment). Although this interaction is a driving force to high T_c in this compound, it does not lead to instability of the crystal structure, since it occupies only a small volume in phase space.

The role of the π band is not completely clear. On the one hand, the π and σ bands are very weakly connected, and for some crude models they can be thought as being completely disconnected. On the other hand, the energy gap of the π band goes to zero at the same T_c as in the bulk, and correspondingly $2\Delta_\pi(0)/kT_c = 1.4$, which is much less than the value predicted by the weak-coupling BCS theory. One can think of the π band as having intrinsically much lower $T_c \approx 10$ K than the bulk,[22] and at higher temperatures its superconductivity is induced by a proximity effect in **k** space from the σ band.[23] This proximity effect is very peculiar. On the one hand, this proximity is induced by the interband scattering between the π and σ sheets of the Fermi surface. On the other, the charge carriers connected with the π band are mainly located along the magnesium planes, which can be considered as a proximity effect in coordinate space for alternating layers of $S-N-S$ structure, although on a microscopic scale. Moreover, many of the unusual properties of MgB_2 may be modeled by an alternating $S-N-S$ layer structure, the limiting case to the crystal structure of MgB_2. In other words, MgB_2 presents a crossover between two-band superconductivity and a simple proximity-effect structure.

2. SAMPLES

We have two kind of samples supplied for us by our colleagues from the Far East.[1)]

The first is a thin film with a thickness of several hundred nanometers (Fig. 6).[24] Similar films have been investigated by several other groups with different methods. These films are oriented with their c axis perpendicular to the substrate. The residual resistance is several tens of $\mu\Omega \cdot$ cm with a residual resistance ratio (RRR) of $\simeq 2.2$. This means that on average the films have disorder between crystallites.

That does not exclude the possibility that on some spots the films contain clean enough small single crystals on which we occasionally may fabricate a point contact; see Fig. 6. Normally, we make a contact by touching the film surface by noble metal counter electrode (Cu, Au, Ag) in the direction perpendicular to the substrate. Thus, nominally the preferential current direction in the point contact is along the c axis. Nevertheless, since the surface of the films contains terraces with small crystallites, point contact to the ab plane of these crystallites is also possible. Sometimes, in order to increase the probability of making the contact along the ab plane, we
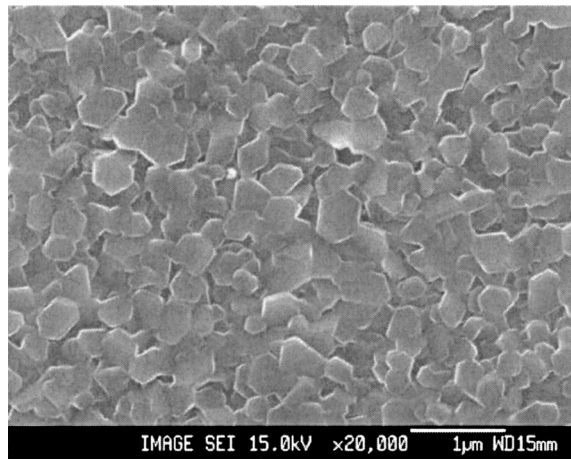
FIG. 6. Scanning electron microscopy image of MgB$_2$ films. After Kang et al.[25]

broke the substrate with the film and made contact to the side face of the sample.

The second type of sample is single-crystal,[26] which also was measured by other groups.[10,27] The crystals are platelike (flakes) and have submillimeter size (see Fig. 7). They were glued by silver epoxy to the sample holder by one of their side faces. The noble metal counter electrode was gently touched in liquid helium by another (the opposite) side face of the crystal. In this way we tried to preferentially make contact along the ab plane. On average, in the bulk, the single crystals are cleaner than the films, but one should be cautious, since the properties of the crystal surface differ from the properties of the bulk, and fabrication of a point contact may introduce further uncontrolled defects into the contact area.

Thus one cannot determine *a priori* the structure and composition of the contacts obtained. Nevertheless, much of that information can be ascertained by measuring various characteristics of a contact. Among those, the most important
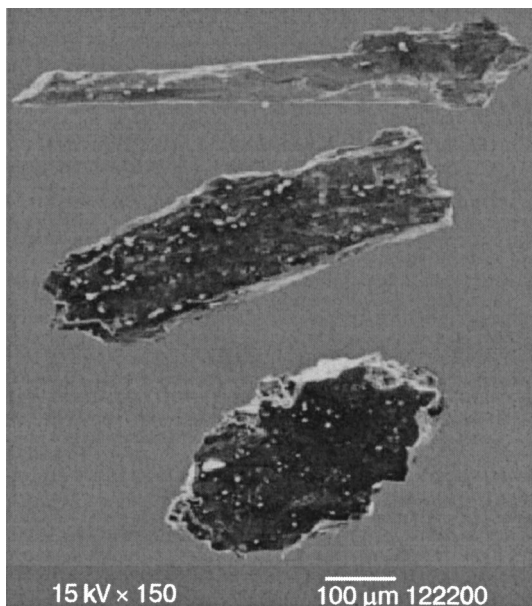

FIG. 7. Scanning electron microscopy image of MgB$_2$ single crystals. After Lee et al.[26]

is the Andreev-reflection nonlinearities of the $I–V$ curves in the superconducting energy-gap range. The magnetic-field and temperature dependences of the superconducting nonlinearities supply us with additional information. And finally, much can be extracted from the $I–V$ nonlinearities in the normal states (the so-called point-contact spectra). The more information we can collect about the electrical conductivity for different conditions of the particular contact, the more detailed and defined picture of it emerges. It is not an easy task, since a contact has limited lifetime, due to electrical and mechanical shocks.

Let us make a rough estimate of the distance scales involved in the problem. The crystallite size of the films is of the order of 100 nm (see Ref. 25). The contact size d in the ballistic regime equals $d \simeq \sqrt{\rho l / R}$ (the Sharvin formula). Taking $\rho l \cong (7 \times 10^{-7}\ \Omega \cdot \text{cm})(7 \times 10^{-6}\ \text{cm}) = 4.9 \times 10^{-12} \Omega \cdot \text{cm}^2$ (Ref. 10) we obtain $d \simeq 7$ nm along both the ab and c directions for a typical resistance of 10 Ω. If we suppose that a grain is dirty (with a very short mean free path), then we apply the Maxwell formula $d \sim \rho / R$, with results for the d values of about 0.7 nm and 2.6 nm for the ab and c directions, respectively, taking ρ for the corresponding directions from the same reference.[10] Thus the contact size can be of the order of or smaller than the electronic mean free path ($l_{ab} = 70$ nm and $l_c = 18$ nm, according to Ref. 10), which means that we are working admittedly in the spectroscopic regime, probing only a single grain.

Rowell,[28] analyzing a large amount of experimental data for the resistivity and its temperature dependence, came to the conclusion that for highly resistive samples only a small part of the effective cross section should be taken into account. The reason is that the grains in MgB$_2$ are to a great extent disconnected by oxides of magnesium and boron. For point-contact spectroscopy previous analysis leads us to the conclusion that the contact resistance is frequently measured only for a single grain or for several grains, with their intergrain boundaries facing the contact interface. This is due to the current spreading on a scale of the order of the contact size d near the constriction.

3. THEORETICAL BACKGROUND OF PCS

3.1. Nonlinearity of $I–V$ characteristic

The nonlinearities of the $I–V$ characteristic of a metallic contact, when one of the electrodes is in the superconducting state, can be written as[29,30]

$$I(V) \simeq \frac{V}{R_0} - \delta I_{\text{ph}}^N(V) + I_{\text{exc}}(V). \tag{1}$$

Here R_0 is the contact resistance at zero bias in the normal state, $\delta I_{\text{ph}}^N(V)$ is the backscattering inelastic current, which depends on the electron mean free path l. For ballistic contact this term is equal in order of magnitude to

$$\delta I_{\text{ph}}^N(V) \sim \frac{d}{l_{\text{in}}} I(V), \tag{2}$$

where l_{in} is the inelastic electron mean free path, and d is the characteristic contact diameter. If the electron flow through the contact is diffusive ($l_{\text{el}} \ll d$, l_{el} being the elastic mean free path) but still spectroscopic, since $\sqrt{l_{\text{in}} l_{\text{el}}} \gg d$, then the ex-

pression (2) should be multiplied by l_{el}/d. This decreases the characteristic size for which the inelastic scattering is important from d to l_{el} ($d \rightarrow l_{el}$), and for short l_{el} makes the inelastic current very small. We notice that the inelastic backscattering current $\delta I_{ph}^N(V)$ in the superconducting state is approximately equal to the same term in the normal state. Its second derivative turns out to be directly proportional to the EPI function $\alpha^2(\omega)F(\omega)$ (Refs. 31, 32),

$$-\frac{d^2 I}{dV^2} \propto \frac{8ed}{3\hbar v_F} \alpha^2(\omega)F(\omega), \tag{3}$$

where α describes the strength of the electron interaction with one or another phonon branch, and $F(\omega)$ stands for the phonon density of states. In point-contact (PC) spectra the EPI spectral function $\alpha^2(\omega)F(\omega)$ is modified by the transport factor, which strongly increases the contribution from backscattering processes.

In the superconducting state the excess current I_{exc} (1), which is due to the Andreev reflection of electron quasiparticles from the $N-S$ boundary in an $N-c-S$ point contact (c stands for "constriction"), can be written as

$$I_{exc}(V) = I_{exc}^0 + \delta I_{exc}(V) \tag{4}$$

where $I_{exc}^0 \approx \Delta/R_0 \approx \text{const}$ for $eV > \Delta$ (Δ being the superconducting energy gap).

The nonlinear term in the excess current (4) can in turn be decomposed in two parts, which depend in different ways on the elastic scattering of electron quasiparticles:

$$\delta I_{exc}(V) = \delta I_{exc}^{el}(V) + \delta I_{exc}^{in}(V) \tag{5}$$

where $\delta I_{exc}^{el}(V)$ is of the order of $(\Delta/eV)I_{exc}^0$, and $\delta I_{exc}^{in}V \sim (d/l_{in})I_{exc}^0$. Notice that the latter behaves very similarly to the inelastic backscattering current $\delta I_{ph}^N(V)$, namely, it disappears if $l_{el} \rightarrow 0$, while the first term in the right-hand side of expression (5) does not depend on l_{el} in the first approximation. This enables one to distinguish the elastic term from the inelastic. Finally, all excess current terms disappear when the superconductivity is destroyed, while $\delta I_{ph}^N(V)$ remains very similar in both the superconducting and normal states.

The expression for the elastic term in the excess current was calculated for *ballistic* $N-c-S$ contacts by Omelyanchuk, Beloborod'ko, and Kulik.[33] Its first derivative equals ($T=0$):

$$\left(\frac{dI_{exc}^{el}}{dV}\right)_{NcS}^{ballistic} = \frac{1}{R_0} \left| \frac{\Delta(eV)}{eV + \sqrt{(eV)^2 - \Delta^2(eV)}} \right|^2. \tag{6}$$

For the *diffusive* limit ($l_i \ll d$), Beloborod'ko *et al.* derived the current–voltage characteristic (see Eq. (21) in Ref. 34), which gives[35] for the first derivative at $T=0$

$$R_0 \left(\frac{dI_{exc}^{el}}{dV}\right)_{NcS}^{diffusive} = \frac{1}{2} \ln \left| \frac{eV + \Delta(eV)}{eV - \Delta(eV)} \right|$$

$$\times \text{Re}\left[\frac{eV}{\sqrt{(eV)^2 - \Delta^2(eV)}}\right] \Big/ \text{Re}\left[\frac{\Delta(eV)}{\sqrt{(eV)^2 - \Delta^2(eV)}}\right]. \tag{7}$$

For the sake of comparison, the similar expression of the nonlinear term in NIS tunnel junctions (I stands for "insulator"), due to the self-energy superconducting energy gap effect, has the form[36]

$$\left(\frac{dI}{dV}\right)_{NIS} = \frac{1}{R_0} \text{Re}\left[\frac{eV}{\sqrt{(eV)^2 - \Delta^2(eV)}}\right]. \tag{8}$$

Equations (6), (7), and (8) are identical in their structure and take into account the same effect, viz., the renormalization of the energy spectrum of a superconductor in the vicinity of characteristic phonon energies.

From the expressions (1), (2), (4), and (5) it becomes clear that only on the relatively *clean* spots can one observe the inelastic backscattering current $\delta I_{ph}^N(V)$, provided that the excess current term $\delta I_{exc}^{in}(V)$ is negligible. The latter can be canceled by suppression of superconductivity either with magnetic field or temperature. On the contrary, in the superconducting state, for dirty contacts, all the inelastic terms are very small, and the main nonlinearity is provided by the $\Delta(eV)$ dependence of the excess current (7).

3.2. Two-band anisotropy

Brinkman *et al.* have shown[11] that in the clean case for an NIS MgB$_2$ junction, the normalized conductance is given by

$$\sigma(V) = \left(\frac{dI}{dV}\right)_{NIS} \Big/ \left(\frac{dI}{dV}\right)_{NIN}$$

$$= \frac{(\omega_p^\pi)^2 \sigma_\pi(V) + (\omega_p^\sigma)^2 \sigma_\sigma(V)}{(\omega_p^\pi)^2 + (\omega_p^\sigma)^2}$$

where $\omega_p^{\pi(\sigma)}$ is the plasma frequency for the $\pi(\sigma)$ band and $\sigma_{\pi(\sigma)}(V)$ is the normalized conductivity of the $\pi(\sigma)$ band separately. The calculated tunneling conductances in the ab plane and along the c axis are[11]

$$\sigma_{ab}(V) = 0.67\sigma_\pi(V) + 0.33\sigma_\sigma(V), \tag{10}$$

$$\sigma_c(V) = 0.99\sigma_\pi(V) + 0.01\sigma_\sigma(V). \tag{11}$$

Hence, even along the ab plane the contribution of the σ band is less than that of the π band, to say nothing of the direction along the c axis, where it is negligibly small. The calculation predicts that if the "tunneling cone" is about several degrees from precisely in the ab plane, then the two superconducting gaps should be visible in the tunneling characteristics. In other directions only a single gap, corresponding to the π band, is visible. We will see below that this prediction is fulfilled in a point-contact experiment, as well.

Things are even worse when one tries to measure the anisotropic Eliashberg function by means of superconducting tunneling. The single-band numerical inversion program[36,37] gives an uncertain result, as was shown in Ref. 38.

Point-contact spectroscopy in the normal state can help in this deadlock situation. It is known that the inelastic backscattering current is based on the same mechanism as an ordinary homogeneous resistance, provided that the maximum energy of the charge carriers is controlled by an applied voltage. The electrical conductivity of MgB$_2$ can be considered as a parallel connection of two channels, corresponding
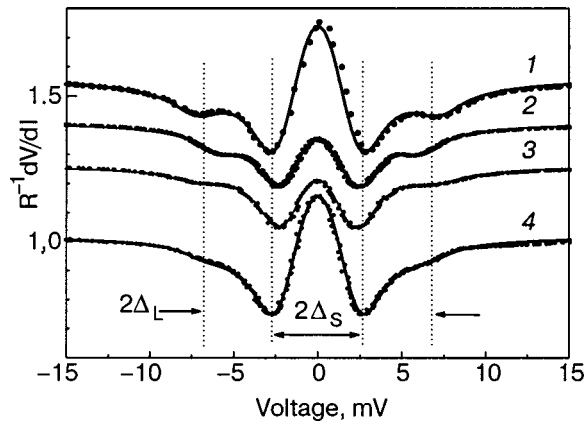
FIG. 8. Typical shapes of dV/dI (experimental dots) for 4 contacts between MgB_2 thin film and Ag with the corresponding BTK fitting (lines). Δ_L and Δ_S stand for large (small) superconducting energy gap. After Naidyuk et al.[40]

FIG. 9. Superconducting energy gap distribution of ~ 100 different junctions prepared on a MgB_2 film. On the lower panel the theoretical distribution is shown. After Naidyuk et al.[40]

4. EXPERIMENTAL RESULTS

4.1. Superconducting energy gaps

c-axis oriented thin films. Our measurements of the superconducting energy gap by means of Andreev reflection from about a hundred NS junctions yield two kinds of dV/dI curves, shown in Fig. 8.

The first one clearly shows two sets of energy gap minima located, as shown in the distribution graph of Fig. 9 (upper panel), at 2.4 ± 0.1 and 7.1 ± 0.4 meV.

These curves are nicely fitted by BTK[39] theory (with small Γ parameter) for two conducting channels with an adjusted gap weighting factor.[40] The second kind is better fitted with a single gap provided an increased depairing parameter Γ [Fig. 9 (middle panel)]. Certainly, the division of the gap structure into the two kinds mentioned is conventional, and depends upon the circumstance that the larger energy gap is explicitly seen. These two kinds of gap structure comprise about equal parts of the total number of junctions. Usually the contribution of the large gap in the double-gap spectra is an order of magnitude lower than that of the small one, which is in line with the small contribution of the σ band to the conductivity along the c axis [see Eq. (11)].

It is important to note that the critical temperature of the material around the contact is not more than a few K below T_c in the bulk material. This is determined by extrapolating the temperature dependence of the PC spectra up to the normal state. Such an insensitivity of T_c on the elastic scattering rate is explained in Ref. 2. Nevertheless, we stress that the gap structure (either double- or single-gap feature, and the
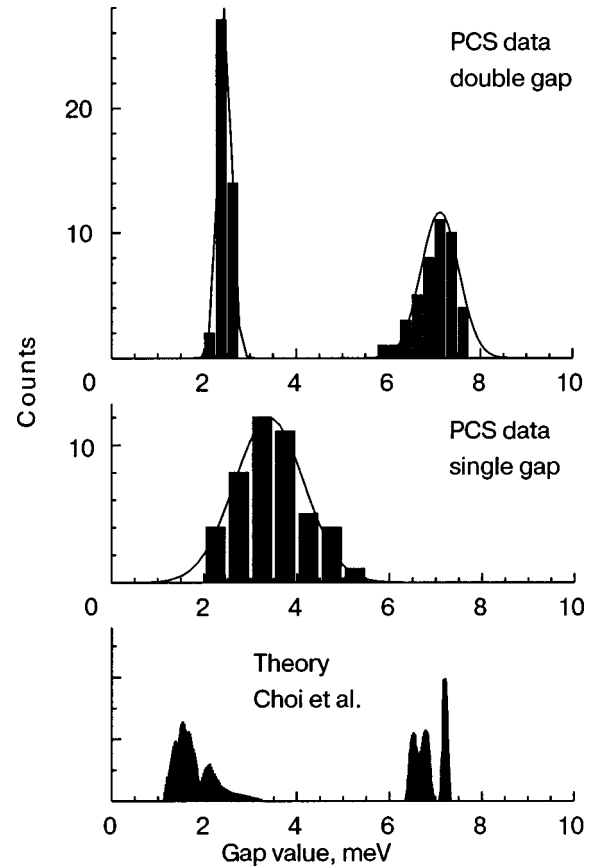
position of the single-gap minimum on dV/dI) depends very much on random variation of the scattering in the contact region. Moreover, since the main part of the junction conductivity is due to the charge carriers of the π band, even the background conductance quite often follows the "semiconductive" behavior, namely, the slope of the dV/dI curve at large biases is negative (Fig. 10). That means that the carriers in the π band are close to localization.[41]

In the lower panel of Fig. 9 the theoretical prediction of the energy gap distribution[18] is shown. One can see that the
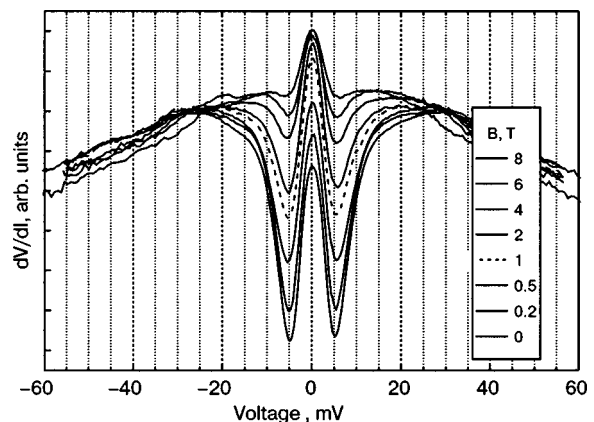

FIG. 10. Negative slope of dV/dI at large biases for a 36 Ω contact between MgB_2 single crystal and Ag showing the magnetic-field gap-structure evolution at 4.2 K.
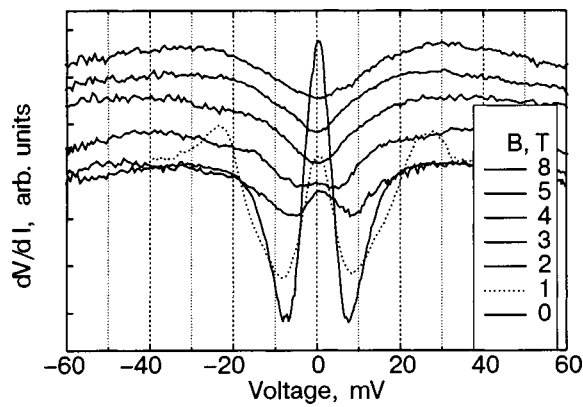
FIG. 11. Large gap structure evolution for single crystal MgB$_2$–Au 87 Ω junction in magnetic field at 4.2 K. The curves are shifted vertically for clarity.

FIG. 13. Temperature dependences of dV/dI curves (solid lines) for the same junction as in Fig. 12 with their BTK fittings (thin lines).

theoretical positions of the distribution maxima coincide approximately with the experimental values. Only the low-lying maximum is not seen in the experiment. It should be noted that, according to Mazin *et al.*,[42] variation of the superconducting gaps inside the σ and π bands can hardly be observed in real samples.

The distribution of the different gaps over the Fermi surface is shown in Fig. 5. One can immediately see that for a *c*-oriented film the main structure should have a smaller gap, which is approximately isotropic. Only if the contact touches the side face of a single crystallite (Fig. 6) is the larger gap visible, since it corresponds to the cylindrical parts of the Fermi surface with Fermi velocity parallel to the *ab* plane.

Single crystals. The same variety of energy gap structure is observed for single crystals as well, but with some peculiarity due to preferential orientation along the *ab* plane. The most amazing of them is the observation of dV/dI-gap structure in Fig. 11 with visually only the larger gap present. This gap persists in a magnetic field of a few tesla, unlike the smaller gap, which, according to Refs. 43 and 44, vanishes above 1 T. Spectra of that kind were not observed in thin films. This means that the conductivity is governed only by
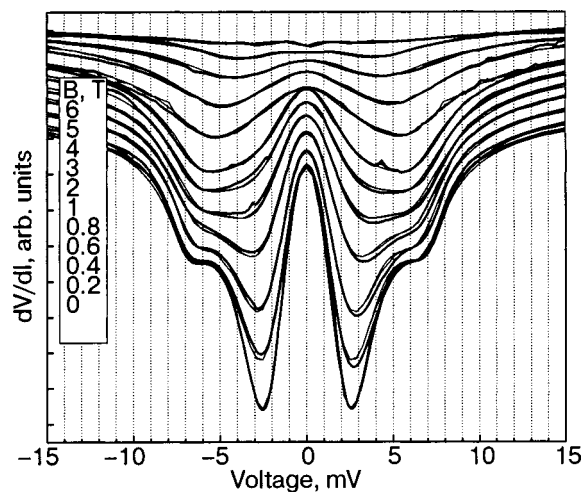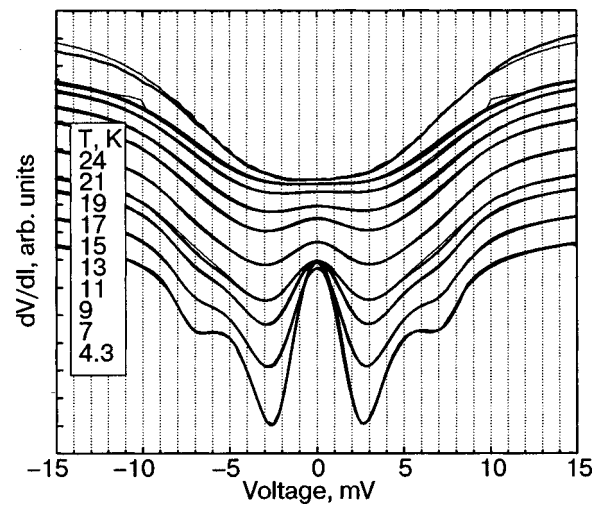
the σ band. This may be caused by the circumstance that the π band is blocked completely by Mg disorder or by oxidation of Mg atoms on the *ab* side surface of the crystal. At the same time, in a single crystal there is much less scattering in the boron planes, due to the robustness of the B–B bonds. We will see below that this circumstance is what enables us to observe directly the most important E_{2g} phonon mode in the electron–phonon interaction within the σ band.

In single crystals the negative slope in the dV/dI curve at large biases is observed quite often, which confirms that the disorder in the π band leads to quasi-localization of charge carriers. An example of this has already been shown in Fig. 10.

Figures 12 and 13 display a series of magnetic-field and temperature dependence of the dV/dI curves with their BTK fittings. Here the two gaps, corresponding to the theoretical prediction [Eq. (11)], are clearly visible in the *ab* direction. The temperature dependence of both gaps follows the BCS prediction (see Fig. 14). For temperatures above 25 K their

FIG. 12. Magnetic field dependences of dV/dI curves (solid lines) for a single-crystal MgB$_2$–Cu 2.2 Ω junction along the *ab* plane with their BTK fittings (thin lines). Two separate sets of gap minima are clearly seen at low fields.
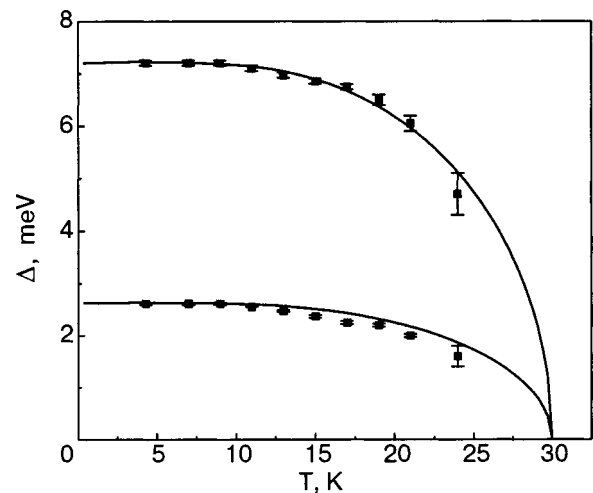

FIG. 14. Temperature dependences of large and small superconducting energy gaps obtained by BTK fitting from Fig. 13. The solid lines represent BCS-like behavior.
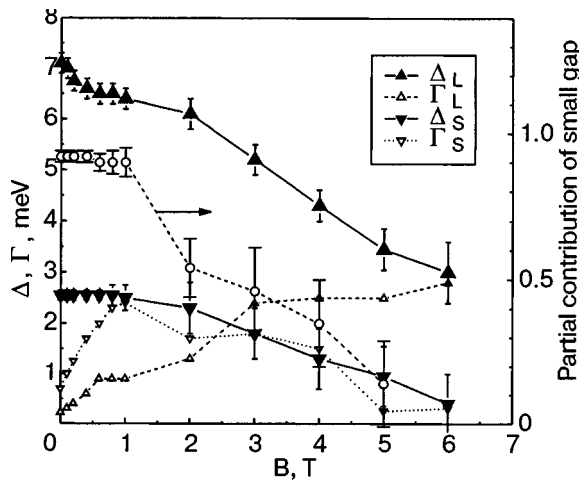
FIG. 15. Magnetic field dependences of the large and small superconducting energy gaps (solid triangles) obtained by BTK fitting from Fig. 12. Open triangles show the Γ value for large and small gap, respectively. The circles demonstrate the depression of the small-gap contribution to the dV/dI spectra by magnetic field. The lines connect the symbols for clarity.

behavior is unknown because this particular contact did not survive the measurements, probably because of thermal expansion of the sample holder.

Figure 15 displays the magnetic-field dependences of large and small gaps. Surprisingly, the small gap value is not much depressed by a field of about 1 T, and the estimated critical field of about 6 T is much higher, as stated in Refs. 44 and 45, although the intensity of the small-gap minima is suppressed rapidly by a field of about 1 T. Correspondingly, the small-gap contribution[2] w to the dV/dI spectra is decreased significantly by magnetic field, from 0.92 to 0.16 (see Fig. 15), while w versus temperature even increases slightly from 0.92 at 4.3 K to 0.96 at 24 K (not shown).

The area under the energy-gap minima in dV/dI (V) is approximately proportional to the excess current I_{exc} [see Eq. (4)] at $eV \gg \Delta$ (or roughly to the superfluid density). The excess current depends on the magnetic field with a positive overall curvature (Fig. 16). $I_{exc}(B)$ decreases abruptly at first and then more slowly above 1 T. This corresponds to a drastic depression of the dV/dI (V) small-gap-minima intensity by a magnetic field of about 1 T and to robustness of the residual superconducting structure against further increase of
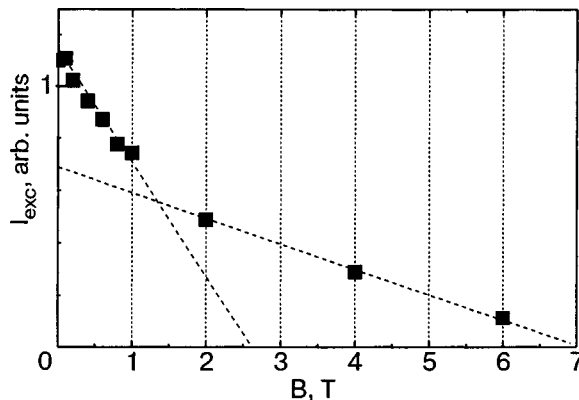

FIG. 16. $I_{exc}(B)$ (squares) for a MgB$_2$–Cu junction from Fig. 12. The dashed lines show the different behavior of $I_{exc}(B)$ at low and high fields.
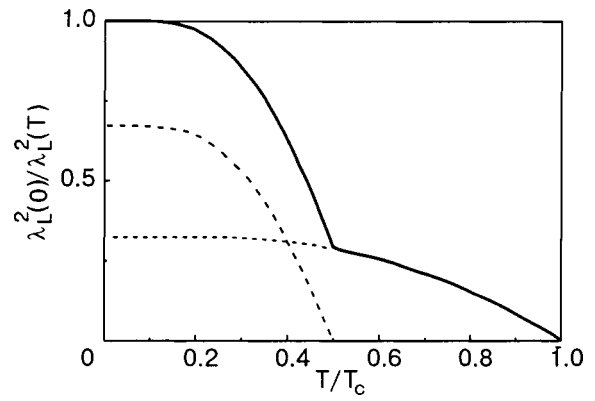

FIG. 17. Temperature dependence of the penetration depth in the model of two independent BCS superconducting bands (dashed and dotted line) with different superconducting gaps. The resulting penetration depth (solid line) clearly shows a non-BCS temperature behavior. The low-temperature behavior will be dominated by the band with the smaller superconducting gap. After Golubov *et al.*[46]

magnetic field. This is a quite different dependence from what is expected for I_{exc}, which is in general proportional to the gap value (4).

In contrast, $I_{exc}(T)$ has mostly negative curvature and shape, similar to the BCS dependence. Often a positive curvature appears above 25 K (see, e.g., Fig. 18).

This kind of anomaly can be due to the two-band nature of superconductivity in MgB$_2$, since magnetic field (temperature) suppresses the superconductivity more quickly in the π band and then, at higher field (temperature), in the σ band. The same consideration is valid for $1/\lambda_L$, which is roughly proportional to the "charge density of superfluid condensate." In the case of zero interband scattering, the simple model of Ref. 46 predicts the temperature dependence shown in Fig. 17 for σ and π parallel channels, which will yield a smooth curve with general positive curvature, taking into account the small interband scattering occurring in reality.
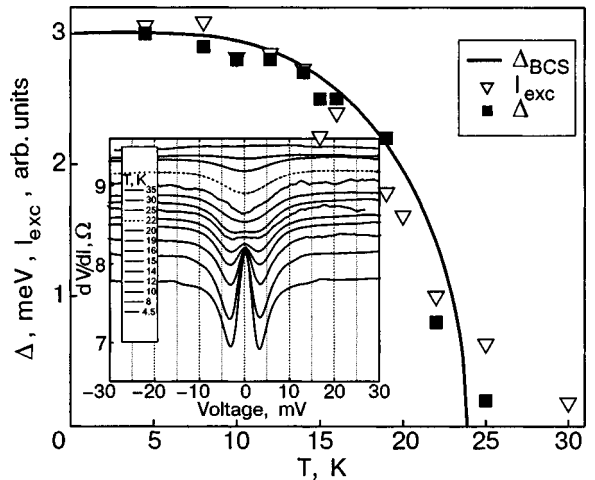

FIG. 18. Temperature dependence of a single superconducting energy gap (squares) obtained by BTK fitting of dV/dI curves from the inset. The solid lines represent BCS-like behavior. The triangles show the dependence of the excess current. Inset: dV/dI curves for a MgB$_2$–Cu 8 Ω contact at different temperatures.
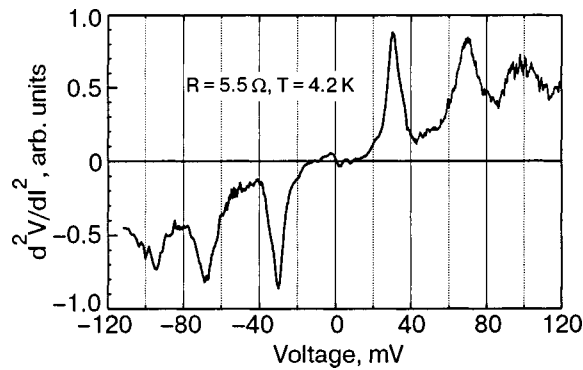
FIG. 19. Raw PC EPI spectrum for a ZrB$_2$ 5.5 Ω point contact at 4.2 K. After Naidyuk *et al.*[47]

FIG. 20. Comparison of high-resolution electron-energy-loss spectroscopy measurements of surface phonon dispersion (bottom panels, symbols)[49] with the PC spectra for ZrB$_2$ and NbB$_2$ after subtraction of the rising background (upper panels).

If the π-band conductivity is blocked by a short mean free path, then the curvature of $I_{exc}(T)$, being proportional to $\Delta_\sigma(T)$, should be negative, which supplies us with additional confirmation of single-band conductivity along the σ band. Thus, measuring the magnetic field and temperature dependences of I_{exc} can elucidate the contact structure.

Figure 18 displays the temperature dependence of the gap for the dV/dI curves with a single-gap structure, which vanishes around 25 K. A magnetic field of 1 T suppresses the gap minima intensity by factor of two, but the minima are clearly seen even at 4 T (not shown), the maximal field in this experimental trial. This excludes an origin of these gap minima due to a small gap. According to the calculation in Ref. 11 a large amount of impurity scattering will cause the gaps to converge to $\Delta \simeq 4.1$ meV and T_c to 25.4 K. Therefore these single-gap spectra reflect a strong interband scattering due to impurities, which likely causes a "semiconducting-like" behavior of dV/dI above T_c (see Fig. 18, inset). $I_{exc}(T)$ behaves nearly as $\Delta(T)$ except in the region $T > 25$ K, where I_{exc} is still nonzero because of a residual shallow zero-bias minimum in dV/dI above 25 K.

4.2. Phonon structure in the I–V characteristics

PC EPI spectra of nonsuperconducting diborides. We have studied the PC EPI spectra $d^2V/dI^2 \propto -d^2I/dV^2$ [see also Eq. (3)] of nonsuperconducting diborides MeB$_2$ (Me = Zr, Nb, Ta).[47] The cleanest sample we have is a ZrB$_2$ single crystal, and its PC EPI spectrum is shown in Fig. 19. One recognizes a classical PC EPI spectrum from which one can estimate the position of 3 main phonon peaks and obtain the lower limit of EPI parameter λ_{PC} (Ref. 47).

Essentially similar spectra were observed for other diborides, taking into account their purity and increased EPI, which leads to a transition from the spectroscopic to a nonspectroscopic (thermal) regime of current flow.[47] The positions of the low-energy peaks are proportional to the inverse square root of the masses of the d metals,[47] as expected. For these compounds the phonon density of states is measured by means of neutron scattering[48] and the surface phonon dispersion is derived by high-resolution electron-energy-loss spectroscopy.[49] The positions of the phonon peaks or $d\omega/dq = 0$ for the dispersion curves correspond to maxima of the PC spectra (Figs. 20 and 21).
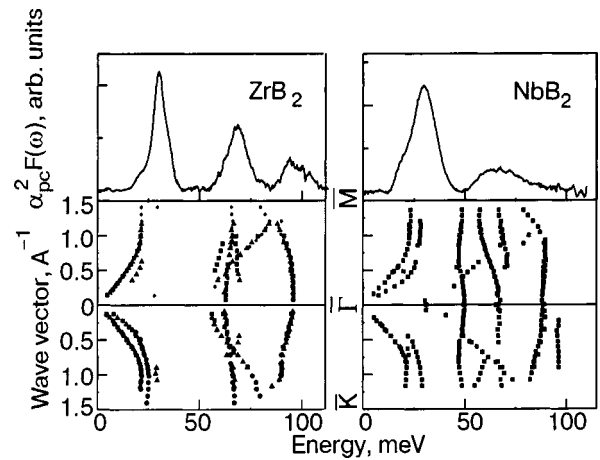
PC EPI spectra of MgB$_2$ *in c-axis oriented films.* From the above considerations we had anticipated that one could easily measure the EPI spectral function of MgB$_2$ in the normal state, provided that the superconductivity is destroyed by magnetic field. Unfortunately, that was not the case. The stronger we suppress the superconductivity in MgB$_2$, the less traces of phonon structure remain in the $I-V$ characteristic and its derivatives (Fig. 22).[23] This is in odd in relation to the classical PCS, since the inelastic phonon spectrum should not depend on the state of the electrodes in the first approximation (see Sec. 3. Theoretical background).

Instead, most of the MgB$_2$ spectra in the superconducting state show reproducible structure in the phonon energy range (Fig. 23) which is not similar to the expected phonon maxima superimposed on the rising background. This structure disappears upon transition to the normal state. Quite
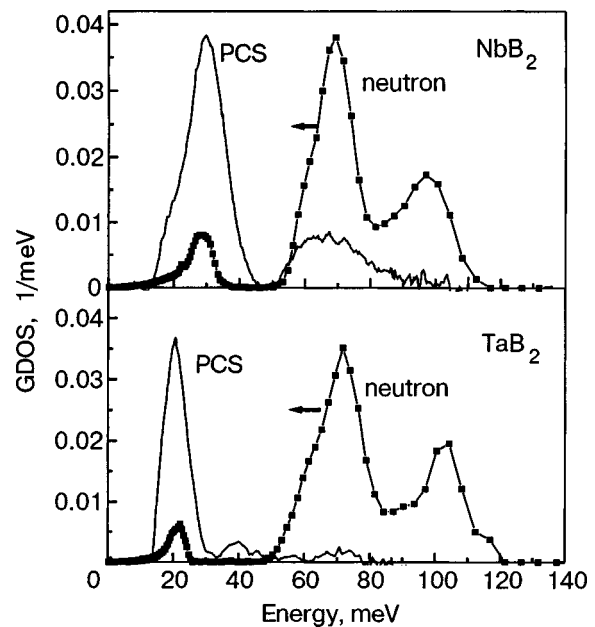
FIG. 21. Comparison of phonon DOS neutron measurements after Heid *et al.*[48] (symbols) with PC spectra for TaB$_2$ and NbB$_2$ after subtraction of the rising background (solid curves).
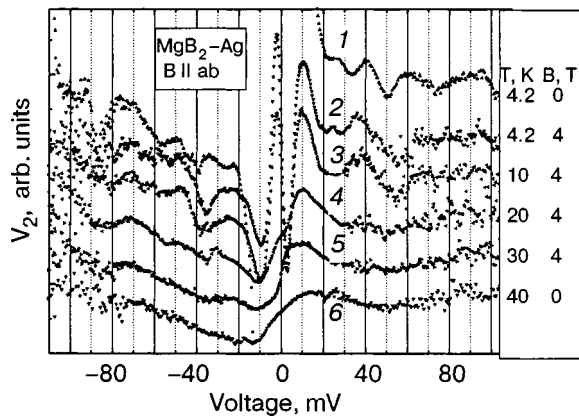
FIG. 22. Phonon singularities in the PC spectra of a MgB_2 thin-film–Ag junction as a function of magnetic field and temperature. T and B are shown beside each curve. After Yanson et al.[23]

interestingly the intensity of this structure increases with increase of the value of the small gap, which means that the gap in the π band and observed phonon structure are connected.[23] Based on the theoretical consideration mentioned in the Introduction, we conclude that the disorder in the π band is so strong that it precludes observation of the inelastic current, and the phonon nonlinearities of the excess current [see Eq. (6)] play the main role, which does not depend on the scattering.

Very rarely did we see signs that the observed characteristics indeed satisfy the conditions imposed on the inelastic PC spectra. One such example is shown in Figs. 24 and 25. For this particular junction the superconducting peculiarities are almost completely suppressed above 20 mV in moderate field (4 T). What remains is a very weak structure ($\sim 1\%$) from the rather high value of the gap (Fig. 24). The background in $dV/dI\,(V)$ rises nearly quadratically up to a few percent of R_0 at large biases (~ 100 mV). This leads to a linear background in $V_2 \propto d^2V/dI^2\,(V)$ with phonon peaks

FIG. 24. dV/dI and $V_2 \propto d^2V/dI^2$ curves for a thin-film MgB_2–Ag junction, revealing the inelastic PC spectrum for the π band. After Bobrov et al.[50]

FIG. 23. Superconducting gap features (upper panel) and phonon structure (bottom panel) in the spectra of thin-film MgB_2–Ag junctions with different resistances at $T = 4.2$ K, $B = 0$. After Yanson et al.[23]

FIG. 25. Comparison of the PC EPI spectrum (upper panel) from Fig. 24 (after subtraction of the linear background and zero-bias maxima below 25 meV) with the phonon DOS measured by neutron scattering[8,13] (bottom panel).

FIG. 26. Calculated Eliashberg functions for the σ and π bands (inset). After Golubov et al.[51]

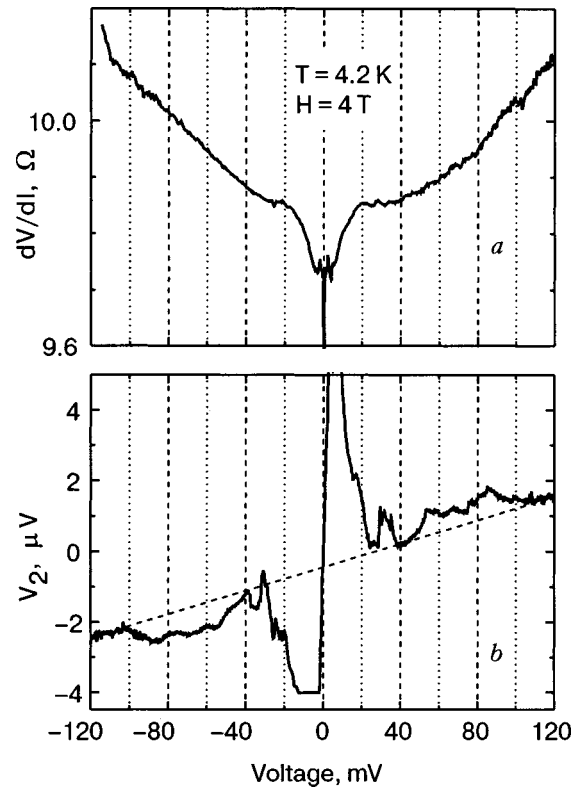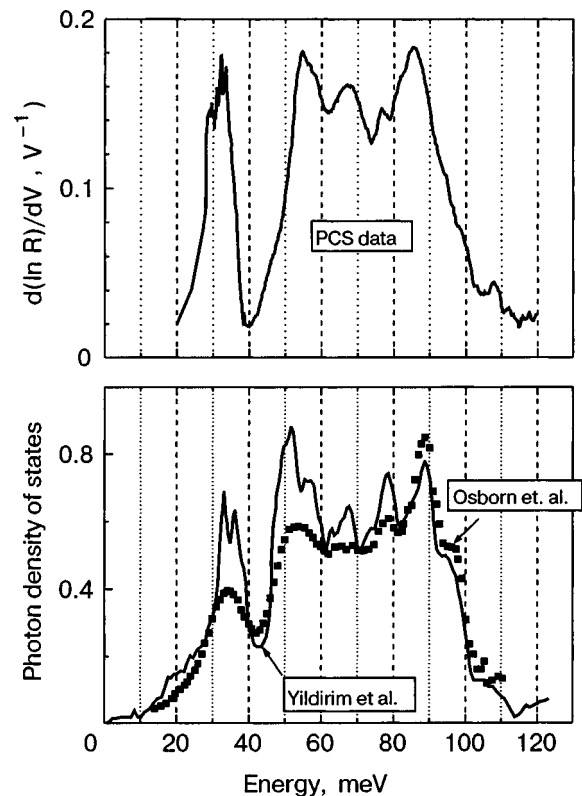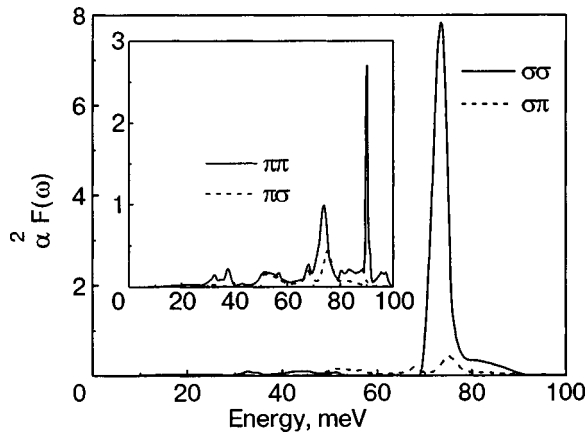FIG. 27. $V_2 \propto d^2V/dI^2$ (for two bias voltage polarities) and dV/dI curves for a single-crystal MgB$_2$–Cu junction ($R_0 = 1.5\ \Omega$) along the ab plane. Here the conductivity along the π band prevails, as is shown by the pronounced small-gap structure for the zero-field dV/dI curve at 4.5 K. The $\alpha^2F(\omega)$ curve is the theoretical prediction for the π-band Eliashberg function from Fig. 26 (inset) smeared similarly to the experimental data. After Naidyuk et al.[52]

superposed above the background both in negative and positive bias polarity (compare with Fig. 19). The structure observed corresponds reasonably in shape above 30 meV to the phonon density of states (Fig. 25). At low voltages (below 30 meV), most probably, the gap peculiarities still prevail over the $d^2V/dI^2\ (V)$ structure. Thus, for this contact we assume to observe the *inelastic* PC spectrum for the π band, which should be compared to the Eliashberg EPI function for the same band calculated in Ref. 51 (Fig. 26). Neither the experimental spectrum nor the π-band Eliashberg function shows anomalously high intensity of the E_{2g} phonon mode, since only the Eliashberg function for the σ band is the principal driving force for high T_c in MgB$_2$. The same conclusion should be ascribed to the excess-current phonon structure, since it also corresponds to the π band. This band has much larger Fermi velocity and plasma frequency along the c axis compared to the σ band.[11]

Thus, in order to register the principal EPI with the E_{2g} phonon mode, we are faced with the necessity of measuring the PC spectra for only the σ band. This can be done in a single crystal along the ab plane with blocked π-band conductivity.

PC EPI spectra of MgB$_2$ *in the ab direction.* The desired situation was described in Ref. 52 for a single crystal oriented in the ab plane. As was mentioned above, merely having the nominal orientation of the contact axis parallel to the ab plane is insufficient to ensure that this situation occurs in reality. Moreover, even if one establishes the necessary orientation (i.e., contact axis parallel to ab plane) the spectra should reflect both bands with a prevalence of the undesired π band, because spherical spreading of the current makes the orientational selectivity of a metallic point contact much worse than that for a plane tunnel junction, where it goes exponentially. The large mixture of π-band contribution is clearly seen from the gap structure in Fig. 27. Beyond the wings, at the biases corresponding to the large gap (supposed to belong to the σ-band gap) the deep minima located at the smaller gap (correspondingly to the π-band gap) are clearly seen (see bottom panel of Fig. 27). The EPI spectrum of the same junction is shown in the upper panel. One can see that the nonlinearities of the I–V characteristic at phonon biases are very small, and a reproducible structure roughly corresponding to the Eliashberg EPI function of the π band[38,51]

appears in the bias range $\sim$20–60 mV. Above 60 mV the PC spectrum broadens sufficiently to hide higher-lying phonon maxima. Even in the normal state $(T \gtrsim T_c)$, where the excess current disappears, one can see the kink at $\approx$20–30 meV, where the first peak of the phonon DOS and the first maximum of the Eliashberg EPI function of the π band occur. At $eV \approx$90–100 meV the PC EPI spectrum of Fig. 27 saturates just where the phonon DOS ends. At $T \gtrsim T_c$ intermediate phonon peaks are hardly seen, since the thermal resolution, which equals $5.44k_BT$, amounts to about 20 meV, and the regime of current flow is far from ballistic, due to the high background observed. No prevalence of the E_{2g} phonon mode is observed, like a big maximum of the EPI at $\approx$60–70 meV or a kink at $T \gtrsim T_c$ for these biases.

A quite different spectrum is shown in Fig. 28, which is our key result. Consider first the $dV/dI\ (V)$ characteristics (see bottom panel). The energy gap structure shows the gap minima corresponding to the large gap (σ-band gap). The increase of $dV/dI\ (V)$ at larger biases is noticeably larger than in the previous case (Fig. 27). One can notice that the relatively small magnetic field ($\sim$1 T) does not decrease the intensity of the gap structure substantially, unlike those for Fig. 12, and even less than for Fig. 27. According to Refs. 43 and 44, a field of about 1 T should depress the small-gap intensity completely.

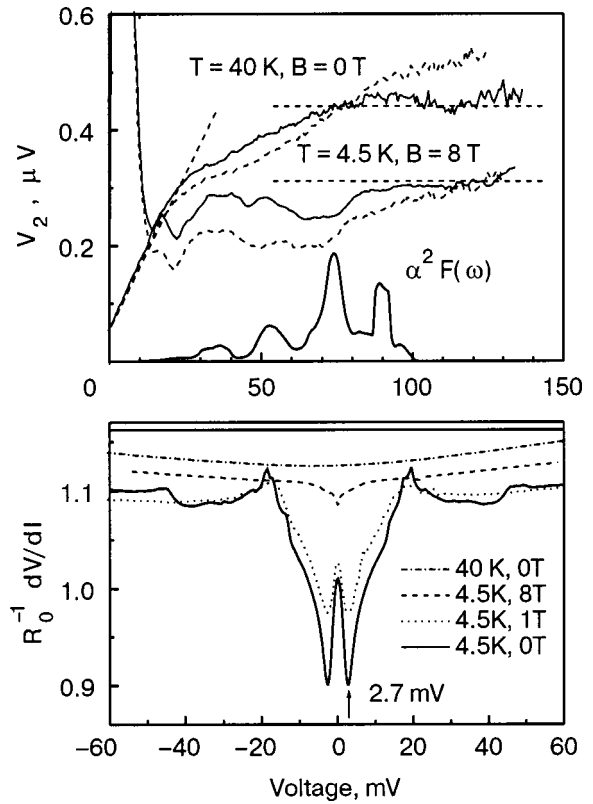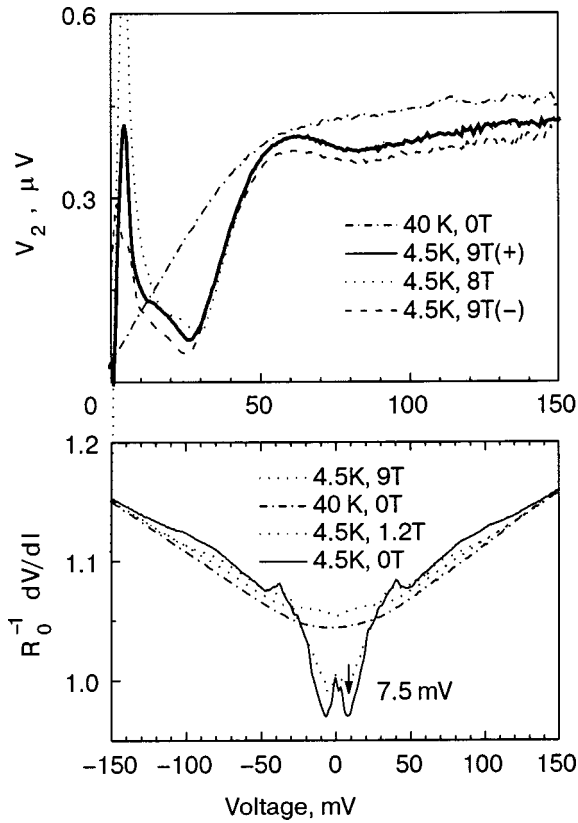All these facts evidence that we obtain a contact in

FIG. 28. $V_2 \propto d^2V/dI^2$ (for two bias voltage polarities at 9 T) and dV/dI curves for a single-crystal MgB_2–Cu junction ($R_0 = 7.2\ \Omega$) along the ab plane. Here the conductivity along the σ band prevails, as is shown by the pronounced large-gap structure for the zero-field dV/dI-curve at 4.5 K. After Naidyuk et al.[52]
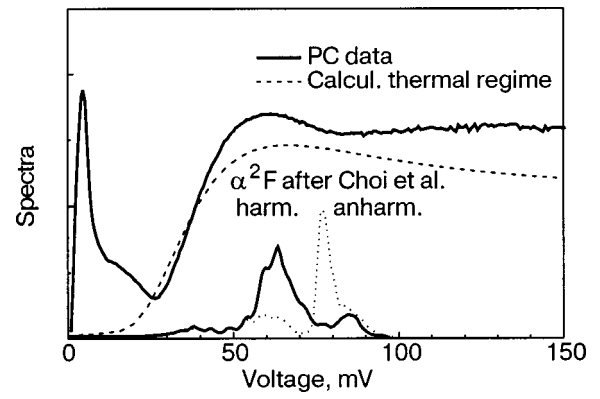

FIG. 29. Comparison of the experimental spectrum of Fig. 28 with the thermal spectrum for a model spectral function in the form of a Lorentzian at 60 meV with a width of 2 meV (dashed line) and with the theoretical EPI spectra (bottom curves). After Naidyuk et al.[52]

which only the σ-band channel in conductivity is in operation.

Let us turn to the PC EPI spectra d^2V/dI^2 (V), which are connected via the following expression to the second harmonic signal V_2 recorded in experiment:

$$\frac{1}{R^2}\frac{d^2V}{dI^2} = 2\sqrt{2}\frac{V_2}{V_1^2}.$$

Here $R = dV/dI$, and V_1 is the rms value of the modulation voltage for the standard techniques of tunneling and point-contact spectroscopy.

The PC EPI spectra for this contact are shown in Fig. 28 (upper panel) for the highest field attainable in our experiments.[52] One can see that 8–9 T is still not enough to destroy completely the superconductivity in the energy-gap low bias range (0–30 meV), which can be taken as characteristic for a strongly superconducting σ band. On the other hand, at larger biases no influence of field is noted, which evidences that this part of $I–V$ characteristic does not contain superconducting peculiarities, likely because of the high current density in the contact. Except for a small asymmetry, the spectrum is reproduced for both polarities. Before saturation at biases $\geqslant 100$ meV, where the phonon DOS ends, a well-resolved wide bump occurs, which is located at about 60 meV. Further on, we will concentrate on this.

First, we rescale it to the spectrum in $R_0^{-1}dR/dV$ units, in order to compare with the theoretical estimation. We will show that the bump is of spectroscopic origin, i.e., the re-

gime of current flow through the contact is not thermal, although the background at large biases ($V \geqslant 100$ meV) is high. To do so, we compare this bump with a PC spectrum in the thermal regime for a model EPI function, which consists of a Lorentzian at 60 meV with small (2 meV) width. The thermal PC EPI spectrum calculated according to Kulik,[53] shown as a dashed line in Fig. 29, is much broader. Any further increase of the width of the model spectra will broaden the curve obtained. Comparing the experimental and model spectra enable us to conclude that, in spite of the large width, the maximum of the experimental spectra still corresponds to the spectroscopic regime. The high-temperature ($T \geqslant T_c$) spectrum in Fig. 28 shows the smeared kink at about 60 meV, unlike that of Fig. 27. By introducing greater disorder in the boron plane by a fabrication procedure or by trying other spots on the side-face surface, smeared thermal spectra were observed, coinciding in shape with the dashed curve in Fig. 30. In this figure another junction is shown, where the energy gap structure also points to the σ-band channel. Other junctions display the kink at about 30–40 meV, like the high-temperature spectrum in Fig. 27, which together with their energy-gap structure can be ascribed to the thermal limit mainly in the π band, despite the rather low bath temperature.

A PC spectrum with broad maxima including one at about 60 mV was observed in Ref. 45 on polycrystalline MgB_2 samples driven to the normal state by applying a moderate magnetic field and increasing the temperature.

The large width of the EPI peak connected with the E_{2g} phonon mode (Fig. 28) is not surprising. Shukla et al.[14] measured the phonon dispersion curves along the ΓA and ΓM directions by means of inelastic x-ray scattering (see Fig. 4). The full width at half maximum for the E_{2g} mode along the ΓA direction amounts about 20–28 meV, which corresponds well to what we observe in the point-contact spectrum. If the phonon lifetime corresponds to this (inverse) energy, then the phonon mean free path is about equal to the lattice constant,[52] and due to phonon reabsorption by accelerating electrons, we should anticipate a large background in the PC spectra as observed. If we compare the position of the bump (≈ 60 meV) with what is predicted for isotropic Eliashberg EPI function[19] (see Fig. 29), then we, together with Shukla
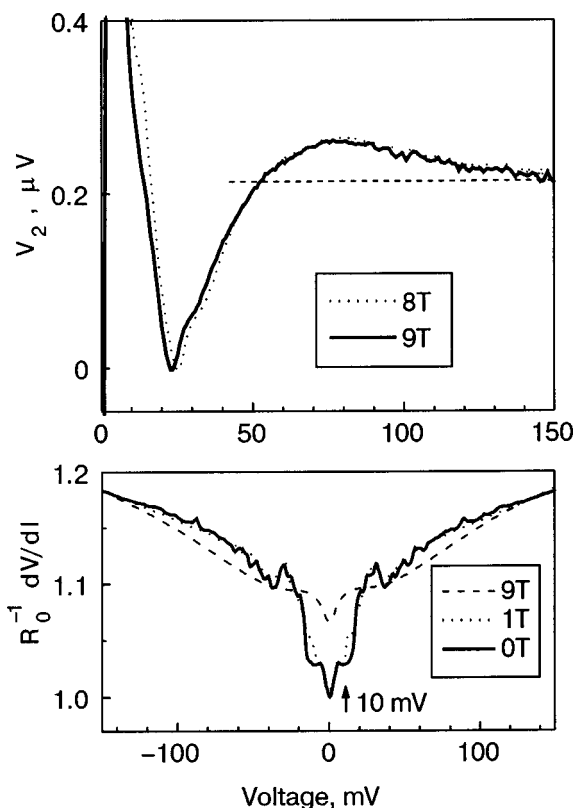
FIG. 30. Thermal limit for the σ band (as is shown by the pronounced large-gap structure for the zero-field dV/dI curve at 4.5 K) in the PC spectrum of a MgB$_2$ single crystal along the ab plane. After Naidyuk et al.[52]

et al., must admit that the phonon–phonon anharmonicity is inessential for this mode, and its high width is due completely to the EPI.

Now turn to the nonlinearity of the $I–V$ curves due to the electron–phonon interaction, which can be estimated from the dV/dI curves as about 10% for contacts with the E_{2g} phonon modes in Fig. 28. This is comparable with the nonlinearity observed for nonsuperconducting diborides[47] with a small electron–phonon coupling constant. The reason for the relatively low nonlinearity of the $I–V$ curves and low intensity of the principal E_{2g} phonon modes in the spectra for the MgB$_2$ contacts can be the fact that anomalously strong interaction is characteristic for a restricted group of phonons with sufficiently small wave vector,[9] whereas in point-contact spectroscopy the large-angle scattering is emphasized.

5. CONCLUSIONS

We have presented an overview of the PCS investigations of c-axis oriented thin films and single crystals of MgB$_2$.

Our conclusions are as follows:

1. There are two different superconducting gaps in MgB$_2$, which are grouped at 2.4 and 7.0 meV. In roughly half of all point contacts studied for c-axis oriented films the two-gap structure merges together due to strong elastic scattering, leaving a single gap at about 3.5 meV.

2. Anomalous temperature and especially magnetic field dependences of the excess current in point-contact junctions

reflect the two-band structure of the superconducting order parameter in MgB$_2$.

3. There are two mechanisms for revealing phonon structure in the point-contact spectra of MgB$_2$: i) through the inelastic backscattering current, like for ordinary point-contact spectroscopy, and ii) through the energy dependence of the excess current, like in the similar tunneling spectroscopy of the electron–phonon interaction. They can be discriminated by destroying the superconductivity with a magnetic field and/or temperature and by varying the electron mean free path.

4. The prevailing appearance of the E_{2g} boron mode, which mediates the creation of Cooper pairs, is seen in the PC spectra only along the $a–b$ direction in accordance with the theory. The relatively small intensity of this mode in the PC spectra is likely due to their small wave vector and restricted phase volume.

5. Related diborides (ZrB$_2$, NbB$_2$, and TaB$_2$) have d^2V/dI^2 spectra proportional to the electron–phonon interaction spectral function, like that in common metals and a small EPI constant corresponding to their nonsuperconducting state.

NOTE ADDED IN PROOF

After the paper was completed we have learned of the paper by Koshelev and Golubov,[54] where the magnetic field dependence of Δ_σ and Δ_π was presented. It turned out that the $\Delta_\sigma(B)$ and $\Delta_\pi(B)$ behavior is different and is governed by diffusion constants depending on the coherence length. However, the critical field is the same both for Δ_σ and Δ_π. This is in line with our observation given in Fig. 15. Additionally, two experimental reports on the effect of magnetic field on both gaps in MgB$_2$ by Gonnelli et al. (cond-mat/0308152) and Bugoslavsky et al. (cond-mat/0307540) appeared in the E-print archive. Bugoslavsky et al. reported that both order parameters persist to a common magnetic field. Gonnelli et al. corrected their previous claims and mentioned that it might not be correct to identify the magnetic field at which the π-band features in dV/dI visually disappear as the critical field for the π band.

*E-mail: yanson@ilt.kharkov.ua

[1]The films were provided by S.-I. Lee from the National Creative Research Initiative Center for Superconductivity, Department of Physics, Pohang University of Science and Technology, Pohang, South Korea. The single crystals were provided by S. Lee from Superconductivity Research Laboratory, ISTEC, Tokyo, Japan.

[2]Since w depends inversely on the value of Γ, the nearly constant w value between 0 and 1 T is due to the fact that Γ rises by factor 4 at 1 T.

[1] Jun Nagamatsu, Norimasa Nakagawa, Takahiro Muranaka, Yuji Zenitani, and Jun Akimitsu, Nature (London) **410**, 63 (2001).

[2] I. I. Mazin, O. K. Andersen, O. Jepsen, O. V. Dolgov, J. Kortus, A. A.

Golubov, A. B. Kuz'menko, and D. van der Marel, Phys. Rev. Lett. **89**, 107002 (2002).

[3] A. Gurevich, Phys. Rev. B **67**, 184514 (2003).

[4] J. M. An and W. E. Pickett, Phys. Rev. Lett. **86**, 4366 (2001).

[5] Y. Kong, O. V. Dolgov, O. Jepsen, and O. K. Andersen, Phys. Rev. B **64**, 02050(R) (2001).

[6] J. Kortus, I. I. Mazin, K. D. Belashchenko, V. P. Antropov, and L. L. Boyer, Phys. Rev. Lett. **86**, 4656 (2001).

[7] Amy Y. Liu, I. I. Mazin, and Jens Kortus, Phys. Rev. Lett. **87**, 087005 (2001).

[8] T. Yildirim, O. Gülseren, J. W. Lynn, C. M. Brown, T. J. Udovic, Q. Huang, N. Rogado, K. A. Regan, M. A. Hayward, J. S. Slusky, T. He, M. K. Haas, P. Khalifah, K. Inumaru, and R. J. Cava, Phys. Rev. Lett. **87**, 037001 (2001).

[9] I. I. Mazin and V. P. Antropov, Physica C **385**, 49 (2003).

[10] Yu. Eltsev, K. Nakao, S. Lee, T. Masui, N. Chikumoto, S. Tajima, N. Koshizuka, and M. Murakami, Phys. Rev. B **66**, 180504(R) (2002).

[11] A. Brinkman, A. A. Golubov, H. Rogalla, O. V. Dolgov, J. Kortus, Y. Kong, O. Jepsen, and O. K. Andersen, Phys. Rev. B **65**, 180517 (2002).

[12] V. G. Kogan and S. L. Bud'ko, Physica C **385**, 131 (2003).

[13] R. Osborn, E. A. Goremychkin, A. I. Kolesnikov, and D. G. Hinks, Phys. Rev. Lett. **87**, 017005 (2001).

[14] Abhay Shukla, Matteo Calandra, Matteo d'Astuto, Michele Lazzeri, Francesco Mauri, Christophe Bellin, Michael Krisch, J. Karpinski, S. M. Kazakov, J. Jun, D. Daghero, and K. Parlinski, Phys. Rev. Lett. **90**, 095506 (2003).

[15] K.-P. Bohnen, R. Heid, and B. Renker, Phys. Rev. Lett. **86**, 5771 (2001).

[16] James William Quilty, Physica C **385**, 264 (2003).

[17] A. F. Goncharov and V. V. Struzhkin, Physica C **385**, 117 (2003).

[18] Hyoung Joon Choi, David Roundy, Hong Sun, Marvin L. Cohen, and Steven G. Louie, Nature (London) **418**, 758 (2002).

[19] Hyoung Joon Choi, David Roundy, Hong Sun, Marvin L. Cohen, and Steven G. Louie, Phys. Rev. B **66**, 020513(R) (2002).

[20] J. M. An, S. Y. Savrasov, H. Rosner, and W. E. Pickett, Phys. Rev. B **66**, 220513(R) (2002).

[21] E. Cappelluti, S. Ciuchi, C. Grimaldi, L. Pietronero, and S. Strässler, Phys. Rev. Lett. **88**, 117003 (2002).

[22] F. Bouquet, Y. Wang, I. Sheikin, P. Toulemonde, M. Eisterer, H. W. Weber, S. Lee, S. Tajima, and A. Junod, Physica C **385**, 192 (2003).

[23] I. K. Yanson, V. V. Fisun, N. L. Bobrov, Yu. G. Naidyuk, W. N. Kang, Eun-Mi Choi, Hyun-Jung Kim, and Sung-Ik Lee, Phys. Rev. B **67**, 024517 (2003).

[24] W. N. Kang, Hyeong-Jin Kim, Eun-Mi Choi, C. U. Jung, and Sung-Ik Lee, Science **292**, 1521 (2001).

[25] W. N. Kang, Eun-Mi Choi, Hyeong-Jin Kim, Hyun-Jung Kim, and Sung-Ik Lee, Physica C **385**, 24 (2003).

[26] Sergey Lee, Physica C **385**, 31 (2003); S. Lee, H. Mori, T. Masui, Yu. Eltsev, A. Yamanoto and S. Tajima, J. Phys. Soc. Jpn. **70**, 2255 (2001).

[27] J. W. Quilty, S. Lee, A. Yamamoto, and S. Tajima, Phys. Rev. Lett. **88**, 087001 (2001).

[28] J. M. Rowell, Supercond. Sci. Technol. **16**, R17 (2003).

[29] V. A. Khlus and A. N. Omel'yanchuk, Fiz. Nizk. Temp. **9**, 373 (1983) [Sov. J. Low Temp. Phys. **9**, 189 (1983)].

[30] V. A. Khlus, Fiz. Nizk. Temp. **9**, 985 (1983) [Sov. J. Low Temp. Phys. **9**, 510 (1983)].

[31] I. O. Kulik, A. N. Omelyanchouk, and R. I. Shekhter, Fiz. Nizk. Temp. **5**, 1543 (1977) [Sov. J. Low Temp. Phys. **3**, 840 (1977)].

[32] I. K. Yanson, in *Quantum Mesoscopic Phenomena and Mesoscopic Devices in Microelectronics*, edited by I. O. Kulik and R. Ellialtioglu, Kluwer Academic Publishers (2000), p. 61, (see also: cond-mat/0008116).

[33] A. N. Omel'yanchuk, S. I. Beloborod'ko, and I. O. Kulik, Fiz. Nizk. Temp. **17**, 1142 (1988) [Sov. J. Low Temp. Phys. **14**, 630 (1988)].

[34] S. I. Beloborod'ko and A. N. Omel'yanchuk, Fiz. Nizk. Temp. **17**, 994 (1991) [Sov. J. Low Temp. Phys. **17**, 518 (1991)].

[35] S. I. Beloborod'ko, private communication.

[36] E. L. Wolf, *Principles of Electron Tunneling Spectroscopy*, Oxford University Press, London (1985).

[37] R. D. Parks, *Superconductivity*, Marcel Dekker, New York (1969).

[38] O. V. Dolgov, R. S. Gonnelli, G. A. Ummarino, A. A. Golubov, S. V. Shulga, and J. Kortus, Phys. Rev. B **68**, 132503 (2003).

[39] G. E. Blonder, M. Tinkham, and T. M. Klapwijk, Phys. Rev. B **25**, 4515 (1982).

[40] Yu. G. Naidyuk, I. K. Yanson, L. V. Tyutrina, N. L. Bobrov, P. N. Chubov, W. N. Kang, Hyeong-Jin Kim, Eun-Mi Choi, and Sung-Ik Lee, JETP Lett. **75**, 283 (2002).

[41] A. B. Kuz'menko, F. P. Mena, H. J. A. Molegraaf, D. van der Marel, B. Gorshunov, M. Dressel, I. I. Mazin, J. Kortus, O. V. Dolgov, T. Muranaka, and J. Akimitsu, Solid State Commun. **121**, 479 (2002).

[42] I. I. Mazin, O. K. Andersen, O. Jepsen, A. A. Golubov, O. V. Dolgov, and J. Kortus, Phys. Rev. B **69**, 056501 (2004).

[43] P. Szabó, P. Samuely, J. Kacmarčik, Th. Klein, J. Marcus, D. Furchart, S. Miragila, C. Marcenat, and A. G. M. Jansen, Phys. Rev. Lett. **87**, 137005 (2001).

[44] R. S. Gonnelli, D. Daghero, G. A. Ummarino, V. A. Stepanov, J. Jun, S. M. Kazakov, and J. Karpinski, Phys. Rev. Lett. **89**, 247004 (2002).

[45] P. Samuely, P. Szabó, J. Kacmarćik, T. Klein, and A. G. M. Jansen, Physica C **385**, 244 (2003).

[46] A. A. Golubov, A. Brinkman, O. V. Dolgov, J. Kortus, and O. Jepsen, Phys. Rev. B **66**, 054524 (2002).

[47] Yu. G. Naidyuk, O. E. Kvitnitskaya, I. K. Yanson, S.-L. Drechsler, G. Behr, and S. Otani, Phys. Rev. B **66**, 140301 (2002).

[48] R. Heid, K.-P. Bohnen, and B. Renker, Adv. Solid State Phys. **42**, 293 (2002); R. Heid, B. Renker, H. Schober, P. Adelmann, D. Ernst, and K.-P. Bohnen, Phys. Rev. B **67**, 180510 (2003).

[49] Takashi Aizawa, Wataru Hayami, and Shigeki Otani, Phys. Rev. B **65**, 024303 (2001).

[50] N. L. Bobrov, P. N. Chubov, Yu. G. Naidyuk, L. V. Tyutrina, I. K. Yanson, W. N. Kang, Hyeong-Jin Kim, Eun-Mi Choi, C. U. Jung, and Sung-Ik Lee, in *New Trends in Superconductivty*, Vol. 67 of NATO Science Series II: Math. Phys. Chem., edited by J. F. Annett and S. Kruchinin, Kluwer Acad. Publ. (2002), p. 225 (see also cond-mat/0110006).

[51] A. A. Golubov, J. Kortus, O. V. Dolgov, O. Jepsen, Y. Kong, O. K. Andersen, B. J. Gibson, K. Ahn, and R. K. Kremer, J. Phys: Condens. Matter **14**, 1353 (2002).

[52] Yu. G. Naidyuk, I. K. Yanson, O. E. Kvitnitskaya, S. Lee, and S. Tajima, Phys. Rev. Lett. **90**, 197001 (2003).

[53] I. O. Kulik, Fiz. Nizk. Temp. **18**, 450 (1992) [Sov. J. Low Temp. Phys. **18**, 302 (1992)].

[54] A. E. Koshelev and A. A. Golubov, Phys. Rev. Lett. **90**, 177002 (2003).

SUPERCONDUCTIVITY, INCLUDING HIGH-TEMPERATURE SUPERCONDUCTIVITY

Features of the local structure of fine-grained HTSC $YBa_2Cu_{2.985}{}^{57}Fe_{0.015}O_y$

A. A. Vishnev, E. F. Makarov, L. G. Mamsurova,* and K. S. Pigalskiy

N. N. Semenov Institute of Chemical Physics of the Russian Academy of Sciences, ul. Kosygina 4, Moscow 119991, Russia

Yu. V. Permyakov

Russian Scientific Research Institute of Physicotechnical and Radiotechnical Measurements, p/o Mendeleevo, Moscow District, 141570, Russia
(Submitted September 16, 2003)
Fiz. Nizk. Temp. **30**, 373–384 (April 2004)

Polycrystalline high-T_c superconductors (HTSCs) with the composition $YBa_2Cu_{2.985}{}^{57}Fe_{0.015}O_y$ ($y \approx 6.92$, $T_c = 91$–91.5 K) with micron and submicron grain sizes are investigated by the method of gamma resonance (Mössbauer) spectroscopy at temperatures of 293, 91, and 78 K. A correlation is found between the changes of the intensities of the components of the Mössbauer spectra and the mean grain sizes $\langle D \rangle$. It is shown that the observed changes in the spectra are caused by an interplane redistribution of oxygen wherein the oxygen content δ in the (CuO_δ) planes increases and the lattice parameter c decreases. This effect is greater for smaller mean grain sizes $\langle D \rangle$. It is concluded that the observed changes in the anion subsystem of the fine-grained HTSCs as compared to bulk equilibrium samples of $YBa_2Cu_3O_{6+\delta}$ are mainly due to a partial interchange of the Y^{3+} and Ba^{2+} cations in them. This interchange may be a result of the nonequilibrium synthesis conditions that must be used to produce HTSCs with micron and submicron grain sizes. © *2004 American Institute of Physics.* [DOI: 10.1063/1.1704613]

INTRODUCTION

In previous studies[1–3] of the magnetic, superconducting, and structural characteristics of polycrystalline high-T_c superconductors $YBa_2Cu_3O_y$ ($T_c \approx 92$ K) with mean grain sizes $\langle D \rangle$ in the micron and submicron range ($\langle D \rangle < 2$ μm) it was found that their properties differ from those of the bulk HTSCs of the same composition and with the same value of T_c. For such samples the values of the lattice parameters, superconducting transition temperature T_c, and oxygen index y do not conform to the relationships established previously for equilibrium HTSCs (see, e.g., Ref. 4), and the variations of a number of magnetic characteristics are correlated with the variation of the mean grain size.

To explain the nature of the variations of the properties observed in fine-grained HTSCs a more detailed study of the real structure of such objects is needed. The integral methods used previously must be supplemented by other methods that are sensitive to features of the local structure. Mössbauer spectroscopy can serve as an effective probe for analysis of the local structure.[5]

In the present study we have used Mössbauer spectroscopy to make a detailed study of the oxygen subsystem of a series of polycrystalline HTSCs with the composition $YBa_2Cu_{2.985}{}^{57}Fe_{0.015}O_y$ ($T_c \approx 91.5$ K) with different mean grain sizes in the range 0.4–2 μm. It will be shown that substantial changes in the shape of the Mössbauer spectra occur with decreasing mean grain size as the result of a redistribution of oxygen around the Cu(1) positions. These

studies have revealed a hitherto unnoticed effect wherein the oxygen content δ in the (CuO_δ) planes of the crystalline cell increases at a constant total oxygen index $y \approx 6.92$. The nature of this effect is apparently due to the existence of a partial antistructure interchange of the Y^{3+} and Ba^{2+} cations in the lattice of HTSCs crystals of small size. It is shown that this effect is more pronounced for smaller mean grain sizes in the HTSC compound under study.

1. EXPERIMENTAL TECHNIQUE

The $YBa_2Cu_{3-x}{}^{57}Fe_xO_y$ ($x = 0.015$) were prepared from a mechanically activated highly disperse mixture of the initial oxides Y_2O_3, CuO, BaO_2, and $^{57}Fe_2O_3$ by the technique described in detail in Refs. 1 and 6. It is known that regulation of the microstructure of HTSCs so as to realize submicron grain sizes is possible only when nonequilibrium synthesis conditions are used.[7] In this study the nonequilibrium conditions were brought about by mechanochemical methods applied to the mixture of initial components in the initial stage of synthesis and also by a subsequent high-speed forming of the structure of the compound at temperatures $T > 800\,°C$. A distinctive feature of this technique is the formation of an orthorhombic lattice of the compound $YBa_2Cu_3O_y$ at $T > 800\,°C$ directly from the amorphous (according to X-ray data) state arising in the initial mixture of oxides as a result of the mechanochemical activation. The main advantage of the method is that it completely eliminates the stage of formation of any intermediate reaction

products. This eliminates any contamination of the final compound by impurities of an accompanying phases, and the complete fixation of the barium ions and the other components in the initial stage of synthesis promotes the chemical purity of the surface of the crystallites.[1,6]

All of the samples were prepared from initial sample No. 1, which was synthesized at the lowest annealing temperature ($T^* = 840\,°C$), by additional high-temperature annealing at temperatures of $T^* = 900$ (sample No. 2) and $T^* = 930\,°C$ (sample No. 3). Saturation of the samples with oxygen is done by the standard method on slow cooling in an atmosphere of oxygen and a subsequent hold for ≈ 2 hours at $500\,°C$. The isothermal high-temperature annealing times were quite long (~ 100 h), since this is necessary for annealing of nonequilibrium defects and the achievement of a quasi-equilibrium state such that further annealing at the same temperature T^* has no effect on the crystal lattice parameters. As was shown in Ref. 1, each quasi-equilibrium state corresponding to a definite T^* is contained by a definite value of the degree of orthorhombic distortion, which is progressively larger the higher the annealing temperature. Since it is the value of T^* that largely determines the parameters of the diffusion of the components, it can be assumed that each quasi-equilibrium state reached in the samples corresponds to a definite degree of cation ordering of the crystal lattice.

The unit cell parameters were calculated from single reflections on X-ray diffraction pattern (a URD-6 diffractometer, CuK_α radiation) in the angle interval $36° < 2\theta < 60°$ using a standard software package (germanium internal standard).

The total oxygen content of the samples was determined from measurements of the magnetic susceptibility in a small alternating magnetic field to an accuracy of $\Delta y = \pm 0.03$.

The value of the superconducting transition temperature T_c was determined to an accuracy of $\Delta T = \pm 0.2$ K from measurements of the magnetic susceptibility in a low alternating magnetic field.

Information about the mean value of the grain size and the size distribution in the samples studied was obtained using a Philips SEM-515 scanning electron microscope.[1)]

The Mössbauer measurements were done on a precision standard gamma-resonance device. The velocity of the gamma-ray source relative to the absorber in this device was set, stabilized, and measured using a laser interferometer, ensuring an accuracy of better than 1 μm/s in the measured values independently of the duration of the experiment and fluctuations of the temperature of the surrounding medium. We used a ^{57}Co source in a Cr matrix at room temperature. The Mössbauer spectra were measured at sample temperatures of 293, 91 and 78 K. The samples for the measurements were mixed in paraffin in the amount of 27 mg/cm^2. The Mössbauer spectra were processed using the program SEFR code. The values of the isomer shifts are given relative to α-Fe.

2. EXPERIMENTAL RESULTS AND DISCUSSION

According to the data of an x-ray analysis, all of the YBa$_2$Cu$_{2.985}$^{57}Fe$_{0.015}$O$_y$ samples were single-phase and had an orthorhombic structure with unit cell parameters a, b, c given in Table I. Also given are the mean value $\langle D \rangle$ and the

TABLE I. Characteristics of the YBa$_2$Cu$_{2.985}$^{57}Fe$_{0.015}$O$_y$ samples.

Sample	$\langle D \rangle$, μm	σ_D, μm	y	T_c, K	a,	b,	c,
					Å		
1	0.4	0.3	6.92	91	3.8355	3.8878	11.6647
2	1	0.55	6.92	91	3.8272	3.8876	11.6790
3	2	1.2	6.93	91.5	3.8246	3.8856	11.690

standard dispersion σ_D of the grain size, the value of the superconducting transition temperature T_c, and the oxygen index y.

It can be seen from Table I that only two parameters were markedly different in the samples studied: the mean grain size $\langle D \rangle$ and the lattice parameter c, and their variations are correlated with each other. This sort of correlation was first established in Ref. 1. The fact that the values of the parameters b, y, and T_c were practically the same for all the samples means that one can correctly do a study of the dependence on the size factor $\langle D \rangle$ in this series of samples.

We note that the values of the parameter b are close to those which are usually realized for equilibrium bulk samples of YBa$_2$Cu$_3$O$_y$ with $y \approx 6.92$.[4] The indicated values of the parameters b and y are optimal for the latter in the sense that they correspond to the highest value of T_c for this compound. Importantly, the characteristics given in Table I practically coincide with those observed in Ref. 1 for samples prepared in a similar way but without iron. The only noticeable change upon the introduction of iron was a slight (not more than 0.5 K) decrease in the value of T_c, as was to be expected for the given concentration $x = 0.015$.[8]

The temperature dependence of the magnetic susceptibility $\chi_{ac}(T)$, from which the value of T_c for the samples was determined, is shown in Fig. 1, where it is seen that the
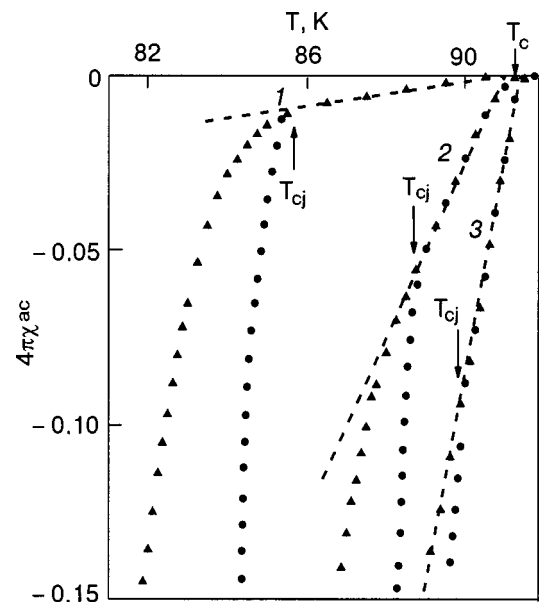

FIG. 1. Temperature dependence of the magnetic susceptibility χ_{ac} measured at two amplitudes of the alternating magnetic field: 0.1 Oe (●) and 3 Oe (▲) for YBa$_2$Cu$_{2.985}$^{57}Fe$_{0.015}$O$_y$ samples (the curves are labeled with the sample No.).

diamagnetic response appears at the same temperature T_c $=91–91.5$ K for all the samples. It is also seen that there are two different regimes of response of the samples to an alternating magnetic field. The first (amplitude-dependent) regime is characterized by the flow of supercurrents around individual crystallite grains and corresponds to the linear part of the $\chi_{ac}(T)$ curve, which intercepts the temperature axis at the point T_c. The second regime sets in at $T_c < T_{cJ}$, where T_{cJ} is the critical temperature for the appearance of supercurrent through the Josephson contacts between grains.

A detailed discussion of these two regimes has been given previously[1,6] and is not pertinent to our present topic. We note only that the differences in the slopes of the linear parts of the $\chi_{ac}(T)$ curves are due to the difference of the mean grain size $\langle D \rangle$ in the samples, since, as was shown in Ref. 1, this slope obeys the relation

$$\frac{d\chi_{ac}}{dT} = \frac{1}{24T_c}\left(\frac{2}{\gamma}+1\right)\left(\frac{\langle D \rangle}{\lambda_{ab}(0)}\right)^2, \qquad (1)$$

where for $YBa_2Cu_3O_y$ the London penetration depth $\lambda_{ab}(0)=0.145$ μm at $T=0$, and the anisotropy parameter $\gamma \approx 7$. The values of $\langle D \rangle$ determined from formula (1) and from the SEM data agree with each other.

Figure 2 shows the Mössbauer spectra obtained for the samples at $T=293$ K. It is seen in Fig. 2 that the Mössbauer spectrum for samples with different grain sizes and, accordingly, different parameters c, are substantially different. A mathematical processing of these spectra showed that they can all be described by a superposition of four symmetric quadrupole doublets with different intensities and different isomer shifts. Table II gives the main parameters of all components of the Mössbauer spectra—the quadrupole splitting QS, the isomer shifts I relative to α-Fe, the relative areas S of the components (normalized to the area of the whole spectrum), and the linewidths HW at half maximum—obtained at $T=293$ K.

The character of the variation of the absolute values of the areas s_i and isomer shifts I_i for each component i of the spectra as the temperature is lowered to 78 K is demonstrated in Fig. 3. (Similar temperature dependence of the analogous quantities for a $YBa_2Cu_{3-x}Fe_xO_7$ sample with $x=0.06$ and $y=6.95$, prepared by the standard ceramic technology, are given in Ref. 9.)

As we see from Tables I and II and Fig. 3a, with decreasing grain size and, accordingly, decreasing lattice parameter c, the relationship of the intensities of the main quadrupole doublets changes substantially. While for sample No. 3 the components $D2$ and $D1$ have the largest area, for the samples with the smaller grain sizes the main doublets are $D2$ and $D4$.

Analysis of published data (see, e.g., Refs. 10–12) shows that the Mössbauer spectra of bulk samples of $YBa_2Cu_{3-x}Fe_xO_7$ ($x \leq 0.1$ and $y > 6.9$) prepared under more equilibrium conditions, as a rule, are superpositions of those same four doublets: $D1(QS \approx 2)$, $D2(QS \approx 1.1)$, $D3(QS \approx 0.6)$, and $D4(QS \approx 1.6)$, where the values of QS are given in millimeters per second. It is important to note, however, that for the fine-grained samples studied here, the relative intensity of the $D4$ doublet is substantially higher, especially for samples Nos. 1 and 2. In addition, the value of the isomer
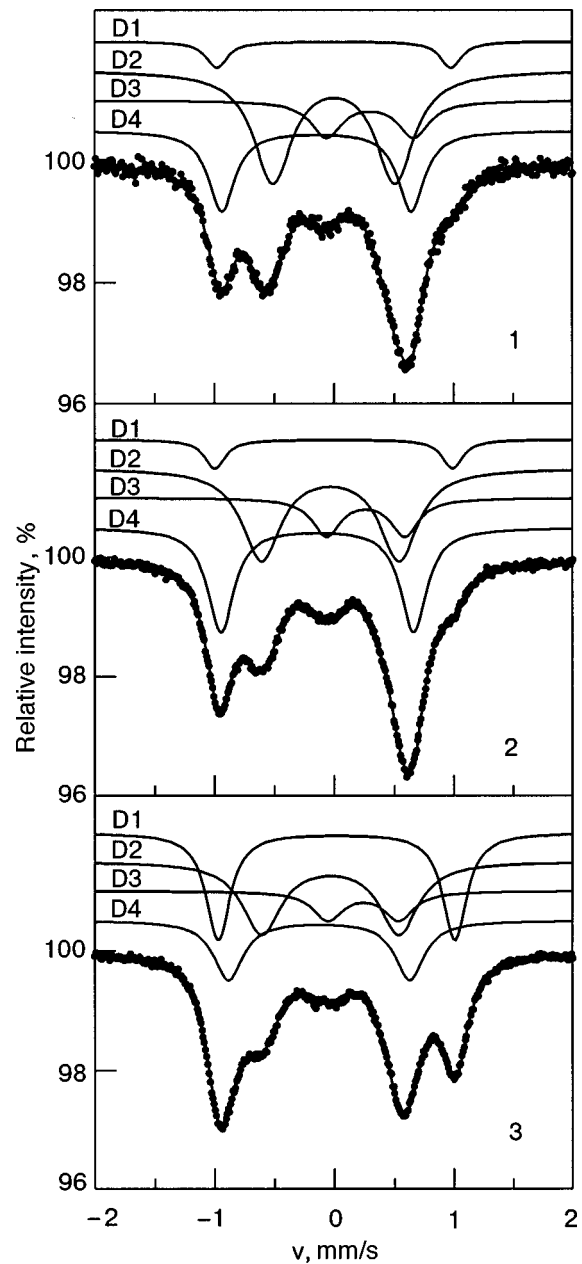
FIG. 2. Mössbauer spectra of polycrystalline samples of $YBa_2Cu_{2.985}{}^{57}Fe_{0.015}O_y$ (at $T=293$ K) with different mean grain sizes and values of the lattice parameter c (the panels are labeled with the sample No.). The solid curves show the components of the spectra.

shift of doublet $D1$ becomes small, and at $T=293$ K is even negative (Table II and Fig. 3b), whereas in the bulk samples the shift is always positive and large in absolute value ($I=0.3–0.6$ mm/s). A similar tendency in the behavior of the isomer shift of the doublet $D1$ was observed under conditions of high pressure in Ref. 13. Apparently this analogy is consistent, since the samples are characterized by predominantly lowered values of the parameter c in comparison with the equilibrium samples of $YBa_2Cu_3O_{6+\delta}$, and decrease of the parameter c can have the same effect as high pressure.

It is well known (see, e.g., Ref. 14) that the ideal crystal lattice of $YBa_2CuO_{6+\delta}$ consists of layers stacked in the following sequence: $\dots-(CuO_\delta)-(BaO)-(CuO_2)-(Y)-(CuO_2)-(BaO)-(CuO_\delta)-\dots$. It is also known[10,11] that upon a weak substitution of copper ions by iron in

TABLE II. Parameters of the Mössbauer spectra obtained at $T = 293$ K.

Sample	Spectrum component	QS	I	HW	S, %
			mm/s		
1	D1	1.95	0.0004	0.21	6.8
	D2	1.08	−0.03	0.39	52.6
	D3	0.73	0.3	0.31	14.0
	D4	1.58	−0.14	0.27	26.6
2	D1	1.99	−0.002	0.21	7.7
	D2	1.16	−0.03	0.37	45.3
	D3	0.62	0.26	0.28	10.7
	D4	1.61	−0.14	0.26	36.3
3	D1	1.97	0.02	0.24	33.4
	D2	1.13	−0.03	0.38	35.4
	D3	0.60	0.28	0.23	7.6
	D4	1.52	−0.12	0.31	23.6

$YBa_2Cu_{3−x}Fe_xO_y$ ($x < 0.1$) practically all the iron ions are located in the Cu(1) sites in the (CuO_δ) planes, and the introduction of iron into this compound leads to trapping of additional oxygen in the amount of one O atom for every two Fe atoms. In the majority of papers (see, e.g., Refs. 11 and 12) it is assumed that the quadrupole doublets $D1$, $D2$, $D3$, and $D4$ correspond to the following oxygen coordinations of ^{57}Fe in the Cu(1) sites (see Fig. 4): doublet $D1$ to a fourfold coordination of a plane rhombus $[2O(1)+2O(4)]$, doublet $D2$ to a fivefold pyramidal coordination (where two types of pyramids can exist, with axes directed along the a and b axes of the crystal, $[2O(1)+2O(4)+O(5)]$ or $[2O(1)+O(4)+2O(5)]$); doublet $D3$ to a sixfold octahedral coordination $[2O(1)+2O(4)+2O(5)]$; doublet $D4$ to a highly distorted tetrahedron $[2O(1)+O(4)+O(5)]$. Here we use the standard notation O(4) and O(5) for the oxygen positions in the (CuO_δ) plane and O(1) for the apical oxygen, which belongs to the (BaO) plane (see Fig. 4).

In analyzing the possible variants of the local environment of the iron atoms found in the Cu(1) sites (Fig. 4) and comparing them with the oxygen coordinations for Cu(1) in the equilibrium samples of $YBa_2CuO_{6+\delta}$ ($0.5 < \delta < 1$), which have close to the ideal crystal lattice (see, e.g., Ref. 14), one notices a difference: in the fine-grained samples the oxygen positions O(5) are populated to a considerable degree, whereas in the equilibrium samples at $0.5 < \delta < 1$ these positions are predominantly vacant.

The oxygen atoms found in the O(5) positions can be divided into two types. Those of the first type form a fourfold coordination corresponding to the doublet $D4$. In this case the oxygen atoms occupy the O(5) instead of the O(4) positions. Because of this, the presence of doublet $D4$ should be regarded as a manifestation of a certain type of structural defect state of the fine-grained samples, since the ideal structure of this compound corresponds only to fourfold coordination of the $D1$ type, which reflects the existence of characteristic chains Cu(1)–O(4)–Cu(1) in the (CuO_δ) planes of the unit cell.

The second type of oxygen atoms in the O(5) positions are those which form five- or sixfold coordination, corresponding to doublets $D2$ and $D3$. In this case the oxygen atoms occupy O(5) positions in addition to the occupied O(4) positions, i.e., there are "extra" atoms in comparison with the ideal structure of the equilibrium compound $YBa_2CuO_{6+\delta}$ ($0.5 < \delta < 1$). Since, as we have said, when Fe^{3+} ions are substituted for Cu^{2+}, "half" of the iron atoms trap an additional oxygen, it is natural to assume that the population of the given O(5) positions corresponding to doublets $D2$ and $D3$ can occur precisely because of this extra trapped oxygen. Then, however, the number of these must not exceed 50% of the number of ^{57}Fe atoms. However, there is another possibility, namely that there is excess oxygen in the (CuO_δ) plane unrelated to the presence of iron in it. In that case the total number of oxygen atoms found in the O(5) positions and forming doublets $D2$ and $D3$ will exceed that value by 50% of the number of iron atoms.

Judging from the experimental values of the relative areas of the Mössbauer components, one can obtain a quantitative estimate of the total fraction of "excess" oxygen atoms in our particular fine-grained HTSC samples.

In the first step we shall compare the value of the relative area of the ith quadrupole doublet $S_{Di} = s_i / \Sigma s_i$ (Table II) with the fractions n_i of iron atoms in the given coordination, neglecting the other factor influencing this relative area—the Mössbauer effect probability f_i for the given coordinate of the iron.[5] The influence of this factor is taken into account in Sec. 3.

It is clear that the formation of the fivefold and sixfold coordinations corresponding to doublets $D2$ and $D3$, respectively, requires one or two "extra" oxygen atoms in the O(5) position in addition to the oxygen atoms located in the O(4) and O(1) positions. If the fractions of the iron in the six- and fivefold coordinations are $n_3 = S_{D3}$ and $n_2 = S_{D2}$, respectively, then the sum $(2S_{D3} + S_{D2})$ will comprise the total fraction of excess oxygen in the O(5) positions. It is easily found from the data of Table II that this sum is equal to approximately 50% only for sample No. 3 ($2 \cdot 7.6\% + 35.4\% = 50.6\%$). For samples Nos. 1 and 2 the sum $2S_{D3} + S_{D2}$ is appreciably higher than 50%. It is 80.6% for sample No. 1 and 66.7% for sample No. 2. These elevated values of the parameter $2S_{D3} + S_{D2}$ are unambiguous evidence of the existence of an appreciable amount of excess oxygen occupying the O(5) positions in the (CuO_δ) plane for samples Nos. 1 and 2, but which here is unrelated to the presence of iron in the Cu(1) positions.

Let us obtain numerical estimates of δ, which reflects the amount of oxygen occupying the O(4) and O(5) positions in the (CuO_δ) plane, for samples Nos. 1 and 2. To do this we must determine the mean coordination number $\langle k \rangle$ realized for the Cu(1) positions:

$$\langle k \rangle = \sum k_i n_i - 0.5 \approx \sum k_i S_{Di} - 0.5 \qquad (2)$$

where k_i is the coordination number for the Cu(1) position
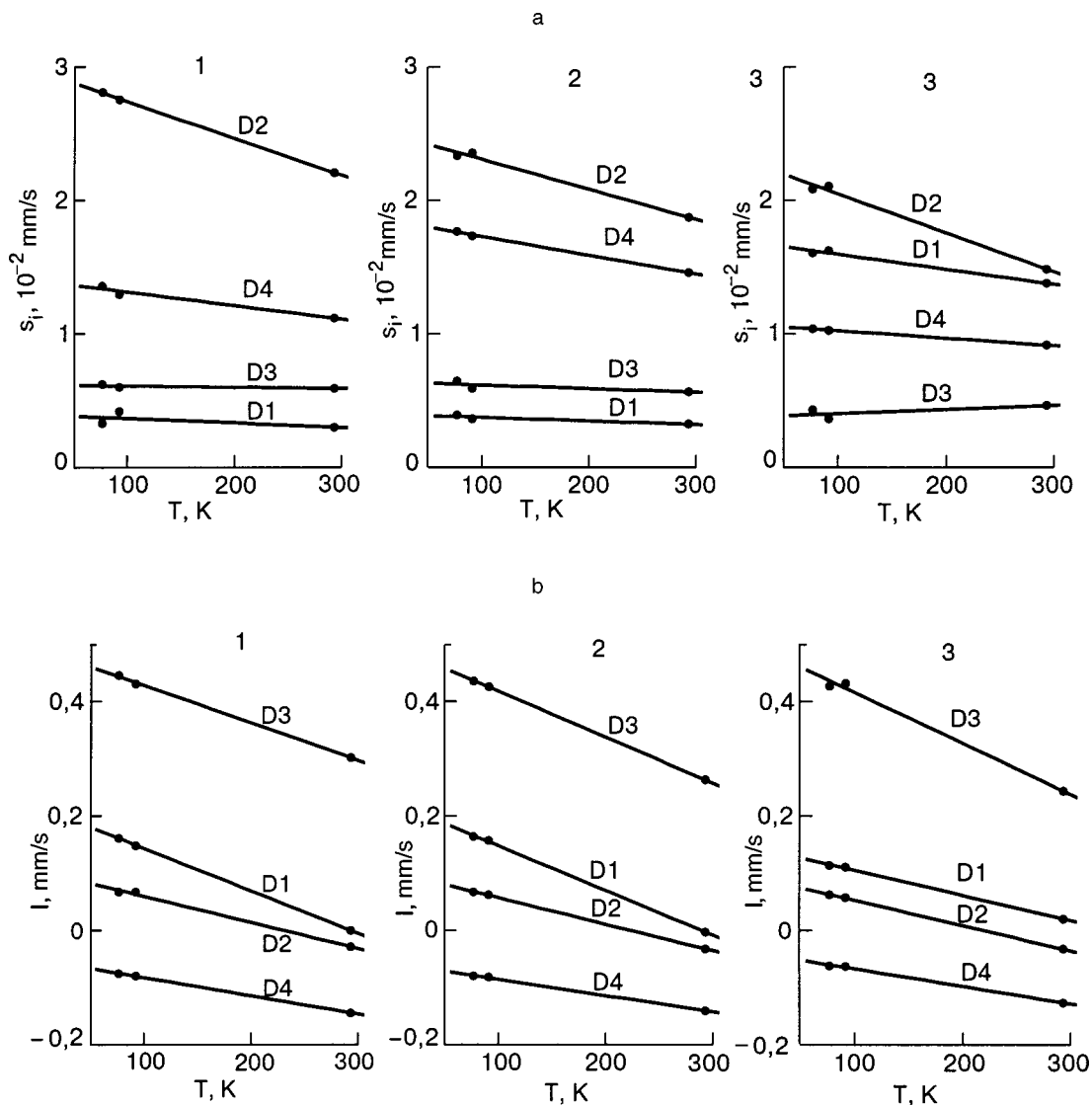
FIG. 3. Temperature dependence of the areas (a) and isomer shifts (b) for four components of the Mössbauer spectra of the $YBa_2Cu_{2.985}{}^{57}Fe_{0.015}O_y$ samples. The numbers 1, 2, and 3 correspond to the sample No.

occupied by iron and corresponding to the ith component of the Mössbauer spectrum. The presence of the second term in expression (2) takes into account that in going from iron ions to copper one must subtract the trapped oxygen in the amount of 0.5 per iron ion. Thus the value of $\langle k \rangle$ characterizes that value of the coordination number for the Cu(1) positions which would obtain in the case of arbitrary distribution of the oxygen over the positions O(1), O(4), and O(5) for any amount of oxygen (here the additional oxygen trapped by the iron is taken out of consideration). As we showed in Ref. 15, in the case of an excess oxygen content in the (CuO_δ) plane, i.e., when the O(5) positions are partially occupied, the oxygen environments of the iron and copper turn out to be practically equivalent, and such an approach is justified.

To obtain the total amount of oxygen in the O(4) and O(5) positions it is necessary to subtract the two oxygen atoms found in the O(1) positions from the value of $\langle k \rangle$ and divide the result by 2 per unit cell. Thus

$$\delta = (\langle k \rangle - 2)/2 \tag{3}$$

By straightforward calculations using formulas (2) and (3) and the data of Table II, we obtain the values $\langle k \rangle = 4.3$ and 4.2, $\delta = 1.15$ and 1.10 for samples Nos. 1 and 2, respectively.

These estimates must be refined by doing additional calculations with allowance for the difference of the Mössbauer effect probabilities in each oxygen coordination. However, as will be shown in Sec. 3, taking the given factor into account has practically no effect on the result given above.

If we assume that the oxygen positions O(1), O(2), and O(3) lying in the interior planes of the unit cell are completely occupied, as in an equilibrium sample of $YBa_2CuO_{6+\delta}$, then the values obtained for the parameter δ mean that our fine-grained samples Nos. 1 and 2 have an oxygen content equal to that which would obtain in equilibrium samples with oxygen index $y = (6 + \delta) = 7.15$ and 7.1, respectively.

However, as we have said, it follows from the iodometric titration data that the total oxygen content in these samples is approximately the same, $y = 6.92 - 6.93$. These
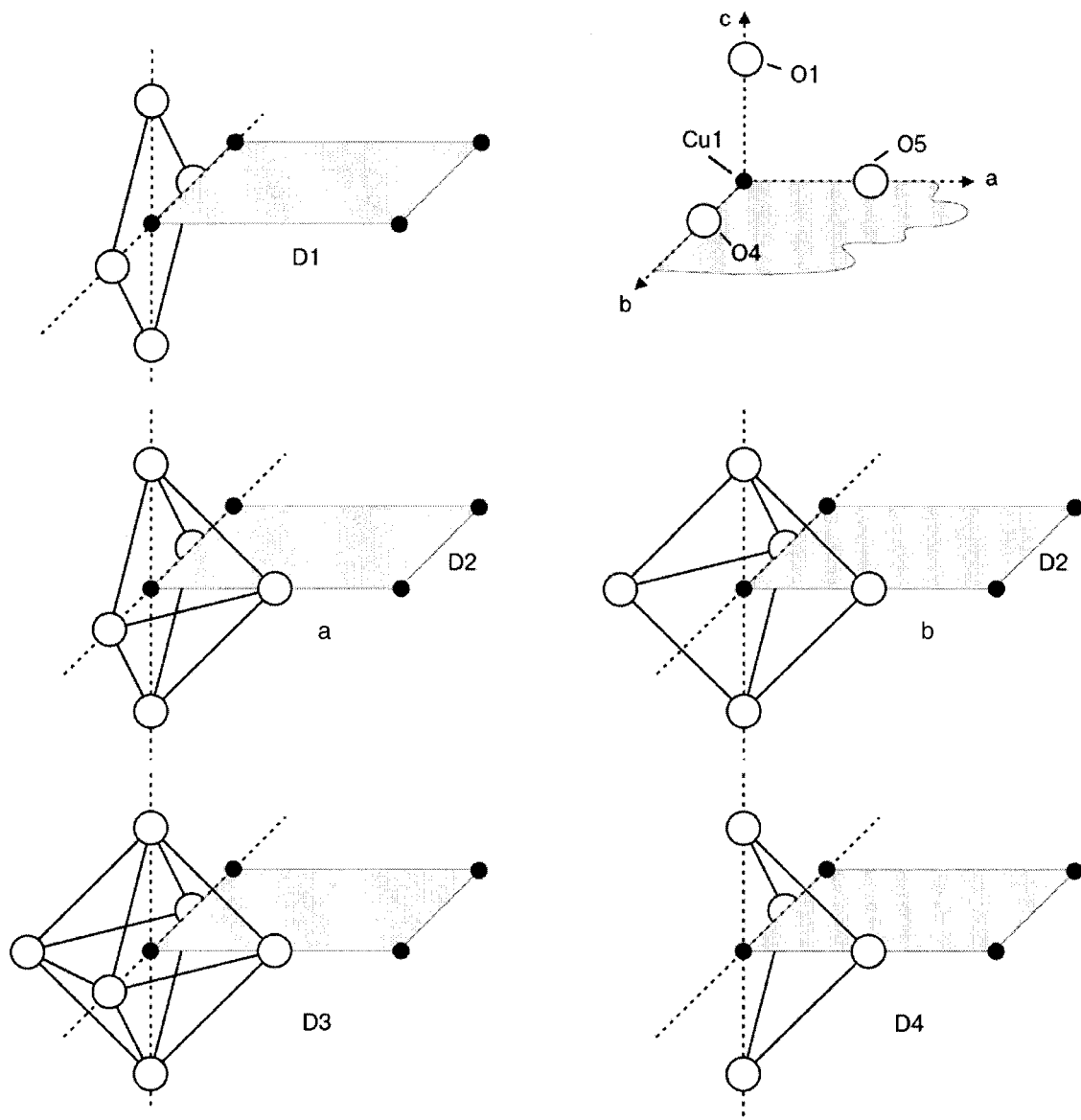
FIG. 4. Variants of the local oxygen environment of iron atoms in the Cu(1) positions of the crystal structure of the compound $YBa_2Cu_{3-x}Fe_xO_y$, corresponding to the components $D1$, $D2$, $D3$, and $D4$ of the Mössbauer spectra. Shown in the upper right-hand corner are the directions of the crystallographic axes and the positions of Cu(1) and oxygen in the nearest environment of the given positions.

two contradictory facts can be reconciled as follows. At a constant total oxygen concentration y an increase in the amount of oxygen in the exterior, (CuO_δ) planes of the unit cell means a decrease in the amount of oxygen in the interior, (CuO_2) and (BaO) planes. Consequently, the second component of y, characterizing the amount of oxygen in the O(1), O(2), and O(3) positions, is smaller in our samples than the value $y-\delta=6$ inherent to equilibrium samples of $YBa_2CuO_{6+\delta}$.

Such a situation is entirely possible in the case when antistructure interchange is present in the cation sublattice, $Y^{3+}\leftrightarrow Ba^{2+}$. An interchange of this kind requires that additional oxygen enter the defective, (CuO_δ) plane. In this case one can speak of enhancement of the Coulomb attraction between layers, which corresponds to a decrease in the structural parameter c, which is actually observed in our samples. We assume that a certain contribution to the realization of the cation disordering comes in because of the use of mechanochemical activation of the mixture of initial components in

the initial stage of the synthesis and also because of the high-speed regime of formation of the crystal structure of these compounds, i.e., the nonequilibrium synthesis conditions that in some form or other are always used to obtain a fine-grained crystal structure of the compounds under study.

3. CALCULATION OF THE RELATIVE FRACTIONS OF ⁵⁷Fe ATOMS LOCATED IN DIFFERENT OXYGEN COORDINATIONS, WITH ALLOWANCE FOR THE MÖSSBAUER EFFECT PROBABILITY

For "thin" samples the experimentally observable area of the ith component s_i of the Mössbauer spectrum can be written in the form[5]

$$s_i(T) \sim \sigma_i f_i(T), \tag{4}$$

where σ_i is the surface density of iron ions in the ith oxygen environment, and $f_i(T)$ is the Mössbauer effect probability

for these ions. Then we obtain the following expression for the relative fraction of iron located in the ith oxygen coordination:

$$n_i = \frac{\sigma_i}{\Sigma_i \sigma_i} = \frac{s_i(T)}{f_i(T)} \left[\sum_{j=1}^{N} \frac{s_j(T)}{f_j(T)} \right]^{-1}, \tag{5}$$

where N is the total number of possible oxygen coordinations (in our case $N=4$), which are labeled by the number j.

The values of $s_i(T)/s_j(T)$ are determined experimentally. Consequently, for correct calculation of the desired n_i values, we must evaluate the ratios $f_i(T)/f_j(T)$.

The Mössbauer effect probability is known to be given by[5]

$$f_i(T) = \exp\left\{ \frac{1}{\hbar^2} \langle x^2 \rangle_i \right\}, \tag{6}$$

where $\hbar = \lambda/2\pi$, λ is the wavelength of the γ ray, and $\langle x'^2 \rangle$ is the mean square projection of the amplitude of the vibrations of the Mössbauer ion in the direction of the γ rays. For a polycrystalline sample with a random orientation of the crystallites, we obtain, after averaging over their orientation angles,

$$f_i(T) = \exp\left\{ -\frac{1}{2\hbar^2} \langle x^2(T) \rangle_i \right\}, \tag{7}$$

where $\langle x^2 \rangle_i$ is the mean square vibrational amplitude of the Mössbauer ion in the ith oxygen coordination in the polycrystalline sample, and the averaging is to be done over all possible modes of its vibrational spectrum.

The result of a calculation of $f_i(T)$ depends on the kind of the model adopted for the vibrational spectrum of the crystal. Among the most often used is the Debye model, which in the case of a cubic monoatomic crystal gives a correct description of the experimental $f(T)$ curves. However, as was shown in Refs. 16 and 17, the Debye model is completely inapplicable in the case of the noncubic polyatomic lattice of $YBa_2Cu_3O_y$.

It is known that the vibrational spectrum of any crystal in the presence of impurity ions (in our case, the iron ions), even in a very low concentration, in the general case consists of energy bands and several discrete levels.[18] Here a substantial part of the energy of the whole vibrational spectrum turns out to be concentrated at the impurity atom (spatially localized) in the form of energy of its motion. Therefore, it becomes possible to consider the impurity atom as a coherent oscillator in accordance with the Einstein model, with its typical equidistant discrete levels of excitation with energies $(n+1/2)\hbar\omega_i$, where $n=0,1,2,\dots$, and $\hbar\omega_i$ is the vibrational energy of the characteristic oscillator for each ith oxygen configuration. Thus, to the ^{57}Fe atom of each oxygen coordination one can associate an eigenfrequency ω_i and a characteristic temperature θ_i, which are related to each other by $k_B\theta_i = \hbar\omega_i$ (k_B is Boltzmann's constant).

In the framework of the harmonic oscillator model the values of ω_i and θ_i can be determined from a joint consideration of the temperature dependences of the areas and isomer shifts of the components of the spectrum. For this it is not necessary to use a concrete form of vibrational energy spectrum.

It follows from formula (7) that

$$\frac{f_i(T_1)}{f_i(T_2)} = \exp\left\{ -\frac{1}{2\hbar^2} [\langle x^2(T_1) \rangle_i - \langle x^2(T_2) \rangle_i] \right\}. \tag{8}$$

On the other hand, the difference of the isomer shifts measured at two different temperatures (the temperature shift) for the ith configuration has the form[5]

$$I_i(T_1) - I_i(T_2) = \frac{1}{2c} [\langle v^2(T_2) \rangle_i - \langle v^2(T_1) \rangle_i], \tag{9}$$

where $\langle v^2(T) \rangle_i$ are the mean square vibrational velocities of the Mössbauer atom in the ith oxygen environment, and c is the speed of light.

In the framework of the harmonic oscillator model we have

$$\langle v^2(T) \rangle_i = (\omega_i)^2 \langle x^2(T) \rangle_i. \tag{10}$$

From Eqs. (8)–(10) we obtain

$$I_i(T_1) - I_i(T_2) = \frac{\hbar^2(\omega_i)^2}{c} \ln\left[\frac{f_i(T_1)}{f_i(T_2)} \right]. \tag{11}$$

It follows from Eq. (4) that

$$\frac{s_i(T_1)}{s_i(T_2)} = \frac{f_i(T_1)}{f_i(T_2)}; \tag{12}$$

and also using that relation and the relation between the wavelength and energy E_0 of a γ quantum, we obtain from Eq. (11) the following expression for the characteristic temperature:

$$\theta_i = \frac{E_0}{k_B\sqrt{c}} \left[\frac{I_i(T_1) - I_i(T_2)}{\ln(s_i(T_1)/s_i(T_2))} \right]^{1/2}. \tag{13}$$

On the other hand, if it is assumed that the vibrational spectrum of the iron ion in the compound under study is described by the Einstein model, then the expression for the temperature dependence of the Mössbauer effect probability is written in the form[5]

$$f_i(T) = \exp\left\{ -\frac{R}{\hbar\omega_i} \coth\left(\frac{\hbar\omega_i}{2k_BT} \right) \right\}, \tag{14}$$

where R is the recoil energy of the free Mössbauer nucleus ^{57}Fe upon the absorption of a γ quantum ($R = E_0^2/2mc^2 = 1.81 \times 10^{-3}$ eV).

With Eq. (12) taken into account, expression (14) allows one to determine the values of ω_i and, hence, θ_i for each oxygen configuration from the experimental values of the area ratios of the corresponding spectral components measured, e.g., at two temperatures T_1 and T_2.

Thus the determination of θ_i (or ω_i) can be done by two methods that, to a certain extent, are independent: either from the temperature dependence $s_i(T)$ with the use of formulas (14) and (12) in the framework of the chosen model, or by additionally invoking the results of measurements of the isomer shifts $I_i(T)$ and using formula (13).

TABLE III. Characteristics of the Mössbauer atom ^{57}Fe in the different oxygen coordinations realized in the HTSC YBa$_2$Cu$_{2.985}$^{57}Fe$_{0.015}$O$_y$.

Spectrum component	θ_i, K	ω_i, 10^{13} rad/s	f_i		
			$T = 0$	$T = 78$ K	$T = 293$ K
D1	230 ± 10	3.0	0.91	0.90	0.77
D2	190 ± 10	2.5	0.89	0.87	0.68
D3	500 ± 10	6.5	0.96	0.96	0.94
D4	210 ± 10	2.7	0.90	0.88	0.73

It turned out that results of a calculation by the two methods for each doublet are in good agreement with each other; this tends to confirm the correctness of the Einstein model for calculating the temperature dependence of the parameters of the Mössbauer spectra for ^{57}Fe impurity atoms in samples of the HTSC YBa$_2$Cu$_3$O$_y$. Table III gives the average values of the characteristic temperatures θ_i and eigenfrequencies for all four oxygen coordinations, corresponding to the doublets $D1$, $D2$, $D3$, and $D4$ of the Mössbauer spectra. Also given there are the corresponding values of the Mössbauer effect probabilities calculated according to formula (14). It should be noted that the differences in the values of θ_i, which might be expected for samples with different grain sizes, are small if they exist at all (the differences do not exceed the error limits).

We also note that in the Einstein model for $T < \theta_i/2$ the values of $f_i(T)$ become practically independent of temperature (as is seen from Table III, the results of the calculation of f_i for $T = 0$ and $T = 78$ K are close). As a result, the values which we seek for the ratios $f_i(T)/f_j(T)$ turn out to be very close to unity and can be ignored when using formula (5) to calculate n_i from the experimental data measured at $T < 100$ K. However, the differences of the values f_i found for the different components of the spectrum at $T = 293$ K are more substantial and must be taken into account in the calculation of n_i.

Table IV gives the calculated values of the relative fractions of ^{57}Fe atoms in different oxygen coordinations according to formula (5) for temperatures of 78 and 293 K (calculated using the values of $f_i(T)$ given in Table III). It is seen that the values of n_i are in good agreement with each other

(this attests to the absence of appreciable redistribution of the oxygen ions with temperature). At the same time, they are somewhat different (they differ, in the main, by no more than 10%) from the values of S_i given in Table II. (Recall that in the first step of the calculations we assumed that $n_i = S_i$.) However, as calculations show, the values of the mean coordination number $\langle k \rangle$ and oxygen content δ in the (CuO$_\delta$) planes (see formulas (2) and (3)) are practically the same for the two versions of the calculations: both with and without allowance for the Mössbauer effect probability. Such agreement can be explained by the features of the temperature dependence of $s_i(T)$ for the different components of the Mössbauer spectra of the compounds under discussion.

CONCLUSION

In this study we have for the first time made Mössbauer measurements at $T = 293$, 91, and 78 K for fine-grained samples of the HTSC YBa$_2$Cu$_{2.985}$^{57}Fe$_{0.015}$O$_{6.92}$ ($T_c \approx 91.5$ K) having different mean grain sizes in the range 0.4–2 μm. The main variation with changing grain size in the samples studied was in the value of the lattice parameter c and, somewhat weaker, in the parameter a, while the values of T_c, the oxygen index y, and the parameter b remain practically unchanged (the latter circumstance makes this series of samples suitable for studying the influence of the size factor).

It was found that the form of the Mössbauer spectra is substantially different for samples with different grain sizes, and in the evolution of the components of the Mössbauer spectra a correlation is observed between the mean grain size $\langle D \rangle$ and the value of the lattice parameter c.

A qualitative analysis of the Mössbauer spectra obtained led us to conclude that the occupation of the O(5) positions in the (CuO$_\delta$) planes is anomalously high. For samples with submicron grain sizes the total fraction of oxygen located in the O(5) positions is markedly larger than what could be due to additional trapping of oxygen by Fe^{3+} ions substituting for Cu^{2+}.

We have for the first time proposed a method of quantitative estimation of the oxygen content δ in the (CuO$_\delta$) planes based on joint consideration of the experimental temperature dependence of the areas and isomer shifts of the Mössbauer components and a calculation of the relative fractions of iron ions in the ith oxygen coordination with allowance for the Mössbauer effect probability in each coordina-

TABLE IV. Relative fractions n_i of ^{57}Fe atoms in different oxygen coordinations corresponding to the different components of the Mössbauer spectra, the mean coordination numbers $\langle k \rangle$ for the Cu(1) positions, and the oxygen content δ in the (CuO$_\delta$) planes.

Sample	$T = 78$ K						$T = 293$ K					
	n_i, %				$\langle k \rangle$	δ	n_i, %				$\langle k \rangle$	δ
	D1	D2	D3	D4			D1	D2	D3	D4		
1	6.2	55.9	11.2	26.7	4.283	1.142	6.6	56.1	10.9	26.4	4.279	1.140
2	7.5	46.3	11.6	34.6	4.190	1.098	7.2	47.7	10.4	34.7	4.185	1.093
3	30.6	41.0	8.3	20.1	4.076	1.038	31.3	38.2	8.6	21.9	4.054	1.027

tion. The estimates obtained for the oxygen content δ for HTSC samples with mean grain sizes of from 1 to 0.4 μm showed elevated values $\delta > 1$ in comparison with the values for equilibrium samples of $YBa_2CuO_{6+\delta}$, for which, as a rule, $\delta < 1$.

The given values for the oxygen content δ in the (CuO_δ) planes, in view of the fact that the total oxygen content in the samples was a practically constant $y \approx 6.92$, allowed us to conclude that the crystal structure of superconductors of micron and submicron size contains antistructure interchange of the type $Y^{3+} \leftrightarrow Ba^{2+}$ in the cation sublattice. This type of interchange should lead not only to an increase of the oxygen content in the (CuO_δ) planes but also to a decrease of the amount of oxygen in the other, internal planes of the unit cell and also to a decrease in the lattice parameter c (as a result of the enhancement of the Coulomb attraction between different planes). The latter is usually observed for HTSC samples with small grain sizes, independently of the methods of preparation.

A possible cause of the inferred changes in the local structure in fine-grained HTSCs in comparison with their bulk equilibrium analogs lies in the nonequilibrium synthesis conditions that must be used to get fine-grained samples. There is reason to assume that the inferred features of the local structure may be an inseparable property of any sample of a HTSC of the $YBa_2Cu_3O_y$ type, the real structure of which is not completely equilibrium, and are the reason for the experimentally observed variations of the physical properties of such objects (see, e.g., Ref. 1).

The results are also of interest in that all of the inferred changes in structure occur without a substantial change in the superconducting transition temperature T_c, which is usually extremely sensitive to defects of the crystal structure. Additional studies will be needed to ascertain the reasons for this behavior of T_c in fine-grained samples of HTSCs.

*E-mail: mamsurova@chph.ras.ru
[1])The SEM studies were done in the Electron Microscopy Laboratory of the Moscow Institute of Electronic Engineering.

[1] A. A. Vishnev, L. G. Mamsurova, K. S. Pigalskiy, and N. G. Trusevich, Khim. Fiz. **21**, 86 (2002).

[2] A. S. Krasil'nikov, L. G. Mamsurova, K. K. Pukhov, N. G. Trusevich, and L. G. Shcherbakova, Zh. Éksp. Teor. Fiz. **109**, 1006 (1996) [JETP **82**, 542 (1996)].

[3] A. S. Krasilnikov, L. G. Mamsurova, N. G. Trusevich, L. G. Shcherbakova, and K. K. Pukhov, Supercond. Sci. Technol. **8**, 1 (1995).

[4] Ch. Kruger, K. Konder, K. Schwer, and E. Kaldis, J. Solid State Chem. **134**, 356 (1997).

[5] V. I. Goldanskii and E. F. Makarov, in *Chemical Applications of Mössbauer Spectroscopy*, edited by V. I. Goldanskii and R. H. Herber, Academic Press, New York and London (1968), Mir, Moscow (1970).

[6] A. A. Vishnev, L. G. Mamsurova, K. S. Pigalskiy, N. G. Trusevich, and L. G. Shcherbakova, Khim. Fiz. **15**, 102 (1996).

[7] Yu. D. Tret'yakov and Kh. Lyapis, *Chemistry and Technology of Solid-Phase Materials* [in Russian], MGU, Moscow (1985).

[8] J. Zhang, L. Liu, Ch. Dong, J. Li, H. Chen, X. Li, and G. Cheng, Phys. Rev. B **65**, 054513 (2002).

[9] V. V. Eremenko, D. V. Lukashev, and V. L. Ponomarchuk, Fiz. Nizk. Temp. **28**, 1163 (2002) [Low Temp. Phys. **28**, 830 (2002)].

[10] A. M. Balagurov, G. M. Mironova, N. S. Lyubutin, V. G. Terziev, and A. Ya. Shapiro, Sverkhprovodimost' (KIAE) **3**, 615 (1990) Superconductivity **3**, 580 (1990)].

[11] N. S. Lyubutin, V. G. Terziev, E. M. Smirnovskaya, and A. Ya. Shapiro, Sverkhprovodimost' (KIAE) **3**, 63 (1990) [Superconductivity **3**, S424 (1990)].

[12] Ch. Blue, Kh. Elgaid, I. Zitkovsky, P. Boolchand, D. McDaniel, W. C. H. Joiner, J. Oostens, and W. Huff, Phys. Rev. B **37**, 5905 (1988).

[13] V. A. Shabashov, V. V. Sagaradze, A. G. Golikov, and T. M. Lapina, Sverkhprovodimost: Fiz., Khim., Tekh. **6**, 1043 (1993).

[14] R. J. Cava, Science **247**, 656 (1990).

[15] Yu. V. Baldokhin, A. A. Vishnev, I. V. Kolbanev, E. F. Makarov, L. G. Mamsurova, K. S. Pigalskiy, and A. S. Solomatin, Khim. Fiz. **22**, 59 (2003).

[16] Yu. M. Kagan, Zh. Éksp. Teor. Fiz. **41**, 659 (1961) [Sov. Phys. JETP **14**, 459 (1962)].

[17] Yu. M. Kagan and V. A. Maslov, Zh. Éksp. Teor. Fiz. **41**, 1296 (1961) [Sov. Phys. JETP **14**, 922 (1962)].

[18] Yu. M. Kagan and Ya. A. Iosilevskiĭ, Zh. Éksp. Teor. Fiz. **42**, 259 (1961) [Sov. Phys. JETP **15**, 182 (1961)].

Translated by Steve Torstveit

Structural and high-frequency (0–110 MHz) resistive characteristics of MgB₂ in the temperature range 5–300 K

V. M. Dmitriev*

B. Verkin Institute for Low Temperature Physics and Engineering, National Academy of Sciences of Ukraine, pr. Lenina 47, Kharkov 61103, Ukraine; International Laboratory of High Magnetic Field and Low Temperatures, 95 Gajowicka St. 53-421, Wroclaw, Poland

N. N. Prentslau, V. N. Baumer, N. N. Galtsov, L. A. Ishchenko, A. L. Prokhvatilov, M. A. Strzhemechny, and A. V. Terekhov

B. Verkin Institute for Low Temperature Physics and Engineering, National Academy of Sciences of Ukraine, pr. Lenina 47, Kharkov 61103, Ukraine

A. I. Bykov, V. I. Liashenko, Yu. B. Paderno, and V. N. Paderno

I. N. Frantsevich Institute of Problems of Materials Science, National Academy of Sciences of Ukraine, ul. Krzhizhanovskogo 3, Kiev 03142, Ukraine

The structure and resistivity of polycrystalline MgB₂ and its impedance at frequencies of 9–110 MHz are determined in the temperature range 5–300 K. It is shown that the lattice type and symmetry of the superconducting phase of MgB₂ remain unchanged over this temperature range. At the superconducting transition temperature $T_c = 39.5$ K a structural instability is observed which is accompanied by an overshoot of the measured lattice parameters. It is concluded that the strain of the crystals upon a change in temperature is of a substantially anisotropic character. Measurements of the temperature and frequency dependence of the surface resistance $R_s(T,f)$ in the superconducting state reveal a transition from the Pippard nonlocal limit at $T \ll T_c$ to the London local limit near T_c. At $T/T_c < 0.76$ the value of $R_s(T)$ is well described by an exponential dependence $\exp(-\Delta(T)/kT)$ in accordance with the BCS theory. © *2004 American Institute of Physics.* [DOI: 10.1063/1.1704614]

INTRODUCTION

Although magnesium diboride MgB₂ was synthesized in the early 1950s,[1] it was only in 2001 that superconductivity with $T_c = 39$ K was discovered in it,[2] and this immediately aroused a heightened interest in this new type of superconductor. It was not long before technologies were developed for preparing magnesium diboride samples of different form (polycrystals, thin films, powders, wires, ribbons, and single crystals), and the characteristics of this compound have been investigated in hundreds of studies. The results of much of the research on the physical properties of MgB₂ in the region of the $N-S$ transition have been systematized in a review article.[3]

Magnesium diboride has a hexagonal lattice of symmetry $P6/mmm$ (D_{6h}^1) with one formula unit in the cell.[4] The structure is substantially anisotropic and consists of an alternation of a hexagonal "honeycomb" network of boron (which is like the carbon network in graphite) and hexagonal close-packed layers of magnesium (Fig. 1). According to the first precision x-ray data,[4] the lattice parameters of MgB₂ at room temperature have the values $a = (3.083 \pm 0.0003)$ Å, $c = (3.5213 \pm 0.0006)$ Å. The nearest distance between neighboring atoms is 3.08 Å in the magnesium layers, 1.78 Å in the boron layers, and 3.52 Å between layers of the same type. The shortest distance between magnesium and boron of neighboring layers is 2.5 Å. It is assumed[3] that the high

transition temperature for a superconductor of the BCS type is due mainly to the quasi-two-dimensionality of the structure and the substantial anisotropy of the interatomic interaction in the boron subsystem. A number of recent studies[2,5–9] at room temperature have found similar but different values of the lattice parameters (Table I).

The differences can be due not only to errors of the diffraction techniques but also to technological features of the synthesis of magnesium diboride in different studies. As a result of this, it is possible, for example, to have a partial substitution of the components of the compound by impurities, breakdowns of stoichiometry, etc. The references cited in Table I deal mainly with the structural characteristics of magnesium diboride. At the same time, there is not much information in the literature on the high-frequency losses of MgB₂, and the papers known to us mainly give data on the electromagnetic properties of this compound in the high-frequency and optical ranges. There are practically no data in the literature on the surface resistance of magnesium diboride.

In this paper we give the following experimental results.

First, we have done x-ray studies of MgB₂ by the powder method not only at room temperature but also in the region of the transition to the superconducting state. The following structural characteristics are obtained in the whole interval 5–293 K: the intensities and half-widths of the re-
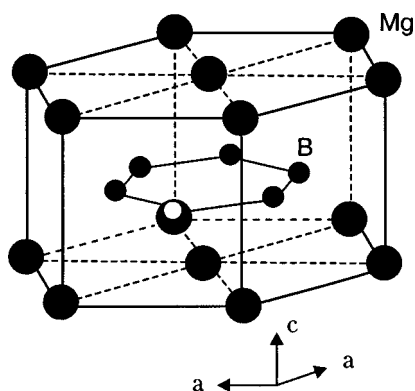
FIG. 1. Crystal structure of magnesium diboride MgB_2 (hexagonal lattice of symmetry $P6/mmm$ (D_{6h}^1)).
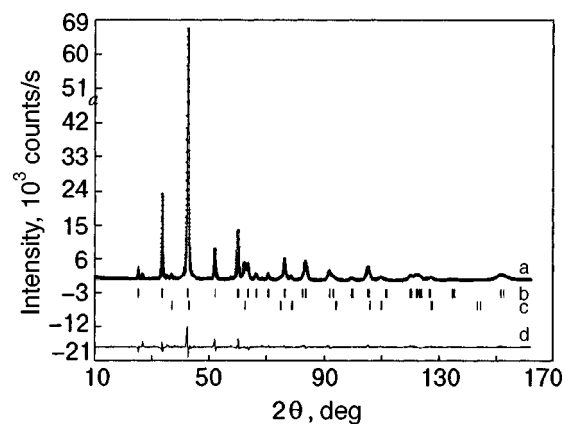

FIG. 2. Typical x-ray diffractometer trace of one of the magnesium diboride samples at room temperature (a), the line x-ray diffraction patterns of the phases MgB_2 (b) and MgO (c), and deviation of the theoretical trace for a two-phase sample from the experimental trace (d).

flections, the unit cell parameters and molar volumes, and refined data on the lattice symmetry and phase composition of the samples. The results are compared with the neutron-diffraction data[8] in the interval 11–297 K. Particular attention is paid to the temperature region around the phase transition point.

Second, we obtain and analyze the results of experimental studies of the Ohmic losses R_s of magnesium diboride pressings at temperatures of 5–300 K in the radio-frequency range 9–110 MHz.

SAMPLES AND MEASUREMENT METHODS

The technique used to prepare the powder and sintered pressings of magnesium diboride is described in detail in Ref. 11. Here we shall only mention that the powder was obtained by solid-state synthesis from the elements Mg (98% pure) and B (99.5% pure) in an atmosphere of argon. The samples for the measurements of the surface resistance in the form of pressed cylinders 5.5 mm in diameter and 6 mm high were prepared by a preliminary pressing of the powder in a high-pressure chamber at pressures up to 1.3 GPa and a subsequent sintering. After the sintering the samples were cooled at a rate of 100 deg/s under pressure, and then the pressure was lowered to standard pressure at a rate of 0.5 GPa/s.

TABLE I. Parameters a, c, and c/a of the hexagonal lattice of magnesium diboride.

a, Å	c, Å	c/a	T, K	Ref.
3.0834	3.521	1.142	293	[4]
3.083	3.521	1.142	293	[6]
3.086	3.524	1.142	293	[2]
3.08489	3.52107	1.141	297	[8]
3.08230	3.51461	1.140	37	[8]
3.0906	3.5287	1.142	293	[9]
3.08589	3.52122	1.141	293	[10]
3.086$_8$	3.525$_5$	1.141	293	Present
3.083$_7$	3.516$_5$	1.140	5	Present

The x-ray studies were done on a DRON-3M diffractometer equipped with a helium cryostat, allowing us to make measurements in the temperature region 5–293 K. The errors of measurement and the stabilization of the temperature of the samples was not worse than 0.05 K, and the errors of the intensity of the diffraction peaks and the lattice parameters were 1% and 0.02%, respectively.

The resistivity ρ and the impedance Z were measured in the temperature interval 5–300 K by a four-contact method, using contacts of beryllium bronze. The surface resistance R_s in the frequency range 9–110 MHz was measured over the temperature interval 5–300 K by a resonator method.[12] Copper was used as a standard. The temperature of the sample was regulated and stabilized to a precision of 0.1 K with the equipment described in Ref. 13. The temperature of the start of the transition of the compound to the superconducting state was determined from the start of the influence of a static magnetic field on the resistance in the four-contact method of measurement and from the start of the influence of a static magnetic field on the Q of an oscillatory measuring circuit incorporating the sample in the measurements of R_s by the resonator method.

The temperature dependence of $\rho(T)$ and $R_s(T)$ and also their absolute values were obtained as a result of an averaging of several measurements.

EXPERIMENTAL RESULTS AND DISCUSSION

1. X-ray studies

To determine the quality of the MgB_2 samples prepared by the technique described above we did x-ray studies at room temperature. A typical diffractometer trace is shown in Fig. 2. Additional reflections appear besides those from the hexagonal lattice. Based on the results of Ref. 14, where it was shown that magnesium oxide MgO can appear as an impurity in the synthesis of MgB_2 powders, and on the basis of the data of the structural studies[15,16] of pure MgO we have been able to identify rather reliably the additional lines on the diffractometer traces as reflections from the cubic MgO structure.

To refine the structure and determine the amount of the observed phases we use the method of Rietveld total-profile

analysis.[15–17] For calculation of the intensities of the diffraction peaks of the observed phases we used the coordinates of the atoms and the initial values of the lattice parameters given in Ref. 2. As a result of several refinement cycles we obtained the minimum confidence factors for the structure of the phases:

$$R = \frac{\Sigma[F_o(hkl) - F_c(hkl)]}{\Sigma F_o(hkl)}, \tag{1}$$

where $F_o(hkl)$ and $F_c(hkl)$ are the observed and calculated structure amplitudes. For magnesium diboride the coefficient R is found to be 1.9% in the framework of the symmetry space group $P6/mmm$. This result again confirms the high confidence in the symmetry $P6/mmm$ for MgB_2 crystals in comparison with the group $P622$ proposed in Ref. 6. If the symmetry group $P622$ is assumed, the confidence factor of the structure comes out substantially lower. As a result of the procedure of refining the structure, we obtained the values of the unit cell parameters of the phases observed. For MgB_2 the refined values of the hexagonal cell parameters at room temperature are given in Table I; for the cubic cell $Fm3m$ of magnesium oxide a value $a = 4.216^3$ Å was obtained. The minimum discrepancies between the calculated and experimental intensities in MgO are less than 14%. Besides the experimental diffractometer trace, Fig. 2 also shows the line diffraction patterns for MgB_2 and MgO and the value of the deviation of the experimental trace from the theoretical. The parameters obtained for the hexagonal lattice of magnesium diboride are in satisfactory agreement with the data of Refs. 2 and 8–10 the slight disparities observed may be due to differences in the sample preparation temperature or in their impurity composition, etc.

Cooling the samples in the region $T < T_c$ to 5 K did not lead to a change in the lattice type or to a redistribution of the intensity of the reflections from MgB_2. A Rietveld total-profile analysis of the data taken at 5 K permitted the conclusion that the superconducting phase of MgB_2 has the same symmetry as at room temperature: $P6/mmm$. The values of the lattice parameter of the low-temperature phase at 5 K are given in Table I.

Of particular interest is the behavior of the structural parameters in the region of the transition to the superconducting state. Jorgensen *et al.*[8] have studied the temperature dependence of the lattice parameters and volume of magnesium diboride by neutron diffraction on polycrystalline samples in the temperature range 11–297 K, with a fine temperature step in the region below 100 K. As the phase transition temperature was approached in the high-temperature phase, in the interval 48–41 K, they observed that, after the usual decrease with decreasing temperature, the lattice parameter a and volume V increased by approximately 0.001 Å and 0.0025 Å^3, respectively. Although in principle the theory of Ref. 18 predicts such an effect for the lattice parameter in layered HTSCs, the increase in volume is surprising (at least, we know of no other cases in which the volume increases with decreasing temperature at the transition to the superconducting phase).

With the goal of checking the effect observed by Jorgensen *et al.*[8] and establishing the behavior of the structural characteristics near T_c, we made a detailed study of the tem-
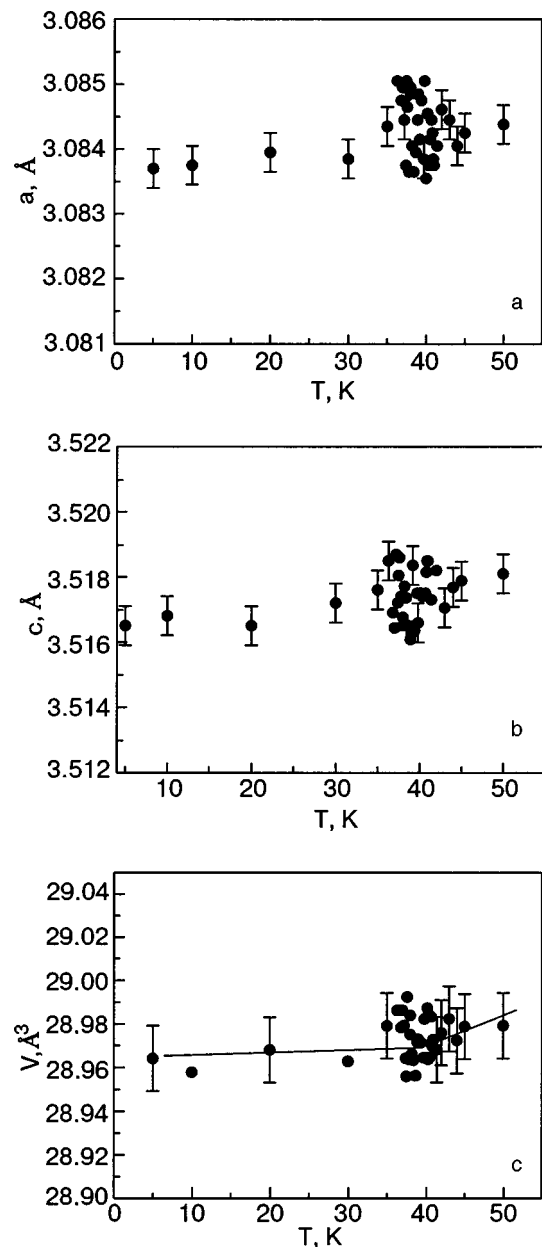
FIG. 3. Temperature dependence of the parameters a (a), c (b), and volume (c) of the hexagonal lattice of MgB_2 in the region of the transition to the superconducting state, $T_c = 39.5$ K.

perature behavior (with a step of 0.1–0.3 K) of the lattice parameters and volume of MgB_2 in the region 35–45 K. Within the error limits of the measurements we did not observe any peculiarities on the temperature dependence of the lattice parameters a and c and volume V or in the widths and intensities of the reflections. The only systematic anomaly that we noticed was an increase in the scatter of the measured values in that temperature interval (Fig. 3). It may be that our sample was insufficiently pure and uniform for unambiguous verification of the result of Jorgensen *et al.* For example, we do not rule out the presence of a nonstoichiometric excess of atomic magnesium, which occupies a boron position, or of Mg–B positional disorder. However, we can state with confidence that our data tell of a noticeable structural instability of the magnesium diboride crystals near the

transition, which, in particular, should be evidence of a rather strong electronic coupling.

On the basis of the known thermodynamic relations,[18] we can state that for the $N-S$ transition, which is second-order, no jump in volume (or in the lattice parameters) should be observed. The quantities having discontinuities are, in particular, the volume coefficient of thermal expansion $\beta = \partial \ln V/\partial T$ and also all of the coefficients of linear expansion $\alpha_i = (1/a_i)\partial a_i/\partial t$, where a_i is the lattice parameter in the ith direction. The jump of the linear expansion coefficients at the $N-S$ transition can be written in the form[18]

$$\Delta \alpha_i = (\alpha_i)_n - (\alpha_i)_s = -\Delta C_V \sum_j s_{ij} \frac{1}{T_c} \frac{\partial T_c}{\partial a_i} a_i. \qquad (2)$$

Here $\Delta C_V = C_n - C_s$ is the jump in the heat capacity (per unit volume in this formula) at a superconducting transition with critical temperature T_c, and s_{ij} is the compliance tensor (the inverse of the tensor of elastic constants c_{ij}). Expression (2) can be transformed to a more convenient form by using the definition of the volume coefficient of thermal expansion $\beta = \Sigma_i \alpha_i$:

$$\Delta \beta = -\Delta C_V \frac{1}{T_c} \frac{\partial T_c}{\partial P}. \qquad (3)$$

All of the quantities appearing in (3) are well known. The value of the derivative $\partial T_c/\partial P_c$ varies depending on the quality and morphology of the sample. Typically one can assume $\partial T_c/\partial P_c = 1$ K/GPa.[19] The jump in the specific heat (per mole) ΔC_m is traditionally expressed in the following form, with allowance for the definition of the direction of the jump in (2):[20]

$$\Delta C_m = -1.09 \gamma_n T_c, \qquad (4)$$

where $\gamma_n = 2.7$ mJ/(mole·K²). The quantity ΔC_V appearing in (2) has the form $\Delta C_V = \Delta C_m/V_m$, where $V_m = 17.35$ cm³/mole is the molar volume of MgB$_2$ at 39 K, according to our data on the lattice parameters. Substituting the numerical values of the parameters into Eq. (3), we finally obtain the calculated value $\Delta \beta = 0.17 \times 10^{-6}$ K⁻¹. The experimental value of the change in thermal expansion at the transition, $\Delta \beta$, according to estimates from our experiment, is somewhat larger but of the same order of magnitude. The data of Ref. 8 imply a value of $\Delta \beta$ approximately an order of magnitude larger.

From our data on the temperature dependence of the lattice parameters in the whole interval studied we can conclude that the strain of the crystals is of a substantially anisotropic character. The change with temperature of the hexagonal lattice of MgB$_2$ is significantly larger along the c axis than in the basal plane (Table I). The mean values of the coefficients of linear thermal expansion in the interval 5–293 K was found to be $\alpha_a = 3.5 \times 10^{-6}$ K⁻¹, $\alpha_c = 8.8 \times 10^{-6}$ K⁻¹. This result is in satisfactory agreement with the values of the change of the lattice parameters with temperature obtained in Ref. 8. Near room temperature the following values of the coefficients of linear thermal expansion were obtained in Ref. 8: $\alpha_a \approx 5.4 \times 10^{-6}$ K⁻¹, $\alpha_c \approx 11.4 \times 10^{-6}$ K⁻¹. The mean values of α in the interval
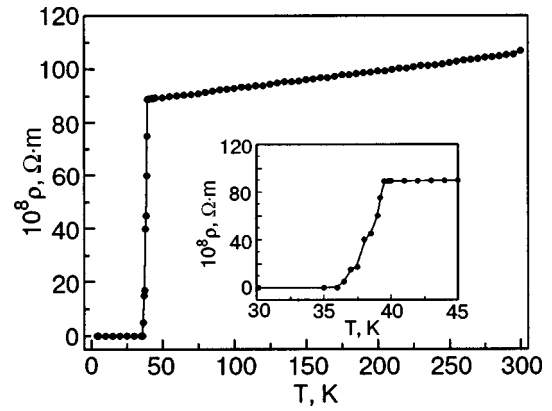

FIG. 4. Temperature dependence of the resistivity ρ of MgB$_2$ in the temperature interval 5–300 K. The inset shows the same dependence in the neighborhood of the transition temperature of MgB$_2$ to the superconducting state in an expanded scale.

from helium to room temperature according to our estimates based on the data of Ref. 8 are $\alpha_a \approx 2.3 \times 10^{-6}$ K⁻¹, $\alpha_c \approx 6.4 \times 10^{-6}$ K⁻¹.

2. Resistivity

Figure 4 shows the temperature dependence of the resistivity ρ of the compound MgB$_2$ in the interval interval 5–300 K. The inset in Fig. 4 shows the interval 30–45 K in an expanded scale. It is seen that $T_c = 39.5$ K is the temperature of the start of the transition to the superconducting state, and that $\rho = 0$ at $T_0 = 36$ K.

It follows from the figure that $\rho(T)$ has a linear character in the temperature range 39.5–300 K. Here $\rho(300 \text{ K}) = 107 \times 10^{-8}$ Ω·m, $\rho(40 \text{ K}) = 89 \times 10^{-8}$ Ω·m, and the slope $\partial \rho/\partial T = 7 \times 10^{-10}$ Ω·m/K. Analysis of the temperature dependence of the resistivity $\rho(T)$ showed that in the interval 39.5–300 K it can be described by the equation

$$\rho(T) = \rho_0(1 + \alpha_\rho T), \qquad (5)$$

where $\rho_0 = 86 \times 10^{-8}$ Ω·m, $\alpha_\rho = 8 \times 10^{-4}$ K⁻¹.

A linear dependence of the resistivity $\rho(T)$ has been observed in several studies devoted to MgB$_2$ (e.g., Ref. 2). In HTSC materials a linear dependence $\rho \sim T$ is discussed in the framework of the two-band model for conductors.[21,22] In this approach a compound is treated as a solid solution with impurities. It is possible that MgB$_2$, as a two-band conductor,[23] can also be treated in terms of such concepts.

3. R_s of MgB$_2$ in the normal state

Figure 5 shows the temperature dependence of the surface resistance R_s of MgB$_2$ in the temperature interval 5–300 K for measurements at different frequencies.

It follows from the figure that in the normal state ($T > 39.5$ K) the temperature dependence $R_s(T)$ is linear and, consequently, $R_s(T) \sim \rho(T)$ at all measurement frequencies. The slope $\partial R_s/\partial T$ in that region is independent of frequency, although the value of R_s itself is a function of frequency. Figure 6 shows the frequency dependence of $R_s(f)$ for two temperatures: 300 and 50 K. These dependences can be described by the expression
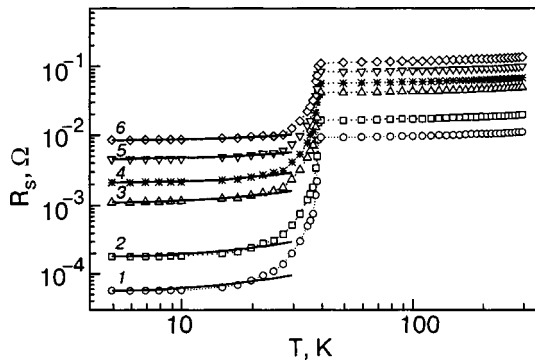
FIG. 5. Experimental temperature dependence of the surface resistance R_s of MgB_2 at frequencies [MHz]: 9 (*1*), 16 (*2*), 40 (*3*), 55 (*4*), 80 (*5*), and 110 (*6*) in the temperature interval 5–300 K. The solid curves are calculated according to formula (7).

$$R_s(T,f) = A\rho(T)f, \qquad (6)$$

where $A = 1.16 \times 10^{-3}$ $m^{-1}Hz^{-1}$.

It is important to note that linear dependences $R_s(T)$ and $R_s(f)$ do not correspond to the standard concepts wherein $R_s \sim (\rho f)^{0.5}$ in metals.[24]

Near the $N–S$ transition in the temperature interval 39.5–45 K the $R_s(T)$ curves exhibit a slight increase of R_s (Fig. 7), while the $\rho(T)$ curves do not (Fig. 7a). The amplitude of the anomalous increase of R_s decreases with increasing frequency. This is seen from a comparison of Figs. 7b and 7c, which show $R_s(T)$ measured at frequencies of 9 and 110 MHz, respectively. Here we note that the amplitude of the increase in R_s before the temperature-induced transition T_c is independent of the value of the the static external magnetic field (within the limits 0–3 kOe).

In our view the observed effect can be explained either as a size effect or as structural instability of MgB_2 near the phase transition from the normal to the superconducting state.

However, the size effect arises at $T \leq T_c$ owing to the appearance of the Meissner effect at the $N–S$ transition at frequencies for which the penetration depth of the electromagnetic field is comparable to the size of the sample (or the grain size). Therefore, if the surface resistance R_s increases at $T \leq T_c$ in the absence of an external static magnetic field (the Fisher–Kao effect),[25] then R_s will decrease in a magnetic field. In our experiments, however, R_s is independent of magnetic field.
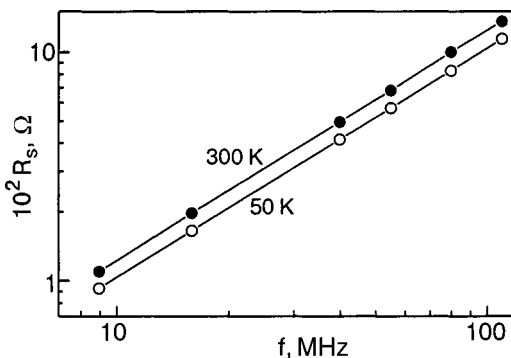
FIG. 6. Experimental frequency dependence of the surface resistance of MgB_2 at 300 and 50 K.
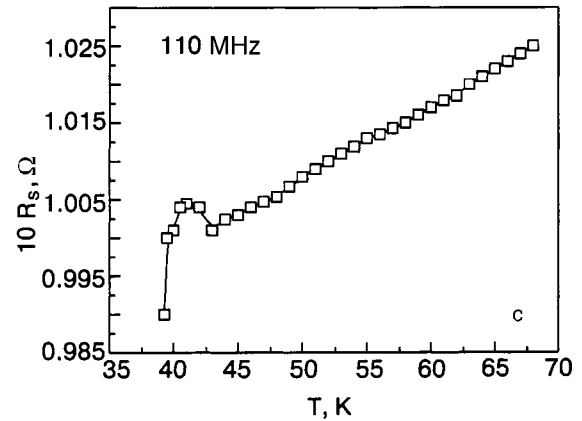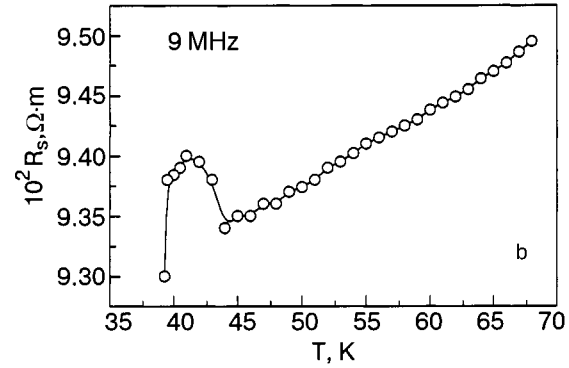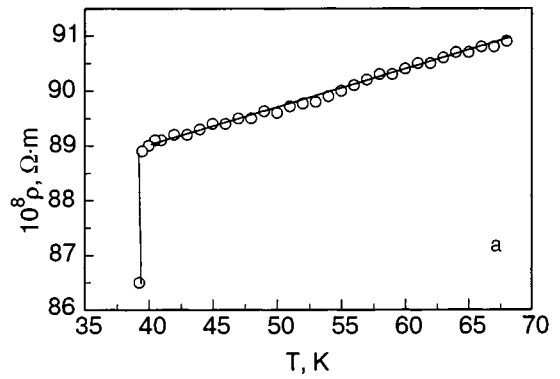
FIG. 7. Experimental temperature dependence of the resistivity (a) and surface resistance of MgB_2 at frequencies of 9 (b) and 110 MHz (c) in the temperature interval 35–70 K.

In addition, the effect is also observed at temperatures slightly above T_c.

Apparently the observed effect is caused by structural instability of MgB_2 in the region of the $N–S$ phase transition. It was in that region that we observed a systematic scatter of the measured quantities in the x-ray diffraction studies (Fig. 3). Most likely this effect depends on the structural state of the sample, and for that reason in measurements of some physical parameter or other it is observed only in some of the samples but not all of them. For example, it was shown in Ref. 21 that the annealing of an MgB_2 film can cause an increase in its resistivity. In Ref. 26 an increase in the surface resistance in the centimeter range near T_c is observed only in the imaginary part of the impedance, while in Ref. 27 it is observed in the active part. In Ref. 28 an anomaly of only the imaginary part of the magnetic suscep-
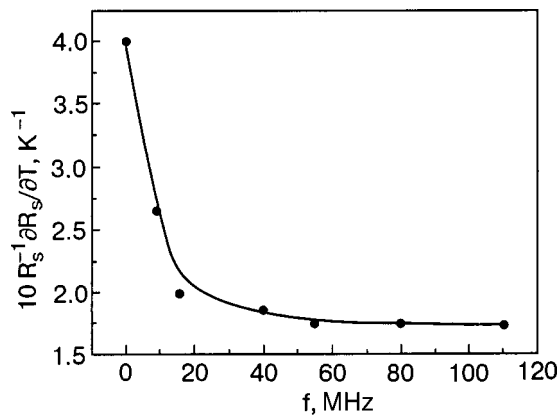
FIG. 8. Experimental frequency dependence of the steepness $R_s^{-1}\partial R_s/\partial T$.

FIG. 9. Experimental frequency dependence $R_s(f^2)$ of MgB$_2$ at a temperature of 5 K.

tibility is observed in the temperatures region of the $N-S$ transition.

4. Intermediate and superconducting states

It follows from Fig. 5 that the critical temperature T_c is independent of the measurement frequency and is equal to 39.5 K. When the temperature is lowered from 39.5 to 35 K the surface resistance R_s at all frequencies decreases by a practically linear law. The steepness $R_s^{-1}\partial R_s/\partial T$ decreases monotonically with increasing frequency, as is shown in Fig. 8. At temperatures below 35 K the linearity of $R_s(T)$ is disrupted, and $R_s(T,f)$ becomes noticeably nonlinear, going to a plateau at $T<10$ K.

Before analyzing the dependence $R_s(T,f)$ let us determine some important parameters of a superconductor which have an influence on $R_s(T,f)$. As we have said, we worked with high-resistance samples having a residual resistivity near T_c of $\rho_r=89\times10^{-8}\ \Omega\cdot$cm (see Fig. 4). Using the values of $R_s(T,f)$ for $T\geqslant T_c$ from Fig. 5 and the relation $\delta=\rho/R_s$, we estimate the values of the skin depth δ for penetration of the electromagnetic field. At the measurement frequencies the values of δ lie between 80 and 8 μm. From the relation $l=3[2N(0)e^2V_F\rho_r]^{-1}$ (Ref. 29) with the values of the Fermi velocity $V_F=4.8\times10^7$ cm/s and charge carrier density $n=6.7\times10^{22}$ cm^{-3} (Ref. 27), we obtain $l=26$ Å, which is many orders of magnitude smaller than δ. Thus, even when the increase in l as the sample is cooled to helium temperatures is taken into account, we remain in the regime of the classical skin effect at all temperatures and frequencies. The coherence length $\xi_0=\hbar V_F/\pi\Delta(0)$ is found with allowance for the small gap value $\Delta(0)=2.45$ meV,[30] which is usually observed in "dirty" samples. We obtain $\xi_0=409$ Å$\gg1$. The value of the London penetration depth $\lambda_L(0)=(mc^2/4\pi ne^2)^{1/2}$ is equal to 206 Å. Since $\lambda_L(0)<\xi_0$ and $l\ll\lambda_L(0),\xi_0$, we use the expression $\lambda=\lambda_L(\xi_0/l)^{1/2}$ (Ref. 29) to find the effective penetration depth $\lambda(0)$, which comes out to be $\lambda(0)=817$ Å. The Ginzburg–Landau parameter for the case $T\ll T_c$ is now defined as $\varkappa=\lambda(0)/l$ and is equal to 31.4. Near T_c for a "dirty" metal the parameter $\varkappa=0.753\lambda_L(0)/l\approx6$. Thus, dc measurements indicate that MgB$_2$ is a London superconductor, since $\varkappa>1$ at all temperatures below T_c. Here the value of $\varkappa$ decreases as T_c is approached, reflecting the ten-

dency toward a transition to the Pippard limit in the normal state.[31]
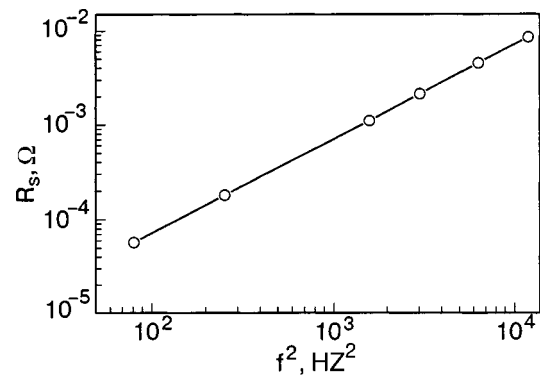
In an alternating field the behavior of MgB$_2$ is completely different. Figure 9 shows a plot of $R_s(f)$ constructed with the use of the data of Fig. 5 for $T=5$ K. It is clearly seen that $R_s(f)\sim f^2$, which, in accordance with BCS theory for $T<T_c$, is a sign of a nonlocal Pippard superconductor, which should have a frequency dependence $R_s(f)\sim f^n$ with $n=2$.[32,33] Figure 10 shows how the exponent n varies with temperature in the range 5 to 50 K, based on the $R_s(T,f)$ curves in Fig. 5. It is seen that n is practically independent of temperature in the interval from 5 to 15 K and has a value of 2, which is characteristic for the Pippard nonlocal limit. Upon further increase in temperature the degree of nonlocality falls off, and n decreases almost linearly to a value $n=1.5$, which is maintained in the temperature interval 35–38 K and is a sign of the local London limit.[32] It is in this narrow temperature interval near T_c that the London limit in alternating fields is realized, according to the theory of Ref. 31. Upon further increase in temperature the London limit is destroyed, and n falls off sharply to the value $n=1$ associated with the normal state.

In classical superconductors with low T_c such transitions from the Pippard to the London region in alternating fields are usually difficult to realize,[31] both because of their "cleanliness" and the anomalous skin effect and also because of the
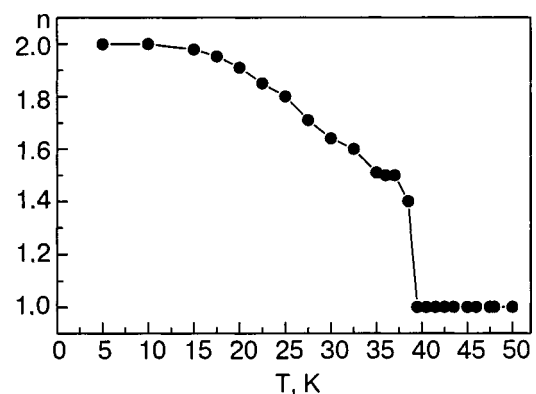
FIG. 10. Experimental temperature dependence of the exponent n in the relation $R_s\sim f^n$.
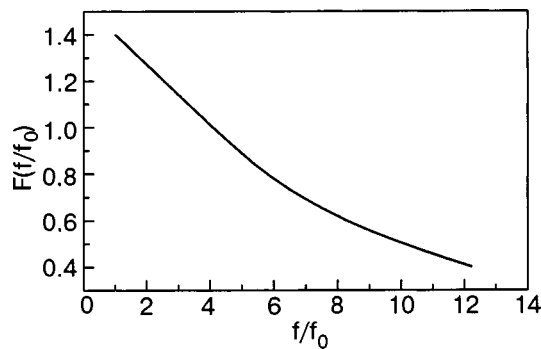
FIG. 11. Frequency dependence of the function $F(f)$ in expression (7).

narrow temperature interval usually accessible to experimenters. In MgB$_2$ these limitations are absent, and this transition can be observed.

Let us now consider the complete $R_s(T,f)$ curves presented in Fig. 5. According to BCS theory, they can be described by an expression containing the residual resistance and cofactors giving the dependence on frequency and temperature.[31,32,34] We therefore write $R_s(T,f)$ in the form

$$R_s(T,f) = R_{s0}(f_0)(f/f_0)^2 [1 + F(f) e^{-(\Delta(T)/\kappa T)}]. \qquad (7)$$

Here $R_{s0} = 5.7 \times 10^{-5}$ Ω is the residual resistance at $T = 5$ K at the lowest frequency $f_0 = 9$ MHz, $\Delta(0) = 2.45$ meV is the value[30] of the small gap for MgB$_2$, $F(f)$ is an adjustable parameter of order unity, the numerical values of which are presented in Fig. 11. The physical significance of this parameter is that with increasing frequency its value tends toward zero, removing the temperature dependence of $R_s(T,f)$ at the superconducting transition at very high frequencies, when the limiting value of $R_s(T,f)$ is independent of temperature and corresponds to the normal metal.[33] The results of calculations according to formula (7) are shown by the solid curves in Fig. 5. In the calculation of $\Delta(T)$ according to BCS theory we used the tabulated data from Ref. 35. It is seen that the calculated and experimental data are in rather good agreement for $T < 30$ K, i.e, for $T/T_c < 0.76$.

Thus the frequency dependence $R_s \sim f^2$ in the Pippard region at $T \ll T_c$ (see Fig. 9), its transformation to a dependence $R_s \sim f^{1.5}$ in the London region when the temperature is increased to $T \approx T_c$ (see Fig. 10), and the exponential dependence of $R(T)$ in the region $T/T_c < 0.76$ (see Fig. 5) eloquently attest to the fact that MgB$_2$ is a superconductor described by the conventional BCS theory.

CONCLUSION

Let us summarize the main results obtained in this study.

We have done the first x-ray study of the compound MgB$_2$ at the temperatures of the transition to the superconducting state. An appreciable anisotropy of the strain of the crystals upon changes in temperature was revealed. The changes of the lattice with temperature along the c axis are substantially larger than those in the basal plane.

We have established that the anomaly of R_s in the temperature interval 39.5–45 K is correlated with features observed in the x-ray analysis of MgB$_2$.

A study of the temperature and frequency dependence of the surface resistance $R_s(T,f)$ in the superconducting state showed that the characteristics of MgB$_2$ measured in dc and ac fields are different: unlike the case for the dc measurements, in an alternating field MgB$_2$ manifests the characteristic signs of a Pippard superconductor at $T \ll T_c$. The transition from the Pippard nonlocal limit for $T \ll T_c$ to the London local limit near T_c was observed, the exponent in the relation $R_s(f) \sim f^n$ changing from $n = 2$ to $n = 1.5$. At $T/T_c < 0.76$ the behavior of $R_s(T)$ is described well by an exponential dependence $\exp(-\Delta(T)/kT)$, in accordance with BCS theory.

The authors thank Yu. G. Naiyuk for helpful discussions and comments.

*E-mail: dmitriev@ilt.kharkov.ua

[1] G. V. Samsonov, T. I. Serebryakova, and V. A. Neronov, *Borides* [in Russian], Atomizdat, Moscow (1975).

[2] J. Nagamatsu, N. Nakagawa, T. Muranaka, Y. Zenitani, and J. Akimitsu, Nature (London) **410**, 63 (2001).

[3] C. Buzea and T. Yamashita, Supercond. Sci. Technol. **14**, R115 (2001).

[4] L. Ya. Markovskiĭ, Yu. D. Kondrashov, and G. V. Kaprutovskaya, Zh. Org. Khim. **25**, 433 (1955).

[5] V. Russell, F. A. Kanda, and J. King, Acta Crystallogr. **6**, 870 (1953).

[6] M. E. Jones and R. E. Marsh, J. Am. Phys. Soc. **76**, 1434 (1954).

[7] N. V. Vekshina, L. Ya. Markovskiĭ, Yu. D. Kondrashov, and T. K. Voevodskaya, Zh. Anal. Khim. **44**, 970 (1971).

[8] J. D. Jorgensen, D. G. Hinks, and S. Short, Phys. Rev. B **63**, 224522 (2001).

[9] K. Prassides, Y. Iwasa, T. Ito, Dam H. Chi, K. Uebara, E. Nishibori, M. Takata, M. Sakata, Y. Ohishi, O. Shimomura, T. Nuranaka, and J. Akimitsu, Phys. Rev. B **64**, 012509 (2001).

[10] T. Vogt, G. Schneider, J. A. Hriljac, G. Yang, and J. S. Abell, Phys. Rev. B **63**, 220505 (2001).

[11] T. V. Ignatova, G. A. Zvyagina, I. G. Kolobov, E. A. Masalitin, V. D. Fil', Yu. B. Paderno, A. N. Bykov, V. N. Paderno, and V. I. Lyashenko, Fiz. Nizk. Temp. **28**, 270 (2002) [Low Temp. Phys. **28**, 190 (2002)].

[12] A. M. Gurevich, V. M. Dmitriev, V. N. Eropkin, L. A. Ishchenko, N. N. Prentslau, and L. V. Shlyk, Fiz. Nizk. Temp. **25**, 15 (1999) [Low Temp. Phys. **25**, 10 (1999)].

[13] M. N. Ofitserov, N. N. Prentslau, N. A. Kucheryavenko, A. P. Beskorsyĭ, and N. M. Levchenko, "Temperature regulation and stabilization system with digital control" [in Russian], Preprint FTINT AN USSR No. 47–88, Kharkov (1988).

[14] N. G. Schmahl and G. F. Eikerling, Z. Phys. Chem. (Frankfurt am Main) **62**, 268 (1968).

[15] J. Rodrigues-Carvajal, Physica B **192**, 55 (1993).

[16] H. M. Rietveld, Acta Crystallogr. **22**, 151 (1967).

[17] H. M. Rietveld, J. Appl. Crystallogr. **2**, 65 (1969).

[18] A. J. Millis and K. M. Rabe, Phys. Rev. B **38**, 8908 (1988)

[19] A. F. Goncharov and V. V. Struzhkin, Physica C (to appear in 2003).

[20] H. D. Yang, T.-Y. Lin, H. H. Li, F. H. Hsu, C. J. Liu, S.-S. Li, R.-C. Yu, and C.-Q. Jin, Phys. Rev. B **87**, 167003 (2001).

[21] A. Plecenic, L. Satrapinsky, P. Kúš, Š. Gaži, Š. Beňačka, J. Vávra, and J. Kostič, Physica C **363**, 224 (2001).

[22] V. P. Galaiko, Fiz. Nizk. Temp. **19**, 123 (1993) [Low Temp. Phys. **19**, 87 (1993)].

[23] Amy Y. Liu, I. I. Mazin, and Jens Kortus, Phys. Rev. Lett. **87**, 087005 (2001).

[24] S. Ramo, J. R. Whinnery, *Fields and Waves in Modern Radio*, Wiley, New York (1947), OGIZ, Moscow–Leningrad (1948).

[25] M. Fisher and Y.-H. Kao, Solid State Commun. **7**, 275 (1969).

[26] A. Dulčić, D. Paar, M. Požek, G. V. M. Williams, S. Krämer, C. U. Jung, Min-Seok Park, and Sung-Jk Lee, Phys. Rev. B **66**, 014505 (2002).

[27] B. B. Jin, N. Klein, W. N. Kang, Hyeong-Jin Kim, Eun-Mi Choi, Sung-Jk Lee, T. Dahm, and K. Maki, Phys. Rev. B **66**, 104521 (2002).

[28] S. E. Lofland, S. D. Tyagi, K. V. Ramanujachary, and M. Botsford, Physica C **370**, 27 (2002).

[29] P. G. De Gennes, *Superconductivity of Metals and Alloys*, Benjamin, New York (1966), Mir, Moscow (1968).

[30] Yu. G. Naidyuk, I. K. Yanson, L. V. Tyutrina, N. L. Bobrov, P. N. Chubov, W. N. Kang, Hyeong-Jin Kim, Eun-Mi Choi, and Sung-Ik Lee, JETP Lett. **75**, 283 (2002).

[31] A. A. Abrikosov, L. P. Gor'kov, and I. M. Khalatnikov, Zh. Éksp. Teor. Fiz. **35**, 265 (1958) [Sov. Phys. JETP **8**, 182 (1959)].

[32] F. F. Mende and A. I. Spitsyn, *Surface Impedance of Superconductors* [in Russian], Naukova Dumka, Kiev (1985).

[33] J. R. Waldram, Adv. Phys. **13**, 1–88 (1964).

[34] M. Tinkham, *Introduction to Superconductivity*, Intern. Series in Pure and Appl. Physics, McGraw-Hill, New York (1975).

[35] B. Mülschlegel, Z. Phys. **155**, 313 (1959).

Translated by Steve Torstveit

LOW-TEMPERATURE MAGNETISM

Temperature dependence of the conductivity, thermopower, and heat capacity of TlCoS$_2$

E. M. Kerimova,* S. N. Mustafaeva, M. A. Aldjanov, and A. I. Jabbarly

Institute of Physics of the National Academy of Sciences of Azerbaijan, H. Javid Ave. 33, Baku 370143, Azerbaijan
(Submitted June 11, 2003; revised December 3, 2003)

The temperature dependence of the conductivity and thermopower of TlCoS$_2$ is studied over a wide range of temperatures (77–400 K). It is found that TlCoS$_2$ is characterized by p-type conductivity in the temperature interval 77–225 K and that an inversion of the sign of the thermopower occurs at 225 K. The heat capacity of the ferromagnetic compound TlCoS$_2$ is also measured in the temperature interval 55–300 K. It is shown that the behavior of the magnetic part of the heat capacity of TlCoS$_2$ is typical of a quasi-low-dimensional magnet. The experimental data on the temperature dependence of the heat capacity are used to calculate the thermodynamic parameters of TlCoS$_2$: the changes in entropy and enthalpy. © *2004 American Institute of Physics.* [DOI: 10.1063/1.1704615]

Compounds with the general chemical formula TlMeX$_2$ (Me = Co, Ni, Fe, Cr, Mn; X = S, Se, Te) belong to the class of low-dimensional magnets. Results on the synthesis of such compounds and the study of their physical properties are reported in Refs. 1–9. For the particular case of thallium–cobalt sulfide only the magnetic properties have been reported.[8] In particular, the magnetization and paramagnetic susceptibility of TlCoS$_2$ were studied, and it was shown that it is a ferromagnet. The Curie temperature of TlCoS$_2$ is 112 K, and the effective magnetic moment is $4.6\mu_B$. The goal of the present study is to investigate the electric, thermoelectric, and thermodynamic properties of TlCoS$_2$.

The synthesis of TlCoS$_2$ was achieved by the interaction of initial components of high purity in quartz ampoules evacuated to a pressure of 10^{-3} Pa. The particulars of the synthesis technology are described in detail in Ref. 8. It has been established on the basis of an x-ray structural analysis that this compound has a hexagonal crystal structure with the following lattice parameters: $a = 3.726$ Å, $c = 22.510$ Å, $z = 3$, $\rho = 6.026$ g/cm^3. Because of the rather large ratio $c/a \sim 6$, it can be assumed that TlCoS$_2$ is a quasi-two-dimensional magnet.

Below we present the results of a study of the temperature dependence of the conductivity and thermopower of TlCoS$_2$ compounds prepared by us. The samples for the electrical measurements were in the form of parallelepipeds. Before deposition of the contacts the samples were annealed at a temperature of ~ 450 K. Ohmic contacts were made by electrolytic deposition of copper. The conductivity σ and thermopower (Seebeck coefficient) α of the samples were measured by the four-probe method in the temperature range 78–400 K with an accuracy of 1% or better.

Figure 1 shows the typical temperature dependence of the conductivity of a TlCoS$_2$ sample. Initially as the temperature is raised from 78 K the conductivity decreases; near 100 K a slight growth of σ occurs; at $T \approx 110$ K it passes through a maximum and again decreases until 225 K. In the temperature interval 225–300 K the conductivity of TlCoS$_2$ remains practically constant. The temperature (~ 110 K) at which we observed the anomaly on the $\sigma(T)$ curve is close to the temperature of the magnetic transformation of TlCoS$_2$ ($T = 112$ K) determined from the temperature dependence of the magnetization.[8]

Figure 2 shows the temperature dependence of the thermopower in TlCoS$_2$. It should be noted that at 112 K this dependence, like $\sigma(T)$, passes through a maximum. In the temperature interval 75–225 K the sign of the thermopower corresponds to conductivity of the hole type. At $T = 225$ K an inversion of the sign of the thermopower is observed, i.e., in the temperature region 225–290 K the TlCoS$_2$ sample is characterized by n-type conductivity. In the temperature re-
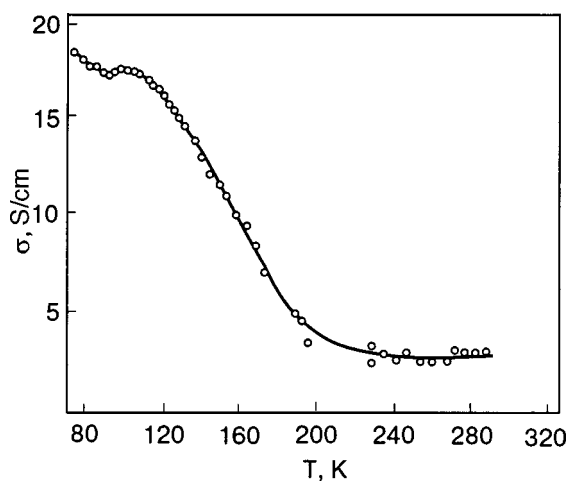

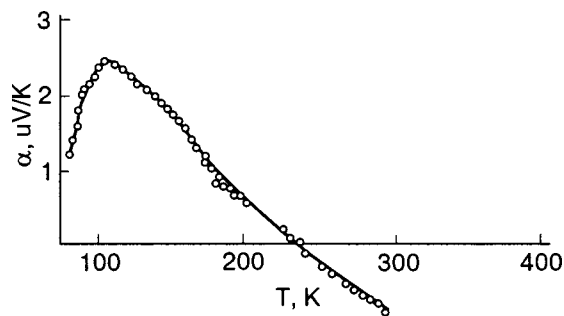FIG. 1. Temperature dependence of the conductivity of a TlCoS$_2$ sample.

FIG. 2. Temperature dependence of the thermopower in TlCoS$_2$.

TABLE I. Values of the entropy change and enthalpy change of TlCoS$_2$.

T, K	$S_T - S_0$, J/(K·mole)	$H_T - H_0$, J/mole
50	28.82	0.748
100	62.58	3.354
150	94.88	7.240
200	120.0	11.60
250	140.6	16.23
300	157.9	21.01

gion 225–290 K, as was mentioned above (see Fig. 1), the conductivity of TlCoS$_2$ is practically independent of temperature.

We also measured the heat capacity of TlCoS$_2$ in the temperature interval 55–300 K and evaluated the main thermodynamic parameters: the changes in entropy and enthalpy. The heat capacity was measured by the an adiabatic method.[10]

Figure 3 shows the temperature dependence of the heat capacity of TlCoS$_2$. Near 118 K a small anomaly is observed on $C_p(T)$, apparently due to the magnetic transition. Unfortunately, because of the smallness of the anomaly it was impossible to determine the critical parameters of the magnetic phase transition. The temperature corresponding to this anomaly is close to the temperature of the three-dimensional transition determined from the magnetization.[8] To determine the magnetic contribution to the heat capacity of a magnetically ordered substance, one generally chooses a nonmag-
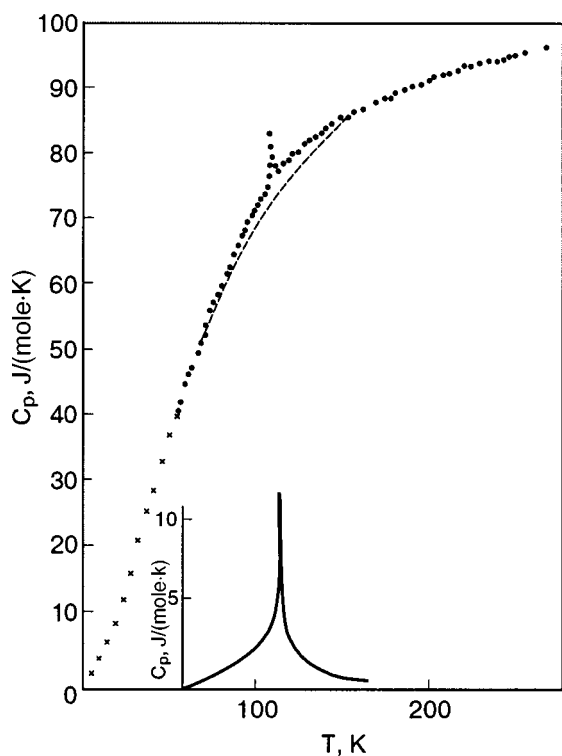
netic reference compound for which the heat capacity and its temperature dependence are very similar to the lattice contribution to the heat capacity of the magnetic substance under study. Because of a lack of the necessary data we could not find an isostructural diamagnetic compound for determining the magnetic heat capacity. We therefore used TlCrS$_2$, which has a structure similar to that of TlCoS$_2$ (Ref. 1). The temperature dependence of the lattice heat capacity of TlCrS$_2$ is described by the Tarasov formula[11] with the characteristic temperatures $\theta_2 = 342$ K and $\theta_3 = 103$ K. We note that despite its simplified nature, the Tarasov model is used, with recourse to a small number of adjustable parameters, to describe the lattice heat capacity of layered and chainlike magnetic compounds in the region $C_{latt} \gg C_{magn}$. We could not compare these values of θ_2 and θ_3 with data on the elastic constants and sound velocity because no such data exist. To calculate C_{latt} of TlCoS$_2$ by comparison with TlCrS$_2$ we used the method of corresponding states, with $r = 1.022$. Also shown in Fig. 3 are the lattice (dashed curve) and magnetic (solid curve) heat capacities ($C_{magn} = C_{exp} - C_{latt}$) of TlCoS$_2$; these are of a qualitative character. It can be seen in Fig. 3 that the magnetic heat capacity has a broad maximum at $T_{C\,max} = 118$ K and approaches zero at a temperature above 180 K. The behavior of the magnetic heat capacity $C_{magn}(T)$ of TlCoS$_2$ is characterized by the presence of a broad maximum with a high-temperature "tail." Such behavior of the magnetic heat capacity is typical of a quasi-two-dimensional system.[12]

The magnetic energy and entropy calculated by integrating C_{magn} and C_{magn}/T are equal to $\Delta H_{magn} = 154.6$ J/mole and $\Delta S_{magn} = 1.41$ J/K·mole.

The temperature dependence of the heat capacity was used to calculate the thermodynamic functions: the change in entropy and enthalpy of TlCoS$_2$ in the temperature interval 0–300 K. Below 55 K $C_p(T)$ was calculated by the Debye law. The values of the entropy and enthalpy of TlCoS$_2$ are given in Table I.

*E-mail: ekerimova@physics.ab.az

FIG. 3. Temperature dependence of the heat capacity of TlCoS$_2$. The dashed curve is the lattice heat capacity; the solid curve, the magnetic heat capacity.

[1] M. Rosenberg, A. Knulle, H. Sabrowsky, and Chr. Platte, J. Phys. Chem. Solids **43**, 87 (1982).

[2] G. I. Makovetskiĭ and E. I. Kasinskiĭ, Neorg. Mater. **20**, 1752 (1984).

[3] A. I. Dzhabbarly, É. M. Kerimova, F. M. Seidov, and A. K. Zamanova, Neorg. Mater. **32**, 118 (1996).

Kerimova *et al.*

[4] M. A. Aldjanov, M. Nadjafzade, Z. Seidov, and M. Gasumov, Doga: Turk. J. Phys. **20**, 1071 (1996).

[5] É. M. Kerimova, F. M. Seidov, S. N. Mustafaeva, and S. S. Abdinbekov, Neorg. Mater. **35**, 157 (1999).

[6] S. N. Mustafaeva, É. M. Kerimova, and A. I. Dzhabbarly (Jabbarly), Fiz. Tverd. Tela (St. Petersburg) **42**, 2132 (2000) [Phys. Solid State **42**, 2197 (2000)].

[7] S. N. Mustafaeva, É. M. Kerimova, F. M. Seidov, and A. I. Jabbarly, *Abstracts of the 13th International Conference on Ternary and Multinary Compounds–ICTMC 13*, Paris, France, October 14–18 (2002), p. P2-1.

[8] R. Z. Sadykhov, É. M. Kerimova, Yu. G. Asadov, and R. K. Veliev, Fiz. Tverd. Tela (St. Petersburg) **42**, 1449 (2000) [Phys. Solid State **42**, 1492 (2000)].

[9] É. M. Kerimova, R. Z. Sadykhov, and R. K. Veliev, Neorg. Mater. **37**, 180 (2001).

[10] M. A. Aldjanov, N. G. Guseinov, G. D. Sultanov, and M. D. Najafzade, Phys. Status Solidi B **159**, 107 (1990).

[11] V. V. Tarasov, Zh. Fiz. Khim. **24**, 111 (1950).

[12] K. S. Aleksandrov, N. V. Fedoseeva, and I. P. Spevakova, *Magnetic Phase Transitions in Halide Crystals* [in Russian], Nauka, Novosibirsk (1983).

Translated by Steve Torstveit

The approximation of geometrical optics for bulk spin waves in spatially inhomogeneous ferromagnetic insulators with an exchange defect

S. A. Reshetnyak*

Institute of Magnetism, National Academy of Sciences of Ukraine, bul'var Vernadskogo 36-b, Kiev 03142, Ukraine

The refractive index for bulk spin waves propagating in a ferromagnetic medium with an inhomogeneous distribution of exchange interaction parameters and uniaxial anisotropy is calculated in the spin density formalism. The reflection and transmission coefficients for spin waves at the boundary between two homogeneous magnets with different exchange interaction constants, uniaxial magnetic anisotropy, and saturation magnetization are calculated with allowance for a δ-function-like exchange at the interface. The dependence of the reflected wave intensity and the refractive index on the frequency of the wave and the value of a homogeneous external dc magnetic field is obtained. © *2004 American Institute of Physics.*
[DOI: 10.1063/1.1704616]

INTRODUCTION

Significant technological progress in the field of nanotechnologies and nanoelectronics necessitates the development of new materials and devices in which the advantages of high-frequency waves can be exploited. In particular, there is interest in the use of the characteristic features of spin waves in applications. As a rule, in the theoretical description of the features of the propagation of spin waves it is traditional to use a wave approach, which has been used successfully, for example, to determine the spectral and some other characteristics of magnetic materials.[1–5] The present study is devoted to the application of the mathematical formalism of geometrical optics to the description of the behavior of spin waves propagating in a ferromagnetic medium with an inhomogeneous distribution of magnetic parameters. This approach makes it possible to obtain the necessary change in the direction of propagation of spin waves (in particular, focusing) with the use of artificially created inhomogeneities of the magnetic parameters of a medium of specified configuration and also by a change in the value of the external magnetic field. In Ref. 6 the refractive index of a spin-wave ray was calculated, and its behavior at the boundary between two homogeneous magnets with different exchange interaction parameters and uniaxial magnetic anisotropy parameters was investigated. In the present paper the results are generalized to the case of a continuous distribution of these parameters in a magnetically uniaxial medium. In addition, the refractive index and reflected spin-wave intensity are calculated at the boundary between two uniaxial ferromagnets with different values of the exchange interaction constants, magnetic anisotropy, and saturation magnetization.

1. DYNAMICAL EQUATIONS FOR THE MAGNETIC MOMENT

We consider an infinite ferromagnet consisting of two semi-infinite parts in contact with each other along the yz plane; the values of the magnetization in the respective half spaces are M_{01} and M_{02}, and the values of the exchange interaction parameter α and uniaxial magnetic anisotropy parameter β are continuously (or piecewise continuously) variable. The easy axis of the magnet and the external dc magnetic field are directed along the $0z$ axis. In the exchange approximation the energy density of the magnet in the configuration described has the form

$$w = \sum_{j=1}^{2} \theta[(-1)^j x] w_j + A\,\delta(x)\mathbf{M}_1\mathbf{M}_2, \tag{1}$$

where

$$w_j = \frac{\alpha}{2}\left(\frac{\partial m_j}{\partial x_k}\right)^2 + \frac{\beta}{2}(m_{jx}^2 + m_{jy}^2) - H_0 M_{jz}, \tag{2}$$

$\theta(x)$ is the Heaviside step function; A is a parameter characterizing the exchange interaction between half spaces at $x=0$; $\mathbf{M}_j = M_{0j}\mathbf{m}_j$, $\mathbf{m}_j$ are unit vectors in the magnetization direction, with $j=1,2$.

We use the spin density formalism,[7] according to which the magnetization can be written in the form

$$\mathbf{M}_j(\mathbf{r},t) = M_{0j}\Psi_j^+(\mathbf{r},t)\sigma\Psi_j(\mathbf{r},t), \quad j=1,2, \tag{3}$$

where Ψ_j are quasiclassical wave functions, which play the role of the order parameter of the spin density, $\mathbf{r}$ is the radius vector of a Cartesian coordinate system, t is the time, and σ are the Pauli matrices.

The Lagrangian equations for Ψ_j have the form

$$i\hbar\frac{\partial\Psi_j(\mathbf{r},t)}{\partial t} = -\mu_0\mathbf{H}_{ej}(\mathbf{r},t)\sigma\Psi_j(\mathbf{r},t), \tag{4}$$

where μ_0 is the Bohr magneton, and

$$\mathbf{H}_{ej} = -\frac{\partial w_j}{\partial\mathbf{M}_j} + \frac{\partial}{\partial x_k}\frac{\partial w_j}{\partial(\partial\mathbf{M}_j/\partial x_k)}.$$

Taking into account that in the ground state the material is magnetized parallel to $\mathbf{e}_z$, and assuming that $M_j^2(\mathbf{r},t)$ = const in each of the half spaces, we shall seek a solution of (4) in the form

$$\Psi_j(\mathbf{r},t) = \exp(i\mu_0 H_0 t/\hbar)\binom{1}{\chi_j(\mathbf{r},t)}. \tag{5}$$

Here the upper element corresponds to the ground state, and $\chi_j(\mathbf{r},t)$ is a small correction characterizing the deviation of the magnetization from the ground state. Linearizing Eq. (4) with allowance for (5), we obtain

$$-\frac{i\hbar}{2\mu_0 M_{0j}}\frac{\partial\chi_j(\mathbf{r},t)}{\partial t} = (\alpha(\mathbf{r})\Delta - \beta(\mathbf{r}) - \tilde{H}_{0j})\chi_j(\mathbf{r},t), \tag{6}$$

where $\tilde{H}_{0j} = H_0/M_{0j}$, $j=1,2$.

2. APPROXIMATION OF GEOMETRICAL OPTICS

Following Refs. 8 and 9, we apply the approximation of geometrical optics to the system described. Representing the time dependence of $\chi_j(\mathbf{r},t)$ by the function $\exp(-i\omega t)$, we rewrite Eq. (6) in the form

$$\Delta\chi_j(\mathbf{r}) + k_0^2 n_j^2(\mathbf{r})\chi_j(\mathbf{r}) = 0, \tag{7}$$

where

$$k_0^2 = (\Omega_1 - \beta_0 - \tilde{H}_{01})/\alpha_0, \quad \Omega_j = \omega\hbar/2\mu_0 M_{0j},$$

and α_0 and β_0 are values of the exchange and anisotropy parameters at, say, infinity on the incident wave side.[10] Thus, according to Ref. 10, k_0^2 is the square of the incident wave vector; $n_j^2(\mathbf{r}) = (\Omega_j - \beta(\mathbf{r}) - \tilde{H}_{0j})/\alpha(\mathbf{r})k_0^2$, and, if the parameters $\alpha(\mathbf{r})$ and $\beta(\mathbf{r})$ are slowly varying, then $n_j^2(\mathbf{r}) = k_j^2(\mathbf{r})/k_0^2$, where $k_j^2(\mathbf{r}) = (\Omega_j - \beta(\mathbf{r}) - \tilde{H}_{0j})/\alpha(\mathbf{r})$.

We transform Eq. (7) using the WKBJ method.[9] Substituting $\chi_j = C\exp[ik_0 s_j(\mathbf{r})]$, where C is a slowly varying amplitude and s_j is the eikonal, under the condition

$$\lambda \ll a, \tag{8}$$

where λ is the wavelength of the spin wave and a is the characteristic size of the inhomogeneities, we obtain from (7) the eikonal equation

$$(\nabla s_j(\mathbf{r}))^2 = n_j^2(\mathbf{r}). \tag{9}$$

Inequality (8) is the condition for the transition to geometrical optics for spin waves. As in optics,[11] we shall assume that the right-hand side of Eq. (9) is the square of the refractive index, i.e.,

$$n_j(\mathbf{r}) = \frac{1}{k_0}\sqrt{(\Omega_j - \beta(\mathbf{r}) - \tilde{H}_{0j})/\alpha(\mathbf{r})}, \tag{10}$$

since the ratio of the moduli of the wave vectors at two different points of space characterizes the change in direction of propagation of the spin wave.

After writing Eq. (9) in the form $H = 1/2[\mathbf{p}^2 - n^2(\mathbf{r})] = 0$, where $\mathbf{p} = \nabla s$, we obtain the ray equations in Hamiltonian form:

$$\dot{\mathbf{r}} = \mathbf{p}, \quad \dot{\mathbf{p}} = \frac{1}{2}\nabla n^2(\mathbf{r}).$$

It follows from Eq. (9) that $|\nabla s(\mathbf{r})| = ds(\mathbf{r})/d\tau = n(\mathbf{r})$, where $d\tau = \sqrt{dx^2 + dy^2 + dz^2}$ is an element of the ray trajectory. Therefore the function s can be determined as a curvilinear integral along the ray trajectory:

$$s = \int_A^B n\,d\tau. \tag{11}$$

Minimizing (11) with the aid of Fermat's principle,[12] we obtain the equation of the ray trajectory:[8]

$$\frac{d}{d\tau}\left(n\frac{dr}{d\tau}\right) = \nabla n.$$

3. REFRACTION OF A SPIN-WAVE RAY AT THE INTERFACE BETWEEN TWO HOMOGENEOUS MAGNETS

Let us apply formula (11) to the particular case of two homogeneous semi-infinite magnets. Suppose we have two magnets with parameters α_1, β_1, M_{01} and α_2, β_2, M_{02}, respectively, in contact along the yz plane, and suppose that a spin wave is incident on the boundary between them from the side of the first magnet. A ray propagates from the point (x_1,y_1,z_1) in medium 1, which has a refractive index $n_0 = 1$, to the point (x_2,y_2,z_2) in medium 2, the refractive index of which, according to Eq. (10), is equal to

$$n = \sqrt{\frac{\alpha_1}{\alpha_2}\frac{\Omega_2 - \beta_2 - \tilde{H}_{02}}{\Omega_1 - \beta_1 - \tilde{H}_{01}}},$$

crossing the interface at a point $(0,y,z)$ with unknown coordinates y and z. It follows from the conditions of an extremum of the function s in this case that

$$\frac{\sin\theta_1}{\sin\theta_2} = \frac{k_2}{k_0} = \sqrt{\frac{\alpha_1}{\alpha_2}\frac{\Omega_2 - \beta_2 - \tilde{H}_{02}}{\Omega_1 - \beta_1 - \tilde{H}_{01}}} = n, \tag{12}$$

where θ_1 is the angle of incidence and θ_2 is the angle of refraction.

4. REFLECTION OF SPIN WAVES AT THE INTERFACE BETWEEN TWO HOMOGENEOUS MEDIA

In all cases when one is talking about processes of reflection and refraction of waves of an arbitrary nature, it is important to estimate the relative intensities of the transmitted and reflected waves. If the intensity of the reflected wave is much greater than that of the transmitted wave, then the structure under consideration can be used to make a mirror of some kind (we are talking about plane, convex, or concave mirrors of the spherical or cylindrical type, etc.). In the opposite case, when the intensity of the transmitted wave is much greater than the intensity of the reflected wave, the structure can be used to make lenses with required parameters.

We obtain the expressions for the reflection and transmission amplitudes of the spin wave, using the boundary conditions for $\chi(\mathbf{r},t)$ at the interface that follow from Eqs. (1) and (2):

$$[A\gamma(\chi_2-\chi_1)+\alpha_1\chi_1']_{x=0}=0,$$

$$[A(\chi_1-\chi_2)-\gamma\alpha_2\chi_2']_{x=0}=0. \qquad (13)$$

Here $\gamma=M_{02}/M_{01}$.

In Eq. (6), we associate the function $\chi_I=\exp(i(\mathbf{k}_0\cdot\mathbf{r}-\omega t))$ with the incident wave, $\chi_R=R\exp(i(\mathbf{k}_1\cdot\mathbf{r}-\omega t))$ with the reflected wave, and $\chi_D=D\exp(i(\mathbf{k}_2\cdot\mathbf{r}-\omega t))$ with

the transmitted wave, where R is the complex reflection amplitude of the spin wave from the interface, D is the transmission amplitude, and $\mathbf{k}_0$, $\mathbf{k}_1$, and $\mathbf{k}_2$ are the wave vectors of the incident, reflected, and transmitted waves, respectively. Substituting these expressions into Eq. (13), we arrive at expressions for the reflection and transmission amplitudes of the spin wave:

$$R=\frac{k_0\alpha_1\alpha_2\gamma\cos\theta_1\sqrt{n^2-\sin^2\theta_1}-iA(\alpha_1\cos\theta_1-\alpha_2\gamma^2\sqrt{n^2-\sin^2\theta_1})}{k_0\alpha_1\alpha_2\gamma\cos\theta_1\sqrt{n^2-\sin^2\theta_1}-iA(\alpha_1\cos\theta_1+\alpha_2\gamma^2\sqrt{n^2-\sin^2\theta_1})},$$

$$D=\frac{-2iA\alpha_1\cos\theta_1}{k_0\alpha_1\alpha_2\gamma\cos\theta_1\sqrt{n^2-\sin^2\theta_1}-iA(\alpha_1\cos\theta_1+\alpha_2\gamma^2\sqrt{n^2-\sin^2\theta_1})}. \qquad (14)$$

We note that for $k_2^2<k_{2y}^2+k_{2z}^2$ (this pertains to the case $k_0^2>0$, $k_2^2<0$) we obtain: $k_{2x}=-i\sqrt{k_{1y}^2+k_{1z}^2-k_2^2}=-i/2h$, $\chi_D(\mathbf{r},t)=D\exp(-x/2h)\exp(i(k_{2y}y+k_{2z}z-\omega t))$, i.e., h plays the role of the penetration depth of the spin wave into the second material and is equal to $h=(k_0\sqrt{\sin^2\theta_1-n^2})^{-1}$. The limiting angle of total reflection is given by the expression

$$\sin\theta_0=\sqrt{\frac{\alpha_1}{\alpha_2}\frac{\Omega_2-\beta_2-\tilde{H}_{02}}{\Omega_1-\beta_1-\tilde{H}_{01}}}.$$

5. ESTIMATES OF THE PARAMETERS OF SPIN-WAVE LENSES AND MIRRORS

Let us estimate the material parameters necessary for achieving the required transparency of a thin lens at small angles of incidence of the spin-wave rays with respect to the optic axis of a lens. Since the intensity of the reflected wave is determined by the square modulus of the reflection amplitude and, as follows from Eq. (14),

$$|R|^2\approx[(\alpha_1-\alpha_2\gamma^2n)/(\alpha_1+\alpha_2\gamma^2n)]^2$$

(for small angles of incidence and $A\to\infty$), by requiring satisfaction of the condition $|R|^2<\eta$, where η is the necessary degree of smallness of the reflection coefficient, we obtain a restriction on n and, hence, on α, β, ω, M_0, and H_0:

$$\frac{1-\sqrt{\eta}}{1+\sqrt{\eta}}<\frac{\alpha_2}{\alpha_1}n<\frac{1+\sqrt{\eta}}{1-\sqrt{\eta}}.$$

In particular, for $\alpha_1=\alpha_2$, $M_{01}=M_{02}$ the reflection coefficient does not exceed 10% if $0.52<n<1.92$. The corresponding restrictions in the case of a mirror have the form

$$\frac{\alpha_2}{\alpha_1}n<\frac{1-\sqrt{\eta}}{1+\sqrt{\eta}} \quad\text{or}\quad \frac{\alpha_2}{\alpha_1}n>\frac{1+\sqrt{\eta}}{1-\sqrt{\eta}}.$$

For example, $|R|^2>0.9$ is achieved in the case $\alpha_1=\alpha_2$, $M_{01}=M_{02}$ for $n<0.03$ or $n>37.97$.

To satisfy the condition of geometrical optics (8) the thickness of the lens or mirror is restricted by the inequality

$$a\gg2\pi\sqrt{\alpha/(\Omega-\beta-\tilde{H}_0)}. \qquad (15)$$

As we see from Eqs. (12), (14), and (15), the parameters for constructing a lens or mirror can be chosen without difficulty for a broad spectrum of magnetic materials.[13] In particular, in the case of iron garnets it follows from condition (15) that for a thin lens one must have $a>10^{-6}-10^{-8}$ m.

The dependence of the reflected intensity $I_R=|R|^2$ and refractive index n on the spin-wave frequency ω at typical values of the material parameters[13] are shown in Figs. 1 and 2. It is clearly seen that suitably by choosing the material parameters one can achieve the necessary relation between the intensities of the reflected and transmitted waves for a chosen frequency. In addition, as follows from Fig. 3, the reflected intensity depends substantially on the value of the external uniform magnetic field, making it possible to control the intensity of the reflected wave over a wide range by changing only the value of the external magnetic field at fixed material parameters. The character of the change in the refractive index in such a case is illustrated in Fig. 4.

CONCLUSION

Thus we have obtained an expression for the refractive index of a spin wave propagating in a magnetically uniaxial
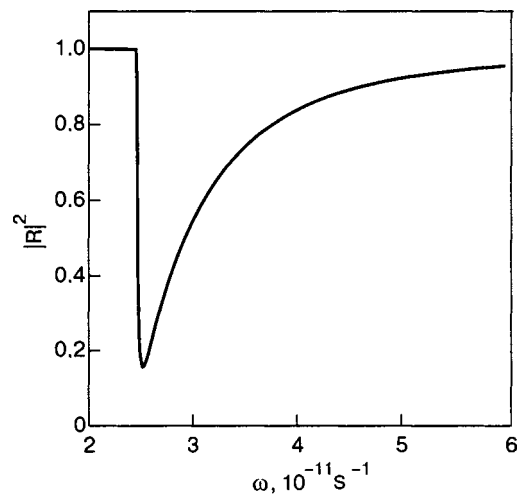

FIG. 1. Dependence of the reflection coefficient $|R|^2$ on the spin-wave frequency ω for $\alpha_2=2\alpha_1$, $\beta_2=2\beta_1$, $M_{01}=90$ G, $M_{02}=125$ G, $A=30$, $\theta_1=\pi/80$, and $H_0=900$ Oe.
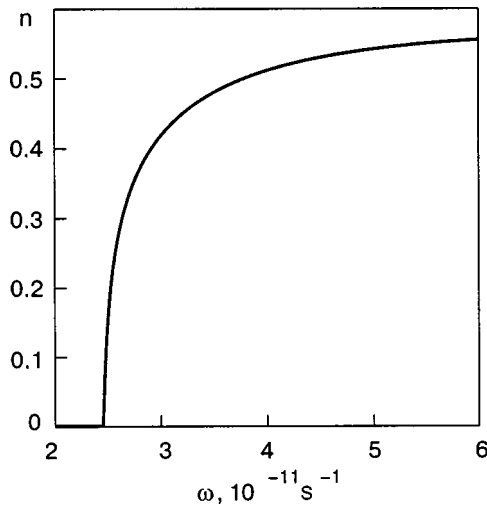
FIG. 2. Dependence of the refractive index n on the frequency ω for $\alpha_2 = 2\alpha_1$, $\beta_2 = 2\beta_1$, $M_{01} = 90$ G, $M_{02} = 125$ G, and $H_0 = 900$ Oe.

medium with slowly varying magnetic parameters and have studied the processes of spin-wave reflection at the interface between two homogeneous media with allowance for a δ-function-like character of the exchange interaction between the media in contact. We have obtained the conditions under which the spin wave manifests ray properties. We have shown that there exists a possibility of achieving the required reflection coefficient from an embedded inhomogeneity, which plays the role of a lens or mirror, by changing the value of a uniform external dc magnetic field. Here the reflection coefficient can be varied practically from zero to
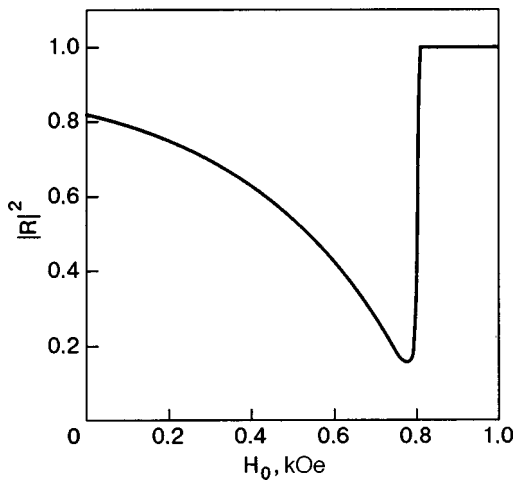
FIG. 3. Dependence of the reflection coefficient $|R|^2$ on the value of the external static magnetic field H_0 for $\alpha_2 = 2\alpha_1$, $\beta_2 = 2\beta_1$, $M_{01} = 90$ G, $M_{02} = 125$ G, $A = 30$, $\theta_1 = \pi/80$, and $\omega = 2.3 \times 10^{11}$ s^{-1}.
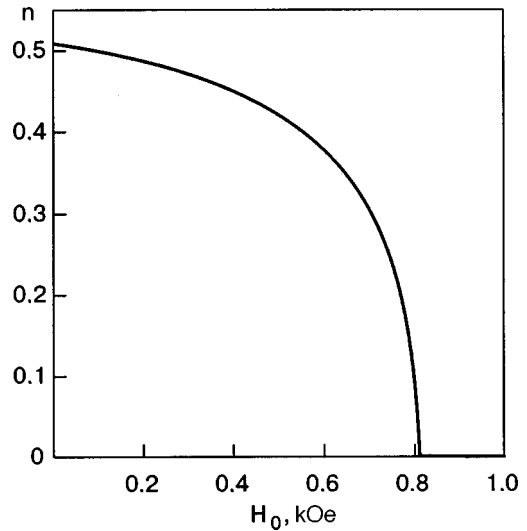
FIG. 4. Dependence of the refractive index n on the value of a uniform external magnetic field H_0 for $\alpha_2 = 2\alpha_1$, $\beta_2 = 2\beta_1$, $M_{01} = 90$ G, $M_{02} = 125$ G, and $\omega = 2.3 \times 10^{11}$ s^{-1}.

unity without changing the parameters of the medium, so that the same inhomogeneity can be used as a spin-wave lens and as a mirror for the same structure parameters.

The results obtained above can be used to design and construct devices for spin-wave microelectronics.

The author thanks Yu. I. Gorobets for participating in a discussion of the results of this study.

[1] A. L. Sukstanskii, E. P. Stefanovskii, S. A. Reshetnyak, and V. N. Varyukhin, Phys. Rev. B **61**, 8843 (2000).
[2] J. Y. Gan, F. C. Zhang, and Z. B. Su, Phys. Rev. B **67**, 144427 (2003).
[3] M. Buchmeier, B. K. Kuanr, R. R. Gareev, D. E. Bürgler, and P. Grünberg, Phys. Rev. B **67**, 184404 (2003).
[4] J. Fransson, E. Holmstrom, O. Eriksson, and I. Sandalov, Phys. Rev. B **67**, 205310 (2003).
[5] V. P. Antropov, J. Magn. Magn. Mater. **262**, L192 (2003).
[6] Yu. I. Gorobets and S. A. Reshetnyak, Zh. Tekh. Fiz. **68**(2), 60 (1998) [Tech. Phys. **43**, 188 (1998)].
[7] V. G. Bar'yakhtar and Yu. I. Gorobets, *Magnetic Bubbles and Bubble Lattices* [in Russian], Naukova Dumka, Kiev (1988).
[8] Yu. A. Kravtsov and Yu. I. Orlov, *Geometrical Optics of Inhomogeneous Media* [in Russian], Nauka, Moscow (1980).
[9] P. M. Morse and H. Feshbach, *Methods of Theoretical Physics*, Vol. II, McGraw-Hill, New York (1953), Izd-vo Inostr. Lit., Moscow (1960).
[10] A. I. Akhiezer, V. G. Bar'yakhtar, and S. V. Peletminski, *Spin Waves*, North Holland, Amsterdam (1968), Nauka, Moscow (1967).
[11] M. Born and E. Wolf, *Principles of Optics*, 4th ed., Academic Press, New York (1973), Nauka, Moscow (1973).
[12] R. Courant, "Partielle Differentialgleichungen," unpublished lecture notes, Göttingen (1932) [Russ. transl., *Uravneniya s Chastnymi Proizvodnymi*, Mir, Moscow (1964)].
[13] A. H. Eschenfelder, *Magnetic Bubble Technology*, Springer-Verlag, Berlin (1980), Mir, Moscow (1983).

Translated by Steve Torstveit

Structural imperfection, phase transitions, and the properties of magnetoresistive ceramic and films of $La_{0.66}Mn_{1.23}V_{0.11}^{(c)}O_{2.84}^{2-}V_{0.16}^{(a)}$

V. P. Paschenko,* A. A. Shemyakov, A. V. Pashechenko, and L. T. Tsymbal

A. A. Galkin Donetsk Physicotechnical Institute, ul. R. Lyuksemburg 72, Donetsk 83114, Ukraine

G. K. Kakazei

IFIMUP, Departamento do Fisica, Universidade do Porto, Rua Do Campo Algro 687, 4169-007 Portu, Portugal; Institute of Magnetism of the National Academy of Sciences of Ukraine, bul. Vernadskogo 37-b, Kiev 03142, Ukraine

V. P. Dyakonov

A. A. Galkin Donetsk Physicotechnical Institute, ul. R. Lyuksemburg 72, Donetsk 83114, Ukraine; Institute of Physics, Polish Academy of Sciences, 32/46 Al. Lotnikow, 02-668 Warsaw, Poland

H. Szymczak

Institute of Physics, Polish Academy of Sciences, 32/46 Al. Lotnikow, 02-668 Warsaw, Poland

J. A. M. Santos and J. B. Sousa

IFIMUP, Departamento do Fisica, Universidade do Porto, Rua Do Campo Algro 687, 4169-007 Portu, Portugal

It is established by x-ray, resistive, NMR, and magnetoresistive studies of ceramic and thin-film laser perovskites $La_{0.7}Mn_{1.3}O_3$ with "excess" manganese that the real structure of these compounds contains heterovalent manganese ions and cationic and anionic vacancies and clusters, the magnetism and resistivity of the latter being manifested near 42 K. The broad, asymmetric [55]Mn and [139]La NMR spectra of the ceramics attest to the presence of high-frequency electron–hole exchange between the heterovalent manganese ions and to a high degree of imperfection and mesoscopic inhomogeneity of nonstoichiometric lanthanum manganite perovskites. The differences of the metal–semiconductor phase transition temperatures and activation energy of the ceramics and films is explained by the different oxygen nonstoichiometry, structural imperfection, and, accordingly, densities of charge carriers and excitons. The low-field magnetoresistive effect of the ceramic is explained by tunneling at grain boundaries. It is conjectured that the decrease in resistance in magnetic field is due to an increase in charge carrier density due to weakening of the electron–hole interaction in excitons. An anomaly of the resistance and magnetoresistive effect observed near 42 K is explained by the presence of clusters. © *2004 American Institute of Physics.* [DOI: 10.1063/1.1704617]

INTRODUCTION

Interest in lanthanum manganite perovskites continues unabated for several reasons: the colossal magnetoresistance (CMR) effect,[1–5] which is observed in them near the temperatures of the metal–semiconductor (T_{ms}) and ferromagnet–paramagnet (T_c) phase transitions, the lack of consensus as to the nature of such a unique coupling of the transport and magnetic properties, and the prospects for practical application of these materials.

The majority of research has been done on lanthanum manganite perovskites doped in the A sublattice:[6–9] $La_{1-x}^{3+}A_x^{2+}Mn_{1-x}^{3+}Mn_x^{4+}O_3^{2-}$ ($A^{2+}=Ca^{2+}$, Sr^{2+}, Ba^{2+}, Pb^{2+}) at the optimal concentration $x=0.3$, or in the B sublattice:[10–12] $La_{0.7}^{3+}A_{0.3}^{2+}Mn_{1-y}^{3+}B_yO_3^{2-}$, where B_y is most often a transition-metal ion.

There has been less research[13,14] on autodoped $LaMnO_3$, in particular, compounds with a breakdown of the La/Mn ratio to the lanthanum deficit side,[15,16] i.e., with an "excess" of manganese ions,[16,17] which are responsible for the electrical and magnetic properties. As was shown in Refs. 18 and 19, increasing the manganese concentration in $La_{1-x}Mn_{1+x}O_3$ and $(La_{0.7}^{3+}Ca_{0.3})_{1-x}Mn_{1+x}O_3$ leads to marked growth in the magnetoresistive effect without lowering the phase transition temperatures T_{ms} and T_c. The lack of consensus in the ideas about the form in which this "excess" manganese is found (either in separate phases of Mn_3O_4 or Mn_2O_3 or dissolved in the lanthanum manganite perovskite phase with the formation of clusters, which are coherently coupled to the matrix structure) makes for additional interest in the study of such materials, both single-crystal[20,21] and polycrystalline/ceramic[22,23] and also magnetron[24,25] or laser[26,27] sputtered thin films. Of particular interest are studies over the wide temperature range in which the different phase transitions can appear, with elucidation of

the role of oxygen nonstoichiometry and structural imperfection in the formation of the properties of the lanthanum manganite perovskites.

SAMPLE PREPARATION TECHNOLOGY AND METHODS OF STUDY

Since it has been established that for autodoped[18] and doped[19] compositions the maximum values of the CMR are characteristically achieved for $x = 0.3$, our studies were done on ceramics and laser films with the formal composition $La_{0.7}Mn_{1.3}O_{3\pm\delta}$ (if one ignores the structural imperfection). Ceramic samples, including the target for deposition of the laser film, were obtained from the corresponding powder mixture of the oxides La_2O_3 ($Ia3$; $a = 11.498$ Å) and Mn_3O_4 (I_1^4/amd; $a = 5.77$ Å; $c = 9.38$ Å) after a twenty-hour synthesizing anneal at 900 °C with a subsequent sintering of the pressings at 1150 °C (24 h) in the regime of slow heating and cooling of samples in the form of tablets (8 mm in diameter and with a height $h = 3$ mm) and targets for laser sputtering (25 mm in diameter, $h = 6$ mm).

Single-crystal laser films of $La_{0.7}Mn_{1.3}O_3$ of thickness $d \approx 1000$ Å were deposited on a $LaSrGaO_4$ substrate having the parameters $a = 3.840$ Å, $c = 12.68$ Å and oriented in the (100) plane. We studied both the initial laser film (f1) and the completely oxidized film (f2), which was subjected to an additional oxidizing anneal at 780 °C with a subsequent slow cooling in air.

The following methods were used in these studies:

1) x-ray structural studies in CuK_α radiation on a DRON-3 device, for determining the phase composition, lattice parameters, and crystallographic orientation of the substrate and film;

2) NMR of ^{139}La and ^{55}Mn by the "spin-echo" method, for determining the resonance frequency, magnetic states, and inequivalence of the environment of those nuclei at 77 K;

3) four-probe resistive method, for studying the temperature dependence of the resistivity ρ and the phase transitions T_{ms};

4) magnetoresistive (MR) method, for determining the temperature dependence of $\Delta\rho/\rho_0$ (where $\Delta\rho = \rho_0 - \rho_H$) over a wide range of temperatures at $H = 0$ and 8 kOe.

The errors of measurement were ~3% for the phase composition, ~0.3% for the lattice parameters, ~0.2% for the resistivity, ~0.3% for the magnetoresistivity, ~0.1% for the NMR of ^{55}Mn, and ~0.05% for the NMR of ^{139}La.

RESULTS AND DISCUSSION

According to the x-ray diffraction data, the ceramic and film samples were practically single-phase and contained a rhombically distorted perovskite structure ($Pnma$). The lattice parameters of the ceramic were $a = 5.464$ Å, $b = 5.515$ Å, and $c = 7.728$ Å.

The NMR spectra of ^{55}Mn and ^{139}La in the ceramic sample are presented in Fig. 1. The broad, asymmetric spectrum of ^{55}Mn in the frequency interval 330–430 MHz attests to both the presence of high-frequency electron exchange in the B positions between Mn^{3+} and Mn^{4+} with their averaged valence and also to the inequivalence of their environ-
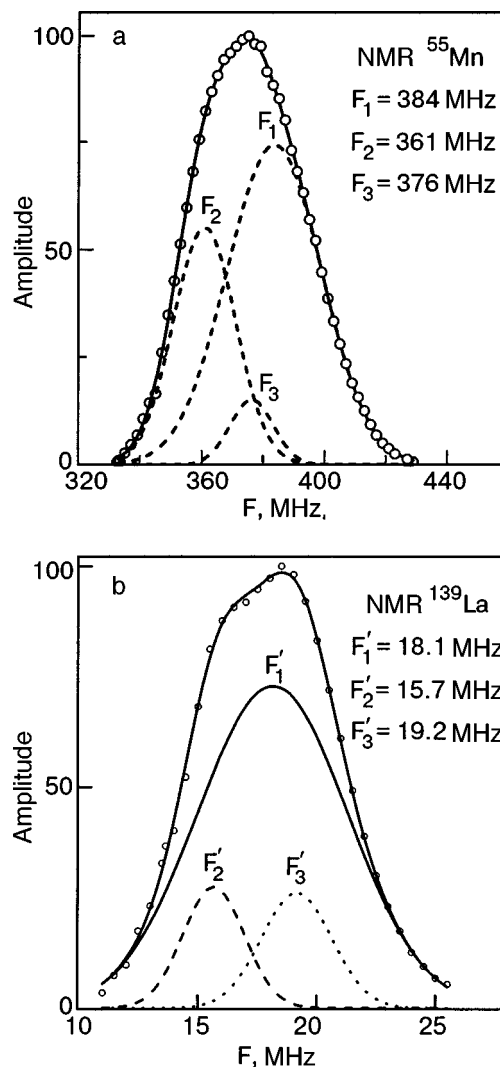
FIG. 1. NMR spectra of ^{55}Mn (a) and ^{139}L (b) of a ceramic sample $La_{0.66}Mn_{1.23}V_{0.11}^{(c)}O_{2.84}^{2-}V_{0.16}^{(a)}$ at 77 K.

ments, which is due to the nonuniformity of the distributions of La^{3+} and of defects in the A positions and also of the more complex defects of the cluster type. A computer decomposition of this spectrum made it possible to separate out 3 components. The main component, with the frequency $F_1 = 384$ MHz, is due to a superposition of the Mn^{3+} and Mn^{4+} ions found in high-frequency electron–hole exchange. The environment of those ions is predominantly La^{3+}. The lowest-frequency component, with $F_2 = 361$ MHz (intermediate in intensity), is apparently due to inhomogeneity in which the ratio of the number of Mn^{3+} to Mn^{4+} ions is smaller, and their environment includes cation vacancies in the A positions. The inhomogeneity of intermediate frequency ($F_3 = 376$ MHz) is apparently due to an intermediate ratio of Mn^{3+}/Mn^{4+}, near which are found clusters due to the excess heterovalent manganese ions and those ions near which are localized the electrons (Mn^{3+}) and holes (Mn^{4+}) that take part in the formation of excitons.

The less broad but no less asymmetric and even bifurcated induced NMR spectrum of ^{139}La confirms the high degree of imperfection and the inhomogeneity of the perovskite structure. This spectrum also decomposes into 3 components. The main component, with frequency F_1'

=18 MHz, corresponds to La^{3+} with a nearest environment of Mn^{3+} and Mn^{4+} found in the B positions of the main matrix structure ($F_1 = 384$ MHz). The lower-frequency part of the ^{139}La spectrum ($F_2' = 15.3$ MHz) is due, we believe, to La^{3+} ions near which are found manganese ions with a lower ratio of Mn^{3+}/Mn^{4+} ($F_2 = 361$ MHz). The highest-frequency component of the spectrum ($F_3' = 19$ MHz) apparently corresponds to La^{3+} ions near which are found manganese ions of the matrix structure and clusters with a superposition of Mn^{2+} and Mn^{4+}.

Taking these data into account along with the mechanism of defect formation[18] and comparing the x-ray and pycnometric density, we can write the molar formula of the real perovskite structure in the following form:

$$\{La^{3+}_{0.66}V^{(c)}_{0.11}\}_A[Mn^{3+}_{0.77}Mn^{4+}_{0.17}]_B(Mn^{2+}_{0.23}Mn^{4+}_{0.06})_{cl}O^{2-}_{2.84}V^{(a)}_{0.16}.$$
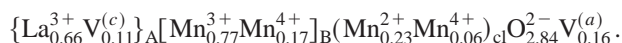
Here $V^{(c)}$ and $V^{(a)}$ are cation and anion vacancies, and the parentheses indicate manganese ions of a cluster. Analyzing this model of the defect state of the crystal lattice, which is similar to the model of Ref. 28 except that it contains not only cation but also anion vacancies and also clusters, we must note the following. Despite the high density of defects in both the cation and anion sublattices, with a ratio close to the stoichiometric (0.75), the vacancy concentration is 5.5%, i.e., it does not exceed the empirical number (15%) associated with the limit of solubility.

The experimental values of the resonance frequencies for the NMR of ^{55}Mn and and the values calculated from that formula for manganese ions in the B positions ($F = 384$ MHz) of the main matrix structure are in good agreement if the frequency corresponding to Mn^{3+} is $F = 403$ MHz and that corresponding to Mn^{4+} is $F = 300$ MHz. NMR studies could not be done on the film because of its insufficient mass. In comparison with the ceramic, the completely oxidized film the contains more oxygen, which can be manifested either in a decrease in the concentration of anion vacancies or in additional formation of cation vacancies. However, the difference of the oxygen nonstoichiometry ($\Delta\delta$) with allowance for the difference of the temperatures T_{ms} ($\Delta T_{ms} = 25$ and 35 K, respectively, for the initial and completely oxidized films in comparison with the ceramic) was only 0.01. These differences in the oxygen nonstoichiometry of the ceramic and film are small. It can therefore be assumed that the real perovskite structures of the ceramic and even the completely oxidized film are not very different.

The good agreement of the experimental and calculated values of the resonance frequencies confirms the correctness of our ideas about the defect structure of lanthanum manganite perovskites, the lattice of which contains heterovalent manganese ions Mn^{3+} and Mn^{4+}, found in high-frequency electron exchange with the averaged valence, in the B positions, anion $V^{(a)}$ and cation $V^{(c)}$ vacancies, found primarily in the A positions, and clusterized defects formed by "excess" manganese in the form of Mn_3O_4 or Mn_2O_3, with a superposition of Mn^{2+}–Mn^{4+} ions and, possibly, partially Mn^{3+} with a "canted" magnetic structure, which is ascribed to the lanthanum manganite perovskite matrix structure.[29] However, we did not detect Mn^{2+} ions at 77 K by the NMR method, since their magnetism is not manifested at that tem-

FIG. 2. Temperature dependence of the resistivity of the ceramic (C) and of the initial (f1) and completely oxidized (f2) laser films.

perature, and we did not have the means to do low-temperature NMR studies. The NMR spectrum of Mn^{2+} in lanthanum manganite perovskites has been observed at lower temperatures of 1.8–4.2 K.[30,31] It should be noted that the A sublattice of the main perovskite structure is filled out by cation vacancies and Mn^{2+}, with a defect of the coordination number ($Z = 8$) owing to anion vacancies. The B sublattice is filled out by Mn^{4+} ions of a cluster, around which the cation vacancies are distributed.

The molar formula of a cluster analogous to the defect cluster $Mn_3O_4 \rightarrow [Mn^{3+}_{1.78}Mn^{2+}_{0.89}V^{(c)}_{0.33}]O^{2-}_{3.56}V^{(a)}_{0.44}$ with allowance for the cation distribution over inequivalent positions of the tetragonal lattice, can be written $\langle Mn^{2+}_{0.89}V^{(c)}_{0.11}\rangle \times [Mn^{3+}_{1.78}V^{(c)}_{0.22}]O^{2-}_{3.56}V^{(a)}_{0.44}$. The molar formula of the more highly oxidized defect cluster $Mn_2O_3 \rightarrow Mn^{3+}_{1.70}V^{(c)}_{0.30}O^{2-}_{2.55}V^{(a)}_{0.45}$ with allowance for the cation distribution can be written in the form $\langle Mn^{2+}_{0.70}V^{(c)}_{0.30}\rangle \times [Mn^{3+}_{0.30}Mn^{4+}_{0.70}]_BO^{2-}_{2.55}V^{(a)}_{0.45}$. It should be noted that the Mn^{3+} and Mn^{4+} ions in both cases are found in octa (B) positions, while the Mn^{2+} ions are found in tetra positions or with a coordination number of 8. Depending on the degree of oxidation in the lanthanum manganite perovskites the clusters can be found in the form of one of these compositions or with a composition intermediate between them, corresponding to their concentration in the sample. The elucidation of the crystal-chemical, magnetic, and resistive nature of such clusters will require doing low-temperature studies. Investigations into the magnetic nature of anomalous clusters have been carried out in Ref. 32, where a preference was given to the "canted" magnetic structure.

Since lanthanum manganite perovskites are of paramount interest as objects with a colossal magnetoresistive effect, we show in Fig. 2 the temperature dependence of the resistivity of a ceramic and of the initial f1 and completely oxidized f2 laser films at $H = 0$ and 8 kOe. For the film that had not undergone an additional low-temperature oxidizing anneal, the measurements were made over a wider temperature interval, including the region of interest to us, 42–45 K. The higher values of the resistivity of the ceramic are apparently due to its porosity. For the ceramic sample, unlike the films, the temperature dependence of ρ is characterized by
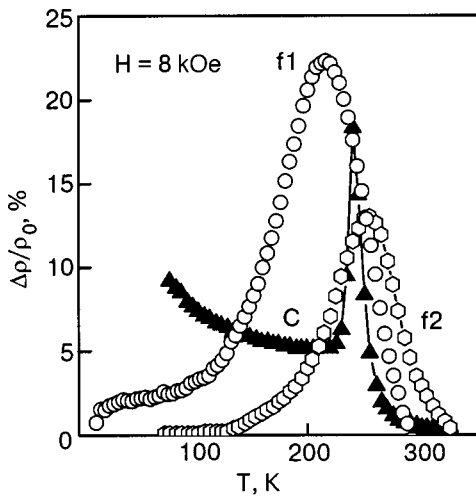
FIG. 3. Temperature dependence of the magnetoresistive effect at $H = 8$ kOe of the ceramic (C) and of the initial (f1) and completely oxidized (f2) laser films.

the presence of two peaks. This is due to the specific inhomogeneity of polycrystalline ceramic samples, which contain crystallites (grains) and intergrain zones. Then the less smeared peak, the temperature of which, $^{c}T_{ms} = 255$ K, is comparable to $^{f1}T_{ms} = 260$ K for the f1 films, is obviously due to the crystallites. The more smeared peak at $^{c}T'_{ms} = 200$ K is apparently due to the contribution from the intergrain zones.

The difference of the temperature of the metal–semiconductor phase transition of the ceramic ($^{c}T_{ms}$) and, especially, of the completely oxidized film ($^{f2}T_{ms}$) we attribute to their different oxygen nonstoichiometries, to which the value of T_{ms} in manganite perovskites is extremely sensitive, the sensitivity being determined by the relation $\Delta\delta/\Delta T = 6 \times 10^{-4}$ K^{-1} (Ref. 33).

The anomaly in the form a smeared minimum near $T = 42$ K (Fig. 2) on the $\rho(T)$ curve in the low-temperature region (15–75 K) for the initial film f1 is worthy of special mention. We link this temperature anomaly of the resistivity at $^{f1}T'_{ms} \approx 42$ K, which we have observed for the first time in lanthanum manganite perovskites, to the appearance of a cluster. As can be seen in the inset to Fig. 2, the character of the variation of $\rho(T)$ at $H = 0$ and 8 kOe for a cluster is opposite to what is observed at the transition temperature T_{ms} of the main matrix structure.

The influence of the intergrain zones on the magnetoresistive effect at $H = 8$ kOe was manifested in an additional increase of the CMR in the low-temperature region (Fig. 3), which is not observed in the single-crystal films, as they do not have intergrain zones. This low-field magnetoresistivity due to the tunneling effect at the grain boundaries[23,34,35] has been attracting increased attention recently in connection with its high sensitivity to magnetic field.

Returning to the nature of the inhomogeneities of lanthanum manganite perovskites, especially those containing "excess" manganese, the magnetism of the clusters in which is manifested in the temperature interval 42–45 K, we should mention that, unlike the case of the individual Mn_3O_4 phase, a decrease of the magnetization with decreasing temperature

and a peculiar temperature hysteresis are observed in weak magnetic fields.[17,36]

There is a paucity of data on the resistive behavior of manganites[37] and practically no information about the magnetoresistive effect in this temperature interval. For this reason our additional studies of the resistivity and magnetoresistive effect of the initial (f1) laser film over a wide range of temperatures, including low temperatures (42–45 K), are of particular interest. We plan to devote more attention to this question in our future studies.

One of the important characteristics in the physics of semiconductors is the activation energy E_a. On the basis of an analysis of the temperature dependence of the resistivity of the ceramic sample (Fig. 2) in the temperature region corresponding to conductivity of a semiconductor character, i.e., for $T > T_{ms}$, we have calculated the activation energy in a field $H = 0$ and 8 kOe, obtaining values which are close: 107.8 and 108.6 meV, respectively. The temperature interval $T = 275$–320 K in which an exponential trend $\rho = \rho_0 \exp(E_a/kT)$ should hold, was chosen so that the deviation of the experimental values of ρ from the linear dependence $\ln\rho = \ln\rho_0 + E_a(kT)^{-1}$ did not exceed the experimental error (i.e., 0.2%). Then the standard deviation $\sigma(E_a) \leqslant 0.16$ MeV.

In accordance with the band theory of semiconductors,[38] the observed change of the activation energy $\Delta E_a = 0.8$ MeV is due to a shift of the top of the valence band downward and the bottom of the conduction band upward in a magnetic field of induction B parallel to the electric field used for measuring the resistivity by the four-probe method. Here ΔE_a is related to the value of B as $\Delta E_a = e\hbar B/2m^*$, where m^* is the effective mass. A numerical estimate of this last relation with the experimental data taken into account and with the approximation that $B \approx 0.8$ T for $H = 8$ kOe in the paramagnetic region, which is based on the experimental data[17] on the behavior of the magnetization of samples of the given composition in magnetic field, yields a value $m^* = 0.06m_e$, where m_e is the mass of the electron. Such a low value of the effective mass suggests the possibility of existence of an exciton with a reduced effective mass $m^* = m_n^* m_p^*/(m_n^* + m_p^*)$, where m_n^* and m_p^* are the effective masses of electrons and holes found near the bottom of the conduction band and the top of the valence band, respectively.

This approach to the determination of m^* cannot be applied to the laser film, since an exponential trend of $\rho(T)$ in the high-temperature region holds only in zero field. The activation energies are $^{f1}E_a(H = 0) = 106.4$ meV and $^{f2}E_a(H = 0) = 69.7$ meV. For a film the deviation from a linear trend of $\ln\rho = \ln\rho_0 + E_a(kT)^{-1}$ in a magnetic field is observed in the entire temperature interval from T_{ms} to 320 K. Such behavior of $\rho(T)$ in the high-temperature region is possible if the thermodynamic equilibrium established between the number of thermally activated electrons and the number of hole recombinations due to other mechanisms is broken. In the present case of a laser film such a mechanism leading to an increase in the charge carrier density can be a magnetic field, which imparts to the exciton a rotational motion at the cyclotron frequency $\omega_c = eB/m^*$.

It is of interest to estimate the exciton velocity and life-

time. A magnetic field gives rise to a perpendicular component of the exciton velocity v_B in the plane normal to the direction of motion of the charge; this component, which can be determined from the expression $p^2/2m^* = \hbar\,\omega_c/2$, has the value $v_B \approx 7 \times 10^4$ m/s in a field of 0.8 T. The exciton lifetime can be estimated from an analysis of the NMR spectrum and the nuclear magnetic relaxation spectrum of ^{55}Mn with the use of the spin echo technique. From Ref. 39 the spin–spin and spin–lattice relaxation times in the perovskites $(La_{1-x}Sr_x)_{1-\delta}MnO_3$ for $x=0$ are $\tau_0 \approx 20\ \mu$m and $\tau_1 \approx 1$ ms, respectively.

Returning to an analysis of our NMR spectrum for ^{55}Mn (Fig. 1a), we propose a model wherein a complex of heterovalent manganese ions found in the matrix structure, i.e., $Mn^{3+} - Mn^{4+}$ can be considered as a possible source of the formation of an electron–hole bound state, i.e., an exciton. Specifically: upon the transition of an electron from the valence band to the conduction band at an Mn^{3+} site, an Mn^{4+} ion with a hole in the valence band is formed. A coupling is established between the electron and hole, leading to the formation of an exciton, the lifetime of which corresponds to the spin–spin relaxation time $\tau_0 \approx 20\ \mu$s. The time the electron spend in the conduction band before recombination with a hole found in the valence band corresponds to the spin–lattice relaxation time, i.e., $\tau_1 \approx 1$ ms.

Such a model explains the F_3 component of the NMR spectrum of ^{55}Mn (Fig. 1a), which is due to the formation of excitons in high-frequency electron–hole exchange between the electron subsystem of the manganese ions of the matrix structure. Furthermore, the large difference in amplitude of the F_3 component of the NMR spectrum from F_1 and F_2 can be explained by the short exciton lifetime τ_0 compared to τ_1 ($\tau_0 \approx 0.02\tau_1$).

As to the deviation from the experimental trend of the $\rho(T)$ curve of the laser film f1 in a magnetic field $H = 8$ kOe in the temperature interval 275–320 K, it is easy to find the thickness d of the boundary layer of the film within which the excitons will scatter on the boundary of the film owing to the appearance of the cyclotron frequency. Taking into account the numerical estimates obtained for m^*, ω_c, and v_B and using the equation for the radius of the cyclotron orbit $r = v_B/\omega_c$, we find that $r \approx 300$ Å in a field $B = 0.8$ T. This result can be paramount for our films, since a large part of even those excitons that move in the plane of the film will be scattered by the boundary of the film in a magnetic field owing to the appearance of the cyclotron component of v_B. Here the mean lifetime of the exciton will be governed by the time spent on traversing the distance to the boundary of the film along a circular orbit of radius r at velocity v_B. In our case, for a film of thickness ≈ 1000 Å, the exciton lifetime will be decreased to $\tau' \approx 10^{-7}\tau_0$.

In our opinion this mechanism of exciton destruction and, hence, of increasing the charge carrier density can be observed not only at the boundary of the laser film but also at grain boundaries in ceramic samples and at domain walls if the grain size or domain size upon magnetic ordering is comparable to the mean free path or, in the case of Frenkel excitons, the radius of the cyclotron orbit. The latter, unlike Wannier excitons, can be localized only within a lattice site and, accordingly, have a size comparable to the lattice pa-

rameter. The size of a Wannier exciton is determined by the band structure and the Coulomb attractive forces between particles of unlike charge, which are screened on account of the dielectric constant ε of the crystal.

A numerical estimate of the exciton size l by the present authors on the basis of the expression $l = \varepsilon(m/m^*)a_0$ (where a_0 is the Bohr radius)[40] gives a value $l \sim 90$–450 Å in lanthanum manganite perovskites with $\varepsilon = 10$–50. This value of the size indicates that bound states between electrons and holes can be localized not only within a single unit cell (~ 10 Å) and not only within a single grain (~ 200 Å)[41] but, thanks to the tunneling effect, can span a rather large spatial region including intergrain zones and clusters. This in turn is evidence that for determining the spin–spin interaction it is necessary to take into account not only the influence of the first coordination sphere but also the variation of the mesoscopic inhomogeneity on a nanostructure scale.

CONCLUSIONS

Our comprehensive studies of ceramic and laser film samples of lanthanum manganite perovskites done by x-ray diffraction, NMR of ^{55}Mn and ^{139}La, resistive, and magnetoresistive methods have established the following.

1. The real structure of the perovskites $\{La_{0.66}V^{(c)}_{0.11}\}_A[Mn^{3+}_{0.77}Mn^{4+}_{0.17}]_B(Mn^{2+}_{0.23}Mn^{4+}_{0.06})_{cl}O^{2-}_{2.84}V^{(a)}_{0.16}$ contains heterovalent manganese ions, cation and anion vacancies, and more complex defects of the cluster type.

2. Analysis of the broad, asymmetric NMR spectra of ^{55}Mn and ^{139}La attests not only to the presence of high-frequency electron exchange between heterovalent manganese ions in the B positions of the main matrix structure but also confirms the high degree of imperfection and inhomogeneity of lanthanum manganite perovskites.

3. The presence of two peaks on the temperature dependence of the resistivity of the ceramic is explained by the contribution of the grains and intergrain zones of the polycrystalline samples.

4. The differences of the metal–semiconductor phase transition temperatures T_{ms} of the ceramic and, especially, of the laser film is due to the different nonstoichiometry of their perovskite structure.

5. The low-field region of the magnetoresistive effect in the ceramic is due to the appearance of tunneling at the grain boundaries.

6. The stronger smearing of the phase transition T_{ms} and of the magnetoresistive effect in the laser film is explained by microstresses caused by the crystallographic differences of the film and substrate.

7. It is conjectured that the decrease of the resistance in the magnetic field is due to a weakening of the electron–hole interaction in excitons.

8. An anomaly of the resistance and magnetoresistive effect at temperatures near 42 K is observed for the first time and attributed to clusters of Mn ions.

9. The different values of the activation energy of the ceramic and laser films is explained by the differences of their structural imperfection and, accordingly, charge carrier density.

investigation on ^{139}La and A. V. Klimov for deposition of the laser film.

*E-mail: pashchen@pashchen.fti.ac.donetsk.ua

[1] H. Y. Hwang, S. W. Cheong, P. G. Radaelli, M. Marezio, and B. Batlogg, Phys. Rev. Lett. **75**, 914 (1995).

[2] É. L. Nagaev, Usp. Fiz. Nauk **166**, 833 (1996).

[3] V. M. Loktev and Yu. G. Pogorelov, Fiz. Nizk. Temp. **26**, 231 (2000) [Low Temp. Phys. **26**, 171 (2000)].

[4] V. E. Arkhipov, V. S. Gaviko, K. M. Demchuk *et al.*, JETP Lett. **71**, 114 (2000).

[5] M. B. Salamon, Rev. Mod. Phys. **73**, 583 (2001).

[6] P. G. Radaelli, M. Marezio, H. Y. Hwang, and S.-W. Choong, J. Solid State Chem. **122**, 1444 (1996).

[7] H. L. Ju and H. Sohn, J. Magn. Magn. Mater. **167**, 2000 (1997).

[8] F. Rivadulla, L. E. Hueso, C. Jazdon, C. Vázquez-Vázquez, M. A. López-Quintela, J. Rivas, M. T. Causa, C. A. Ramos, and R. D. Sánchez, J. Magn. Magn. Mater. **196−197**, 470 (1999).

[9] I. O. Troyanchuk, S. V. Trukhanov, D. D. Khalyavin, and H. Szymczak, J. Magn. Magn. Mater. **208**, 217 (2000).

[10] F. Damay, C. Martin, A. Maignan, and B. Raveau, J. Magn. Magn. Mater. **183**, 143 (1998).

[11] G. Turilli and F. Licci, Phys. Rev. B **54**, 13052 (1996).

[12] A. I. Tovstolytkin, A. N. Pogorilyi, A. G. Belous, and O. Z. Yanchevski, Fiz. Nizk. Temp. **27**, 500 (2001) [Low Temp. Phys. **27**, 366 (2001)].

[13] A. Anane, C. Dupas, K. Le Dung, J. P. Renard, P. Veillet, L. Pinsard, and A. Revcolevschi, Appl. Phys. Lett. **69**, 1160 (1996).

[14] A. Chakraborty, D. Bhattacharya, and H. S. Maiti, Phys. Rev. B **56**, 8828 (1997).

[15] S. De Brion, G. Chouteau, P. Lejay, R. Calemczuk, C. Chaillont, and P. Radaelli, *Proceedings of the 21st International Conference on Low Temperatures Physics*, Prague, part S4-LT (1996).

[16] V. S. Abramov, V. P. Pashchenko, S. I. Khartsev, and O. P. Cherenkov, Funct. Mater. **6**, 64 (1999).

[17] V. P. D'yakonov, V. P. Pashchenko, É. E. Zubov, V. I. Mikhaĭlov, Yu. Bukhantsev, I. M. Fita, V. A. Turchenko, N. A. Doroshenko, A. Szevczik, R. Zhuberek, and G. Szymczak, Fiz. Tverd. Tela (St. Petersburg) **45**, 870 (2003) [Phys. Solid State **45**, 914 (2003)].

[18] V. P. Pashchenko, S. I. Khartsev, O. P. Cherenkov, A. A. Shemyakov, Z. A. Samoĭlenko, A. D. Loĭko, and V. I. Kamenev, Neorg. Mater. **35**, 1509 (1999).

[19] V. P. Pashchenko, V. K. Prokopenko, A. A. Shemyakov, V. N. Varyukhin, V. N. Derkachenko, A. D. Loĭko, V. P. D'yakonov, G. Shimchak, and A. Gladchuk, Metallofizika i noveĭshie tekhnologii **32**, 18 (2000).

[20] L. I. Koroleva, R. V. Demin, and A. M. Balbashov, JETP Lett. **65**, 474 (1997).

[21] V. Markovich, I. Fita, A. I. Shames, R. Puzniak, E. Rozenberg, Ya. Yuzhelevski, D. Mogilyansky, A. Wisniewski, Ya. M. Mukovski, and Gorodetsky, J. Phys.: Condens. Matter **15**, 1 (2003).

[22] S. S. Kucherenko, V. P. Pashchenko, P. I. Polyakov, V. A. Shtaba, and A. A. Shemyakov, Fiz. Nizk. Temp. **27**, 761 (2001) [Low Temp. Phys. **27**, 559 (2001)].

[23] V. T. Dovgii, A. I. Linnik, V. P. Pashchenko, V. N. Derkachenko, V. K. Prokopenko, V. A. Turchenko, N. V. Davydeiko, V. Ya. Sycheva, V. P. Dyakonov, A. V. Klimov, and H. Szymczak, Fiz. Nizk. Temp. **29**, 380 (2003) [Low Temp. Phys. **29**, 285 (2003)].

[24] S. I. Khartsev, V. N. Krivoruchko, and V. P. Pashchenko, Fiz. Nizk. Temp. **23**, 840 (1997) [Low Temp. Phys. **23**, 631 (1997)].

[25] V. N. Krivoruchko, V. P. Pashchenko, Yu. V. Medvedev, S. I. Khartsev, and A. A. Shemyakov, Phys. Lett. A **245**, 163 (1998).

[26] G. J. Chen, Y. H. Chang, and H. W. Hsu, J. Magn. Magn. Mater. **219**, 317 (2000).

[27] V. Dyakonov, A. Prohorov, V. Shapovalov, V. Krivoruchko, V. Pashchenko, E. Zubov, V. Mihailov, P. Aleshkevich, M. Berkowski, S. Piechota, and H. Szymczak, J. Phys.: Condens. Matter **13**, 4049 (2001).

[28] J. A. M. Van-Roosmalen, E. H. P. Cordfunke, and R. B. Helmholdt, J. Solid State Chem. **110**, 100 (1994).

[29] N. N. Loshkareva, A. V. Korolev, T. I. Arbuzova, N. I. Solin, N. A. Viglin, I. B. Smolyak, N. G. Bebenin, Yu. P. Sukhorukov, S. V. Naumov, N. V. Kostromitina, and A. M. Balbashov, Fiz. Tverd. Tela (St. Petersburg) **44**, 1827 (2002) [Phys. Solid State **44**, 1916 (2002)].

[30] G. J. Tomka, P. C. Riedi, Gr. Kapusta, G. Balakrieshnan, D. Mck. Paul, M. R. Lees, and J. Barrutt, J. Appl. Phys. **83**, 7151 (1998).

[31] Gr. Kapusta and P. C. Riedi, J. Magn. Magn. Mater. **196−197**, 446 (1999).

[32] É. E. Zubov, V. P. Dyakonov, and H. Szymczak, Zh. Éksp. Teor. Fiz. **122**, 1212 (2002) [JETP **95**, 1044 (2002)].

[33] V. P. Pashchenko, S. S. Kucherenko, P. I. Polyakov, A. A. Shemyakov, and V. P. Dyakonov, Fiz. Nizk. Temp. **27**, 1370 (2001) [Low Temp. Phys. **27**, 1010 (2001)].

[34] A. P. Nosov, V. G. Vasil'ev, V. V. Ustinov, and E. V. Vladimirova, Fiz. Met. Metalloved. **93**, 27 (2002).

[35] V. P. Pashchenko, A. Ul'yanov, A. A. Shemyakov, S. I. Khartsev, N. I. Mezin, Yu. V. Medvedev, G. V. Gusakov, and V. A. Turchenko, Neorg. Mater. **38**, 378 (2002).

[36] G. Dezanneau, A. Sin, H. Roussel, H. Vincent, and M. Audier, Solid State Commun. **121**, 133 (2002).

[37] Z. A. Samoĭlenko, V. D. Okunev, E. I. Pushenko, T. A. D'yachenko, A. Cherenkov, P. Gierlowski, S. J. Lewandowski, A. Abal'oshev, A. Klimov, and A. Szewczyk, Zh. Tekh. Fiz. **73**(2), 118 (2003) [Tech. Phys. **48**, 250 (2003)].

[38] K. V. Shalimova, *Physics of Semiconductors* [in Russian], Énergiya, Moscow (1976).

[39] M. M. Savosta, V. I. Kamenev, V. A. Borodin, P. Novak, M. Marisko, J. Heytmanek, K. Dorr, and M. Sahana, Phys. Rev. B **67**, 094403 (2003).

[40] N. Ashkroft and N. Merlin, *Solid State Physics* [in Russian], Mir, Moscow (1979).

Translated by Steve Torstveit

Electronic structure and x-ray magnetic circular dichroism in uranium monochalcogenides

V. N. Antonov* and B. N. Harmon

Ames Laboratory, Iowa State University, Iowa 50011, USA

O. V. Andryushchenko and L. V. Bekenev

Institute of Metal Physics, 36 Vernadsky St., Kiev 03142, Ukraine

A. N. Yaresko

Max Planck Institute for Physics of Complex Systems, Dresden D-01187, Germany

The electronic structure and x-ray magnetic circular dichroism (XMCD) spectra of US, USe, and UTe are investigated theoretically from first principles, using the fully relativistic Dirac LMTO band structure method. The electronic structure is obtained with the local spin-density approximation (LSDA), as well as with a generalization of the LSDA+U method which takes into account that in the presence of spin–orbit coupling, the occupation matrix of localized electrons becomes nondiagonal in the spin indices. The origin of the XMCD spectra in the compounds is examined. © *2004 American Institute of Physics.* [DOI: 10.1063/1.1704618]

1. INTRODUCTION

The uranium compounds US, USe, and UTe belong to the class of uranium monochalcogenides that crystallize in the NaCl structure and order ferromagnetically (on the uranium sublattice) at Curie temperatures of 178, 160, and 102 K, respectively (see, e.g., the review[1]). These uranium compounds exhibit several unusual physical phenomena, which are the reason for a continuing ongoing interest in these compounds. Despite their relatively simple and highly symmetrical NaCl structure, it has been found that the magnetic ordering on the uranium atoms is strongly anisotropic,[2,3] with the uranium moment favoring a [111] alignment. The magnetic anisotropy in US, e.g., is one of the largest measured in a cubic material, with a magnetic anisotropy constant K_1 of more than 2×10^8 erg/cm³ (Ref. 4). Also the magnetic moment itself is unusual, consisting of an orbital moment that is about twice as large as the spin moment, and of opposite sign.[5–7] A bulk magnetization measurement[3] yields an ordered moment of $1.55\mu_B$ per formula unit, and neutron scattering measurements[8] show a slightly larger value of $1.70\mu_B$, which is assigned to the $5f$ magnetic moment. These values are far smaller than that expected for the free ion, indicating that some sort of "solid state effect" takes place with the $5f$ states. From several experimental results (for instance, photoemission,[9] electrical resistivity,[10] pressure dependence of Curie temperature,[11] and specific heat measurements,[12,13]) the $5f$ electrons of US are considered to be itinerant.

It has been suggested that uranium monochalcogenides are mixed valence systems.[14] Low-temperature ultrasonic studies on USe and UTe were performed in the context of questioning the possibility of the coexistence of magnetism and intermediate valence behavior.[15] They found a monotonic trend of the Poisson's ratio, which decreases with in-

creasing chalcogenide mass and is positive in US and negative in USe and UTe. This indicates the possibility of intermediate valence in the last two compounds. Indeed, a negative Poisson's ratio, i.e., a negative elastic constant C_{12}, is quite common for intermediate valence systems, and its occurrence seems to be due to an anomalously low value of the bulk modulus. A negative C_{12} means that it costs more energy to distort the crystal from cubic to tetragonal structure than to modify the volume. Thus, when uniaxially compressed along a [100] direction, the material will contract in the [010] and [001] directions, trying to maintain a cubic structure. An explanation for a negative C_{12} may be given through a breathing deformability of the actinide ion due to a valence instability.[16]

The dependence of the Curie temperatures T_C of US, USe, and UTe on hydrostatic pressure up to 13 GPa has been determined in Ref. 17. For USe and UTe, T_C initially increases with applied pressures, passing through maxima at pressures of about 6 GPa and 7 GPa, respectively. For US, T_C decreases monotonically with pressure, which is consistent with pressure-dependent itinerant electron magnetism. Pressure increases the bandwidth and correspondingly decreases the density of states at the Fermi level, which leads to a decrease of T_C. The behavior of USe and UTe is suggestive of localized interacting $5f$ moments undergoing Kondo-type fluctuations, which begin to exceed the magnetic interaction when T_C passes through a maximum. A theoretical analysis of these experiments is given in Ref. 18. On the basis of band structure calculations it is argued that the nonmonotonic behavior of T_C under pressure is solely the result of pressure-driven increased $5f$ itinerancy.

It must be remarked that the behavior of uranium monochalcogenides cannot be explained entirely by a simple trend of increasing localization with increasing chalcogen mass.[19] Whereas such a trend is evident in the dynamic mag-

netic response, in the pressure dependence of the Curie temperatures, and in the value of the ordered moment, the behavior of Poisson's ratio and of the Curie temperature is the opposite from what one would naively expect.

There are several band structure calculations of uranium monochalcogenides in the literature.[7,20–28] Kraft *et al.*[23] have performed a local spin-density approximation (LSDA) calculation with the spin–orbit interaction (SOI) in a second variational treatment for ferromagnetic uranium monochalcogenides (US, USe, and UTe) using the ASW method, and they found that the magnitude of the calculated orbital magnetic moment M_l is larger than that of the spin moment M_s and that they couple to each other in an antiparallel way. However, the magnitude of the total magnetic moment ($M_s + M_l$) is too small compared to the experimental data, indicating that the calculated M_l is not large enough.

The optical and magnetooptical (MO) spectra of uranium monochalcogenides have been investigated theoretically in Refs. 20, 21, 23, and 25. These theoretical spectra are all computed from first principles, using Kubo linear-response theory, but it appears that there are large differences among them. Cooper and coworkers[22] find good agreement with experiment for the real part of the diagonal conductivity ($\sigma_{xx}^{(1)}$) of UTe, but the much more complicated off-diagonal conductivity ($\sigma_{xy}^{(2)}$) of US and UTe is about 4 times larger than experiment, and also the shape of their spectrum is different from the experimental one. Halilov and Kulatov[20] also find an off-diagonal conductivity which is much larger than the experimental one, but they additionally obtain a diagonal conductivity $\sigma_{xx}^{(1)}$ that differs substantially from experiment. Gasche[21] finds a Kerr rotation spectrum of US that is quite different from experiment, and subsequently considers the effect of an orbital polarization term to improve the *ab initio* Kerr spectra. Kraft *et al.*[23] obtained reasonable agreement with experiment for the absolute value of the Kerr spectra of US, USe, and UTe. However, the shape of the Kerr spectra is not reproduced by LSDA theory, since the theoretical spectra exhibit a double-peak structure, while the experimental spectra have only a single-peak structure. The LSDA+U calculations presented in Ref. 25 take into account the strong Coulomb correlations among the $5f$ orbitals and greatly improve the agreement between theory and experiment for all three materials. This finding appears to be consistent with the quasilocalized nature of the $5f$ electrons in these compounds.

The x-ray magnetic circular dichroism (XMCD) technique has developed in recent years into a powerful magnetometry tool for investigating the orbital and spin contributions to magnetic moments. XMCD measures the difference in absorption of a compound for x rays with two opposite (left and right) states of circular polarization. The study of the $5f$ electron shell in uranium compounds is usually performed by tuning the energy of the x-ray close to the $M_{4,5}$ edges of uranium (located at 3552 and 3728 eV, respectively) where electronic transitions between $3d_{3/2,5/2}$ and $5f_{5/2,7/2}$ states are involved. Recently XMCD measurements have been successfully performed on US at the $M_{4,5}$ edges.[29] The XMCD spectrum for U $3d{\rightarrow}5f$ transitions in US has been calculated in Ref. 27 on the basis of the HF approximation for an extended Hubbard model. The parameters involved in

the tight-binding model were determined by fitting the energy of Bloch electrons in the paramagnetic state obtained in an LDA band structure calculation. There are no XMCD calculations for USe and UTe in the literature.

With the aim of undertaking a systematic investigation of the trends in uranium compounds we present the theoretically calculated electronic structure and XMCD spectra at the $M_{4,5}$ edges for the UX (X=S, Se, and Te) compounds.

This paper is organized as follows. Section 2 presents a description of the crystal structure of the U monochalcogenides and the computational details. Section 3 is devoted to the electronic structure and XMCD spectra of US, USe, and UTe calculated in the LSDA and LSDA+U approximations. The XMCD theoretical calculations are compared to the experimental measurements. Finally, the results are summarized in Sec. 4.

2. COMPUTATIONAL DETAILS

Magnetooptical effects refer to various changes in the polarization state of light upon interaction with materials possessing a net magnetic moment, including rotation of the plane of linearly polarized light (Faraday, Kerr rotation), and the complementary differential absorption of left and right circularly polarized light (circular dichroism). In the near-visible spectral range these effects result from excitation of electrons in the conduction band. Near x-ray absorption edges, or resonances, magnetooptical effects can be enhanced by transitions from well-defined atomic core levels to transition-symmetry-selected valence states. There are at least two alternative formalisms for describing resonant soft x-ray MO properties. One uses the classical dielectric tensor.[30] Another uses the resonant atomic scattering factor including charge and magnetic contributions.[31,32] The equivalence of these two descriptions (within the dipole approximation) is demonstrated in Ref. 33.

For the polar Kerr magnetization geometry and a crystal of tetragonal symmetry, where both the fourfold axis and the magnetization **M** are perpendicular to the sample surface and the z axis is chosen parallel to them, the dielectric tensor is composed of the diagonal ε_{xx} and ε_{zz} components and the off-diagonal ε_{xy} component in the form

$$\varepsilon = \begin{pmatrix} \varepsilon_{xx} & \varepsilon_{xy} & 0 \\ -\varepsilon_{xy} & \varepsilon_{xx} & 0 \\ 0 & 0 & \varepsilon_{zz} \end{pmatrix}. \tag{1}$$

A complete description of MO effects in this formalism is given by the four nonzero elements of the dielectric tensor or, equivalently, by the complex refractive index $n(\omega)$

$$n(\omega) \equiv \sqrt{\varepsilon(\omega)} = 1 - \delta(\omega) + i\beta(\omega) \tag{2}$$

for several normal modes corresponding to the propagation of pure polarization states along specific directions in the sample. The solution of Maxwell's equations yields these normal modes.[34] One of these modes is for circular components of opposite ($\pm$) helicity, with wave vector **h**∥**M**, and having indices

$$n_{\pm} = 1 - \delta_{\pm} + i\beta_{\pm} = \sqrt{\varepsilon_{xx} \pm i\varepsilon_{xy}}. \tag{3}$$

The other two cases are for linear polarization with $\mathbf{h} \perp \mathbf{M}$.[33] One has electric vector $\mathbf{E} \| \mathbf{M}$ and index $n_\| = 1 - \delta_\| + i\beta_\| = \sqrt{\varepsilon_{zz}}$. The other has $\mathbf{E} \perp \mathbf{M}$ and $n_\perp = 1 - \delta_\perp + i\beta_\perp = \sqrt{(\varepsilon_{xx}^2 + \varepsilon_{xy}^2)/\varepsilon_{xx}}$.

At normal light incidence the complex Faraday angle is given by[33,35]

$$\varphi_F(\omega) = \theta_F(\omega) - i\,\eta_F(\omega) = \frac{\omega l}{2c}(n_- - n_-), \tag{4}$$

where c is the speed of light and $\theta_F(\omega)$ and $\eta_F(\omega)$ are the Faraday rotation and the ellipticity. The complex Faraday response describes the polarization changes to the incident linear polarization on propagation through a film of thickness l. (The incident linearly polarized light is a coherent superposition of two circularly waves of opposite helicity.)

Magnetic circular dichroism is of first order in M (or ε_{xy}) and is given by $\beta_+ - \beta_-$ or $\delta_+ - \delta_-$, respectively, the latter representing the magnetooptical rotation (MOR) of the plane of polarization (Faraday effect). Magnetic linear dichroism (MLD) $n_\perp - n_\|$ (also known as the Voigt effect) is quadratic in M. The Voigt effect is present in both ferromagnets and antiferromagnets, while the first-order MO effects in the forward scattering beam are absent with the net magnetization in antiferromagnets.

The alternative consideration of the MO effects is based on the atomic scattering factor $f(\omega, q)$, which provides a microscopic description of the interaction of x-ray photons with magnetic ions. For forward scattering $(q=0)$ $f(\omega) = Z + f'(\omega) + if''(\omega)$, where Z is the atomic number. $f'(\omega)$ and $f''(\omega)$ are the anomalous dispersion corrections, related to each other by the Kramers–Kronig transformation. The general equivalence of these two formalisms can be seen by noting the one-to-one correspondence of terms describing the same polarization dependence for the same normal modes.[33] For a multicomponent sample they are related to δ and β through

$$\delta(\omega) = \frac{2\pi c^2 r_e}{\omega^2} \sum_i Z_i f_i'(\omega) N_i, \tag{5}$$

$$\beta(\omega) = \frac{2\pi c^2 r_e}{\omega^2} \sum_i f_i''(\omega) N_i, \tag{6}$$

where the sum is over atomic spheres, each having number density N_i, and r_e is the classical electron radius. The x-ray absorption coefficient $\mu^\lambda(\omega)$ of polarization λ may be written in terms of the imaginary part of $f_\lambda(\omega)$ as

$$\mu^\lambda(\omega) = \frac{4\pi r_e c}{\Omega \omega} f_\lambda''(\omega), \tag{7}$$

where Ω is the atomic volume. The x-ray MCD, which is the difference in x-ray absorption for right- and left-circularly polarized photons $(\mu^+ - \mu^-)$ can be represented by $(f''_+ - f''_-)$. The Faraday rotation $\theta_F(\omega)$ of the linear polarization measures the MCD in the real part f'_λ of the resonant magnetic x-ray scattering amplitude, i.e.,[36]

$$\theta_F(\omega) = \frac{\omega l}{2c}\mathrm{Re}[n_+ - n_-] = \frac{\pi l r_e}{\Omega \omega}(f'_-(\omega) - f'_+(\omega)). \tag{8}$$

Finally, the x-ray scattering intensity from an elemental magnet at Bragg reflection measured in the resonant magnetic

x-ray-scattering experiments is just the squared modulus of the total scattering amplitude, which is a linear combination of $(f'_\pm + if''_\pm, f'_z + if''_z)$, with coefficients completely determined by the experimental geometry.[35] Multiple scattering theory is usually used to calculate the resonant magnetic x-ray scattering amplitude $(f' + if'')$.[30,35,37]

We should mention that the general equivalence of the dielectric-tensor and scattering-factor descriptions holds only in the case when one is considering the contribution of dipole transitions to the atomic scattering factor $f(\omega)$. Higher-order multipole terms have different polarization dependence.[31]

Using straightforward symmetry considerations, it can be shown that all magnetooptical phenomena (XMCD, MO Kerr and Faraday effects) are caused by symmetry reduction, in comparison to the paramagnetic state, caused by magnetic ordering.[38] XMCD properties are manifested only when SO coupling is considered in addition. To calculate the XMCD properties one has to take magnetism and SO coupling into account at the same time when dealing with the electronic structure of the material considered. The theoretical description of magnetic dichroism can be cast into four categories. On the one hand, there are one-particle (ground-state) and many-body (excited-state) theories; on the other hand, there are theories for single atoms and those which take into account the solid state. To name a few from each category, for atomic one-particle theories we refer to Refs. 39 and 40, for atomic many-particle multiplet theory to Refs. 41–44, for solid many-particle theories to Ref. 45, and for solid one-particle theories (photoelectron diffraction) to Refs. 46–49. A multiple-scattering approach to XMCD, a solid-state one-particle theory, has been proposed by Ebert *et al.*[50–52] and Tamura *et al.*[53]

Within the one-particle approximation, the absorption coefficient μ for an incident x ray of polarization λ and photon energy $\hbar\omega$ can be determined as the probability of electron transition from an initial core state (with wave function ψ_j and energy E_j) to a final unoccupied state (with wave function $\psi_{n\mathbf{k}}$ and energy $E_{n\mathbf{k}}$)

$$\mu_j^\lambda(\omega) = \sum_{n\mathbf{k}} |\langle \Psi_{n\mathbf{k}} | \Pi_\lambda | \Psi_j \rangle|^2 \delta(E_{n\mathbf{k}} - E_j - \hbar\omega)$$
$$\times \theta(E_{n\mathbf{k}} - E_F). \tag{9}$$

Π_λ is the dipole electron–photon interaction operator

$$\Pi_\lambda = -e\,\alpha \mathbf{a}_\lambda, \tag{10}$$

where α are the Dirac matrices, and $\mathbf{a}_\lambda$ is the λ polarization unit vector of the photon potential vector $[a_\pm = 1/\sqrt{2}(1, \pm i, 0), a_z = (0,0,1)]$ (here $\pm$ denotes, respectively, left and right circular photon polarizations with respect to the magnetization direction in the solid). More-detailed expressions of the matrix elements for the spin-polarized fully relativistic LMTO method may be found in Refs. 52 and 54.

While XMCD is calculated using equation (9), the main features can be understood already from a simplified expression for paramagnetic solids. With restriction to electric dipole transitions, keeping the integration only inside the atomic spheres (due to the highly localized core states) and averaging with respect to polarization of the light, one ob-

tains the following expression for the absorption coefficient of the core level with (l,j) quantum numbers:[55]

$$\mu_{lj}^0(\omega)=\sum_{l',j'}\frac{2j+1}{4}\left(\frac{\delta_{l',l-1}\delta_{j',j+1}}{j+1}+\frac{\delta_{l',l-1}\delta_{j',j-1}}{j}\right.$$
$$\left.+\frac{\delta_{l',l+1}\delta_{j',j}}{j(j+1)(2j+1)}\right)N_{l',j'}(E)C_{l,j}^{l',j'}(E), \quad (11)$$

where $N_{l',j'}(E)$ is the partial density of empty states and the $C_{l,j}^{l',j'}(E)$ radial matrix elements.[55]

Equation (11) allows only transitions with $\Delta l=\pm1$, $\Delta j=0,\pm1$ (dipole selection rules) which means that the absorption coefficient can be interpreted as a direct measure for the sum of (l,j)-resolved DOS curves weighted by the square of the corresponding radial matrix element (which usually is a smooth function of energy). This simple interpretation is also valid for the spin-polarized case.[30]

The application of standard LSDA methods to f-shell systems meets with problems in most cases, because of the correlated nature of the f electrons. To account better for the on-site f-electron correlations, we have adopted as a suitable model Hamiltonian that of the LSDA+U approach.[56] The main idea is the same as in the Anderson impurity model:[57] the separate treatment of localized f electrons for which the Coulomb $f-f$ interaction is taken into account by a Hubbard-type term in the Hamiltonian $1/2U\Sigma_{i\neq j}n_in_j$ (n_i are the f-orbital occupancies), and delocalized s, p, and d electrons for which the local density approximation for the Coulomb interaction is regarded as sufficient.

Hubbard[58,59] was one of the first to point out the importance, in the solid state, of Coulomb correlations which occur inside atoms. The many-body crystal wave function has to reduce to many-body atomic wave functions as the lattice spacing is increased. This limiting behavior is missed in the LDA/DFT. The spectrum of excitations for the shell of an f-electron system is a set of many-body levels describing processes of removing and adding electrons. In the simplified case, when every f electron has roughly the same kinetic energy ε_f and Coulomb repulsion energy U, the total energy of the shell with n electrons is given by $E_n=\varepsilon_{fn}+Un(n-1)/2$ and the excitation spectrum is given by $\varepsilon_n=E_{n-1}-E_n=\varepsilon_f+Un$.

Let us consider an f ion as an open system with a fluctuating number of f electrons. The correct formula for the Coulomb energy of $f-f$ interactions as a function of the number of f electrons N given by the LDA should be $E=UN(N-1)/2$ (Ref. 60). If we subtract this expression from the LDA total energy functional and add a Hubbard-like term (neglecting for now exchange and nonsphericity) we will have the following functional:

$$E=E^{LDA}-UN(N-1)/2+\frac{1}{2}U\sum_{i\neq j}n_in_j. \quad (12)$$

The orbital energies ε_i are derivatives of (12):

$$\varepsilon_i=\frac{\partial E}{\partial n_i}=\varepsilon^{LDA}+U\left(\frac{1}{2}-n_i\right). \quad (13)$$

This simple formula gives the shift of the LDA orbital energy $-U/2$ for occupied orbitals ($n_i=1$) and $+U/2$ for unoccupied orbitals ($n_i=0$). A similar formula is found for the

orbital dependent potential $V_i(\mathbf{r})=\delta E/\delta n_i(\mathbf{r})$, where the variation is taken not on the total charge density $\rho(\mathbf{r})$ but on the charge density of a particular ith orbital $n_i(\mathbf{r})$:

$$V_i(\mathbf{r})=V^{LDA}(\mathbf{r})+U\left(\frac{1}{2}-n_i\right). \quad (14)$$

Expression (14) restores the discontinuous behavior of the one-electron potential of the exact density functional theory.

The functional (12) neglects exchange and nonsphericity of the Coulomb interaction. In the most general rotationally invariant form the LDA+U functional is defined as[61,62]

$$E^{LDA+U}[\rho(\mathbf{r}),\hat{n}]=E^{L(S)DA}[\rho(\mathbf{r})]+E^U(\hat{n})-E^{dc}(\hat{n}), \quad (15)$$

where $E^{L(S)DA}[\rho(\mathbf{r})]$ is the LSDA (or LDA as in Ref. 60) functional of the total electron spin densities, $E^U(\hat{n})$ is the electron–electron interaction energy of the localized electrons, and $E^{dc}(\hat{n})$ is the so-called "double counting" term which cancels approximately the part of the electron–electron energy which is already included in E^{LDA}. The last two terms are functions of the occupation matrix $\hat{n}$ defined using the local orbitals $\{\varphi_{lm\sigma}\}$.

The matrix $\hat{n}=\|n_{\sigma m,\sigma'm'}\|$ generally consists of both spin-diagonal and spin-nondiagonal terms. The latter can appear due to the spin–orbit interaction or a noncollinear magnetic order. Then, the second term in Eq. (15) can be written as:[61–63]

$$E^U=\frac{1}{2}\sum_{\sigma,\sigma',\{m\}}(n_{\sigma m_1,\sigma m_2}U_{m_1m_2m_3m_4}n_{\sigma'm_3,\sigma'm_4}$$
$$-n_{\sigma m_1,\sigma'm_2}U_{m_1m_4m_3m_2}n_{\sigma'm_3,\sigma m_4}), \quad (16)$$

where $U_{m_1m_2m_3m_4}$ are the matrix elements of the on-site Coulomb interaction, which are given by

$$U_{m_1m_2m_3m_4}=\sum_{k=0}^{2l}a_{m_1m_2m_3m_4}^kF^k, \quad (17)$$

with F^k being the screened Slater integrals for a given l and

$$a_{m_1m_2m_3m_4}^k=\frac{4\pi}{2k+1}\sum_{q=-k}^k\langle lm_1|Y_{kq}|lm_2\rangle\langle lm_3|Y_{kq}^*|lm_4\rangle. \quad (18)$$

The $\langle lm_1|Y_{kq}|lm_2\rangle$ angular integrals of a product of three spherical harmonics Y_{lm} can be expressed in terms of Clebsch–Gordan coefficients, and Eq. (18) becomes

$$a_{m_1m_2m_3m_4}^k=\delta_{m_1-m_2+m_3,m_4}(C_{k0,l0}^{l0})^2$$
$$\times C_{km_1-m_2,lm_2}^{lm_1}C_{km_1-m_2,lm_3}^{lm_4}. \quad (19)$$

The matrix elements $U_{mmm'm'}$ and $U_{mm'm'm}$ which enter those terms in the sum in Eq. (16) which contain a product of the diagonal elements of the occupation matrix can be identified as pair Coulomb and exchange integrals:

$$U_{mmm'm'}=U_{mm'},U_{mm'm'm}=J_{mm'}. \quad (20)$$

The averaging of the matrices $U_{mm'}$ and $U_{mm'}-J_{mm'}$ over all possible pairs m,m' determine the averaged Cou-
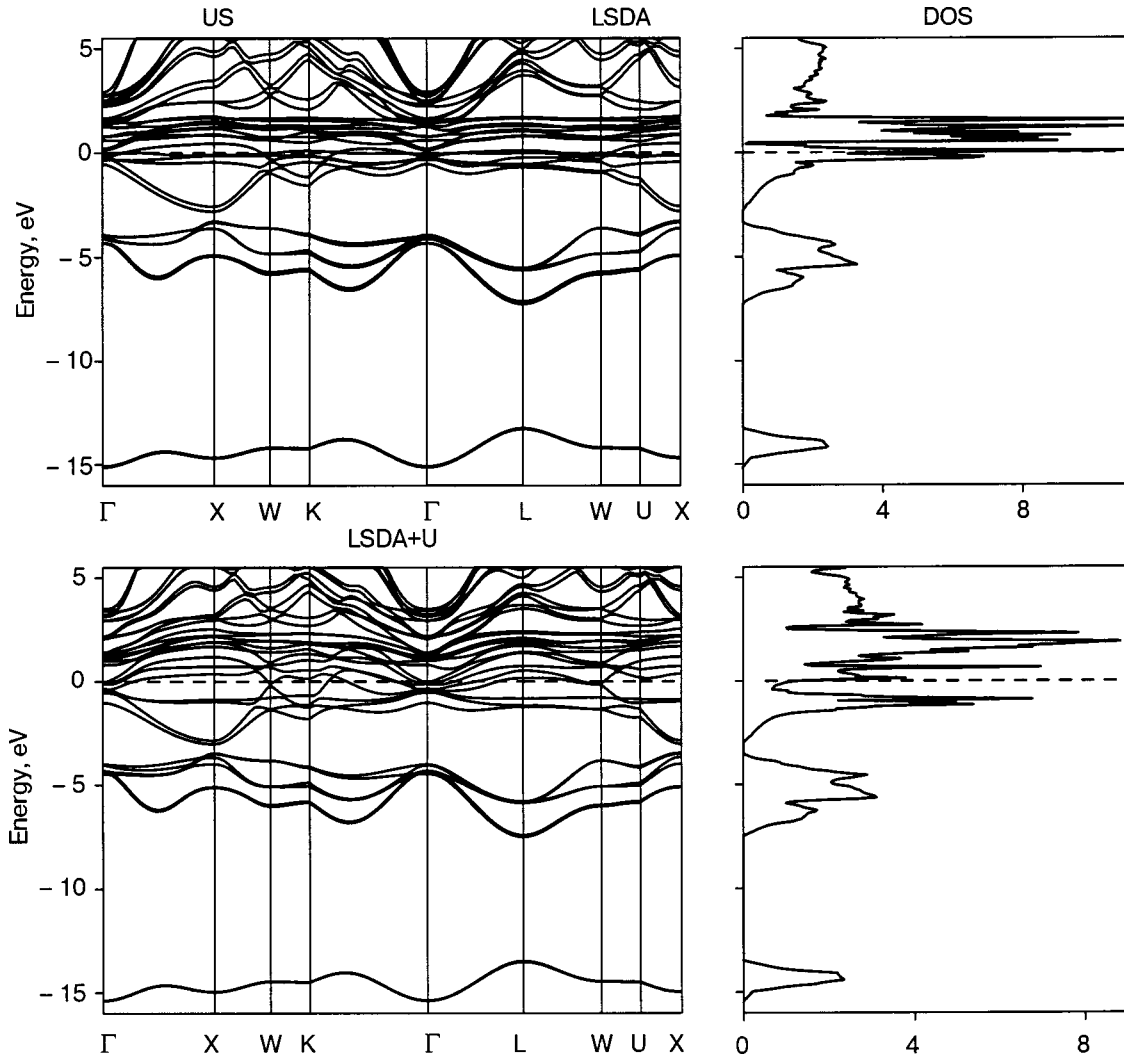
FIG. 1. Self-consistent fully relativistic energy band structure and total DOS (in states/(unit cell·eV)) of US calculated within the LSDA and LSDA+U approximations with $U=2$ eV and $J=0.5$ eV.

lomb U and exchange J integrals which enter the expression for E^{dc}. Using the properties of the Clebsch–Gordan coefficients, one can show that

$$U = \frac{1}{(2l+1)^2} \sum_{mm'} U_{mm'} = F^0, \qquad (21)$$

$$U - J = \frac{1}{2l(2l+1)} \sum_{mm'} (U_{mm'} - J_{mm'}) = F^0$$

$$-\frac{1}{2l} \sum_{k=2}^{2l} (C_{n0,l0}^{l0})^2 F^k, \qquad (22)$$

where the primed sum is over $m' \neq m$. Equations (21) and (22) allow us to establish the following relation between the average exchange integral J and Slater integrals:

$$J = \frac{1}{2l} \sum_{k=2}^{2l} (C_{n0,l0}^{l0})^2 F^k, \qquad (23)$$

or explicitly

$$J = \frac{1}{14} (F^2 + F^4), \text{ for } l=2, \qquad (24)$$

$$J = \frac{1}{6435} (286F^2 + 195F^4 + 250F^6) \text{ for } l=3. \qquad (25)$$

The meaning of U has been carefully discussed by Herring.[64] For example, in an f-electron system with n f electrons per atom, U is defined as the energy cost for the reaction

$$2(f^n) \rightarrow f^{n+1} + f^{n-1}, \qquad (26)$$

i.e., the energy cost for moving an f electron between two atoms which both initially had n f electrons. It should be emphasized that U is a renormalized quantity which contains the effects of screening by fast s and p electrons. The number of these delocalized electrons on an atom with $n+1$ f electrons decreases, whereas their number on an atom with $n-1$ f electrons increases. The screening reduces the energy cost for the reaction given by Eq. (26). It is worth noting that because of the screening the value of U in L(S)DA+U calculations is significantly smaller then the bare U used in the Hubbard model.[58,59]

In principle, the screened Coulomb U and exchange J integrals can be determined from supercell LSDA calcula-

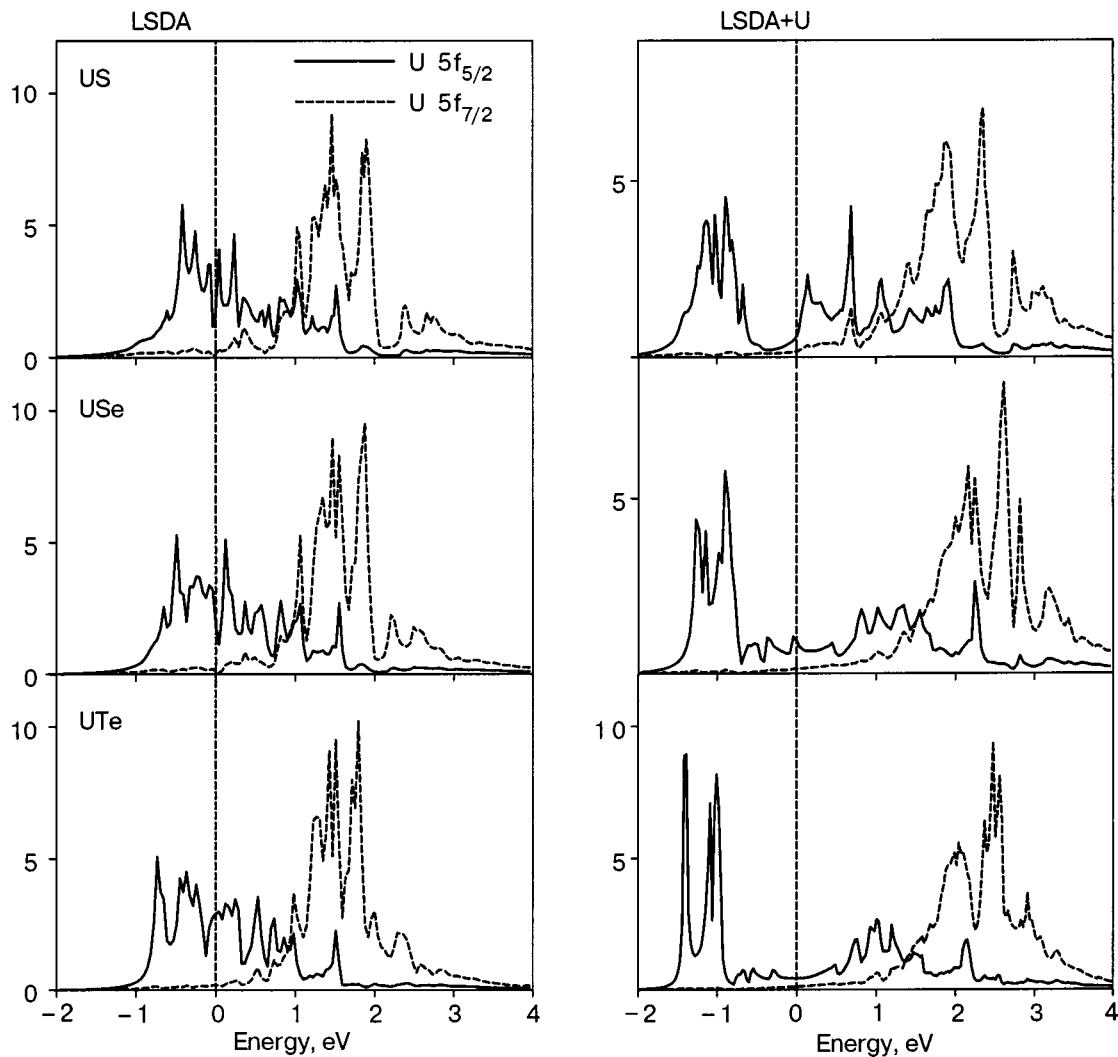FIG. 2. The partial $5f_{5/2}$ and $5f_{7/2}$ density of states (in states/(atom·eV)) within US, USe, and UTe calculated in the LSDA and LSDA+U approximations.

tions using Slater's transition state technique[65] or from constrained LSDA calculations.[66–68] Then, the LDA+U method becomes parameter-free. However, in some cases, as for instance for bcc iron,[65] the value of U obtained from such calculations appears to be overestimated. Alternatively, the value of U estimated from the photoemission spectroscopy (PES) and x-ray bremsstrahlung isochromat spectroscopy (BIS) experiments can be used. Because of the difficulties of unambiguous determination of U it can be considered as a parameter of the model. Then its value can be adjusted so as to achieve the best agreement of the results of LDA+U calculations with PES or optical spectra. While the use of an adjustable parameter is generally considered an anathema among first-principles practitioners, the LDA+U approach does offer a plausible and practical method for the approximate treatment of strongly correlated orbitals in solids. It has been found that many properties evaluated by the LDA+U method are insensitive to small variations of the value of U around some optimal value. Indeed, the optimal value of U determined empirically is often very close to the value obtained from supercell or constrained density functional calculations.

All three chalcogenides, namely, US, USe, and UTe, considered in the present work crystallize in the NaCl type

structure (B1) with space group symmetry $Fm3m$. The uranium atom is positioned at (0,0,0) and the chalcogen at (1/2,1/2,1/2).

The details of the computational method are described in our previous papers,[69,70] and here we only mention several aspects. The calculations were performed using the fully relativistic LMTO method for the experimentally observed lattice constants $a = 5.86$, 6.06, and 6.436 Å for US, USe, and UTe, respectively. To improve the potential we include additional empty spheres in the (1/4,1/4,1/4) positions. We used the von Barth–Hedin parametrization[71] for the exchange-correlation potential. Brillouin zone (BZ) integrations were performed using the improved tetrahedron method[72] and the charge was obtained self-consistently with 1330 irreducible **k** points. The basis consisted of U s, p, d, f, and g; chalcogen s, p, and d; empty spheres s and p LMTOs.

We have adopted the LSDA+U method[56] as a different level of approximation to treat the electron–electron correlation. We used a generalization of the LSDA+U method which takes into account that in the presence of spin–orbit coupling the occupation matrix of localized electrons becomes nondiagonal in the spin indices.[61] The screened Coulomb U and exchange J integrals enter the LSDA+U energy

FIG. 3. The partial $5f_{5/2}$ density of states (in states/(atom·eV)) in US, USe, and UTe calculated within the LSDA, LSDA+U(OP), and LSDA+U approximations.

functional as external parameters and have been set to the value $U=2$ eV derived from XPS measurements and $J=0.5$ eV.

3. RESULTS AND DISCUSSION

3.1. Band structure and magnetic moments

In our band structure calculations we have performed two independent fully relativistic spin-polarized calculations. We consider the $5f$ electrons as: itinerant electrons, using the local spin-density approximation; and partly localized, using the LSDA+U approximation.

Figure 1 shows the energy band structure of US for both the approximations. The LSDA energy band structure of US can be subdivided into three regions separated by energy gaps. The bands in the lowest region around -15 eV have

mostly S s character with a small amount of U sp character mixed in. The next six energy bands are S p bands separated from the s bands by an energy gap of about 6 eV. The width of the S p band is about 4 eV. U $6d$ bands are broad and extend between -2.5 and 10 eV. The sharp peaks in the DOS just below and above the Fermi energy are due to the $5f_{5/2}$ and $5f_{7/2}$ states, respectively. Figure 1 also shows the energy bands and total density of states of US in the LSDA +U approximation.[61,62] The Coulomb repulsion splits partially occupied U $5f_{5/2}$ states, and the LSDA+U calculations give a solution with three localized $5f$ electrons in US. U $5f$ states just above the Fermi level are formed by the remaining $5f_{5/2}$ states, whereas the peak of the $5f_{7/2}$ states is pushed about 1 eV upward from its LSDA position.

Figure 2 shows the calculated fully relativistic spin-polarized partial $5f$ density of states of ferromagnetic ura-

nium monochalcogenides calculated in the LSDA and LSDA+U approximations. Because of large spin–orbit interaction of $5f$ electrons, the $j=5/2$ and $j=7/2$ states are fairly well separated, and the occupied states are composed mostly of the $j=5/2$ states. The $5f_{7/2}$ states are almost empty.

In magnets, the atomic spin M_s and orbital M_l magnetic moments are basic quantities and their separate determination is therefore important. Methods of their experimental determination include traditional gyromagnetic ratio measurements,[73] magnetic form factor measurements using neutron scattering,[74] and magnetic x-ray scattering.[75] In addition to these, the recently developed x-ray magnetic circular dichroism combined with several sum rules[76,77] has attracted much attention as a method of site- and symmetry-selective determination of M_s and M_l. Table I presents a comparison between the calculated and experimental magnetic moments in uranium monochalcogenides. For comparison, we also list the results of previous band structure calculations. Our LSDA results obtained by the fully relativistic spin-polarized LMTO method are in good agreement with the ASW results of Kraft *et al.*[23] The LSDA calculations for ferromagnetic uranium monochalcogenides (US, USe, and UTe) give a magnitude of the total magnetic moment M_t too small compared to the experimental data, indicating that the calculated M_l is not large enough.

It is a well-known fact, however, that the LSDA calculations fail to produce the correct value of the orbital moment of uranium compounds.[7,78,80–82] In LSDA, the Kohn–Sham equation is described by a local potential including the spin-dependent electron density. The electric current, which describes M_l, is, however, not included. This means that although M_s is self-consistently determined in LSDA, there is no framework to simultaneously determine M_l self-consistently.

Numerous attempts have been made to better estimate M_l in solids. They can be roughly classified into two categories. One is based on the so-called current density functional theory[83–85] that is intended to extend density functional theory to include the orbital current as an extra degree of freedom, which describes M_l. Unfortunately the explicit form of the current density functional is at present unknown. The other category includes the orbital polarization (OP),[7,78,81,82] self-interaction correction (SIC),[86] and LSDA $+U$[61,62] approaches, which provide a means beyond the LSDA scheme to calculate M_l.

For a better description of M_l, the OP functional form of BL_z^2 with the Racah parameter B has been deduced[7] from an atomic multiplet ground state without SOI, whose S and L are given by Hund's rules. However, the OP method does not assure us that it will give a good description when the SOI is included and thus S and L are no longer good quantum numbers. Using the LSDA+OP method, Brooks[7] obtained larger magnitude of M_l and improvement in M_t. However, they have stated that the individual magnitudes of M_s and M_l are considered to be too large from the analysis of the magnetic form factor, and the ratio M_l/M_s is still far from the experimental value for all three uranium monochalcogenides (Table I).

Solovyev *et al.*[62] argue that the key parameter respon-

TABLE I. The experimental and calculated spin M_s, orbital M_l, and total M_t magnetic moments at the uranium site (in μ_B) of US, USe, and UTe.

Compound	Method	M_s	M_l	M_t	$-M_l/M_s$
US	LSDA	−1.53	2.14	0.60	1.41
	LSDA+U(OP)	−1.48	3.21	1.72	2.17
	LSDA+U	−1.35	3.42	2.07	2.53
	LSDA [23]	−1.6	2.5	0.9	1.6
	LSDA+OP [7]	−2.1	3.2	1.1	1.5
	OP scaled HF [78]	−1.51	3.12	1.61	2.07
	HF(TB) [27]	−1.49	3.19	1.70	2.14
	exper. [8]	−1.3	3.0	1.7	2.3
	exper. [3]	–	---	1.55	---
USe	LSDA	−1.75	2.54	0.79	1.45
	LSDA+U(OP)	−1.65	3.65	2.00	2.21
	LSDA+U	−1.96	4.61	2.65	2.35
	LSDA [23]	−1.8	2.8	1.0	1.5
	LSDA+OP [7]	−2.4	3.4	1.0	1.4
	exper. [8]	–	–	2.0	–
	exper. [3]	–	–	1.8	–
UTe	LSDA	−2.12	3.12	1.00	1.47
	LSDA+U(OP)	−1.91	4.09	2.17	2.14
	LSDA+U	−2.13	4.95	2.81	2.32
	LSDA [23]	−2.2	3.4	1.2	1.5
	LSDA+OP [7]	−2.6	3.4	0.8	1.3
	exper. [79]	−1.57	3.48	1.91	2.21
	exper. [8]	–	–	2.2	–
	exper. [3]	–	---	1.9	---

sible for the exchange-correlation enhancement of the orbital magnetic moments in solids is the ''Hubbard U'' rather than the intra-atomic Hund's second rule coupling, being consistent with a more general concept of the orbital polarization. This leads to a unified rotationally invariant LSDA+U prescription for the orbital magnetism. Table I presents the calculated magnetic moments in uranium monochalcogenides using a generalization of the LSDA+U method.[61,62] In these calculations we used $U=2.0$ eV and $J=0.5$ eV. Table I presents also the LSDA+U calculated magnetic moments with $U=J=0.5$ eV. Since in that case $U_{\text{eff}}=0$ the effect of LSDA+U comes from nonspherical terms which are determined by F^2, F^4, and F^6 Slater integrals. Since the basic idea of such an approach is similar to the OP method,[7,81] we denote the last approximation as LSDA+U(OP). The LSDA+U(OP) approximation describes the correlations between spin and orbital magnetic moment directions.

Figure 3 shows the $5f_{5/2}$ partial density of states in US calculated within the LSDA, LSDA+U(OP), and LSDA $+U$ approximations. The LSDA+U(OP) approximation strongly affects the relative energy positions of the m_j-projected $5f$ density of states and substantially improves
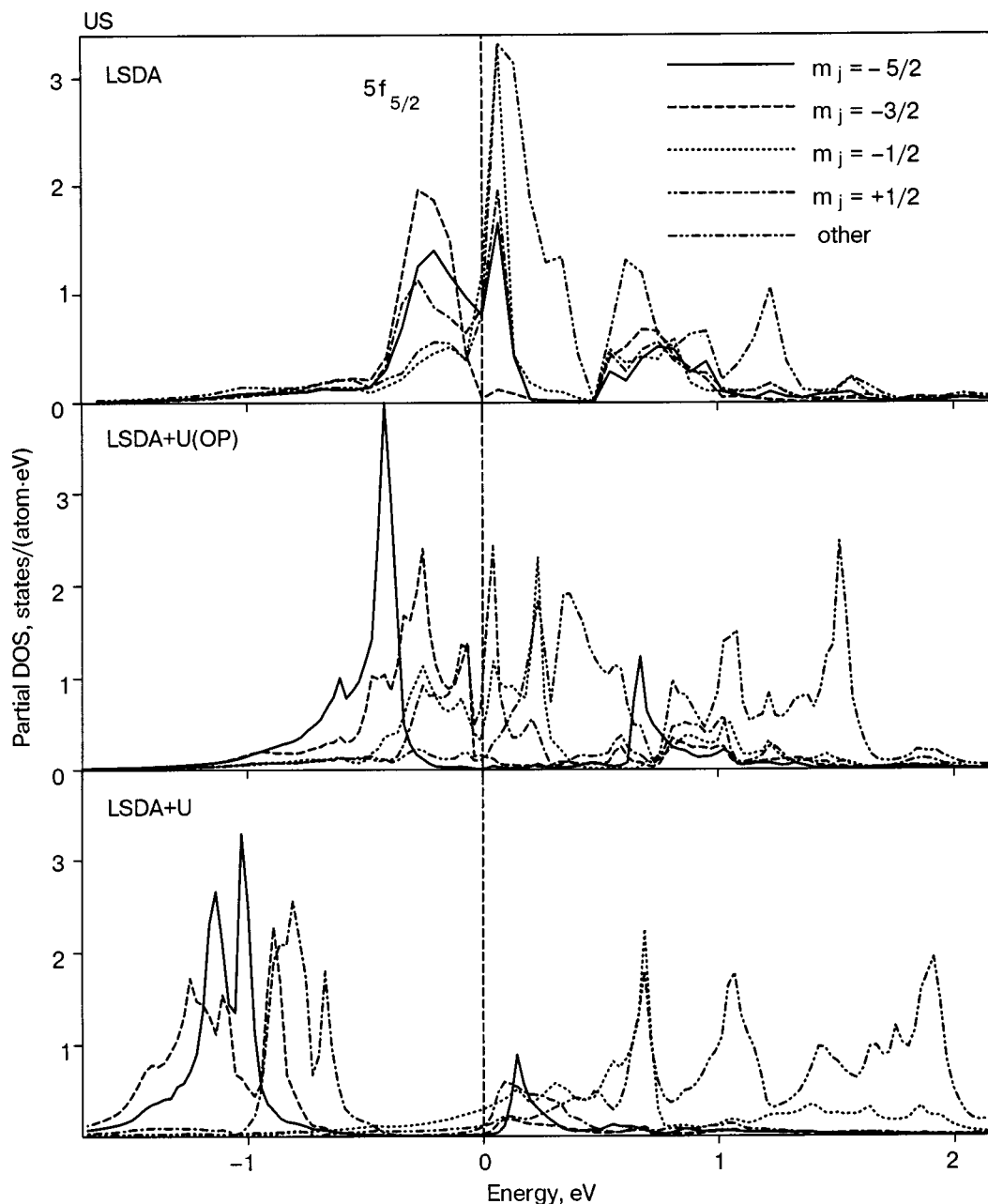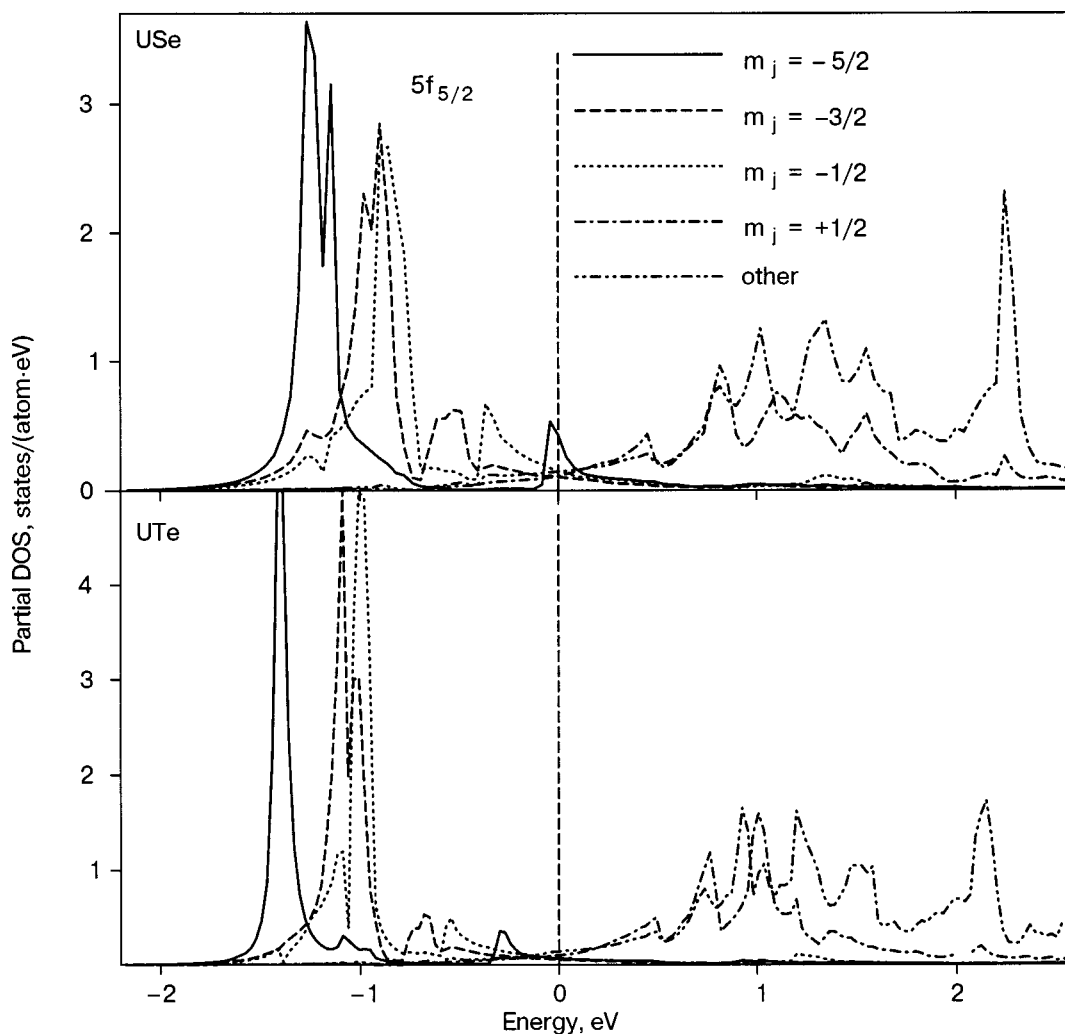
FIG. 4. The partial $5f_{5/2}$ density of states (in states/(atom·eV)) in US, USe, and UTe calculated within the LSDA+U approximation.

their orbital magnetic moments (Table I). For example, the ratio M_l/M_s in the LSDA+U(OP) calculations is equal to -2.17 and -2.14 for US and UTe, respectively. The corresponding experimental values are -2.3 for US from the neutron measurements[8] and -2.21 for UTe from the magnetic Compton profile measurements.[79]

The $5f$ spin M_s and orbital M_l magnetic moments in US have been also calculated in Ref. 27 on the basis of the HF approximation for an extended Hubbard model. The tight-binding model includes the intra-atomic $5f-5f$ multipole interaction and the SOI in the $5f$ state. The parameters involved in the model were determined by fitting with the energy of Bloch electrons in the paramagnetic state obtained in the LDA band structure calculation. The calculated ratio of the moments M_l/M_s of -2.14 and M_l of $3.19\mu_B$ are in good agreement with available experimental results (Table I).

We should mention that the results of the LSDA $+U$(OP) calculations are in close agreement with the results obtained using the HF approximation for an extended Hubbard model[27] (Table I). Both approximations take into account the SOI and the intra-atomic $5f-5f$ Coulomb interaction in the Hubbard model. The small differences in magnetic moments are due to slightly different values of U_{eff}. In our calculations we used $U=J=0.5$ eV, which gives $U_{\text{eff}}=0$. The authors of Ref. 27 used $U=0.76$ eV and

$J=0.5$ eV, which gives $U_{\text{eff}}=0.26$ eV. Besides, there are some small differences in the F^2, F^4, and F^6 Slater integrals in two the calculations.

Figure 3 also shows the m_j-projected $5f_{5/2}$ density of states in US calculated in the LSDA+U approximation with $U=2.0$ eV and $J=0.5$ eV. The corresponding partial DOSs for USe and UTe are presented in Fig. 4. The degree of localization of occupied $5f_{5/2}$ states is increasing from US to UTe. In US the $5f_{5/2}$ states with $m_j=-5/2$ are strongly hybridized with other occupied states, while the hybridization in USe and particularly in UTe almost vanishes. The $5f_{5/2}$ states with $m_j=-5/2$ are responsible for the narrow single peak in UTe (Fig. 4). The orbital magnetic moments calculated in the LSDA+U approximation are larger than those calculated in the LSDA+U(OP) approximation, which leads to a slightly overestimated ratio M_l/M_s in comparison with the experimental data for the LSDA+U calculations (Table I).

3.2. XMCD spectra

The XMCD measurements on the U $M_{4,5}$ edges of US have been presented in Ref. 29. The measured dichroic M_4 line consists of a simple nearly symmetric negative peak that has no distinct structure. Such a peak is characteristic of the
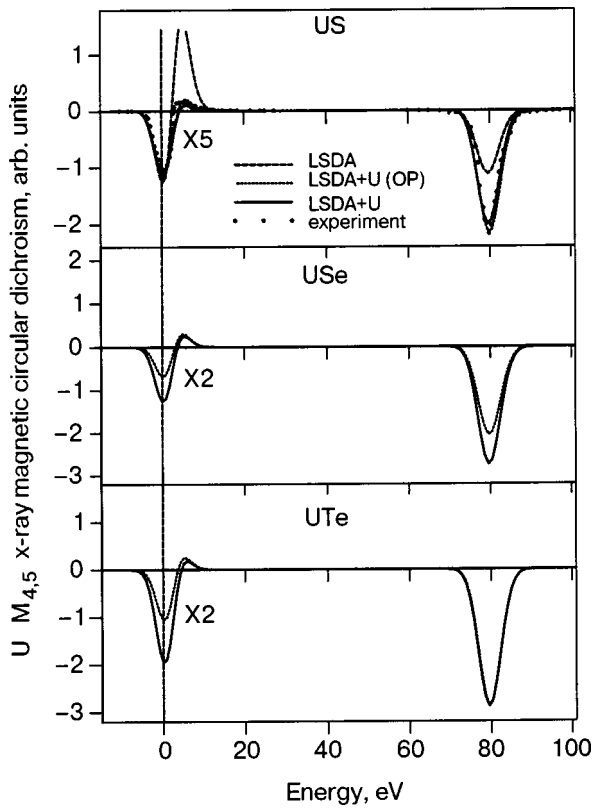
FIG. 5. The XMCD spectra of US, USe, and UTe at the uranium $M_{4,5}$ edges calculated within the LSDA (dashed lines), LSDA$+U$(OP) (dotted lines), and LSDA$+U$ (solid lines) approximations. Experimental spectra of US (Ref. 87; open circles) were measured at a magnetic field of 2 T. The U M_4 spectra are shifted by -95 eV to include them in the figure.

M_4 edge of all uranium systems. The dichroic line at the M_5 edge has an asymmetric *s* shape with two peaks—a stronger negative peak and a weaker positive peak. The dichroism at the M_4 edge is more than one order of magnitude larger than at the M_5 edge.

We recall that the M_4 (M_5) edge corresponds to $3d_{3/2}(3d_{5/2})\rightarrow 5f$ transitions. The created $3d$ core hole has electrostatic interaction with the $5f$ shell. However, in a first approximation, this interaction can be neglected since no clear multiplet structure is distinguished in the absorption spectra. This approximation is supported theoretically since the Slater integrals $F_k(3d,5f)$ and $G_k(3d,5f)$ are small compared to the $F_k(5f,5f)$ integrals and $3d$ spin–orbit interaction.[29] In neglect of the core-level splitting, the measured spectra reflect the density of states above the Fermi level E_F weighted by the dipole transition probabilities. Since the XMCD technique uses circularly polarized x rays, the dichroism contains information about the character of the magnetic sublevels in the DOS.

Because of the electric dipole selection rules ($\Delta l = \pm 1$; $\Delta j = 0, \pm 1$) the major contribution to the absorption at the M_4 edge stems from the transitions $3d_{3/2}\rightarrow 5f_{5/2}$ and that at the M_5 edge originates primarily from $3d_{5/2}\rightarrow 5f_{7/2}$ transitions, with a weaker contribution from $3d_{5/2}\rightarrow 5f_{5/2}$ transitions. For the later case the corresponding $3d_{5/2} \rightarrow 5f_{5/2}$ radial matrix elements are only slightly smaller than for the $3d_{5/2}\rightarrow 5f_{7/2}$ transitions. The angular matrix elements, however, strongly suppress the $3d_{5/2}\rightarrow 5f_{5/2}$ contribution. Therefore the contribution to the XMCD spectrum at the M_5

edge from the transitions with $\Delta j = 0$ is 15 times smaller than the transitions with $\Delta j = 1$ [see Eq. (11)].

Figure 5 shows the XMCD spectra of US, USe, and UTe at the uranium $M_{4,5}$ edges calculated within the LSDA and LSDA$+U$ approximations. It is clearly seen that the LSDA calculations give inappropriate results. The major discrepancy between the LSDA calculated and experimental XMCD spectra is the size of the M_4 XMCD peak. The LSDA underestimates the integral intensity of the XMCD at M_4 edge. As the integrated XMCD signal is proportional to the orbital moment[76] this discrepancy could be related to an underestimation of the orbital moment by LSDA-based computational methods (Table I). On the other hand, the LSDA$+U$ approximation produces good agreement with the experimentally measured intensity for the M_4 XMCD spectrum. In the case of the M_5 XMCD spectrum, the LSDA strongly overestimates the value of the positive peak. The LSDA $+U$(OP) approximation gives good agreement in the shape and intensity of the XMCD spectrum at the M_5 edge.

The behavior of the $5f$ electrons ranges from nearly delocalized to almost localized: US is considered to be nearly itinerant,[88] while UTe is considered to be quasilocalized.[89] So the failure of the LSDA description of the XMCD spectra in US comes as a surprise, because if the $5f$ electrons are itinerant, one would expect the delocalized LSDA approach to be applicable. However, as the integrated XMCD signal is proportional to the orbital moment,[76] this discrepancy could be related to an underestimation of the orbital moment by LSDA-based computational methods.

It is interesting to note that the LSDA$+U$(OP) and LSDA$+U$ calculations give similar results for the XMCD spectrum at the M_5 edge in the case of US and became relatively more different going through USe and UTe, probably reflecting the increase of degree of localization of the $5f$ electrons. Besides, the relative intensity of the M_5 and M_4 XMCD spectra is strongly increased in going from US to UTe. Experimental measurements of the XMCD spectra in USe and UTe are highly desired.

4. SUMMARY

We have studied the electronic structure and the x-ray magnetic circular dichroism in US, USe, and UTe by means of an *ab initio* fully-relativistic spin-polarized Dirac linear muffin-tin orbital method. We found that the degree of localization of occupied $5f_{5/2}$ states is increasing in going from US to UTe. In US the $5f_{5/2}$ states with $m_j = -5/2$ are strongly hybridized with other occupied states, while this hybridization in USe and particularly in UTe almost vanishes. The $5f_{5/2}$ states with $m_j = -5/2$ form a narrow single peak in UTe.

The LSDA calculations for ferromagnetic uranium monochalcogenides (US, USe, and UTe) give too small a magnitude of the total magnetic moment M_t compared to the experimental data, indicating that the calculated M_l is not large enough. On the other hand, the LSDA$+U$ method (with $U_{\text{eff}}=0$, the so-called LSDA$+U$(OP) approximation) provides good agreement with neutron and XMCD experimental data. The orbital magnetic moments calculated in the LSDA$+U$ approximation are larger than those calculated in

the LSDA+U(OP) approximation, which leads to a slightly overestimated ratio M_l/M_s in comparison with the experimental data for the LSDA+U calculations.

The experimentally measured dichroic U M_4 line in US consists of a simple, nearly symmetric negative peak that has no distinct structure. The dichroic line at the M_5 edge has an asymmetric *s* shape with two peaks—a stronger negative peak and a weaker positive peak. The major discrepancy between the LSDA-calculated and experimental XMCD spectra is the size of the M_4 XMCD peak. The LSDA underestimates the integral intensity of the XMCD at the M_4 edge. As the integrated XMCD signal is proportional to the orbital moment this discrepancy could be related to an underestimation of the orbital moment by LSDA-based computational methods. The LSDA calculations also strongly overestimate the value of the positive peak of the XMCD spectrum at the M_5 edge. On the other hand, the LSDA+U(OP) approximation gives good agreement in the shape and intensity of the U XMCD spectra at the M_4 and M_5 edges.

*E-mail: antonov@ameslab.gov; antonov@imp.kiev.ua; Permanent address: Institute of Metal Physics, 36 Vernadsky St., Kiev 03142, Ukraine

[1] J.-M. Fournier and R. Troch, in *Handbook on the Physics and Chemistry of the Actinides*, edited by A. J. Freeman and G. H. Lander, North-Holland Amsterdam (1985), Vol. 2, p. 29.

[2] D. L. Tillwick and P. de V. du Plessis, J. Magn. Magn. Mater. **3**, 329 (1976).

[3] G. Busch, O. Vogt, A. Delpalme, and G. H. Lander, J. Phys. C **12**, 1391 (1979).

[4] G. H. Lander, M. S. S. Brooks, B. Lebech, P. J. Brown, O. Vogt, and K. Mattenberger, J. Appl. Phys. **69**, 4803 (1991).

[5] M. S. S. Brooks and P. J. Kelly, Phys. Rev. Lett. **51**, 1708 (1983).

[6] G. H. Lander, Physica B **186–188**, 664 (1993).

[7] M. S. S. Brooks, Physica B **130**, 6 (1985).

[8] F. A. Wedgwood, J. Phys. C **5**, 2427 (1972).

[9] B. Reihl, J. Less-Common Met. **128**, 331 (1987).

[10] J. Schoenes, B. Frick, and O. Vogt, Phys. Rev. B **30**, 6578 (1984).

[11] J. Schoenes, B. Frick, and O. Vogt, Phys. Rev. B **30**, 6578 (1984).

[12] C. Y. Huang, R. J. Laskowski, C. E. Olsen, and J. L. Smith, J. Phys. C **40**, 26 (1979).

[13] E. F. Westrum, R. R. Walters, H. E. Flotow, and D. W. Osborne, J. Chem. Phys. **48**, 155 (1968).

[14] P. Erdoes and J. Robinson, *The Physics of Actinide Compounds*, Plenum Press, New York, London (1983).

[15] J. Neuenschwander, O. Vogt, E. Vogt, and P. Wachter, Physica B **144**, 66 (1986).

[16] H. Bilz, G. Guentherodt, W. Kleppmann, and W. Kress, Phys. Rev. Lett. **43**, 1998 (1979).

[17] A. L. Cornelius, J. S. Schilling, O. Vogt, K. Mattenberger, and U. Benedict, J. Magn. Magn. Mater. **161**, 169 (1996).

[18] O. G. Sheng and B. R. Cooper, J. Magn. Magn. Mater. **164**, 335 (1996).

[19] P. Santini, R. Lemanski, and P. Erdoes, Adv. Phys. **48**, 537 (1999).

[20] S. V. Halilov and E. T. Kulatov, J. Phys.: Condens. Matter **3**, 6363 (1991).

[21] T. Gasche, Ph. D. Thesis, Uppsala (1993).

[22] B. R. Cooper, Q. G. Sheng, S. P. Lim, C. Sánchez-Castro, N. Kioussis, and J. M. Wills, J. Magn. Magn. Mater. **108**, 10 (1992).

[23] T. Kraft, P. M. Oppeneer, V. N. Antonov, and H. Eschrig, Phys. Rev. B **52**, 3561 (1995).

[24] J. Trygg, J. M. Wills, and M. S. S. Brooks, Phys. Rev. B **52**, 2496 (1995).

[25] P. M. Oppeneer, V. N. Antonov, A. Y. Perlov, A. N. Yaresko, T. Kraft, and H. Eschrig, Physica B **230–232**, 544 (1997).

[26] H. Yamagami, J. Phys. Soc. Jpn. **67**, 3176 (1999).

[27] T. Shishidou, T. Oguchi, and T. Jo, Phys. Rev. B **59**, 6813 (1999).

[28] T. Shishidou and T. Oguchi, Phys. Rev. B **62**, 11747 (2000).

[29] S. P. Collins, D. Laundy, C. C. Tang, and G. van der Laan, J. Phys.: Condens. Matter **7**, 9325 (1995).

[30] H. Ebert, Rep. Prog. Phys. **59**, 1665 (1996).

[31] J. P. Hannon, G. T. Trammel, M. Blume, and D. Gibbs, Phys. Rev. Lett. **61**, 1245 (1988).

[32] S. W. Lovsey and S. P. Collins, *X-Ray Scattering and Absorption in Magnetic Materials*, Oxford University Press, Oxford (1996).

[33] J. B. Kortight and S.-K. Kim, Phys. Rev. B **62**, 12216 (2000).

[34] M. I. Friezer, IEEE Trans. Magn. **4**, 152 (1968).

[35] G. Y. Guo, Phys. Rev. B **55**, 11619 (1998).

[36] P. N. Argyres, Phys. Rev. **97**, 334 (1955).

[37] P. J. Durham, in *The Electronic Structure of Complex Systems*, edited by P. Phariseu and W. M. Temmerman, Plenum, New York (1984).

[38] W. H. Kleiner, Phys. Rev. **142**, 318 (1966).

[39] F. U. Hillebrecht, C. Roth, H. B. Rose, W. G. Park, E. Kisker, and Kirschner, Phys. Rev. B **55**, 2594 (1997).

[40] J. G. Menchero, Phys. Rev. B **57**, 993 (1998).

[41] G. van der Laan, J. Magn. Magn. Mater. **148**, 53 (1995).

[42] G. van der Laan, J. Electron Spectrosc. Relat. Phenom. **86**, 41 (1997).

[43] G. van der Laan, J. Phys.: Condens. Matter **9**, L259 (1997).

[44] G. van der Laan, Phys. Rev. B **57**, 5250 (1998).

[45] J. G. Menchero, Phys. Rev. B **57**, 1001 (1998).

[46] A. Fanelsa, R. Schellenberg, F. U. Hillebrecht, E. Kisker, J. G. Menchero, A. P. Kaduwela, C. S. Fadley, and M. A. V. Hove, Phys. Rev. B **54**, 17962 (1996).

[47] J. G. Menchero, C. S. Fadley, G. Panaccione, F. Sirotti, G. J. Henk, and R. Feder, Phys. Rev. B **55**, 11476 (1997).

[48] J. G. Menchero, Phys. Rev. B **55**, 5505 (1997).

[49] R. Schellenberg, E. Kisker, A. Fanelsa, F. U. Hillebrecht, J. G. Menchero, A. P. Kaduwela, C. S. Fadley, and M. A. V. Hove, Phys. Rev. B **57**, 14310 (1998).

[50] H. Ebert, L. Baumgarten, C. M. Schneider, and J. Kirschner, Phys. Rev. B **44**, 4406 (1991).

[51] H. Ebert and G. Y. Guo, J. Magn. Magn. Mater. **148**, 178 (1995).

[52] G. Y. Guo, H. Ebert, W. M. Temmerman, and P. J. Durham, Phys. Rev. B **50**, 3861 (1994).

[53] E. Tamura, G. D. Waddill, J. G. Tobin, and P. A. Sterne, Phys. Rev. Lett. **73**, 1533 (1994).

[54] V. N. Antonov, A. I. Bagljuk, A. Y. Perlov, V. V. Nemoshkalenko, Vl. N. Antonov, O. K. Andersen, and O. Jepsen, Fiz. Nizk. Temp. **19**, 689 (1993) [Low Temp. Phys. **19**, 494 (1993)].

[55] V. V. Nemoshkalenko, V. N. Antonov, V. N. Antonov, W. John, H. Wonn, and P. Ziesche, Phys. Status Solidi B **111**, 11 (1982).

[56] V. I. Anisimov, J. Zaanen, and O. K. Andersen, Phys. Rev. B **44**, 943 (1991).

[57] P. W. Anderson, Phys. Rev. **124**, 41 (1961).

[58] J. Hubbard, Proc. R. Soc. London, Ser. A **276**, 238 (1963).

[59] J. Hubbard, Proc. R. Soc. London, Ser. A **277**, 237 (1964).

[60] V. I. Anisimov, I. V. Solovyev, M. A. Korotin, M. T. Czyzyk, and G. A. Sawatsky, Phys. Rev. B **48**, 16929 (1993).

[61] A. N. Yaresko, V. N. Antonov, and P. Fulde, Phys. Rev. B **67**, 155103 (2003).

[62] I. V. Solovyev, A. I. Liechtenstein, and K. Terakura, Phys. Rev. Lett. **80**, 5758 (1998).

[63] H. Harima, J. Magn. Magn. Mater. **226–230**, 83 (2001).

[64] C. Herring, in *Magnetism*, G. T. Rado and H. Suhl (eds.), Academic, New York (1966), V. IV.

[65] V. I. Anisimov and O. Gunnarsson, Phys. Rev. B **43**, 7570 (1991).

[66] P. H. Dederichs, S. Blügel, R. Zeller, and H. Akai, Phys. Rev. Lett. **53**, 2512 (1984).

[67] I. V. Solovyev, P. H. Dederichs, and V. I. Anisimov, Phys. Rev. B **50**, 16861 (1994).

[68] W. E. Pickett, S. C. Erwin, and E. C. Ethridge, Phys. Rev. B **58**, 1201 (1998).

[69] V. N. Antonov, B. N. Harmon, and A. N. Yaresko, Phys. Rev. B **63**, 205112 (2001).

[70] V. N. Antonov, B. N. Harmon, and A. N. Yaresko, Phys. Rev. B **66**, 165208 (2002).

[71] U. von Barth and L. Hedin, J. Phys. C **5**, 1629 (1972).

[72] P. E. Blöchl, O. Jepsen, and O. K. Andersen, Phys. Rev. B **49**, 16 (1994).

[73] G. G. Scott, J. Phys. Soc. Jpn. **17**, 372 (1962).

[74] W. Marshall and S. W. Lovsey, *Theory of Thermal Neutron Scattering*, Oxford University Press, Oxford (1971).

[75] M. Blume, J. Appl. Phys. **57**, 3615 (1985).

[76] B. T. Thole, P. Carra, F. Sette, and G. van der Laan, Phys. Rev. Lett. **68**, 1943 (1992).

[77] P. Carra, B. T. Thole, M. Altarelli, and X. Wang, Phys. Rev. Lett. **70**, 694 (1993).

[78] L. Severin, M. S. S. Brooks, and B. Johansson, Phys. Rev. Lett. **71**, 3214 (1993).

[79] H. Sakurai, H. Hashimoto, A. Ochiai, T. Suzuki, M. Ito, and F. Itoh, J. Phys.: Condens. Matter **7**, L599 (1995).

[80] M. S. S. Brooks and B. Johansson, in *Handbook of Magnetic Materials*, edited by K. H. J. Buschow, Amsterdam, North-Holland, (1993), V., 7, p. 139.

[81] O. Eriksson, M. S. S. Brooks, and B. Johansson, Phys. Rev. B **41**, 7311 (1990).

[82] A. Mavromaras, L. Sandratskii, and J. Kübler, Solid State Commun. **106**, 115 (1998).

[83] G. Vignale and M. Rasolt, Phys. Rev. Lett. **59**, 2360 (1987).

[84] P. Skudlarski and G. Vigmale, Phys. Rev. B **48**, 8547 (1993).

[85] M. Higuchi and A. Haegawa, J. Phys. Soc. Jpn. **66**, 149 (1997).

[86] S. V. Beiden, W. M. Temmerman, Z. Szotek, and G. A. Gehring, Phys. Rev. Lett. **79**, 4970 (1997).

[87] M. Kucera, J. Kunes, A. Kolomiets, M. Divis, A. V. Andreev, V. Sechovsky, J. P. Kappler, and A. Rogalev, Phys. Rev. B **66**, 144405 (2002).

[88] M. S. S. Brooks, T. Gasche, and B. Johansson, J. Phys. Chem. Solids **56**, 1491 (1995).

[89] B. Reihl, N. Martensson, and O. Vogt, J. Appl. Phys. **53**, 2008 (1982).

LOW-DIMENSIONAL AND DISORDERED SYSTEMS

Boundary friction on molecular lubricants: rolling mode?

V. M. Loktev

Bogolyubov Institute for Theoretical Physics, National Academy of Sciences of Ukraine,
Metrologichna St. 14-b, Kiev, 03143 Ukraine

Yu. G. Pogorelov*

CFP/Departamento de Física, Universidade do Porto, 4169-007 Porto, Portugal

A theoretical model is proposed for low-temperature friction between two smooth, rigid solid surfaces separated by lubricant molecules, admitting their deformations and rotations. The appearance of different modes of energy dissipation (by ''rocking'' or ''rolling'' of lubricants) at slow relative displacement of the surfaces is shown to be accompanied by stick-and-slip features and reveals a nonmonotonic (mean) friction force versus external load. © *2004 American Institute of Physics.* [DOI: 10.1063/1.1705439]

INTRODUCTION

In modern tribology there is a still increasing interest in studies of wearless friction on atomically smooth surfaces[1,2] as a possibility for providing information about the basic processes of energy losses on the microscopic level, important for the purposes of optimization in many technological applications. This is also connected with the search for the best coating and lubricant materials. The principal physical picture usually considered in relation to boundary friction on few molecular layers of lubricant liquid is a sequence of ''freezing—melting'' processes of the lubricant, giving rise to discontinuous (stick-and-slip) displacement of sliding surfaces.[3] Recently a new theoretical approach was proposed for microscopic sliding processes at extremely low velocities of motion and upon a monolayer of lubricant atoms,[4] as can be the case for friction force microscopy (FFM). Based on the adiabatic formation of metastable states (similar to dislocations in usual deformed crystals or defects in the Frenkel—Kontorova model[5,6]) and their following relaxation, this treatment shows how the (average) microscopic friction coefficient depends upon the material parameters of the contacting solids and lubricants and also how stick-and-slip jumps with atomic periodicity can develop in the microscopic friction force. It should be noted that a similar microscopic mechanism of dislocation-assisted sliding was recently proposed for contacting asperities in dry friction.[7]

Ultimately, with the discovery of the almost spherical fullerene C_{60} molecule[8] (and/or cylindrical carbon nanotubes[9]) a hope had arisen to use such closed molecular structures as ''free rotating'' lubricants, for considerable reduction of the friction coefficient. For instance, a reduction of the sliding friction coefficient had already been discussed, due to involvement of spinning motion of surfaces in contact.[10] However, the FFM experiments with use of C_{60} monolayers deposited over atomically smooth solid surfaces brought some contradictory results.[11–13] To get a better understanding of them, a further theoretical insight on the elementary processes of boundary friction is desirable.

The present communication is aimed at extention of the above-mentioned adiabatic approach to processes of boundary friction which include the internal degrees of freedom of the lubricant molecules. Within an extremely simple model, we make an attempt to show that, due to the discrete atomic structure of such a molecule, qualitatively different modes of slow motion, either dissipative or nondissipative, are possible, depending on the applied external load on the contact. For dissipative modes there are energy losses resulting from stick-and-slip discontinuities, but these losses turn out much lower than for similar processes at sliding solid surfaces upon atomic lubricants. Besides, the mean value of the friction force is found to be a nonmonotonic function of the external load and can be sensitive to temperature in the cryogenic range.

THE MODEL

Let us consider a two-dimensional model for the boundary friction system which includes two semi-infinite atomic arrays, ''solids,'' with identical triangular lattice structure and a spatial separation d between their surfaces, and clusters of four atoms, the ''molecular lubricants,'' confined between the solids (Fig. 1). The distances between nearest neighbor atoms in both solids and in clusters are assumed invariable[1)] (that means, corresponding to ''absolutely rigid'' bonds), and the bond length for the molecule is equal to the lattice parameter a for the solid surfaces.

The model includes certain ''soft links,'' which determine the energy variation versus relative displacement of the solids. In the first turn, this is a weak Lennard-Jones interaction between an atom of solid and a lubricant molecule at distance r:
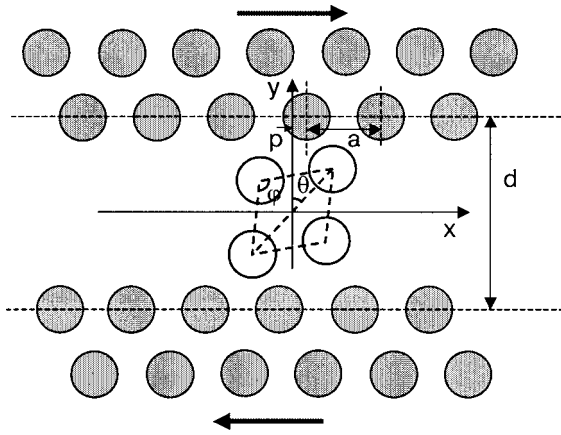
FIG. 1. Schematic of the friction system: two solid arrays (gray circles) with identical lattice structures are separated by a four-atom lubricant molecule (white circles). The molecule center rests at the origin, and its configuration is determined by the tilt angle θ and rhombic angle φ, while the symmetric displacements of the solids are described by the parameter p (see the text).

$$V_{L-J}(r) = \varepsilon_0 \left[\left(\frac{r_0}{r} \right)^{12} - 2 \left(\frac{r_0}{r} \right)^6 \right], \tag{1}$$

characterized by the adhesion energy ε_0 and equilibrium distance r_0. Besides, a lubricant molecule can experience rhombic deformation which changes its energy as $k \sin^2 \varphi$, where k and φ are the elastic constant and rhombic angle, respectively. We neglect the interaction between different lubricants, that is, we omit their possible collective modes. Thus the molecular lubricants are supposed to contribute independently to the total friction force. Then we choose one particular molecule and set its center of mass as the origin of the reference frame, so its configuration is determined by the "internal" rhombic angle φ and the "external" orientation angle θ (say, with respect to the normal to the interface). In such a frame, the two solids are supposed to be displaced symmetrically with respect to the lubricant molecule, and their configuration is fully defined by the displacement parameter p, chosen, e.g., as the smallest positive longitudinal coordinate of the atoms of the upper solid. All this permits us to write the total energy (per lubricant) in the simple form:

$$E = \sum_{n,m} V_{L-J}(|\mathbf{r}_n - \mathbf{R}_m|) - k \sin^2 \varphi, \tag{2}$$

where $\mathbf{r}_n$ and $\mathbf{R}_m$ are, respectively, the positions of the atoms of solids and the atoms in the lubricant molecule. Obviously, this extremely simplified model does not pretend to give a quantitative description, and explanation of friction experiments in real systems with complex and typically incommensurate solid and molecular structures. It serves mainly to illustrate some new qualitative possibilities for weakly dissipative processes associated with the internal (rolling or rotational) degrees of freedom of molecular (including nanotubes) lubricants, in contrast to the dissipation by only translational motions of the "point-like" (atomic) lubricants.

THE ADIABATIC DYNAMICS

The adiabatic treatment of the system, corresponding to the expression (2), follows the lines suggested in Ref. 4. The equilibrium distance for Lennard-Jones interaction (1) is
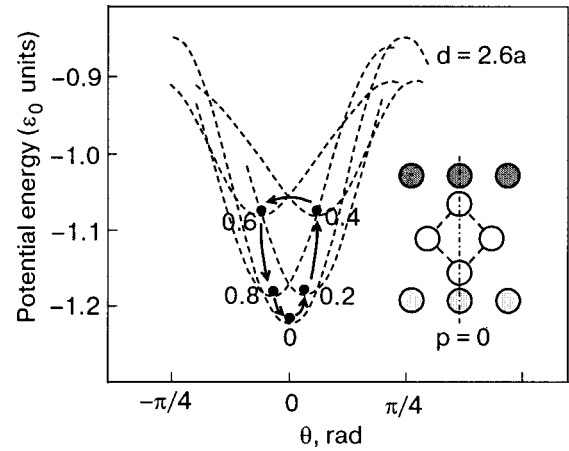

FIG. 2. Series of profiles of potential energy versus orientation (at optimal deformation, see the text) and the related equilibrium states (bold circles) of a lubricant molecule at growing displacement of the solids (the numbers indicate p/a values) and at the highest separation between them. The phase trajectory (arrows) shows that the molecule performs continuous "rocking" motions and after the full cycle (at $p/a = 1$) returns to its initial state with no energy dissipation. Inset: the rhombic configuration at $p = 0$.

taken equal to the interatomic distance in the solids: $r_0 = a$. At a given separation d between the surfaces, we calculate numerically the total energy profile $E(p, \theta, \varphi)$ as a function of the displacement parameter p, and also of the angles θ and φ. Next this function is optimized with respect to the deformation angle φ to result in profiles $E(p, \theta)$ such as those displayed in Figs. 2–5 (for different values of p, through the whole displacement period from 0 to a, and at different separations d).

The primary optimization in φ refers to the stronger elastic deformation constant (we took $k = 0.5\varepsilon_0$, while the amplitude of relevant energy oscillations in θ is $\sim 0.1\varepsilon_0$) and hence to a faster relaxation in φ than in θ.[2] Then the system behavior at very slow uniform variation of the parameter p with time (that is, the slow dynamics) is obtained from analysis of the profile $E(p, \theta)$. Below we analyze how this
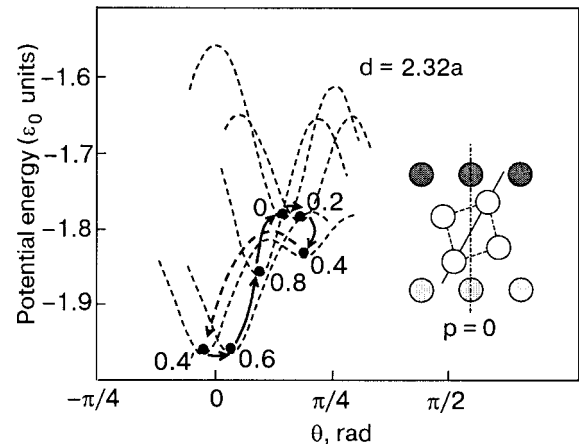
FIG. 3. The same as in Fig. 2 but at closer separation between the solids (higher external load). The lubricant molecule after "rocking" returns to its initial state, but in this course it experiences a thermally activated jump (the dotted arrow over the potential barrier for $p/a = 0.4$) between the metastable (0.4) and stable ($0.4'$) minima, and the corresponding energy difference is irreversibly lost. Inset: the configuration at $p = 0$ corresponds to one of the split minima.
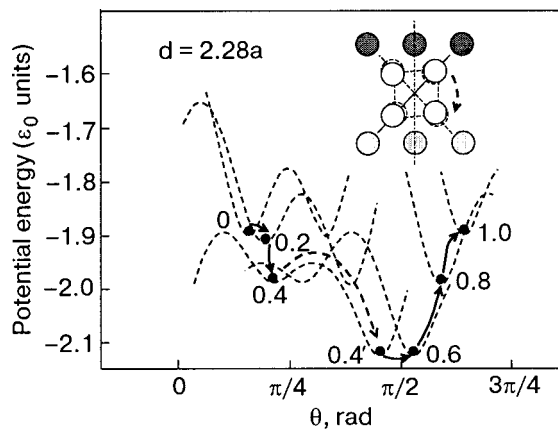
FIG. 4. The same as in Figs. 2 and 3 but at still higher load. The thermally activated jump changes its direction and the lubricant molecule rotates by the angle $\pi/2$ after every period in p ("rolling mode"). The energy loss and hence the friction force is somewhat larger than that in Fig. 3.

profile changes with growing external load, which is here simulated by a gradual decrease of the separation distance d.

i) At the greatest separations (evidently corresponding to the lowest loads), it is seen from Fig. 2 that the energy profile has a single $\pi/2$ periodicity in θ. This means that, for any given p, there is a single equilibrium state for the molecule, characterized by its orientation $\theta(p)$ (up to a C_4 rotation) and energy $E(\theta(p))$, such that $(\partial E/\partial\theta)_{\theta(p)}=0$, $(\partial^2 E/\partial\theta^2)_{\theta(p)}>0$ In this case, the phase trajectory $E(\theta)$ (shown by the sequence of bold dots linked by arrows, for growing displacement) is closed and continuous. Thus, the system energy changes in a fully reversible way and, though some forces are exerted in the process, their mean value over the cycle and thus the mean friction force are exactly zero. This reversible variation of the angle θ around its median position (such that the long diagonal of the rhombus points vertically; inset to Fig. 2), corresponds to a "rocking mode" of the molecular motion.

ii) As the two solid surfaces draw closer (at increasing load), the first qualitative change that appears in the system behavior is the doubling of its energy minima. Now there are two split minima at the initial configuration $p=0$ (Fig. 3), which correspond to a twofold degenerate equilibrium state
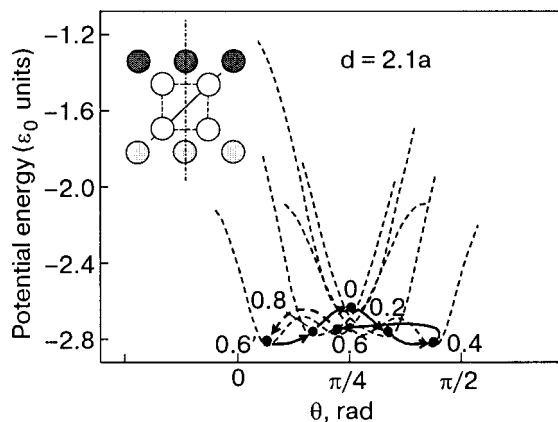

FIG. 5. The same as in Figs. 2–4 at futher growing load. The molecule returns from "rolling" to "rocking" regime with an intermediate jump, but at much smaller energy loss than in Figs. 3 and 4.

of the deformed lubricant molecule: the long diagonal of the rhombus can deviate by a finite angle $<\pi/2$ to both sides from the vertical (inset to Fig. 3). Since the molecule is considered a classical object, it initially occupies only one of the minima (the left one is chosen in Fig. 3).

However, the degeneracy gets lifted for $p>0$, so that one of the split minima turns into a stable (s) and the other a metastable (m) equilibrium state. As is seen from the consecutive curves in Fig. 3, the energy barrier h between the m state and the nearest s state (here that to the left of m) decreases by many times with growing p, as a certain function $h(p)$. Since the adiabatic lifetime for the m state is $\tau_m = \tau_a \exp(\beta h)$ (where $\tau_a \sim 10^{-12}$ s is the atomic oscillation time and β is the inverse temperature), it decreases in this course by many orders of magnitude. Eventually, this lifetime gets comparable to the characteristic time τ_0 of slow displacement by an atomic period, at a very sharply defined instant when $p=p_0$, such that $h(p_0)=h_0=\beta^{-1}\ln(\tau_0/\tau_a)$. Hence it is almost exactly at this instant that a thermally activated jump from the m to the s state is realized. After the jump, the energy difference between the m and s states (to the moment of transition) is irreversibly lost, through the creation of quasiparticles (phonons, for insulating solids) which are finally thermalized in the bulk. For typical displacement rates in FFM, $\sim 10^2$ Å/s, one has $\tau_0 \sim 10^{-2}$ s, so that the barrier to the transition moment is still as high as $h_0 \sim 23\beta^{-1}$. For the situation presented in Fig. 4, the transition corresponds to $p_0=0.4a$ (the potential profile shown by the solid line). It is also seen that, with further increase of p, up to a, the system returns to its initial state; thus the phase trajectory is still closed ("rocking mode" again), though discontinuous. This discontinuity produces stick-and-slip features in the microscopic behavior of the force versus displacement and it is the only source of irreversible losses in our model system, in full similarity to the model of sliding solids upon atomic lubricants.

There are, however, some distinctions between the two systems. First, the stick-and-slip profile for molecular lubricants is more complicated than the simple triangular sawtooth for atomic lubricants. But especially important is the fact that the irreversible forces for molecular lubricants are *smaller* than the elastic, reversible forces (the jump heights in Figs. 3–5 are noticeably lower than the amplitudes of the smooth oscillations), while the irreversible forces for atomic lubricants are orders of magnitude *higher* than the reversible ones. Since the reversible forces in both cases are characterized by the same energy scale ε_0, this indicates a possibility of substantially reducing the dissipation by molecular (rotating) lubricants versus that by atomic lubricants. Note, at least, that if the molecule occurs initially (at $p=0$) in the right minimum, it simply spends a period, $0<p<a$, in the s state, but then passes to the m state during the next period and eventually comes to the same closed discontinuous rocking.

iii) Now let us bring the surfaces yet a little bit closer, as by a very small change of the distance d between the solids (Figs. 3 and 4). Then the system evolution acquires yet a new quality: now at the transition moment the nearest s state is to the right of the given m state. As a result, after the transition, at $p>p_0$, the molecule does not return to its initial state but

will eventually be rotated by an angle $\pi/2$ (the dashed circles and arrow in the inset to Fig. 4), and this rotation will be repeated in each successive period. Thus in this case we have both unclosed (corresponding to the "rolling mode") and discontinuous regimes of lubricant motion.

iv) With still increasing loads, the situation of a single minimum for $E(0,\theta)$ will be restored again (though displaced by the angle $\pi/4$, corresponding to a "square" molecule (inset to Fig. 5). But now, unlike the case of low loads, this minimum gets split with increasing displacement p (here at $p \approx 0.3$). The molecule returns from the "rolling" to "rocking" regime ("rock-n-roll dance"), but with considerably reduced energy dissipation: the energy loss at a jump for $d=2.1a$ (Fig. 5) is about 2.5 times smaller than for $d = 2.28a$ (Fig. 4), i.e., it *decreases* with increasing load. We do not present here detailed results of numerical simulations for even higher loads, noting only that they reveal a number of subsequent dissipative regimes, either with growing or falling friction forces.

Finally, it should be noticed that the irreversible processes considered above are triggered by the actual temperature, and this parameter can be as important as the applied pressure for changing the dissipated energy, for changing the dissipation regime, and for the very presence of energy losses. Thus, using typical a LJ energy for a C–C pair ε ~ 1 eV, the critical condition $p_0=0.4a$ for the rolling process iii) in Fig. 4 is expected at $\beta^{-1} \sim 15$ K, but it will change to $p_0=0.2a$ with about a twofold decrease of the dissipated energy at $\beta^{-1} \sim 40$ K.

CONCLUSIONS

The above simple analysis demonstrates that boundary friction with participation of molecular (spheroidal or cylindrical) lubricants can possess quite unusual properties, such as the existence of various regimes of molecular motion, either nondissipative or dissipative, with abrupt transitions from one regime to another upon continuous variation of the external load. In the sequence of regimes ("rocking" and "rolling") the obtained friction force versus load displays nonmonotonic and hence nonlinear behavior. This model (of course, with due improvements to be incorporated) may provide a mechanism for explaining the data of real experiments[14,15] with the C_{60} fullerenes as lubricants and give indications for an optimal regime of their practical applications.

[*]E-mail: ypogorel@fc.up.pt
[1)]Here mean distances are meant, as the only relevant ones for adiabatic equilibrium states, while small thermal fluctuations become important for activation of relatively fast transitions between these equilibrium states.
[2)]A similar hierarchy of relaxation rates between two degrees of freedom was also reported for point-like lubricants, corresponding to their normal (transverse) and longitudinal displacements.[4]

[1] B. Bhushan, J. N. Israelashvili, and U. Landman, Nature (London) **374**, 607 (1995).

[2] G. M. McClelland and J. N. Glosli, in *Fundamentals of Friction: Macroscopic and Microscopic Processes*, edited by I. L. Singer and H. M. Pollock, Kluwer, Dordrecht (1992), p. 405.

[3] J. N. Israelachvili, *Intermolecular and Surface Forces*, Academic Press, London (1991).

[4] Yu. G. Pogorelov, Preprint cond-mat/0309117 (2003).

[5] Y. I. Frenkel and T. Kontorova, Zh. Éksp. Teor. Fiz. **8**, 1340 (1938).

[6] J. B. Sokoloff, Phys. Rev. B **42**, 760 (1990).

[7] B. Bhushan and M. Nosonovsky, Acta Mater. **51**, 4331 (2003).

[8] H. Kroto, J. R. Heath, S. C. O'Brian, R. F. Curl, and R. E. Smalley, Nature (London) **318**, 162 (1985).

[9] S. Iijima, Nature (London) **354**, 56 (1991).

[10] Z. Farkas, G. Bartels, T. Unger, and D. E. Wolf, Phys. Rev. Lett. **90**, 248302 (2003).

[11] B. Bhushan, B. K. Gupta, G. W. van Geef, C. Capp, and J. V. Coe, Appl. Phys. Lett. **62**, 3253 (1993).

[12] R. Luthi, E. Meyer, H. Haefke, L. Howald, W. Gutmannsbauer, M. Guggisberg, M. Bammerlin, and H.-J. Guntherodt, Surf. Sci. **338**, 247 (1995).

[13] U. D. Schwarz, W. Allers, G. Gensterblum, and R. Wiesendanger, Phys. Rev. B **52**, 14976 (1995).

[14] K. Miura, S. Kamiya, and N. Sasaki, Phys. Rev. Lett. **90**, 055509 (2003).

[15] S. Okita, A. Matsumuro, and K. Miura, Thin Solid Films **443**, 66 (2003).

QUANTUM EFFECTS IN SEMICONDUCTORS AND DIELECTRICS

Charge ordering and interlayer phase coherence in quantum Hall superlattices

S. I. Shevchenko*

B. Verkin Institute for Low Temperature Physics and Engineering, National Academy of Sciences of Ukraine, pr. Lenina 47, Kharkov 61103, Ukraine

D. V. Fil

Institute of Single Crystals of the National Academy of Sciences of Ukraine, pr. Lenina 60, Kharkov 61001, Ukraine

A. A. Yakovleva

National Technical University "Kharkov Polytechnical Institute," ul. Frunze 21, Kharkov 61002, Ukraine

The possibility of the existence of states with a spontaneous interlayer phase coherence in multilayer electron systems in a high perpendicular magnetic field is investigated. It is shown that phase coherence can be established in such systems only within individual pairs of adjacent layers, while such coherence does not exist between layers of different pairs. The conditions for stability of a state with interlayer phase coherence against transition to a charge-ordered state are determined. It is shown that in a system with $N \leqslant 10$ layers there is stability at any value of the interlayer distance d. For $N > 10$ there are two intervals of stability: at sufficiently large and at sufficiently small d. For $N \to \infty$ the stability interval in the region of small d vanishes. © *2004 American Institute of Physics.* [DOI: 10.1063/1.1705440]

1. INTRODUCTION

In the last 10 years a the study of the quantum Hall effect and its accompanying phenomena has focused on two-layer systems. One of the most interesting features of two-layer quantum Hall systems is the possibility of realizing a superfluid phase in them due to spontaneous interlayer phase coherence of the charge carriers. This phenomenon is analogous to superfluidity of electron–hole pairs with spatially separated components. The possibility of superfluidity of this type in a two-layer electron–hole system in zero magnetic field was first predicted in Refs. 1 and 2 (see also Refs. 3 and 4). In Ref. 5 it was shown that the application of a high perpendicular magnetic field to a two-layer electron–hole system promotes the formation of a superfluid phase (see also Refs. 6–9, where a more detailed investigation of this question is carried out), since, unlike the situation considered in Refs. 1 and 2, in the latter case it is not necessary to satisfy the condition of nesting of the Fermi surfaces of the electrons and holes.

Owing to the electron–hole symmetry, a two-layer electron–electron system in a quantizing magnetic field with filling factors of the layers equal to ν and $1 - \nu$ ($\nu < 1$) is a practically complete analog of a two-layer electron–hole system, and a transition to a superfluid phase is possible in such a system as well.[10–16] Interest in this question has risen significantly of late in connection with experiments[17,18] in which an effect of the Josephson type was observed (a sharp increase in the differential tunneling conductance at a small potential difference between layers). Furthermore, in a recent experiment on the interlayer drag in two-layer systems[19] a sharp suppression of the longitudinal drag and an increase in the Hall component of the drag were observed in the situation when the value of the total filling factor of the layers became close to unity. The effects observed in Refs. 17–19 can be explained on the assumption that a spontaneous interlayer phase coherence arises in the system and a transition of the system to a superfluid state occurs. We note also that direct experimental proof (based on the measured temperature dependence of the luminescence spectra) of Bose condensation of interwell excitons (photoexcited electron–hole pairs with spatially separated components) was obtained recently in double quantum wells in zero magnetic field.[20]

A natural development of this topic is to study the superfluid properties of multilayer electron systems. Multilayer systems are of particular interest for studying collective properties of the superfluid state of electron–hole pairs by optical and acoustic methods, since the integrated intensity of the interaction of such systems with external fields increases in proportion to the number of layers. The present study is devoted to investigation of the effect of interlayer phase coherence in quantum Hall superlattices.

The realization of multilayer quantum Hall systems was reported in Refs. 21–23. The research in Refs. 21–23 was mainly concerned with analysis of the properties of chiral edge states in such systems.

Previously the question of interlayer phase coherence in multilayer quantum Hall systems was considered in Refs. 24 and 25. The authors of Ref. 25 showed that a state in which phase coherence arises between all layers can be realized in

such systems (this will be referred to below as a state with global phase coherence). It was shown in Ref. 24 that in a multilayer quantum Hall system another state can arise (which we shall call a dimer state) in which the system separates into pairs of adjacent layers and the interlayer phase coherence is established only within each pair, while between layers belonging to different pairs there is no such coherence. This raises the question of reconciliation of the results of Refs. 24 and 25. In the present paper we show that the states of Refs. 24 and 25 correspond to two different solutions of the self-consistency equations for the order parameters describing the interlayer phase coherence. We shall find that the energy of the dimer state is less than the energy of the state found in Ref. 25 and, hence, it is the dimer state that should be considered as a candidate for the ground state of such a system.

It was shown in Ref. 25 that the existence conditions for the state with interlayer phase coherence in multilayer systems are more restrictive than for two-layer systems. A multilayer quantum Hall system, unlike the two-layer system, demonstrates a tendency toward the formation of a charge-ordered state (when the filling factors of adjacent layers become equal to 0 and 1). In Ref. 25 the stability conditions for the state with interlayer phase coherence were analyzed under the assumption that the phase coherence has a global character. Since this assumption is not confirmed, the stability conditions will have to be reexamined. We shall find that in the limit of an infinite number of layers (the case considered in Ref. 25) the dimer state is stable against transition to a charge-ordered state already at $d > d_c \approx 1.45 l_B$ (l_B is the magnetic length), which is less than the critical value ($d_c \approx 1.7 l_B$) obtained in Ref. 25.

In connection with the fact that the properties of systems with numbers of layers $N = 2$ and $N \to \infty$ are substantially different, and in real physical systems the number of layers is always finite, an important question arises as to how the stability conditions depend on N. In this paper we shall consider this question under the restriction that the number of layers is even. It is found that for $N \leqslant 10$ the state with interlayer phase coherence is stable for arbitrary d. For $N > 10$ stability is present only for $d < d_{c1}$ or for $d > d_{c2}$, where d_{c1} decreases and d_{c2} increases with increasing N while remaining in the interval $0 \leqslant d_{c1} < d_{c2} \leqslant d_c$.

2. INTERLAYER PHASE COHERENCE IN A TWO-LAYER SYSTEM WITH TOTAL FILLING FACTOR $\nu_{\text{tot}} = 1$

Before turning to multilayer systems, let us describe the approach used in this paper for the example of the simplest case $N = 2$ and recall the situation that exists in a two-layer system.

We consider a two-layer electron system in a high magnetic field perpendicular to the layers, with a filling factor $\nu_{\text{tot}} = \nu_1 + \nu_2$ equal to unity. Tunneling between layers will be assumed to be so weak that this interaction can be neglected in the Hamiltonian. If the cyclotron frequency is substantially higher than all the other characteristic energies of the problem, then for the description of such a system one can restrict consideration to the approximation of the lowest Landau level, where the influence of the upper unfilled Landau levels on the dynamics of the system is neglected.

The Hamiltonian of this system has the form

$$H = \frac{1}{2} \sum_{n,n'=1,2} \int \int d^2 r_n d^2 r_{n'} \Psi_n^+(\mathbf{r}_n) \Psi_{n'}^+(\mathbf{r}_{n'})$$

$$\times V_{nn'}(|\mathbf{r}_n - \mathbf{r}_{n'}|) \Psi_{n'}(\mathbf{r}_{n'}) \Psi_n(\mathbf{r}_n)$$

$$- \sum_{n=1,2} \int d^2 r_n \mu_n \Psi_n^+(\mathbf{r}_n) \Psi_n(\mathbf{r}_n) + H_{BG}, \quad (1)$$

where Ψ^+ and Ψ are Fermi field operators,

$$V_{nn'}(r) = \frac{e^2}{\varepsilon [r^2 + (n - n')^2 d^2]^{1/2}} \quad (2)$$

is the Coulomb potential, d is the distance between layers, ε is the dielectric constant, and μ_n is the chemical potential in layer n. The term H_{BG} in (1) describes the interaction of electrons with positively charged impurities in doping layers. For definiteness we shall consider the case when the densities of the positive neutralizing charge in the doping layers are the same. For simplicity we shall also assume that the z coordinates of the electron layers and doping layers coincide (the difference of the z coordinates of the electron and doping layers which exists in the real physical situation does not influence the effects studied in this paper).

For further analysis it is convenient to transform to the operators of the Fourier components of the electron density $\rho_n(\mathbf{q})$, in terms of which the Hamiltonian (1) can be written in the form

$$H = \frac{1}{2S} \sum_{n,n'=1,2} \sum_{\mathbf{q}} \left\{ V_{nn'}(q) \left[\rho_n(\mathbf{q}) \rho_{n'}(-\mathbf{q}) \right. \right.$$

$$\left. \left. - \delta_{nn'} \exp\left(-\frac{q^2 l_B^2}{2} \right) \rho_n(0) \right] \right\}$$

$$- \sum_{n=1,2} \mu_n \rho_n(0) + H_{BG}, \quad (3)$$

where S is the area of the layer. The value of $\rho(\mathbf{q})$ is expressed as follows in terms of the creation and annihilation operators for electrons on the lower Landau level $(a^+(X), a(X))$ with the center of the orbit at the point X:

$$\rho_n(\mathbf{q}) = \sum_X a_n^+ \left(X + \frac{q_y l_B^2}{2} \right) a_n \left(X - \frac{q_y l_B^2}{2} \right)$$

$$\times \exp\left(i q_x X - \frac{q^2 l_B^2}{4} \right). \quad (4)$$

In Eq. (3) the quantity

$$V_{nn'}(q) = \frac{2\pi e^2}{\varepsilon q} \exp(-qd|n - n'|) \quad (5)$$

is the Fourier component of the Coulomb potential.

We consider the interaction between electrons in the mean field approximation. In this approximation the Hamiltonian (3) takes the form

$$H_{MF} = \sum_X \left\{ \varepsilon_1 a_1^+(X) a_1(X) + \varepsilon_2 a_2^+(X) a_2(X) \right.$$

$$\left. - [J\Delta a_1^+(X) a_2(X) + \text{h.c.}] \right\}. \quad (6)$$

The energy ε_n in (6) has the form

$$\varepsilon_n = V_n - I\nu_n - \mu_n, \tag{7}$$

where V_n is the Fourier component of the Coulomb interaction at $q=0$ with allowance for its screening by positively charged doping impurities. For a two-layer system these quantities are equal to

$$V_1 = \frac{1}{2\pi l_B^2} \lim_{q\to 0}\left[V_{11}(q)\left(\nu_1 - \frac{1}{2}\right) + V_{12}(q) \right.$$
$$\left. \times \left(\nu_2 - \frac{1}{2}\right)\right] = W\tilde{\nu},$$

$$V_2 = \frac{1}{2\pi l_B^2} \lim_{q\to 0}\left[V_{22}(q)\left(\nu_2 - \frac{1}{2}\right) + V_{21}(q) \right.$$
$$\left. \times \left(\nu_1 - \frac{1}{2}\right)\right] = -W\tilde{\nu}. \tag{8}$$

The parameter $\tilde{\nu} = (\nu_1 - \nu_2)/2$ describes the value of the interlayer imbalance of the filling factors. In Eq. (6) Δ is the order parameter, defined as $\Delta = \langle a_2^+(X)a_1(X)\rangle$. In the general case $\Delta = |\Delta|e^{i\varphi}$ is complex valued. We restrict consideration to the case when the modulus $|\Delta|$ and phase φ of the order parameter are independent of X. In deriving Eq. (6) we have also taken into account that the averages $\langle a_n^+(X)a_n(X)\rangle$ are equal to ν_n.

In Eqs. (6), (7), and (8) we have used the following energy parameters. The parameter W, equal to

$$W = \frac{e^2 d}{\varepsilon l_B^2}, \tag{9}$$

describes the energy of the direct Coulomb interaction between layers. The parameters

$$I = \frac{1}{S}\sum_{\mathbf{q}} V_{11}(q)\exp\left(-\frac{q^2 l_B^2}{2}\right) = \sqrt{\frac{\pi}{2}}\frac{e^2}{\varepsilon l_B} \tag{10}$$

and

$$J = \frac{1}{S}\sum_{\mathbf{q}} V_{12}(q)\exp\left(-\frac{q^2 l_B^2}{2}\right)$$
$$= \sqrt{\frac{\pi}{2}}\frac{e^2}{\varepsilon l_B}\exp\left(\frac{d^2}{2l_B^2}\right)\mathrm{erfc}\left(\frac{d}{l_B\sqrt{2}}\right) \tag{11}$$

describe the energy of the intralayer and interlayer exchange interactions.

In a state in which the order parameter Δ is nonzero, the motion of electrons in one layer is correlated with the motion of holes (the single-particle states on the lower Landau level are unoccupied by electrons) in the other layer. This state can be treated as a gas of electron–hole pairs, which are composite bosons. The Bose condensation of such pairs (a true condensate at $T=0$ or a quasi-condensate with a fluctuating phase at $T\neq 0$) will have superfluid properties. In the superfluid motion of electron–hole pairs a nondissipative electric current in one layer is accompanied by an equal and oppositely directed nondissipative electrical current in the other layer.

For finding the self-consistency conditions for the order parameter Δ and chemical potentials μ_1 and μ_2 we subject the operators a_1 and a_2 to a $(u-v)$ transformation of the form

$$a_1 = u\alpha + v^*\beta^+, \quad a_2 = u^*\beta^+ - v\alpha. \tag{12}$$

The operators α and β will satisfy the Fermi commutation relations if $|u|^2 + |v|^2 = 1$. This allows us to seek the coefficients of the $(u-v)$ transformation in the form $u = \cos(\Theta/2)$ and $v = \sin(\Theta/2)e^{i\chi}$. From the conditions that terms nondiagonal in α and β in the transformed Hamiltonian are zero, we find that

$$\sin\Theta = \frac{J|\Delta|}{\sqrt{\tilde{\varepsilon}^2 + (J|\Delta|)^2}}, \quad \cos\Theta = \frac{\tilde{\varepsilon}}{\sqrt{\tilde{\varepsilon}^2 + (J|\Delta|)^2}}, \tag{13}$$

and that χ coincides with the phase φ of the order parameter. Here we have introduced the notation $\tilde{\varepsilon} = (\varepsilon_1 - \varepsilon_2)/2$.

Using Eqs. (12) and (13), we obtain the following self-consistency equations:

$$\nu_1 + \nu_2 = 1 = \langle a_1^+ a_1\rangle + \langle a_2^+ a_2\rangle = 1 + N_F(\mathcal{E}_\alpha) - N_F(\mathcal{E}_\beta), \tag{14}$$

$$2\tilde{\nu} = \langle a_1^+ a_1\rangle - \langle a_2^+ a_2\rangle = -\frac{\tilde{\varepsilon}}{\sqrt{\tilde{\varepsilon}^2 + (J|\Delta|)^2}}$$
$$\times [1 - N_F(\mathcal{E}_\alpha) - N_F(\mathcal{E}_\beta)], \tag{15}$$

$$\Delta = \langle a_2^+ a_1\rangle = \frac{J\Delta}{2\sqrt{\tilde{\varepsilon}^2 + (J|\Delta|)^2}}[1 - N_F(\mathcal{E}_\alpha) - N_F(\mathcal{E}_\beta)], \tag{16}$$

where

$$\mathcal{E}_{\alpha(\beta)} = \sqrt{\tilde{\varepsilon}^2 + (J|\Delta|)^2} \pm \frac{\varepsilon_1 + \varepsilon_2}{2} \tag{17}$$

is the energy of elementary excitations and $N_F(\mathcal{E}) = [\exp(\mathcal{E}/T) + 1]^{-1}$ is a the Fermi distribution function. It follows from Eq. (14) that $\mathcal{E}_\alpha = \mathcal{E}_\beta$, which leads to the condition $\varepsilon_1 + \varepsilon_2 = 0$. From Eqs. (15) and (16) we easily find the dependence of the modulus of the order parameter on the value of the imbalance and temperature. Below we shall restrict consideration to the case of zero temperatures, where this dependence has the form

$$|\Delta(\tilde{\nu})| = \sqrt{\frac{1}{4} - \tilde{\nu}^2}. \tag{18}$$

The differential of the free energy of a two-layer system for $\nu_1 + \nu_2 = 1$ and $T=0$ is equal to

$$dF = \mu_1 d\nu_1 + \mu_2 d\nu_2 = 2\tilde{\mu}d\tilde{\nu}, \tag{19}$$

where we have introduced the notation $\tilde{\mu} = (\mu_1 - \mu_2)/2$. Here and below the energy per electron is given. If the explicit form of the function $\tilde{\mu}(\tilde{\nu})$ is known, then, by using (19), one can easily find the energy of the system at a specified value of the imbalance:

$$F(\tilde{\nu})=F(-1/2)+2\int_{-1/2}^{\tilde{\nu}}d\tilde{\nu}'\tilde{\mu}(\tilde{\nu}'), \qquad (20)$$

where $F(-1/2)$ is the energy of the system for $\tilde{\nu}=-1/2$, i.e., for $\nu_1=0$ and $\nu_2=1$. At such values of the filling factors the energy of the system is the sum of the energies of the direct Coulomb interaction between layers and the intralayer exchange interaction in layer 2, i.e., $F(-1/2)=W/4-I/2$. Using Eq. (7) and the relation $\tilde{\varepsilon}=-J\tilde{\nu}$ (which follows from Eqs. (15) and (16)), we find the following expression for $\tilde{\mu}$:

$$\tilde{\mu}(\tilde{\nu})=(W-I+J)\tilde{\nu}.$$

Accordingly,

$$F(\tilde{\nu})=-\frac{I+J}{4}+(W-I+J)\tilde{\nu}^2. \qquad (21)$$

It is also useful to write expression (21) in the form

$$F=W\tilde{\nu}^2-\frac{I}{2}[\nu_1^2+(1-\nu_1)^2]-J|\Delta|^2, \qquad (22)$$

from which the physical meaning of each of the terms becomes obvious. The first term is the energy of the direct Coulomb interaction at a filling factor imbalance of $\tilde{\nu}$. The second term is the sum of the energies of the intralayer exchange interaction in layers 1 and 2. The third term is the energy due to the appearance of interlayer phase coherence.

Since energy (22) is independent of the phase φ of the order parameter, the interlayer phase coherence is of a spontaneous character. The minimum energy of a state with interlayer phase coherence is reached in the case when the modulus and phase of the order parameter are independent of the coordinate. The superfluid current state that arises at nonzero gradients of the phase lies higher in energy, but in the case when the gradient of the phase is less than a critical value (which depends on the ratio d/l_B), such a state is stable against the onset of elementary excitations that lead to energy dissipation (i.e., the Landau criterion of superfluidity is satisfied).

In concluding this Section we turn our attention to an important conclusion that follows from formula (21). Using Eqs. (9)–(11), we easily see that the coefficient of the $\tilde{\nu}^2$ term on the right-hand side of (21) is positive for arbitrary $d\neq0$. This plays a fundamental role from the standpoint of the possibility of realizing the state with interlayer phase coherence in two-layer systems. Indeed, if the sign of the expression $W-I+J$ were negative, then the system would go to a state with a maximum imbalance of the filling factors, $\tilde{\nu}=\pm1/2$, for which $|\Delta|=0$ (see Eq. (18)) and, consequently, interlayer phase coherence is absent. Skipping ahead, we note that in multilayer systems, in contrast, such a mechanism of destroying the phase coherence can indeed be realized in a certain range of d values. A detailed analysis of this question is the subject of Sec. 4.

3. STATES WITH INTERLAYER PHASE COHERENCE IN A MULTILAYER SYSTEM

Let us consider a system with the number of layers $N\to\infty$ and with an average filling factor per layer equal to 1/2. The Hamiltonian of such a system can be written in the form

(3) with the sum over two layers in it replaced by a sum over an infinite number of layers. Going to the mean field approximation, we have

$$H_{MF}=\sum_n\sum_X\left\{\varepsilon_n a_n^+ a_n\right.$$
$$\left.-\frac{1}{2}\sum_{m\neq0}[J_m\Delta(n,m)a_n^+ a_{n+m}+\text{h.c.}]\right\}, \qquad (23)$$

where the energy parameters J_m are equal to

$$J_m=\sqrt{\frac{\pi}{2}}\frac{e^2}{\varepsilon l_B}\exp\left(\frac{d^2m^2}{2l_B^2}\right)\text{erfc}\left(\frac{d|m|}{l_B\sqrt{2}}\right) \qquad (24)$$

(the parameter J introduced in the previous Section coincides with $J_{\pm1}$) and the order parameters are defined as

$$\Delta(n,m)=\langle a_{n+m}^+ a_n\rangle. \qquad (25)$$

In the general case the quantities $\Delta(n,m)$ can be nonzero for arbitrary m and not only for $m=\pm1$. This corresponds to the situation when a correlation arises in the system between the electrons not only of adjacent layers but also in layers arbitrarily far apart. Since the Coulomb potential is long-ranged, such correlations carry an appreciable contribution to the energy, and it is important to take them into account when finding the ground state of the system.

It is natural to expect from physical considerations that if a imbalance of the filling factors should arise in such a system it will have a periodic character. Let us consider the situation when the period does not exceed twice the distance between adjacent layers. As will be shown below, period doubling can arise in the system even in the absence of imbalance of the filling factors when a state with interlayer phase coherence of the dimer type is realized in the system.

Let the filling factors of the layers be equal to $\nu_n=1/2+(-1)^n\tilde{\nu}$. In this case the quantity $\tilde{\nu}$ can be treated as a charge-ordering parameter. Proceeding from the assumption of periodicity of the system, we seek the order parameter $\Delta(n,m)$ in the form

$$\Delta(n,m)=\Delta_1(m)+(-1)^n\Delta_2(m). \qquad (26)$$

In the general case the quantities $\Delta_{1(2)}(m)$ can be complex valued, i.e., they can contain phase factors $e^{i\varphi_{1(2)}(m)}$. The phase factors can no longer be specified independently, since the self-consistent equations impose certain conditions on the phase difference $\varphi_{1(2)}(m)$. However, these conditions do not fix all of the phases, and a certain arbitrariness in the choice of the quantities $\varphi_{1(2)}(m)$ remains. It can be shown that the energy of the system is independent of the phases of the order parameters if the latter satisfy the self-consistency equations (we stress that we are considering the case when the modulus and phase of the order parameter are independent of X). The arbitrariness in the choice of phases is a reflection of the fact that the phase coherence is spontaneous. In connection with what we have said, for finding the ground state of the system we can restrict consideration to the simplest case for analysis, when all the phases are equal to zero, i.e., the quantities $\Delta_1(m)$ and $\Delta_2(m)$ are real valued.

Transforming in Eq. (23) to the Fourier components of the operators a_n

$$a_n = \frac{1}{\sqrt{N}} \sum_{q_z} e^{i q_z n} a_{q_z}, \tag{27}$$

we obtain the following expression for the Hamiltonian of the system:

$$H_{MF} = \sum_X \sum_{q_z} \{ [\varepsilon - \Delta_1(q_z)] a_{q_z}^+ a_{q_z} + [\tilde{\varepsilon} - \Delta_{2r}(q_z)]$$
$$- i \Delta_{2i}(q_z)] a_{q_z + \pi}^+ a_{q_z} \}. \tag{28}$$

Here we have introduced the notation $\varepsilon = (\varepsilon_{2k} + \varepsilon_{2k-1})/2$, $\tilde{\varepsilon} = (\varepsilon_{2k} - \varepsilon_{2k-1})/2$. The quantities ε and $\tilde{\varepsilon}$ in view of the assumed periodicity in z are independent of k. The functions $\Delta_1(q_z)$ and $\Delta_{2r(i)}(q_z)$ in (28) are defined as

$$\Delta_1(q_z) = 2 \sum_{m=1}^{\infty} J_m \Delta_1(m) \cos(m q_z), \tag{29}$$

$$\Delta_{2r}(q_z) = 2 \sum_{m=1}^{\infty} J_{2m} \Delta_2(2m) \cos(2 m q_z), \tag{30}$$

$$\Delta_{2i}(q_z) = 2 \sum_{m=1}^{\infty} J_{2m+1} \Delta_2(2m+1) \sin[(2m+1) q_z]. \tag{31}$$

Diagonalizing the Hamiltonian (28) and calculating the averages of (26), we arrive at the self-consistency conditions for the order parameters. Let us give these equations for the case $T=0$:

$$\tilde{\nu} = -\frac{1}{2\pi} \int_{-\pi/2}^{\pi/2} dq_z \frac{\tilde{\varepsilon} - \Delta_{2r}(q_z)}{E(q_z)}, \tag{32}$$

$$\Delta_1(2m) = 0, \tag{33}$$

$$\Delta_1(2m+1) = \frac{1}{2\pi} \int_{-\pi/2}^{\pi/2} dq_z \frac{\cos[(2m+1) q_z] \Delta_1(q_z)}{E(q_z)}, \tag{34}$$

$$\Delta_2(2m) = -\frac{1}{2\pi} \int_{-\pi/2}^{\pi/2} dq_z \frac{\cos(2 m q_z)[\tilde{\varepsilon} - \Delta_{2r}(q_z)]}{E(q_z)}, \tag{35}$$

$$\Delta_2(2m+1) = \frac{1}{2\pi} \int_{-\pi/2}^{\pi/2} dq_z \frac{\sin[(2m+1) q_z] \Delta_{2i}(q_z)}{E(q_z)}. \tag{36}$$

In equations (32) and (34)–(36) the spectrum of energies of elementary excitations $E(q_z)$ is determined by the following relation:

$$E(q_z) = \sqrt{[\tilde{\varepsilon} - \Delta_{2r}(q_z)]^2 + \Delta_1^2(q_z) + \Delta_{2i}^2(q_z)}. \tag{37}$$

As we see from the self-consistency conditions, a state with global phase coherence can be realized in the system. The state considered in Ref. 25 corresponds to the case when all the quantities $\Delta_2(2m+1)$ are identically zero (in which case Eq. (36) is satisfied automatically) but $\Delta_1(2m+1) \neq 0$ for arbitrarily large m. This means that phase coherence is established between all layers.

However, it is easy to see that the self-consistency conditions (32)–(36) are also satisfied by a solution of an essentially different type: $\Delta_1(\pm 1) = \pm \Delta_2(\pm 1) \neq 0$ and $\Delta_1(m)$

$= \Delta_2(m) = 0$ for $m \neq \pm 1$. In this case $\Delta(2k,1) = \Delta(2k+1, -1) \neq 0$ (or $\Delta(2k-1,1) = \Delta(2k,-1) \neq 0$, and all the remaining $\Delta(n,m)$ are zero. In the state corresponding to such a solution, the system separates into pairs of layers, and the interlayer phase coherence is established only within each pair. Such a state will be called a dimer state.

Writing the differential of the free energy of a multilayer system and integrating it over $\tilde{\nu}$, we obtain an expression for the free energy at arbitrary values of the order parameters satisfying Eqs. (32)–(36). The energy we seek has the form

$$F(\tilde{\nu}) = V_c(\tilde{\nu}) - I\left(\frac{1}{4} + \tilde{\nu}^2\right) - 2 \sum_{m=1}^{\infty} J_m[\Delta_1^2(m) + \Delta_2^2(m)], \tag{38}$$

where the first term $V_c(\tilde{\nu})$ corresponds to the energy of the direct Coulomb interaction, which is independent of the concrete form of $\Delta_{1(2)}(m)$.

Using the answer (38), let us compare the energies of the state with global phase coherence and of the dimer state for $\tilde{\nu} = 0$. In this case Eqs. (32)–(36) give the following expressions for the order parameters $\Delta_{1,2}(m)$. For a state with global coherence we have

$$\Delta_1(m) = \frac{\sin(\pi m/2)}{m\pi}, \quad \Delta_2(m) = 0. \tag{39}$$

For a dimer state $\Delta_1(m) = \pm \Delta_2(m) = \delta_{1,|m|}/4$. Consequently, the energy difference of the dimer state and the state with global phase coherence satisfies the condition

$$F_d - F_g = -\frac{J_1}{4} + \frac{2}{\pi^2} \sum_{k=0}^{\infty} J_{2k+1} \frac{1}{(2k+1)^2} \leqslant -\frac{J_1}{4}$$

$$\times \left(1 - \frac{8}{\pi^2} \sum_{k=0}^{\infty} \frac{1}{(2k+1)^2}\right) = 0. \tag{40}$$

In deriving Eq. (40) it was taken into account that for $d \neq 0$ the parameters J_m fall off with increasing m. For $d=0$, when all the J_m are identical, the energies of the two states under consideration are equal. A numerical analysis of the self-consistency equations shows that the inequality $F_d < F_g$ holds for arbitrary values of $\tilde{\nu}$ and $d \neq 0$. Since the energy of the state with global phase coherence is higher than the energy of the dimer state, it is the dimer state and not the state considered in Ref. 25 that should be regarded as a possible candidate for the ground state of the system.

4. COMPARISON OF THE ENERGIES OF THE DIMER AND CHARGE-ORDERED STATES

Let us now consider the question of the stability of the dimer state in a multilayer system with even number of layers against a transition to a charge-ordered state. For this we find the explicit form of the energy of the direct Coulomb interaction $V_c(\tilde{\nu})$. This energy is equal to the energy of the electric field induced inside the superlattice by the charged electron layers (since the system on the whole remains electrically neutral, the electric field outside the superlattice is equal to zero).

If the filling factors of the layers were equal to $\nu_{2k-1} = 1/2 - \tilde{\nu}$, $\nu_{2k} = 1/2 + \tilde{\nu}$ ($k = 1, 2, ..., N/2$), the electric field would be nonzero between layers 1 and 2, 3 and 4, 5 and 6,

etc., while between layers 2 and 3, 4 and 5, etc. it should be zero. Accordingly, the electric field energy per electron, as in the two-layer system, would be equal to $V_c = W\tilde{\nu}^2$. However, in contrast to the two-layer system, in a multilayer system one can achieve a substantial benefit in the energy of the direct Coulomb interaction by changing the filling factors of only the two outer layers. Indeed, if the filling factors of the outer layers were to take the values $\nu_1 = 1/2 - \tilde{\nu}/2$ and $\nu_N = 1/2 + \tilde{\nu}/2$, then an electric field would be induced between all the layers, and its absolute value would be smaller by a factor of two than in the previous case (the direction of the field would change sign on crossing a layer). Consequently, the energy V_c per electron will be half as large (to an accuracy of $1/N$) as in the two-layer system. For $N \to \infty$ the total energy would be

$$F = -\frac{I+J}{4} + \left(\frac{W}{2} - I + J\right)\tilde{\nu}^2. \tag{41}$$

In deriving Eq. (41) we took into account that in the dimer state the order parameter $\Delta = 2\Delta_{1(2)}$ has the same dependence on $\tilde{\nu}$ as in the two-layer system (Eq. (18)).

In contrast to Eq. (21), the sign of the coefficient of the $\tilde{\nu}^2$ term in Eq. (41) depends on d: for $d < 1.45 l_B$ this coefficient is negative, while at larger d it is positive. Consequently, for $d < 1.45 l_B$ and $N \to \infty$ the minimum energy will correspond to the state with the maximum charge ordering, in which all the $\Delta(n,m)$ go to zero and phase coherence is absent. In the case $d > 1.45 l_B$ the minimum of energy (41) is reached for $\tilde{\nu} = 0$, i.e., charge ordering becomes energetically unfavorable.

The above analysis is easily generalized to the case of finite, even values of N. Let us consider the configuration when the inner layers are found in a completely or partially charge-ordered state, and for these layers the imbalance of the filling factors is equal to $\tilde{\nu}_{in}$. The imbalance of the filling factor of the outer layers will be described by the parameter $\tilde{\nu}_{ex} = (\nu_N - \nu_1)/2$. We shall assume that phase coherence is established only between the inner layers and has the dimer character. The energy (per electron) of such a state is equal to

$$F(\tilde{\nu}_{ex}, \tilde{\nu}_{in}) = W\left[\tilde{\nu}_{ex}^2 + \frac{N-2}{N}(\tilde{\nu}_{in} - \tilde{\nu}_{ex})^2\right]$$
$$- I\left[\frac{N-2}{N}\left(\frac{1}{4} + \tilde{\nu}_{in}^2\right) + \frac{2}{N}\left(\frac{1}{4} + \tilde{\nu}_{ex}^2\right)\right]$$
$$- J\frac{N-2}{N}\left(\frac{1}{4} - \tilde{\nu}_{in}^2\right). \tag{42}$$

Because the function $F(\tilde{\nu}_{ex}, \tilde{\nu}_{in})$ has an extremum (or saddle point) only for $\tilde{\nu}_{ex} = \tilde{\nu}_{in} = 0$, its minimum value can be reached either at the point of the extremum or at the edge of the region of allowed values of $\tilde{\nu}_{ex}$, $\tilde{\nu}_{in}$ (when $|\tilde{\nu}_{in}| = 1/2$, $|\tilde{\nu}_{ex}| \leq 1/2$ or $|\tilde{\nu}_{ex}| = 1/2$, $|\tilde{\nu}_{in}| \leq 1/2$). Therefore, for determining the stability region of the dimer phase it is sufficient for us to find the minimum value of expression (42) at the edge of the allowed region and compare it to the energy of the dimer phase in the absence of charge ordering, $F_d = -(I+J)/4$.
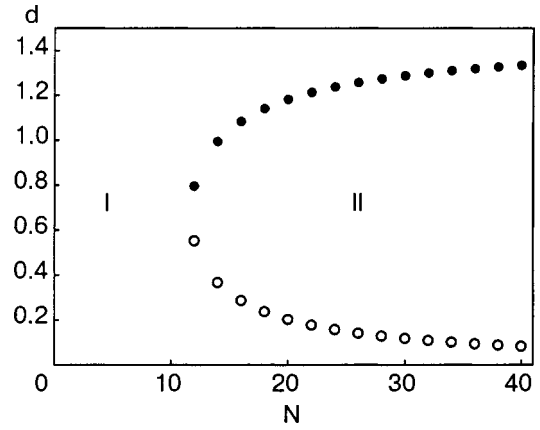

FIG. 1. Existence regions of the dimer (I) and charge-ordered (II) states. d_{c1} ($\bigcirc$), d_{c2} ($\bullet$) as functions of the number of layers N. The interlayer distance d is given in units of the magnetic length l_B.

If $WN < 2I$ the minimum of expression (42) at the edge of the allowed region is reached for $\tilde{\nu}_{in} = \tilde{\nu}_{ex} = \pm 1/2$ and $F(\pm 1/2, \pm 1/2) = W/4 - I/2 > F_d$.

Under conditions such that the opposite inequality holds, $WN > 2I$, the minimum is reached at the points

$$\tilde{\nu}_{ex} = \pm\frac{1}{4}\frac{N-2}{N-1-I/W}, \quad \tilde{\nu}_{in} = \pm\frac{1}{2}, \tag{43}$$

where the value of the energy is equal to

$$\frac{I}{2N} - \frac{I}{2} + \frac{W(WN-2I)(N-2)}{2N(WN+I-W)}. \tag{44}$$

We note that, in particular, it follows from (43) that $\tilde{\nu}_{ex} = \tilde{\nu}_{in}/2 = 1/4$ for $N \to \infty$.

The value of expression (44) can be larger or smaller than F_d. Therefore, in the general case, there is a region of instability of the dimer phase in the space of parameters (d, N), determined by the system of inequalities

$$\frac{I}{2N} - \frac{I-J}{4} + \frac{W(WN-2I)(N-2)}{2N(WN+I-W)} < 0, \quad WN > 2I. \tag{45}$$

A numerical analysis shows that for $N \leq 10$ the system of inequalities (45) is not satisfied for any d. It follows that in a multilayer system in which the number of layers is even and equal to 10 or less the dimer state is stable against transition to the charge-ordered phase at any values of d.

For $N > 10$ condition (45) holds in a region $d_{c1} < d < d_{c2}$. In this region of parameters there will be complete charge ordering of the inner layers and no phase coherence between those layers. The dependence of d_{c1} and d_{c2} on N is shown in Fig. 1. For $N \to \infty$ the domain of values d for which the dimer state can exist is restricted by the condition $d > 1.45 l_B$ ($\lim_{N \to \infty} d_{c1}(N) = 0$). However, even at large but finite N there exists a region of small d ($d \lesssim l_B\sqrt{2\pi/N}$) in which the formation of the dimer state is possible.

It was shown in Ref. 25 that a factor that opposes charge ordering in multilayer systems is interlayer tunneling. Based on a comparison of the energy of the system for $\tilde{\nu} = 0$ and $\tilde{\nu} = \pm 1/2$ the authors of that paper arrived at the conclusion that in the case when the tunneling parameter t exceeds a

value $0.05e^2/\varepsilon l_B$ the charge ordering becomes energetically unfavorable for any values of the parameter d/l_B.

In the presence of tunneling between layers the polarization coherence is no longer spontaneous, since tunneling leads to fixing of the phase of the order parameter. In that case the superfluid state with a constant phase gradient cannot be realized, but superfluidity of a ''soliton'' type can exist.[16,26,27] According to the results of Ref. 16, for $t \gtrsim 0.01e^2/\varepsilon l_B$ such a state will be unstable with respect to the onset of normal excitations leading to energy dissipation. Therefore, from the standpoint of realization of the superfluid state in multilayer systems, tunneling plays more of a negative than a positive role.

On the contrary, the use of multilayer systems with parameters lying in the stability region of the dimer state (Fig. 1) and with a small value of the tunneling is more promising.

CONCLUSION

Thus we have shown that a state with spontaneous interlayer phase coherence can be realized in multilayer quantum Hall systems in a certain range of parameters. The phase coherence in such systems has a two-dimensional rather than a three-dimensional character; specifically, the system separates into pairs of adjacent layers, and coherence is established only within each pair, and coherence is absent between electrons belonging to different pairs.

If the number of layers $N \leq 10$, then for an arbitrary distance between layers the state with spontaneous interlayer phase coherence is stable against transition to a charge-ordered phase. If the number of layers $N > 10$, the state with spontaneous phase coherence is stable only for sufficiently small or sufficiently large distances between layers. In the intermediate region of interlayer distances in a system with more than 10 layers a transition occurs to a charge-ordered state in which interlayer phase coherence is absent.

Since the phase coherence has a two-dimensional character, the superfluidity of the electron–hole pairs will also be two-dimensional. A multilayer quantum Hall system can therefore be considered to be a solid-state analog of ultracold atomic Bose gases in optical superlattices (see, e.g., Ref. 28). Among the interesting effects that can be observed in such systems, in particular, is the nondissipative interlayer dragging of superfluid flow.[29–31]

[*]E-mail: shevchenko@ilt.kharkov.ua

[1] Yu. E. Lozovik and V. I. Yudson, Zh. Éksp. Teor. Fiz. **71**, 738 (1976) [Sov. Phys. JETP **44**, 389 (1976)].

[2] S. I. Shevchenko, Fiz. Nizk. Temp. **2**, 505 (1976) [Sov. J. Low Temp. Phys. **2**, 251 (1976)].

[3] I. O. Kulik and S. I. Shevchenko, Fiz. Nizk. Temp. **2**, 1405 (1976) [Sov. J. Low Temp. Phys. **2**, 687 (1976)].

[4] S. I. Shevchenko, Phys. Rev. Lett. **72**, 3242 (1994).

[5] Y. Kuramoto and C. Horie, Solid State Commun. **25**, 713 (1978).

[6] D. Paquet, T. M. Rice, and K. Ueda, Phys. Rev. B **32**, 5208 (1985).

[7] D. Yoshioka and A. H. MacDonald, J. Phys. Soc. Jpn. **59**, 4211 (1990).

[8] S. I. Shevchenko, Phys. Rev. B **57**, 14809 (1998).

[9] S. I. Shevchenko, Phys. Rev. B **67**, 214515 (2003).

[10] K. Moon, H. Mori, K. Yang, S. M. Girvin, A. H. MacDonald, L. Zheong, D. Yoshioka, and S. C. Zhang, Phys. Rev. B **51**, 5138 (1995).

[11] H. A. Fertig, Phys. Rev. B **40**, 1087 (1989).

[12] A. H. MacDonald and E. H. Rezayi, Phys. Rev. B **42**, 3224 (1990).

[13] R. Cote, L. Brey, and A. H. MacDonald, Phys. Rev. B **46**, 10239 (1992).

[14] X. G. Wen and A. Zee, Phys. Rev. Lett. **69**, 1811 (1992).

[15] K. Yang, Phys. Rev. Lett. **87**, 056802 (2001).

[16] M. Abolfath, A. H. MacDonald, and L. Radzihovsky, Phys. Rev. B **68**, 155318 (2003).

[17] I. B. Spielman, J. P. Eisenstein, L. N. Pfeiffer, and K. W. West, Phys. Rev. Lett. **84**, 5808 (2000).

[18] I. B. Spielman, J. P. Eisenstein, L. N. Pfeiffer, and K. W. West, Phys. Rev. Lett. **87**, 036803 (2001).

[19] M. Kellogg, I. B. Spielman, J. P. Eisenstein, L. N. Pfeiffer, and K. W. West, Phys. Rev. Lett. **88**, 126804 (2002).

[20] A. A. Dremin, V. B. Timofeev, A. V. Larionov, J. Hvam, and K. Soerensen, JETP Lett. **76**, 450 (2002).

[21] H. L. Stormer, J. P Eisenstein, A. C. Gossard, W. Wiegmann, and K. Baldwin, Phys. Rev. Lett. **56**, 85 (1986).

[22] J. Jo, M. Santos, M. Shayegan, Y. W. Suen, L. W. Engel, and A. M. Lanzinotto, Appl. Phys. Lett. **57**, 2130 (1990).

[23] D. P. Druist, P. J. Turley, K. D. Maranowski, E. G. Gwinn, and A. C. Gossard, Phys. Rev. Lett. **80**, 365 (1998).

[24] V. A. Bezugly and S. I. Shevchenko, Physica B **284−288**, 1205 (2000).

[25] C. B. Hanna, J. C. Diaz-Velez, and A. H. MacDonald, Phys. Rev. B **65**, 115323 (2002).

[26] S. I. Shevchenko, Fiz. Nizk. Temp. **3**, 605 (1977) [Sov. J. Low Temp. Phys. **3**, 293 (1977)].

[27] T. Iida and M. Tsubota, Phys. Rev. B **60**, 5802 (1999).

[28] O. Morsch and E. Arimondo, ''Ultracold atoms and Bose-Einstein condensates in optical lattices,'' in *Dynamics and Thermodynamics of Systems with Long Range Interactions*, edited by T. Dauxois, S. Ruffo, E. Arimondo, and M. Wilkens, Vol. 602 of Lecture Notes in Physics, Springer (2002) (also available as cond-mat/0209034).

[29] B. Tanatar and A. K. Das, Phys. Rev. B **54**, 13827 (1996).

[30] S. V. Terentjev and S. I. Shevchenko, Fiz. Nizk. Temp. **25**, 664 (1999) [Low Temp. Phys. **25**, 493 (1999)].

[31] D. V. Fil and S. I. Shevchenko, cond-mat/0305290.

Translated by Steve Torstveit

Low-temperature anomalies of the mobility and Shubnikov–de Haas oscillations due to electron resonance scattering on donor impurities in semiconductors. Explanation based on the Friedel approach

V. I. Okulov,* L. D. Sabirzyanova, and K. S. Sazonova

Institute of Metal Physics, Urals Branch of the Russian Academy of Sciences, ul. S. Kovalevskoĭ 18, Ekaterinburg 620219, Russia

S. Yu. Paranchich

Chernovtsy National University, ul. Kotsyubinskogo 2, Chernovtsy 58012, Ukraine

Manifestations of electron resonance scattering by donor impurities in the low-temperature conductivity of semiconductors are investigated in the case when the donor resonance energy level of the impurities lies in the conduction band. It is shown that the application of resonance scattering theory in the framework of the Friedel approach can explain the stabilization of the electron density, the maximum of the electron mobility, and the minimum of the Dingle temperature as a function of the concentration of donor impurities and also the anomalous temperature dependence of the mobility due to the resonance. New experimental data are obtained on the concentration, mobility, and Dingle temperature of electrons in mercury selenide crystals containing iron impurities, and it is found that these new results, like those known previously, are in complete agreement with the behavior predicted in the proposed approach. The relation of this approach to the previous interpretation of the concentration maximum of the mobility is discussed, and arguments for its applicability are presented. © *2004 American Institute of Physics.* [DOI: 10.1063/1.1705441]

INTRODUCTION

One of the interesting and complex problems of the physics of the electronic properties of semiconductors involves the interpretation of the manifestations of the energy levels of donor impurities in the conduction band. According to the existing ideas, the interaction of the conduction electrons with impurity ions at energies close to the energy of a donor level is of a resonance character and is described by the quantum theory of resonance scattering. Effects due to manifestations of such resonances become appreciable at low temperatures, when, with increasing impurity concentration, the Fermi energy reaches the energy of an impurity level. With further increase in impurity concentration the Fermi energy and the electron density stabilize, i.e., remain almost unchanged with increasing donor concentration. The behavioral regularities observed under such conditions are in many ways still poorly understood. This is particularly true of the gapless semiconductor systems containing impurities of transition elements. Among such systems, mercury selenide containing iron impurities has attracted the most attention; the maximum of the electron mobility as a function of impurity concentration has been investigated in this system, and other unusual effects due to the influence of the iron ions have been observed.[1,2] Investigators working on an explanation of the observed anomalies have disregarded the possibility of explaining them as being a direct manifestation of resonance scattering of electrons, assuming that the latter can only to a decrease of the mobility. For this reason they have used models based on the hypothesis of the existence of bound states

of electrons on the impurity ions and the existence of spatial ordering of the latter.[3,4] However, it is difficult to justify such an assumption for systems in which the impurity states are strongly coupled with conducting states. At the same time, it should be kept in mind that under conditions of stabilization of the electron density with increasing number of impurities the effective charge of an individual impurity decreases, and this can lead to a maximum of the mobility.[5] Thus it is a topical problem to carry out a detailed study of the electron resonance scattering effects under conditions of stabilization of the electron density in a semiconductor containing donor impurities. That is the task of the present study. Based on the theory of resonance scattering in the framework of the Friedel approach a description is given for the stabilization of the electron density, and the predictions as to the concentration and temperature dependence of the electron mobility that follow from well-known theoretical ideas are clarified. Then our new experimental data on the concentration and temperature dependences of the electron mobility and of the Dingle temperature in the Shubnikov–de Haas oscillations for mercury selenide containing iron impurities are presented, and the agreement of the data with the theoretical predictions is demonstrated.

STABILIZATION OF THE ELECTRON DENSITY AND MOBILITY DUE TO RESONANCE SCATTERING

Consider a lightly doped semiconductor with singly ionized impurities having resonance energy levels ε_d in the conduction band. The mean electron density $n(\varepsilon)$ as a function of the electron energy ε can be written as the following sum:

$$n(\varepsilon) = n_e(\varepsilon) + n_i z(\varepsilon), \tag{1}$$

which contains the electron density in the conduction band $n_e(\varepsilon)$ and a term that is proportional to the impurity concentrations n_i and describes the contribution of the electron density localized on the impurities. Adopting an isotropic model for the energy spectrum of the electrons and the scattering potential, we can express the function $z(\varepsilon)$ as a linear combination of the scattering phases for definite values of the orbital angular momentum.[6] Far from resonance, at low energies ($\varepsilon \ll \varepsilon_d$) the function $z(\varepsilon)$ equals zero, since there is no localized contribution to $n(\varepsilon)$, while at high energies ($\varepsilon \gg \varepsilon_d$) the localized contribution to $n(\varepsilon)$ is close to maximum and the value of $z(\varepsilon)$ is close to unity. These conditions lead to the well-known Friedel sum rules for the scattering phases.[6] Near the resonance the function $z(\varepsilon)$ is expressed in terms of the resonant scattering phase $\delta_d(\varepsilon)$ and has the following form:

$$z(\varepsilon) = (1/\pi)\delta_d(\varepsilon) = 1/2 + (1/\pi)\arctan[(\varepsilon - \varepsilon_d)/\Delta],$$

$$|\varepsilon - \varepsilon_d| \lesssim \Delta, \tag{2}$$

where Δ is the width of the resonance, which is small compared to ε_d. The influence of the resonance is manifested in the mean free path $\Lambda(\varepsilon)$, which is expressed in a known way in terms of the scattering phase. In the vicinity of the resonance the nonresonant phases are small compared to the resonant phase, and one can obtain the following simple formula for $\Lambda^{-1}(\varepsilon)$:

$$\Lambda^{-1}(\varepsilon) = \Lambda_m^{-1}[a + \sin^2(\delta_d(\varepsilon) - \varphi)], \tag{3}$$

where the parameters Λ_m, a, and φ are practically unchanged with energy over an interval of the order of Δ. The small constants a and φ describe the contributions of the nonresonant phases, and the phase φ reflects the difference of the transport relaxation time from the lifetime of the electronic state. In determining the Dingle temperature one should set $\varphi = 0$ in the formula analogous to (3) and take into account the possible difference of the constant a.

Considering the ground state (the temperature $T = 0$ and the energy ε is equal to the Fermi energy ε_F) and assuming that all the electrons originate from the donors under consideration, we should set $n(\varepsilon_F) = n_i$ in Eq. (1). Then the density of conduction electrons $n_e(\varepsilon_F)$ depends on the relationship of the Fermi energy ε_F to the resonance energy ε_d. Far from the resonance, at $\varepsilon_F \ll \varepsilon_d$ the usual equality of the number of electrons to the number of donors is valid. As the concentration of impurities is increased, the equality $\varepsilon_F = \varepsilon_d$ comes to hold, whereupon we have $z(\varepsilon_F) = 1/2$ in formula (1), so that $n_i = 2n_e(\varepsilon_d)$. The resonant values of the Fermi energy ε_d and conduction electron density $n_e(\varepsilon_d) = n_0$ differ little from the limiting values to which the values of ε_F and $n_e(\varepsilon_F)$ slowly tend with further increase in donor concentration. Thus the equation

$$n_i = n_e(\varepsilon_F) + n_i \delta_d(\varepsilon_F)/\pi \tag{4}$$

describes an effect in the which the electron density and Fermi energy are stabilized with increasing concentration of donor impurities above the value $2n_0$.

Within the domain of applicability of formula (2) in the vicinity of a resonance, one can set $n_e(\varepsilon_F) \approx n_0$ in formula

(4), and the resonant phase is equal to $\pi(1 - n_0/n_i)$. Using this and formula (3), we can obtain the electron mobility $\mu(T)$ at $T = 0$ in the following form:

$$\mu(0) = \mu_0(2n_0/n_i)[a + \sin^2(\pi n_0/n_i + \varphi)]^{-1}. \tag{5}$$

This expression describes a concentration dependence of the mobility having a minimum near the resonance $n_i \approx 2n_0$ (a value close to the constant μ_0) and a maximum at substantially larger values of the impurity concentration. Because the position of the maximum and the value of the mobility at the maximum are slowly varying functions of the parameters a and φ and variation of the parameter φ does not lead to any qualitative features, the inverse lifetime of the electronic states will have a similar dependence.

The temperature dependence of the mobility $\mu(T)$ in the region of stabilization of the electron density at low temperatures is described by the following formula:

$$\mu(T)/\mu(0) = \int d\varepsilon [\Lambda(\varepsilon)/\Lambda(\varepsilon_F)](-\partial f/\partial \varepsilon), \tag{6}$$

where f is the Fermi function, and the integration region is restricted to a neighborhood of the resonance in which the formulas (3)–(5) given above are valid. A characteristic feature of the given temperature dependence is that the mobility near the concentration maximum goes to a constant value $\mu(0)$ at a significantly lower temperature than does the mobility outside the maximum. The scale of the dropoff of the mobility with increasing temperature is mainly determined by the parameter $\Delta(\Lambda_m/\Lambda(\varepsilon_F))$. Such behavior of the mobility and the concentration maximum itself are among the main effects of electron resonance scattering on donor impurities.

EXPERIMENTAL DATA FOR MERCURY SELENIDE CONTAINING IRON IMPURITIES

The behavioral regularities which, as was shown above, are predicted by the theory of resonance scattering are known and have been observed in mercury selenide crystals containing iron impurities. The experimental data have been set forth in detail and discussed in review articles.[1,2] For a quantitative comparison of the experimental data with the theoretical predictions we have made new measurements of the electron density and Hall mobility and the Dingle temperature of the Shubnikov oscillations in HgSe:Fe crystals with different concentrations of iron impurity atoms. The measurements were made and the samples prepared by the techniques described in previous papers cited in Ref. 2. The results obtained are presented in Figs. 1–4.

Figure 1 shows the data on the electron density in the vicinity of the limiting value $n_0 = 4.6 \times 10^{18}$ cm^{-3}, which practically coincides with the value obtained in a number of studies cited in Refs. 1 and 2. The fitting curve was constructed according to formula (1) for $\varepsilon = \varepsilon_F$, $n(\varepsilon_F) = n_i$ with expression (2) taken into account, and it corresponds to $\Delta = 3$ K.

The data on the concentration dependence and temperature dependence of the mobility, given in Figs. 2 and 3, are also in good agreement with the previously known data. Their fitting by curves constructed according to formulas (3)–(6) was done with a single set of parameters which in-
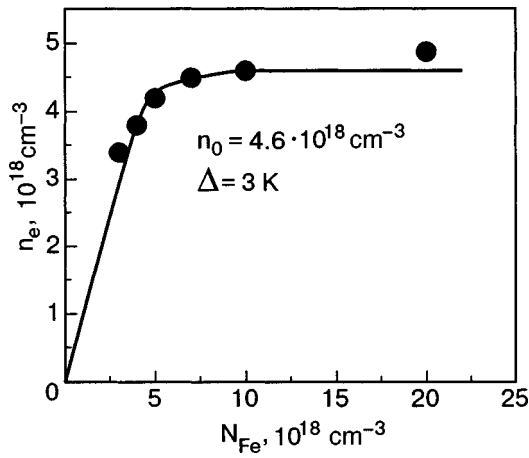
FIG. 1. Electron density n_e versus the concentration N_{Fe} of iron impurities in HgSe:Fe at $T=4.2$ K. The points are experimental data, and the solid curve was obtained from formulas (1) and (2) with $\varepsilon = \varepsilon_F$.

cluded, besides the values of μ_0, a, and φ, the density of electrons from uncontrolled donor impurities, which is a constituent of n_0 and was taken equal to 2×10^{18} cm^{-3}, corresponding to the known estimates. The parameters $a=0.2$ and $\varphi=0.1$ were found by fitting the data in Fig. 2 by a curve obtained according to formula (5) on the assumption that the value of n_0/n_i is small. The inset in Fig. 2 illustrates the inessential change in the position and height of the mobility maximum upon a more precise fitting.

The Shubnikov–de Haas oscillations were studied in magnetic fields up to 50 kOe in the temperature interval 1.3 K $\leqslant T \leqslant$ 4.2 K on the same HgSe:Fe samples with different iron concentrations that were used in our study of the electron mobility. From the magnetic-field dependence of the amplitudes of the oscillations we found the Dingle temperature T_D. In keeping with the task of this study, we shall not discuss the possible dependence on the electron scattering of the other parameters of the oscillations (periods, spin splitting, etc.), since that would require additional investigations. In the determination of T_D the data were processed only for those crystals in which the field dependence of the oscillation amplitude was monotonically increasing; this attested to the absence of beat nodes in the oscillation pattern for the cho-
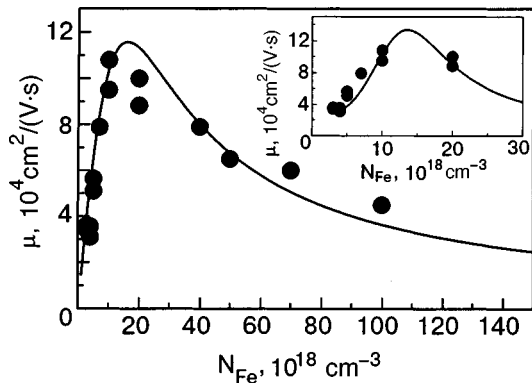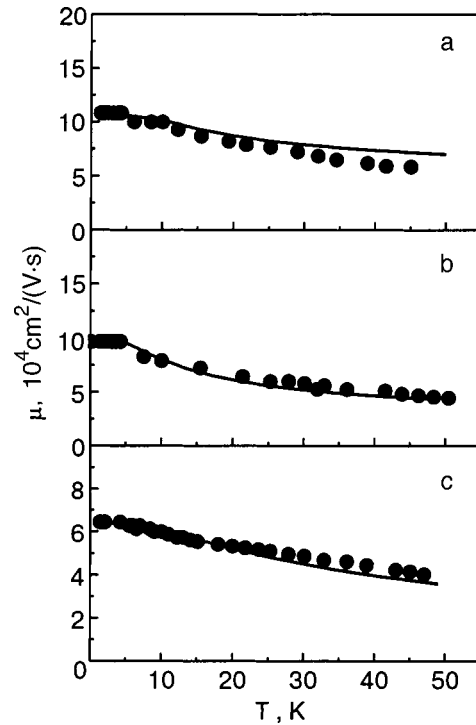

FIG. 3. Temperature dependence of the electron mobility at $T=4.2$ K for three HgSe:Fe samples with different concentrations N_{Fe} of iron impurities [10^{19} cm^{-3}]: 1 (a), 2 (b), 5 (c). The points are experimental data, and the curves were obtained from formula (6).

sen direction of the field and of the current through the sample. Figure 4 shows how the value of the Dingle temperature depends on the impurity concentration. The fitting curve was constructed according to a formula of the form (3) for $\varepsilon = \varepsilon_F$, $\varphi = 0$, and $a = 0.06$. The position of the minimum of the concentration dependence of T_D is correlated with the maximum of the mobility.

DISCUSSION OF THE RESULTS

According to the results which we obtained, the experimental data on the anomalies of the mobility and Dingle temperature in HGSe:Fe crystals are described well in the

FIG. 2. Dependence of the electron mobility μ on the concentration N_{Fe} of iron impurities at $T=4.2$ K. The points are experimental data; the curves were obtained from formula (5) with $a=0.2$ and $\varphi=0.1$ in the approximation $n_0/n_i \leqslant 1$. The inset shows the fitting in the region of the maximum for nearly the same values of the parameters.
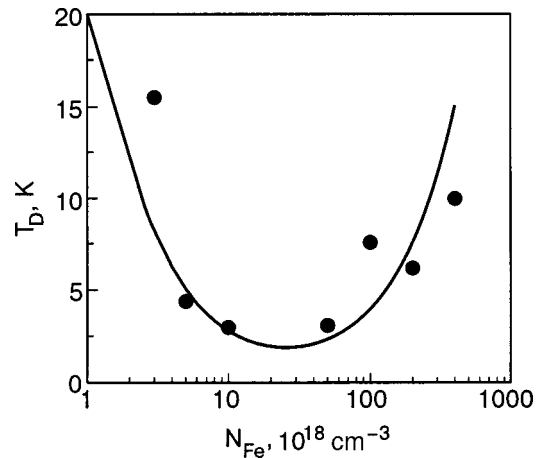

FIG. 4. Dependence of the Dingle temperature T_D on the concentration N_{Fe} of ion impurities for HgSe:Fe samples. The points are experimental data; the solid curve was obtained from formula (3) with $\varphi = 0$, $a = 0.06$.

framework of the theoretical concepts set forth above, which correspond to a generalized Friedel approach. In the studies done previously, which are reflected in the review articles mentioned above,[1,2] the observed maximum of the mobility has been interpreted on the basis of a different approach, the principles of which were stated in Ref. 3. Its main assumption is that ionized and un-ionized donor states exist simultaneously at the resonance $\varepsilon_F = \varepsilon_d$. That assumption in essence means that the state of an electron on a donor is assumed to be not a resonance state but a bound state, similar to states in the forbidden band of a crystal. In adopting that approach for the description of the observed mobility maximum it was argued in addition, on the basis of model calculations, that an ordering of the ionized donors exits,[3,1,4] and other assumptions were made about the structure of the impurity system. A detailed analysis of the whole picture shows that such an interpretation of the mobility maximum contains model assumptions that are hard to justify adequately. At the same time, the experimental facts are most likely consistent with the concept of a resonance state (in the usual understanding of this term in quantum scattering theory) of an electron on an impurity and, accordingly, to the same partially ionized state of all the donors. This concept underlies the approach proposed in this paper. In the framework of this approach to the explanation of the behavior of the mobility it is not necessary to assume that the donors exhibit spatial ordering, the existence of which in HgSe:Fe crystals can scarcely be considered proven at the present time.

Of course, a rigorous determination of which of the two approaches should be applied to a particular system should be based on experiments whose interpretation can unambiguously distinguish the effects of resonance and bound states. This is a complex problem because the distinction is of no significance for a qualitative interpretation of individual (e.g., local) experiments and is ignored by investigators. Therefore, for the HgSe:Fe system this avenue is difficult to take at present, since such questions have been practically ignored in the experiments that have been done.

CONCLUSION

We have shown that the scattering of electrons on donor impurity having a resonance energy level in the conduction band of a semiconductor leads to stabilization of the electron density, to a maximum of the electron mobility and a minimum of the Dingle temperature as functions of the impurity concentration, and also to characteristic anomalies of the temperature dependence of the mobility. These effects are predicted by the theory of resonance scattering in the Friedel approach. The available experimental data obtained on mercury selenide crystals containing iron impurities, both previously existing data and data newly obtained by us in the present study, are in good agreement with the aforementioned predictions.

[*]E-mail: okulov@imp.uran.ru

[1] Z. Wilamowski, Acta Phys. Pol. A **77**, 133 (1990).

[2] I. M. Tsidil'kovskiĭ, Usp. Fiz. Nauk **35**, 85 (1992).

[3] J. Mycielski, Solid State Commun. **60**, 165 (1986).

[4] I. M. Tsidilkovski and I. G. Kuleev, Semicond. Sci. Technol. **11**, 625 (1996).

[5] G. A. Alshanskii, V. L. Konstantinov, A. V. Korolyov, E. A. Neifeld, V. I. Okulov, S. U. Paranchich, and L. D. Sabirzyanova, Phys. Met. Metallogr. **93**, Suppl. 1, 142 (2002).

[6] J. Friedel, Nuovo Cimento, Suppl. **2**, 287 (1958).

Translated by Steve Torstveit

LOW-TEMPERATURE PHYSICS OF PLASTICITY AND STRENGTH

Structural mechanisms of low-temperature work hardening and fracture of cryogenic metallic materials

Yu. O. Pokhyl*

Special Research and Development Bureau for Cryogenic Technologies of B. Verkin Institute for Low Temperature Physics and Engineering, National Academy of Sciences of Ukraine (SRDB ILTPE NASU), pr. Lenina 47, Kharkov 61103, Ukraine
(Submitted June 12, 2003; revised October 22, 2003)
Fiz. Nizk. Temp. **30**, 447–457 (April 2004)

On the basis of the results of original research, various physical aspects of work hardening and fracture of metallic materials at low temperatures (the macroscopic behavior, microstructural processes governing plastic flow and work hardening, the mechanisms of nucleation and propagation of fracture in the final stage of plastic deformation) are analyzed from a unified point of view: the evolution of the microstructural state during plastic deformation of different groups of structural metallic materials in the temperature range 300–4.2 K. The characteristic physical situations realized in low-temperature plastic deformation and fracture of solids are generalized and classified. © *2004 American Institute of Physics.*
[DOI: 10.1063/1.1705442]

1. INTRODUCTION

Research on the processes of work hardening and fracture of metallic materials at low temperatures (down to 4.2 K) is extremely topical both for the basic physics of plasticity and strength and from the standpoint of the applied problem of formulating scientific principles for obtaining high-quality and functional structural materials for modern cryogenic vacuum and aerospace technique.[1)]

The processes of plastic flow, work hardening, and fracture of solids should be thought of as continuously coupled links of a unified process of plastic deformation—from its onset (yield point) to its completion (macroscopic fracture). The connective material for such a treatment is provided by data on the character of the evolution of the structural state of the material on the microscopic level in the course of plastic deformation under the influence of a continuously increasing load. It is the evolution of the defect structure that leads to all of the macroscopic manifestations in the behavior of a deformable solid.

Such an approach makes it possible to treat the various physical aspects of the problem from a unified point of view, to establish the relationships between them, and to bring them into a unified conceptual framework for the process of plastic deformation. This position is, in principle, "textbook" and cannot raise objections, but in practice it is not often realized because of the rather complex experimental technique. A convincing example of the fruitfulness of the approach proposed here is the recently published study[2] in that vein.

In the present paper we carry out an analysis and generalization of many years' worth of results of our own experimental research and model calculations[1] devoted to establishing qualitative and quantitative correlations between the macroscopic parameters and plasticity, work hardening, and

fracture and the characteristics of the defect structure created in various types of metallic materials under the influence of low-temperature plastic deformation (in the temperature interval 300–4.2 K). The goal of this analysis is to establish the microstructural mechanisms that govern the process of low-temperature plastic deformation in its different phases in characteristic groups of real metallic materials.

2. METHODS OF STUDY

The mechanical properties of all the materials were studied in experiments on active uniaxial tension at constant rates of loading (10^{-4}–10^{-3} s^{-1}) in the temperature range 300–4.2 K. The methods used in these studies have been described in detail in a monograph.[3]

The structural–phase state of the materials was investigated by direct methods: transmission and scanning electron microscopy (TEM and SEM) with statistical processing, low-temperature qualitative x-ray diffraction analysis, and optical microscopy, and an indirect method: low-temperature resistometry.

In the latter case the temperature dependence of the resistivity $\rho(T)$ in the undeformed state was determined *in situ* under a mechanical stress $\sigma < \sigma_{pr}$, and the change in resistance $\Delta R/R_0$ in the deformation process was also determined as a function of the elongation Δl of the sample, which was registered simultaneously with the curves of the mechanical load P versus elongation Δl.

The methodological details of the experiments are described in Refs. 4–8.

3. RESULTS AND DISCUSSION

A quantitative study of the evolution of the defect structure and phase state with the deformation from the time of its onset to the completion of the fracture of the object made it

possible to identify the main microstructural mechanisms that govern the various phases of the low-temperature plastic deformation as a unified process in different groups of real materials used in cryogenics. This, in turn, made it possible to propose a classification of the existing real materials and the modes of their deformation, hardening, and fracture from the standpoints of macromechanical and mictrostructural criteria; this proposed classification is set forth in Sec. 3.1.

3.1. Classification of the objects of study according to the physical signs of their behavior under loading

Of the whole diversity of metallic materials investigated and the features of their behavior on the macro- and microscopic levels under low-temperature deformation, one can single out the following characteristic groups:

1. Structurally stable[2)] materials with ''hard'' work hardening, i.e., single-phase or pseudo-single-phase materials, characterized in low-temperature plastic deformation by a high work hardening coefficient $\theta = d\sigma/d\varepsilon$ ($\theta \sim G/20$, where G is the shear modulus of the material at the deformation temperature), relatively low macroscopic plasticity δ ($\delta \leqslant 10\%$), a macroscopically uniform plastic deformation (the absence of macronecking on fracture), and a strong interaction of dislocations on the microscopic level (a dislocation–dislocation coupling constant $\alpha > 1$).[3)] A typical representative of such a group of materials is the alloy Ti–5% Al, for which the results of a study are presented below.

2. Structurally stable materials with ''soft'' work hardening, i.e., mono- or polyphase materials with a relatively low work hardening coefficient θ ($\theta \sim G/100$), high macroscopic plasticity ($\delta \approx 30$–70%), a plastic deformation which is substantially nonuniform macroscopically (with a tendency towards necking upon fracture), and a weak dislocation interaction (with a constant $\alpha < 1$). The Fe–Cr–Ni–Ti alloys considered in this paper are materials of this type.

3. Polyphase structurally unstable materials, i.e., materials which on cooling or during low-temperature plastic deformation undergo phase transformations of the martensitic type, with the formation of phase boundaries induced by the low-temperature deformations. Representatives of this group of materials among the alloys of the Ti–Nb system are NT-45 and NT-50.

4. Heterophase materials, i.e., materials with pre-existing phase boundaries between constituents having different crystal lattice types and different elastic, strength, and thermophysical properties. The mechanical behavior of this type of material is examined for the particular case of the commercial composite Cu–(Nb–Ti) (a superconducting cable made of thin filaments of the alloy NT-50 pressed into a copper matrix).

Let us consider the features of the behavior of this group of materials during their low-temperature plastic deformation and fracture.

3.2. Behavior of hard-hardening materials

Representing this group of materials in our study was the single-phase commercial titanium α alloy Ti–5% Al, which prior to mechanical testing was annealed in vacuum at 800 °C for 1 hour and then cooled in air.

TABLE I. Mechanical properties of the alloy Ti–5% Al.

T, K	$\sigma_{0.2}$, MPa	σ_u, MPa	δ, %	θ, %
300	529	595	5	1320
77	774	1009	7	3480
4.2	853	1098	8	3700

Mechanical properties. In the temperature interval 300–77 K the plastic deformation occurs monotonically, and the hardening curves are smooth. The deformation at 4.2 K is of a jumplike character, with the depth of the drops in load increasing with increasing degree of deformation.

In Table I we show the temperature dependence of the mechanical characteristics of the alloy ($\sigma_{0.2}$ is the yield stress, σ_u is the ultimate strength, δ is the maximum elongation, and $\theta = d\sigma/d\varepsilon$ is the work hardening coefficient; the values given for θ correspond to the average over the deformation part of the σ–ε curve). It is seen that when the temperature is lowered from 300 to 4.2 K, the strength characteristics of the alloy increase monotonically and the plasticity of the material increases somewhat.

Structural studies. In the undeformed annealed state the alloy has an average grain size of the order of 10 μm. The defect structure of the alloy in the initial state is characterized by the presence of isolated dislocations of a mixed orientation and dislocation pileups belonging to the prismatic slip system $\{1\bar{1}00\}\langle11\bar{2}0\rangle$, and also low-angle tilt and twist grain boundaries. The distribution of defects in the initial state is nonuniform, with an average density of dislocations $\approx 2 \times 10^8$ cm^{-2}. The alloy studied is a single-phase α alloy with the hcp lattice.

Plastic deformation of the alloy in the investigated temperature interval occurs by prismatic slip along intersecting planes of the $\{1\bar{1}00\}$ type. Dislocations with the same type of Burgers vector $\mathbf{b} = \frac{1}{3}\langle11\bar{2}0\rangle$ which lie in intersecting planes of the prism enter into a reaction with one another and form dislocation networks of various configurations. The density of the dislocation network in the structure of the deformed alloy is high. The observed dislocation ensembles often have appreciable long-range stresses, as is attested to by the significant bending of the individual dislocations near these groups. Activation of secondary systems of prismatic slip and the related formation of stable dislocation groups with long-range stress fields is an important structural factor that makes for significant work hardening of the alloy.

A distinctive feature of the structural state of the alloy deformed at 4.2 K is the presence of twins belonging to the system $\langle10\bar{1}2\rangle\langle10\bar{1}1\rangle$. Twinning gives rise to a new interface, i.e., it leads to a subdividing of the initial grain, and, hence to additional hardening of the alloy (the Hall–Petch effect) at 4.2 K in comparison with the hardening at room temperature.

Based on the structural studies we can give some ideas as to the nature of the jumplike deformation of this alloy at helium temperature. Apparently the low-temperature jumplike deformation is due to both an avalanche discharging of dislocation pileups and to twinning. The jumplike character of the plastic deformation at helium temperature nevertheless
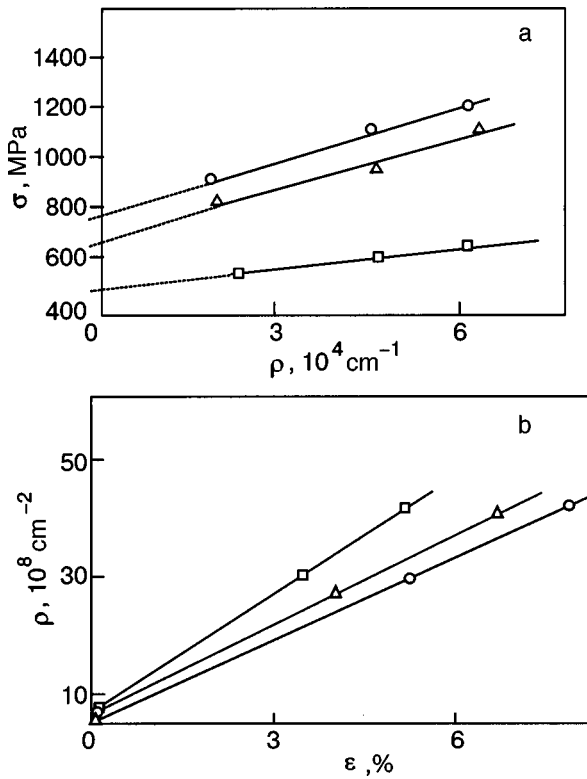
FIG. 1. Dependence of the flow stress σ on the dislocation density ρ (a) and the dependence of the dislocation density on the deformation ε (b) for a Ti–5% Al alloy at different deformation temperatures T [K]: 4.2 (○), 77 (△), 300 (□).

does not lead to the appearance of macronecking in the sample, and in this sense the alloy Ti–5% Al must be classed among the materials with macroscopically uniform deformation. At higher temperatures there is a possibility for the internal stresses to relax owing to thermally activated multiple cross slip or the pressing through of dislocations between thermally insurmountable obstacles. Macroscopically this is manifested in the smoothness of the deformation curves.

A quantitative processing of the results of structural studies made it possible to obtain the dependence of the flow stress σ on the dislocation density ρ and the dependence of the dislocation density on the deformation ε at different temperatures (Fig. 1a 1b). It turned out that these dependences are described by the same analytical expressions, differing at different temperatures only in the parameters that enter into them:

$$\sigma = \sigma_0 + \alpha G b \rho^{1/2}, \tag{1}$$

$$\rho = \rho_0 + A \varepsilon^n, \tag{2}$$

where σ_0 is the internal stress component of nondislocation origin (impurities, grain boundaries, lattice friction, etc.), G is the shear modulus at the corresponding temperature, b is the Burgers vector of the prismatic dislocations, α is a coefficient characterizing the contribution of the elastic interaction of the dislocations to the value of the flow stress, ρ_0 is the density of dislocations in the undeformed alloy, and A is the dislocation accumulation coefficient. The experimentally determined values of the parameters in Eqs. (1) and (2) are given in Table II.

TABLE II. Values of the structural parameters for the alloy Ti–5% Al.

T, K	σ_0, MPa	$\rho_0 \cdot 10^{-8}$, cm^{-2}	α	$A \cdot 10^{-11}$, cm^{-2}	n
300	480	2	1.7	5.8	1
77	690	2	3.3	5.3	1
4.2	790	2	3.9	4.1	1

Let us analyze the data given in Table II. The coupling coefficient α of the dislocations has a substantial temperature dependence. It has been shown experimentally[9] and in model calculations[10] that the value of the coefficient α reflects the contribution of different types of dislocation interactions to the value of the flow stress, and, according to Ref. 19, the value of α can be written in the form

$$\alpha = \alpha_G + \alpha_S, \tag{3}$$

where α_G is the athermal part, which is due to the long-range dislocation interaction, α_S is the thermally activated part, which is determined by the short-range interaction of the dislocations. The microstructural data show the presence of both forms of interaction: long-ranged (planar pileups, networks, recombination segments) and short-range (intersections, jogs, dipoles). The increase of the component α_S with decreasing temperature is due to the temperature dependence of the flow stress of the alloy.

From the joint solution of equations (1) and (2) one can establish a relation between the parameters α and A and the work hardening coefficient θ:

$$\theta \approx \frac{1}{2} n \alpha G b A^{1/2} \varepsilon^{(n/2-1)}. \tag{4}$$

It follows from Eq. (4) that for a fixed value of the deformation the following relation should hold (if the temperature dependence of G is neglected):

$$\frac{\theta(T_1)}{\theta(T_2)} \approx \frac{\alpha(T_1) A^{1/2}(T_1)}{\alpha(T_2) A^{1/2}(T_2)}, \tag{5}$$

where T is the temperature of the experiment. Substitution of the experimentally measured values (see Table II) into relation (5) confirms its validity; hence we can conclude that the features of the formation of the dislocation structure in the alloy at different temperatures determine the trend of the macroscopic work hardening curve. The hardening of the single-phase α alloy is apparently governed mainly by the attractive interactions of dislocations of intersecting slip systems, and that leads to higher values of the work hardening coefficient and dislocation coupling constant with decreasing temperature.

Electron fractography. In the temperature interval 4.2–300 K the fracture surfaces contain similar elements of structure typical of different fracture types. This is indicative of simultaneous realization of several mechanisms of nucleation and propagation of the defects responsible for fracture of the alloy. One also observes a number of structural components specific to testing at different temperatures.

A detailed analysis[11,12] of the dislocation configurations and morphology of the fracture surfaces showed that the nucleation of microcracks occurs as a result of dislocation
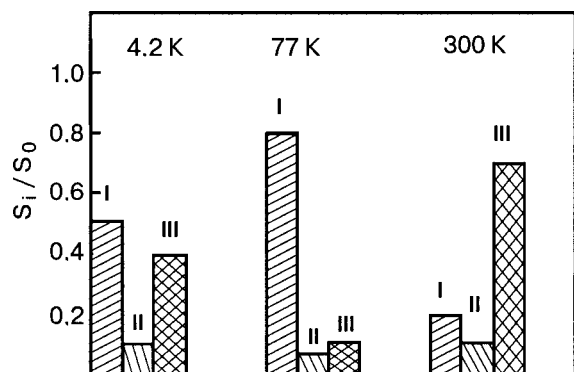
FIG. 2. Distribution of the structural components of fracture over areas for different testing temperatures in the alloy Ti–5% Al: pits (I), breaking crests at 4.2 K and delamination at 77 and 300 K (II), quasi-spalling (III). S_i is the area of the fracture surface occupied by the characteristic morphological signs of fracture; S_0 is the total area of the fracture surface.

mechanisms and that the further propagation of the cracks, leading to fracture of the material, can occur in different ways, from viscous to quasibrittle, under identical external conditions.

To ascertain the leading fracture mechanism in a particular situation we carried out a statistical analysis of the distribution of different structural components over the areas for different testing temperatures. The histograms shown in Fig. 2 attest to the increase in the relative fraction of the viscous fracture component and a decrease of the fraction of quasibrittle components with decreasing temperature, which correlates qualitatively with the increasing of the macroscopic plasticity at low temperatures. Obviously the viscous character of the fracture becomes predominant as the temperature is lowered.

On the basis of the results of a statistical processing of the geometrical parameters of the fracture reliefs, we were able to estimate the true value (ε_{loc}) of the plastic deformation localized in microvolumes in the fracture of an alloy.[12]

The results, $\varepsilon_{loc}^{300}=3.7$ and $\varepsilon_{loc}^{4.2}=4.5$, attest to an increase in the localization of the plastic deformation in microvolumes as the temperature is lowered. The ratio of the deformation localized in micronecks at different temperatures is fairly well correlated quantitatively with the ratio of the macroscopic plasticity δ of the alloy at the corresponding temperatures:

$$\varepsilon_{loc}^{300}/\varepsilon_{loc}^{4.2} \approx \delta^{300}/\delta^{4.2},$$

and this also indicates that the mechanism of viscous fracture of an alloy plays the leading role in the temperature range studied.

3.3. Behavior of soft-hardening materials

As we said in Sec. 3.1, this group of materials is represented by four alloys of the Fe–Cr–Ni–Ti system, with the concentrations Cr ≈ 16.5%, Ni ≈ 31.4%, and Ti = 1.6, 1.9, 2.05, and 2.5%.

The heat treatment of all the alloys consisted in quenching from a temperature of 1000 °C (1 hour) in water and aging at 720 °C for 16 hours, followed by cooling in air. This heat treatment makes for the precipitation of a maximal amount of disperse γ' phase, which in turn makes for the
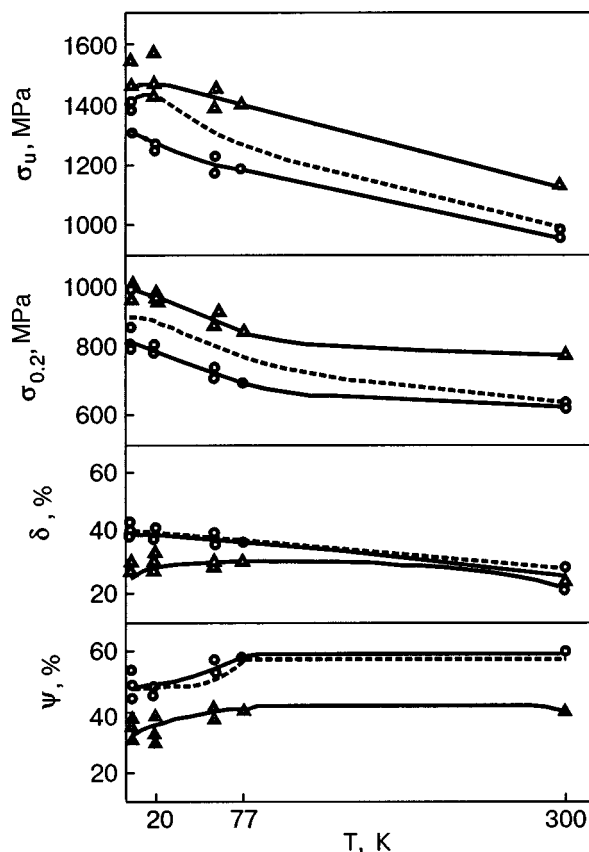

FIG. 3. Temperature dependence of the yield stress $\sigma_{0.2}$, ultimate strength σ_u, elongation to fracture δ, and relative cross section area reduction ψ of Fe–Cr–Ni–Ti alloys with Ti concentrations of 1.6% (○), 1.9% (– – –), and 2.5% (△).

maximal strength characteristics to the alloy.[13] The grain size in the samples studied, determined by the method of optical metallography, was 20–50 μm.

Mechanical properties of the alloys. The deformation curves of alloys of all the compositions studied have a monotonic, parabolic character at temperatures of 300, 77, and 55 K, with the load maximum achieved prior to fracture and the subsequent drop which are reflective of the appearance of macronecking in the sample. At $T=20$ K several irregular jumps in the load appear on the strain curve not long before fracture. The work hardening coefficient of the alloys is small in absolute value and increases slightly with decreasing deformation temperature.

The temperature dependence of the mechanical properties of the alloys is presented in Fig. 3. It is seen that lowering the temperature from 77 to 4.2 K leads to growth of the yield point $\sigma_{0.2}$, the ultimate strength σ_u, and the relative elongation δ for the alloys of all compositions (except for the alloy with Ti = 2.5%). The value of the relative cross section area reduction ψ decreases at temperatures below 77 K. Characteristically the strength of the alloys at all the temperatures studied increases with increasing titanium concentration, while the plasticity of the alloy with 2.5% Ti is lowered in comparison with the plasticity of the other alloys, which is practically independent of the Ti concentration. It is important to note that, even so, the high plasticity of the material is preserved down to a deformation temperature of 4.2 K.

TABLE III. Fracture micromechanisms of Fe–Cr–Ni–Ti alloys.

Composition (Ti concentration, %)	Deformation temperature, K		
	4.2	20	77
Composition I (1.6)	Transcrystallite combined: viscous (90%) +quasiviscous, micronecking.	Transcrystallite+intercrystallite combined: viscous (75%) + quasi-cleavage.	Transcrystallite viscous (96%), micronecking.
Composition II (1.9)	Transcrystallite combined: viscous (87%)+quasiviscous + quasi-cleavage	Transcrystallite+intercrystallite combined: viscous (75%) +quasi-cleavage.	Transcrystallite viscous (98%), micronecking.
Composition III (2.05)	Transcrystallite combined: viscous (80%)+quasiviscous + quasi-cleavage.	Transcrystallite+intercrystallite, combined: viscous (76%) +quasi-cleavage.	Transcrystallite viscous (93%), micronecking.
Composition IV (2.5)	Transcyrstallite combined: viscous (82%)+quasi-cleavage, micronecking, decohesion.	Transcrystallite+intercrystallite, combined: viscous (70%) +quasi-cleavage, decohesion.	Transcrystallite viscous (95%), micronecking, decohesion.

Measurements of the macroscopic mechanical properties (including the work hardening coefficient, the deformation to fracture) attest that Fe–Cr–Ni–Ti alloys belong to the materials with soft work hardening in the proposed classification. This is confirmed by the results of an electron-microscope study of the defect structure and of the character of the fracture, which are presented below.

Features of the structure of the alloys deformed at low temperature. TEM study. A study of the evolution of the dislocation structure of the alloys with low-temperature deformation showed that, independently of the Ti concentration in the material, a relation of type (1) holds between the flow stress σ and the density ρ of dislocations belonging to the $\{111\}\langle110\rangle$ slip system. Here the dislocation coupling constant α typically takes on values ≈ 0.4–0.6 which are weakly dependent on the deformation temperature and the Ti concentration in the alloys (a weak tendency toward growth of α with decreasing T and increasing Ti concentration is observed).

The TEM study of the structure of the alloys deformed to fracture[14] revealed the presence of intersecting coarse slip bands of the $\{111\}\langle110\rangle$ type, a misoriented stripe substructure, and steplike subboundaries with crystallographically oriented steps. The existence of this kind of dislocation substructure also explains the zigzag microcracks observed in the fractured samples, the steps of which open along powerful slip bands.

In the alloys studied the nucleation of microcracks during low-temperature deformation occurs at places with a high concentration of internal stresses—at dislocation subboundaries and at the interfaces between the matrix and intermetallide inclusions. The further propagation of the the crack, leading to fracture of the material, can occur in various combined ways—from viscous to quasibrittle.

Fractographic study. The fracture of the alloy samples for all Ti concentrations and at all temperatures in the interval studied (77–4.2 K) occurs with the formation of pronounced macronecking. In this region the fracture has a "cup–cone" shape, which is typical for viscous materials.[15]

The results of a quantitative microfractographic study are presented by the histogram in Fig. 4 and in Table III (the numbers in parentheses indicate the fraction of the fracture surface area which shows signs of viscous fracture).[14]

Reviewing the results presented, we must conclude that the main mechanism of fracture in these alloys in the temperature range 77–4.2 K is a transcrystallite viscous mechanism of nucleation, growth, and coalescence of microdiscontinuities. Lowering the temperature below 50 K leads to a noticeable manifestation of quasiviscous and quasibrittle components, i.e., at low temperatures the fracture is of a combined viscobrittle character. Especially noticeable is the contribution of nonviscous fracture mechanisms at 20 K owing to the appearance of intercrystallite anisotropic fracture that is apparently due to the embrittling influence of the liquid hydrogen medium. Increasing the Ti concentration in the alloys causes an increase in the relative fraction of the nonviscous fracture mechanisms at low temperatures, which leads to a lowering of the macroscopic plasticity of the alloys. Furthermore, the lowered macroscopic plasticity of the alloy with 2.5% Ti is due to the presence of rather large inclusions of an intermetallide phase $(Fe,Ni_2)Ti$, which promote the action of an additional mechanism of microvoid nucleation—the decohesion mechanism.

Based on our fractographic study, the fracture process for these alloys can be represented as follows. When the external stress reaches the value of the ultimate strength, the deformation localizes in a macronecking region, where the uniaxial stress state gives way to a triaxial one (the most rigid state of plane deformation), and the maximum stress is developed at the center of the sample. In this case microdiscontinuities arise in the central region of the sample at nonuniformities of the dislocation substructure, and under the influence of the increasing true stress and with increasing deformation they grow and merge by the mechanism of formation of internal micronecking, forming an initial microcrack.

This initial microcrack, causing stress concentration at its tip, propagates from the central part of the sample to the periphery along a zigzag surface, forming alternating planes at $\pm 45°$ angles, where the maximum shear stresses act. This process corresponds to the formation of the observed relief of the "cup bottom" macroscopically normal to the axis of tension and containing equiaxial pits against the background of the riffled surface. Further development of the central crack occurs by means of local shearing in the bands at angle of $\leqslant 45°$ to the axis of tension, where the final fracture oc-

TABLE IV. Values of the relative macroscopic deformations (elongation δ, cross section area reduction ψ) and the plastic deformation ε_{loc} localized in the micronecks at their fracture at different temperatures in an Fe–Cr–Ni–Ti alloy with a Ti concentration of 1.9%.

T, K	δ, %	ψ, %	ε_{loc}
4.2	42.6	49	6.02
20	41.8	50	6.54
77	36.1	57	7.30

curs and which corresponds to extended shear pits on the walls of the "cup."

The results of an estimate of the local plastic deformation ε_{loc} realized in partitions (micronecks) bounding the pits at the fracture surface for the alloy with 1.9% Ti are presented in Table IV.

From the data listed in Table IV, we see that plastic deformation localized in microvolumes at the fracture of an alloy is more than an order of magnitude greater than the values of the macroscopic elongation of the samples, and it increases noticeably with increasing testing temperature. This last conclusion is in qualitative agreement with the observed increase of the role of the viscous mechanism of fracture with increasing temperature (see Fig. 4). One notices that the temperature trend of ε_{loc} and ψ is the same, which attests to the fact that under conditions of nonuniform plastic deformation the value of the relative cross section area reduction reliably characterizes the plasticity of the material.

The correlation noted may be qualitatively linked to the temperature dependence of the work hardening coefficient of alloys with soft hardening. With decreasing temperature the work hardening coefficient increases somewhat, and that in turn should lead to an increase in the uniformity of the plastic deformation (a decrease of ψ and ε_{loc}), since the active zone of the deformation hardens more rapidly, and the deformation is carried along the sample to another cross section. Raising the deformation temperature results in a certain decrease in the work hardening coefficient, the deformation proceeds further, all the way to fracture, in one (the "weakened") band; this is manifested in an increase in the nonuniformity of the deformation (ψ and ε_{loc}) and to a greater tendency toward necking during fracture.

3.4. Regularities of the low-temperature plasticity and fracture in the case of polyphase structurally unstable and heterophase materials

Studies of the mechanical properties, structure–phase state (in the interval $T = 300–4.2$ K) and their interrelation for typical representatives of two groups (3 and 4; see Sec. 3.1) of materials[16] for the examples:

—bcc deformable superconducting alloys of the NbTi system (45–50 mass % Nb) in various initial structural states;

—a heterophase composition material Cu–(Nb–Ti), the components of which have different crystal lattices—fcc (Cu) and bcc (Nb–Ti) and, hence, have substantially different strength, plasticity, and elastic properties.

Both groups of materials were subjected to different thermomechanical treatments, consisting in multiple stretching, drawing, intermediate annealing, quenching, and hydroextrusion in various combinations.

3.4.1. Mechanical properties and deformation structure of Ti–Nb alloys

Studies of the mechanical properties and structure–phase state of the bcc alloy Ti–45% Nb have shown the following.

It has been established[4,5] for the first time by direct (x-ray) and indirect (resistometry) methods that a $\beta \to \alpha''$ martensitic transformation occurs on cooling in the quenched and drawn samples of the alloy Ti–45% Nb under an applied stress $\sigma < \sigma_{0.2}^{293\,K}$ and in the quenched samples also after predeformation to the yield point at 293 K. The temperature interval in which the $\beta \to \alpha''$ transformation occurs depends on the applied stress and on the preliminary thermomechanical treatment (TMT). In particular, under a stress amounting to $\sim 0.8\sigma_{0.2}^{239\,K}$ the $\beta \to \alpha''$ transformation begins below ~ 140 K in the quenched samples and below ~ 90 K in the drawn samples. The lattice type (orthorhombic) and lattice parameters of the α'' martensite have been determined[4] by x-ray diffraction in the temperature interval 293–5 K (at 293 K they are: $a = 0.303(8)$ nm, $b = 0.470(7)$ nm, $c = 0.462(6)$ nm).

A low-temperature structural nonuniformity common to all the materials of this group is the sharp localization of the plastic deformation. It has been shown by the method of quantitative electron fractography that the value of the deformation localized in microvolumes during fracture increases markedly and that the deformable volume decreases with decreasing temperature. The sharpest increase in ε_{loc} (by a factor of two) with decreasing temperature from 20 to 4.2 K is observed in an NT-50 and Nb wire after intermediate
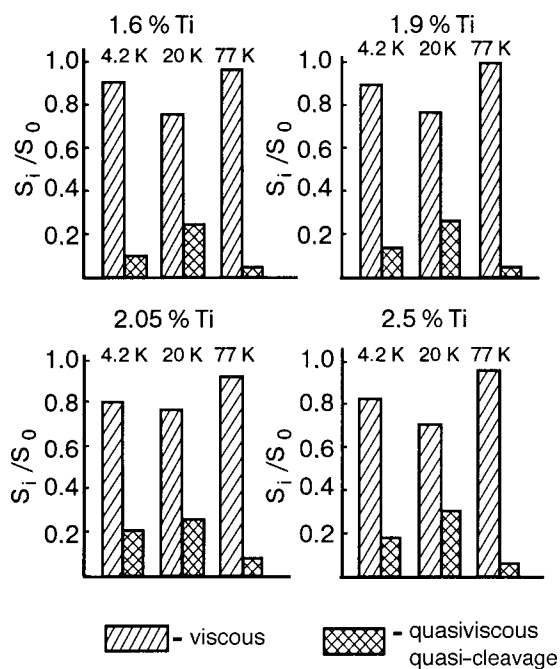

FIG. 4. Distribution over areas of the structural components of the fracture of Fe–Cr–Ni–Ti alloys at different testing temperatures (S_i is the area occupied by the corresponding relief, and S_0 is the total area of the fracture surface).
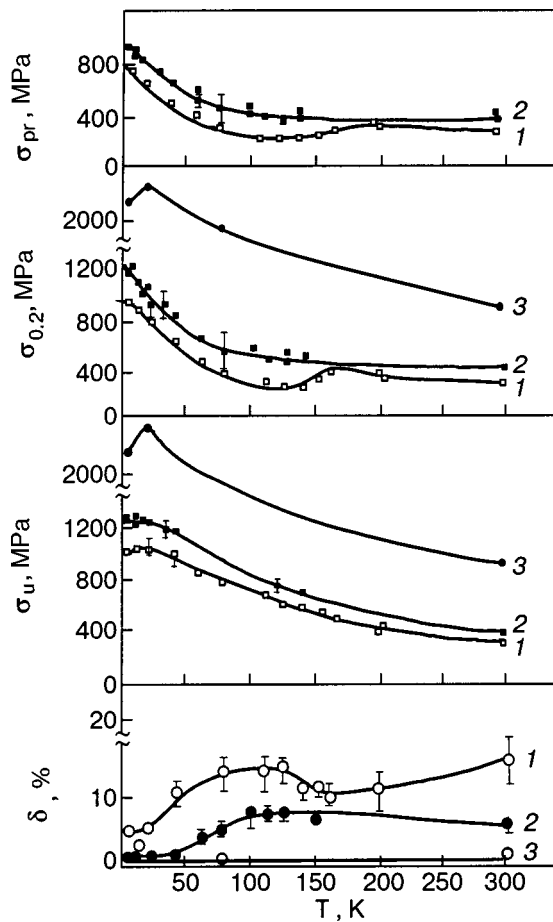
FIG. 5. Temperature dependence of the mechanical properties of quenched (*1*) and drawn (*2*) samples of the alloy Ti–45% Nb and the commercial wire Ti–50% Nb (*3*).

anneals.[7,17] One notices the influence of the large absolute value $\varepsilon_{loc} = 3-6$ characterizing the reserve of plasticity of the material in the microvolumes.

It has been established on the basis of the data of a quantitative fractographic analysis that in the temperature interval 300–4.2 K, including in the region 20–4.2 K, the leading micromechanism for the fracture of Ti–Nb alloys (45 and 50% Nb) after all the TMTs is viscous fracture by the formation, growth, and coalescence of microdiscontinuities.[7,18]

A study of the character of the plastic deformation and the mechanical characteristics of bcc superconducting materials revealed the following features in the Ti–45% Nb alloy and the NT-50 wire in the interval 300–4.2 K (Fig. 5): a) a change in sign of the derivatives $d\sigma_{pr}/dT$ and $d\sigma_{0.2}/dT$ for the quenched samples in the region 160–140 K; b) an increase of the plasticity in the quenched and drawn samples with decreasing temperature in the intervals 160–70 K and 130–70 K, respectively; c) a nonmonotonic character of the $\sigma_u(T)$ curves for all types of samples in the temperature region 20–4.2 K; d) pseudoelasticity and reversible stress jumps on the deformation curves $P(\Delta l)$, manifested in an interval which depends on the TMT.

A comparison of the results of the studies of the mechanical properties and structural state of the alloys suggested that observed nonmonotonicity on the $\sigma_{pr}(T)$, $\sigma_{0.2}(T)$, $P(\Delta l)$, and $\delta(T)$ curves of Ti–Nb alloys are deter-

mined by processes of $\beta \leftrightarrow \alpha''$ transformation, which accompanied by a significant volume effect and occurs by means of an oriented shear. In addition, twinning contributes to the increase of the plasticity of the quenched samples (in the interval 160–70 K).

To elucidate the causes of the anomaly on the $\sigma_u(T)$ curve, which is clearly expressed in wire samples of the Ti–Nb alloys in the 20–4.2 K region, and of the decrease of the level of plasticity of the quenched and drawn Ti–Nb alloys in the region 77–4.2 K, we have considered the influence of the following factors: a viscobrittle transition, the superconducting transition, the development of twinning, and temperature dependence of the work hardening coefficient. As was shown above, a viscobrittle transition is not observed in any of the materials of this group. Similarly, the superconducting transition does not cause a lowering of the ultimate strength of the alloys; twinning occurs only in the quenched samples of the Ti–45% Nb alloy.[18]

At the same time, the substantial growth of ε_{loc} and the decrease in the volume of the active plastic deformation at a temperature of 4.2 K are evidence that even at such a low temperature the work hardening in the zone of active plastic deformation is insufficient to restrain the localization of the deformation and the transfer of slip to adjacent regions. In such a case an accumulation of deformation defects, which are sources of nucleation of discontinuities, occurs in a narrow zone of active plastic deformation; this ultimately leads to catastrophic failure of the material at an insignificant macroscopic deformation. This is apparently also the cause of the anomalous decrease of σ_u in this temperature interval.

3.4.2. Mechanical properties and the character of the fracture of composite materials

A study of the mechanical properties of a heterophase multifilament composite consisting of a structurally unstable "reinforcing" component—thin wires of the alloy NT-50 and a copper matrix—showed that in the temperature region 9.5–4.2 K there is a lowering of both the strength properties and, especially, of the plastic properties of the material subjected to TMT with the use of intermediate anneals, whereas the plasticity of a hydroextruded composite is maintained at an order-of-magnitude higher level in this same temperature region (Fig. 6).

Structural studies[16] have shown that the sharp decrease in plasticity of the composite at low temperatures cannot be explained by a viscobrittle transition in the "reinforcing" component.

It turned out that in the composites with a "soft" matrix (obtained by technologies employing intermediate anneals) multiple necking occurs in the "reinforcing" component, and breaks of the individual filaments appear in the necking regions at 30 K, and at 9–9.5 K the multiple breaks of the "reinforcing" component are observed. At the same time, in composites with a "hard" matrix (obtained without anneals) the deformation occurs in a macroscopically uniform manner in the filaments and in the matrix, leading to the simultaneous failure of the composite as a whole.

Our studies permit the assertion that the level of low-temperature plasticity of composites consisting of metallic materials with different crystal lattices (bcc and fcc), both in
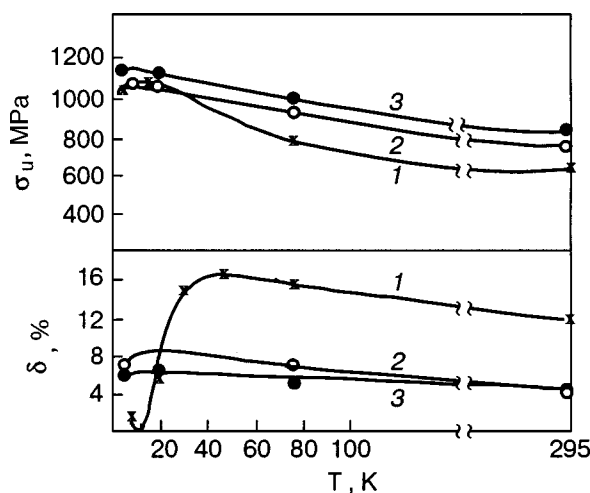
FIG. 6. Temperature dependence of the ultimate strength σ_u and relative elongation δ of composites obtained with the use of intermediate anneals (*1*) and by hydroextrusion with ultrafine filaments of diameter 0.2 (*2*) and 0.1 μm (*3*).

the case of structurally stable and in the case of the metastable bcc component, is determined by the relationship between the strength and plastic properties of the matrix and the "reinforcing" fiber with the sharply growing (as the temperature is lowered from 20 to 4.2 K) localization of the plastic deformation of the latter taken into account. At a high strength of the matrix the localization of the plastic deformation of the "reinforcing" component is suppressed by the transfer of stress to the matrix, the deformable volume of which hardens locally, and the subsequent deformation of the composite is translated along the axis of the sample to a new cross section. This is a structural mechanism of maintaining the high strength in combination with the appreciable plasticity of the composite at the very lowest temperatures of its deformation. At a low strength of the matrix the low-temperature deformation of the composite in a given local cross section occurs to the failure of the "reinforcing" component and the composite as a whole; this is the cause of the embrittlement of the heterophase material at low temperatures.

CONCLUSION

In this paper we have carried out a systematic analysis and classification of the various (differing in their physical nature and their external manifestations on different levels) mechanisms governing plasticity, work hardening, and fracture of real metallic materials at low temperatures. We have proposed principles for dividing different materials into groups from the standpoint of their behavior under low-temperature deformation.

Such a systematization turned out to be possible thanks to an analysis of multistage and multifactor process of plastic deformation in all of its stages from the standpoint of the governing role in the evolution of the defect microstructure and the establishment of qualitative and quantitative correlations between the microscopic parameters of the structure and the macroscopic mechanical characteristics of the materials.

The approach developed has turned out to be rather effective for developing criteria for estimating and selecting structural materials capable of serving under extreme conditions of service in cryogenic and aerospace technique and also for the development of unconventional methods of cryogenic thermomechanical treatment of a number of materials.[1]

In closing, the author expresses profound gratitude to Prof. F. F. Lavrentev for many years of collaboration and to V. A. Lototskaya, V. V. Sergienko, and I. N. Bogaenko for assistance in preparing the manuscript for publication.

[1] Yu. O. Pokhyl, Metallofizika i Noveĭshie Tekhnologii **21**, No. 6, 3 (1999).

[2] V. A. Moskalenko, A. R. Smirnov, V. N. Kovaleva, and V. D. Natsik, Fiz. Nizk. Temp. **28**, 1310 (2002) [Low Temp. Phys. **28**, 935 (2002)].

[3] B. I. Verkin and V. V. Pustovalov, *Low-Temperature Research on Plasticity and Strength. Devices, Technique, and Methods* [in Russian], Énergoizdat, Moscow (1982).

[4] V. A. Lototskaya, V. Ya. Il'ichev, A. I. Prokhvatilov, and A. P. Isakina, Metallofizika (Kiev) **12**, 78 (1990).

[5] V. A. Lototskaya and V. Ya. Il'ichev, Fiz. Met. Metalloved. **9**, 141 (1990).

[6] V. Ya. Il'ichev and V. A. Lototskaya, Problemy Prochnosti **5**, 61 (1980).

[7] Yu. O. Pokhyl, V. A. Lototskaya, F. F. Lavrent'ev, and V. Ya. Il'ichev, Fiz. Met. Metalloved. **64**, 549 (1987).

[8] V. Ya. Ilichev, F. F. Lavrentev, V. A. Lototskaya, and Yu. O. Pokhyl, Crystallogr. Rep. **23**, 387 (1983).

[9] Yu. O. Pokhyl, *Interaction of Dislocations and Work Hardening of Single Crystals of Magnesium and Zinc* [in Russian], Candidate's Dissertation, Kharkov (1975).

[10] F. F. Lavrentev, Yu. O. Pokhyl, and I. N. Zolotukhina, Mater. Sci. Eng. **23**, 69 (1976).

[11] P. P. Dudko, F. F. Lavrentev, and Yu. O. Pokhyl, *Cryogenic Properties of Metals and Welds. Proceedings of the International Conference*, K. A. Yuschenko, D. A. Wigley, and A. F. Clark (eds.), Boulder, Colorado, pub. (1987), p. 345.

[12] B. I. Verkin, F. F. Lavrentev, Yu. O. Pokhyl, and V. V. Sergienko, *Cryogenic Properties of Metals and Welds. Proceedings of the International Conference*, K. A. Yuschenko, D. A. Wigley, and A. F. Clark (eds.), Boulder, Colorado, pub. (1987), p. 357.

[13] M. M. Khimushin, *Heat Resistant Steels and Alloys* [in Russian], Metallurgiya, Moscow (1964).

[14] F. F. Lavrentev, Yu. O. Pokhyl, V. V. Sergienko, P. P. Dudko, V. Ya. Ilichev, G. I. Maslii, A. I. Telegon, P. Petza, and I. Krczicz, Mater. Sci. Eng., A **158**, 157 (1992).

[15] D. A. Wigley, *Mechanical Properties of Materials at Low Temperatures*, New-York–London.: Plenum Press. 373 (1971) (in Russian).

[16] V. A. Lototskaya and Yu. O. Pokhyl, Metallofizika i Noveĭshie Tekhnologii **22**, No. 2, 70 (2000).

[17] Yu. O. Pokhyl, V. A. Lototskaya, and F. F. Lavrentev, Crystallogr. Rep. **33**, 1053 (1993).

[18] V. A. Lototskaya, Yu. O. Pokhyl, V. Ya. Ilichev, F. F. Lavrentev, and S. P. Zabolotin, Crystallogr. Rep. **25**, 146 (1985).

[19] F. F. Lavrentev and V. L. Vladimirova, Mater. Sci. Eng. **30**, 131 (1977).

Features of the low-temperature creep of a Nb−Ti alloy after large plastic deformations at 77 K

V. K. Aksenov,[†] O. I. Volchok,* E. V. Karaseva, and Ya. D. Starodubov

National Science Center "Kharkov Institute of Physics and Technology," ul. Akadmeicheskaya 1, Kharkov 61108, Ukraine
(Submitted July 10, 2003; revised July 21, 2003)
Fiz. Nizk. Temp. **30**, 458–462 (April 2004)

The low-temperature (77 K) creep and the corresponding changes in the resistivity of a niobium–titanium alloy subjected to plastic deformation by drawing at 77 K are investigated. It is shown that after large plastic deformations ($\varepsilon > 99\%$) one observes anomalies of the low-temperature creep which do not appear in tests of samples subjected to low and medium deformations. The creep rate in the transient stage is significantly higher than would follow from the classical ideas about the mechanisms of low-temperature creep (logarithmic law), and the time dependence of the creep deformations is described by a power law, which corresponds to recovery creep. In the creep process oscillations appear on the resistivity curves; these are especially pronounced after drawing in liquid nitrogen. Possible causes of the observed effects are discussed. © *2004 American Institute of Physics.* [DOI: 10.1063/1.1705444]

The regularities of structure formation in metals and alloys at large plastic deformations go beyond the description in terms of the mobility of individual dislocations. One of the manifestations of collective effects in the dynamics of dislocations in such structures is the onset of structural instability, which can cause a number of macroscopic effects, e.g., a nonmonotonic change in the mechanical properties as functions of the degree of deformation, etc.[1,2] In niobium–titanium alloys the maximally distorted structure, in the form of fine dislocation fragments and particles of the titanium-based α phase (α-Ti) of large volume density, is formed in deformations at cryogenic (77 K) conditions in combination with heat treatments.[3] As was shown in Ref. 4, such a structural state is characterized by high critical currents and evolves under the influence of tensile stresses which are close to the breaking strength, bringing about a process of structural instability in the form martensitic phase transformations.[5] The latter is one of the main causes of an effect that occurs in superconducting coils of niobium–titanium alloys in powerful magnet systems: degradation of the critical current under the influence of tensile loads. Since the scheme of mechanical loading in that case is close to conditions of low-temperature ($T < 0.2T_m$) creep, and there are no data in the literature on the low-temperature creep of alloys of the Nb–Ti system, the goal of the present study was to investigate the features of the low-temperature (77 K) creep and the corresponding changes in the structural state of wires of niobium–titanium alloy.

SAMPLES AND TECHNIQUES

The material investigated was the niobium–titanium alloy NT-50 (48.5 wt. % Ti) obtained by electrospark melting. Single-filament wire samples were prepared by the pressing of bimetal preforms (NT-50 alloy in a copper sheath) and a subsequent drawing to a degree of deformation $\varepsilon = 99.4\%$ at 300 K. Then a finishing deformation to 99.93% by drawing at 77 K (in a medium of liquid nitrogen) was carried out on

a special apparatus.[6] Some of the samples obtained in this way were annealed for 10 hours at 675 K to permit the diffusive decay of the the β solid solution and the precipitation of particles of the α phase.

Creep tests were carried out on the device described in Ref. 7 in a medium of liquid nitrogen and at 300 K, at tensions $\sigma = 0.9\sigma_B$, where σ_B is the breaking strength of the alloy for the respective temperature. Prior to the measurements the copper sheath of the wires was etched off. For mounting the wire samples in the jaws of the device, copper tips were grown on the ends of the samples by an electrolytic method. The working length of the samples was 50 mm. Measurements of the resistivity in the course of the creep process were made by a compensation scheme using an R-348 potentiometer.

RESULTS AND DISCUSSION

Figure 1 shows the creep $\Delta\varepsilon$ in the transient stage, without allowance for the instantaneous deformation, as a function of the testing time t at 77 K for samples of the alloy NT-50 after drawing at 77 K and also after drawing at 77 K and annealing at 675 K. Figure 2 shows the same data plotted in the coordinates $\Delta\varepsilon - \ln t$ and $\Delta\varepsilon - t^{1/3}$. It is seen in Fig. 1 that the creep deformation attenuates with time and that the value of $\Delta\varepsilon$ is larger for the annealed sample. It is known[8,9] that the dependence of the creep deformation on the testing time at $T < 0.2T_m$ in the transient stage obeys a logarithmic law $\varepsilon \sim \alpha \ln t$. The data presented in Fig. 2 attest to the fact that for the alloy NT-50 the logarithmic law is obeyed only in the initial part of the transient stage, and then $\varepsilon \sim \beta t^{1/3}$, which is typical of the so-called recovery creep. Thus one observes an anomalous character of the low-temperature creep of NT-50 alloy samples that have an extremely distorted structure after large plastic deformations.

Figure 3 shows the dependence of the variation of the resistivity ρ during creep at 77 K for NT-50 alloy samples after they have been subjected to various kinds of action. It is
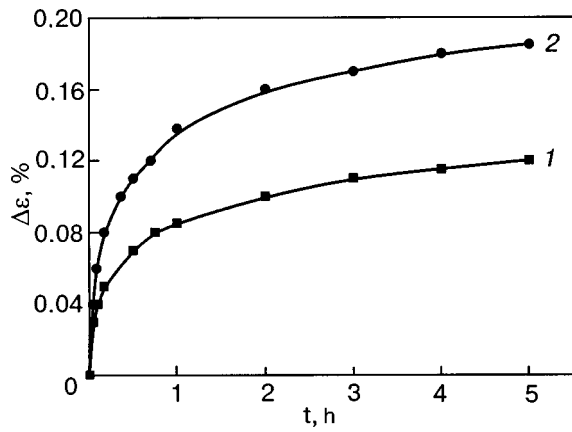
FIG. 1. Dependence of the creep deformation $\Delta\varepsilon$ at 77 K on the time t for the alloy NT-50 at $\sigma=0.9\sigma_B$: *1*—after drawing to 99.93% at 77 K; *2*—after drawing to 99.93% at 77 K followed by annealing at 675 K.
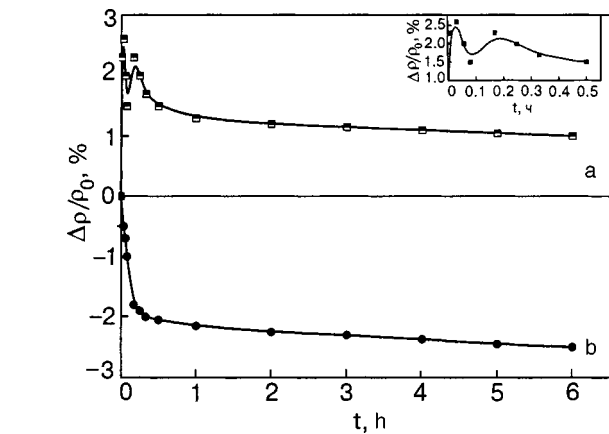

FIG. 3. Variation of the resistivity increment $\Delta\rho/\rho_0$ for the alloy NT-50 during creep at 77 K; drawing to 99.93% at 77 K (the inset shows the initial part of the $\Delta\rho/\rho_0$ curve for 0.5 h) (a); drawing to 99.93% at 77 K followed by annealing at 675 K (b).

seen that for $t<0.3$ h the character of the $(\Delta\rho/\rho_0)(t)$ curve is predetermined by the structural state of the alloy. For example, for alloy samples that had been subjected to drawing at in a medium of liquid nitrogen and having (as was shown in Ref. 3) a highly distorted finely disperse fragmented structure, nonmonotonicity of the $(\Delta\rho/\rho_0)(t)$ curves appears, and the increment $\Delta\rho/\rho_0$ is fixed immediately after application of the load. At the same time, for samples annealed after deformation, which have a relatively equilibrium structure, one observes only a monotonic decrease of ρ immediately after application of the load. For $t>0.3$ h the general tendency for all the samples is to have a monotonic decrease of $\Delta\rho/\rho_0$ after relatively brief (~ 0.3 h) holds of the material under load. We note that in this case a transition from logarithmic creep to recovery creep occurs earlier (at $\ln t \approx 4.8$, where t is in seconds).

Let us analyze the data obtained. The change in the decay law of the creep attests to the appearance of new pro-

cesses that substantially influence the character of the development of the deformation during a hold of the material under load. According to published data,[8,9] logarithmic creep is described well in the framework of thermally activated mobility of individual dislocations in the slip plane. Violation of this law has been observed previously when there is a change in the mechanism of dislocation motion, e.g., in climb and transverse slip, and also when phase transitions occur under load.[8,9] We note that under these conditions the violation of the logarithmic law was registered immediately after application of the load.

Let us turn to the results of a measurement of the resistivity, which to a significant degee reflects the character of the structural changes in the material during the creep process. It is known[8,9] that in pure metals the decreases in the creep rate and electronic resistance in the transient stage at a stress below the yield point are due to the mechanisms of
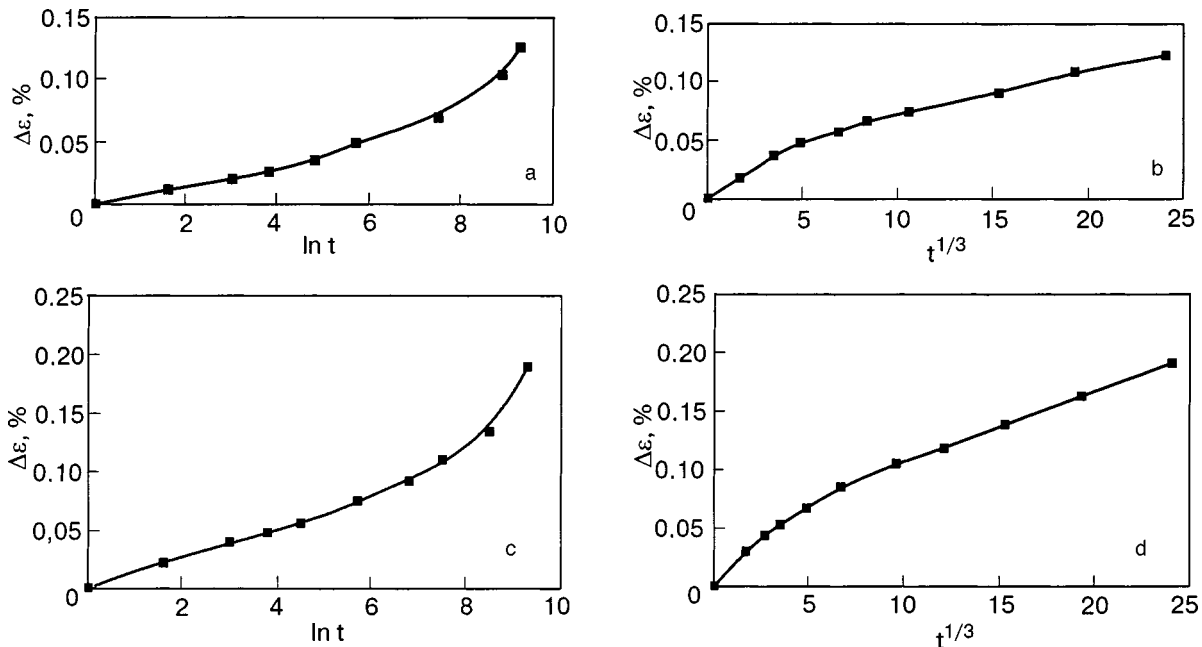

FIG. 2. The data of Fig. 1 replotted in the coordinates $\varepsilon - \ln t$ and $\varepsilon - t^{1/3}$ (t is in seconds): after drawing to 99.93% at 77 K (a,b); after drawing to 99.93% at 77 K followed by annealing at 675 K (c,d).

dislocation creation and to a decrease in the degree of imperfection of the structure. In the present study, though, the anomalous decrease in the resistivity is observed for $\sigma > \sigma_{0.2}$. To link this decrease with a decrease in the degree of imperfection of the material is impossible, since martensitic transformations occur during the low-temperature deformation of the alloy NT-50. The phases that arise at these, e.g., α'' martensite, have a typical metallic conductivity with a lower residual resistivity than for the β matrix,[10] and the development of a martensitic transformation during the creep process may be one of the causes of the decrease in the resistivity ρ and of the change in the character of the creep.

Let us analyze the possible influence of the martensitic transformation on the resistivity during the creep process for samples which have been annealed after drawing, in which the structure of the alloy is rather equilibrium, since the appearance of the diffusive phase α-Ti in the overstressed regions (boundaries of fragments) as a result of annealing leads to processes of internal stress relaxation. During loading in this case, processes of plastic deformation of the β solid solution develop, and there is a corresponding increase in the degree of imperfection of the structure and also a martensitic transformation stimulated by the deformation. The superposition of these contributions to the resistivity at a relatively low level of imperfection of the matrix is reflected by the $(\Delta\rho/\rho_0)(t)$ curves (Fig. 3b).

A more complex situation arises in the creep of the unannealed, highly imperfect samples, since in those cases oscillations of $\Delta\rho/\rho_0$ are observed, which reflect the substantial structural instability of the alloy with respect to active loading. It appears that the main cause of the oscillations is the reversibility of the martensitic transformation under conditions of a markedly nonuniform distribution (in magnitude and sign) of the internal stresses in the β matrix and also in the higher-strength anisotropic α'' phase. The martensite phase appears at places where the stress concentration is high as a result of strong dislocation pileups. At places where it appears, a mutual orientation of the lattices of the initial and martensite phase is realized which leads to relief of the stresses, unblocking of the pileups, and lowering of the level of imperfection. The development of plastic flow in the creep process gives rise to new stress concentrators and repeated initiation of phase instability, a consequence of which will be the observed oscillations of the resistivity.

Let us consider the possible causes of a change in the decay law of the creep; in particular, the influence of the phase instability of the β matrix on this effect. It is known that an increase in the deformation temperature to 300 K suppresses the martensitic transformation almost completely. It is natural to assume that in creep testing at 300 K the suppression of that transformation will lead to a change in the decay law of the creep in comparison with testing at 77 K. Figure 4 shows the results of creep testing at 300 K of an NT-50 alloy that had been deformed by drawing at 77 K. It is seen that damping of the creep under these conditions is described by the logarithmic law only, although the character of the $(\Delta\rho/\rho_0)(t)$ curves remains the same as in testing of an annealed sample at 77 K—the resistivity decreases with increasing t. Moreover, the decrease of ρ after creep at 300 K is 1.5 times larger than at 77 K. The observed character of
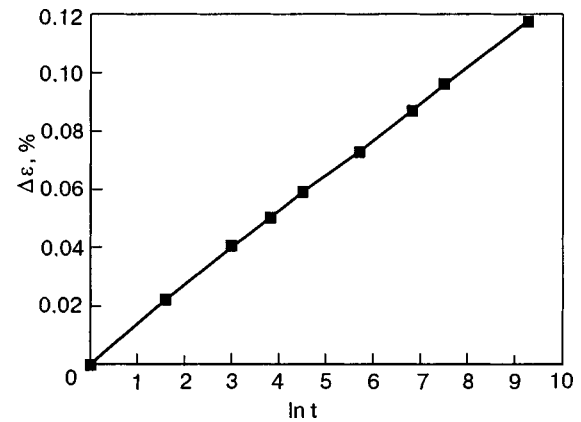

FIG. 4. Dependence of the creep deformation $\Delta\varepsilon$ at 300 K on $\ln t$ (t is in seconds) for the alloy NT-50 after drawing to 99.93% at 77 K.

the time dependence of the resistivity can be explained by the appearance of a martensite phase, but such an assumption does not explain the fact that the damping law of the creep remains unchanged. If a martensite phase does not appear, then there must be another mechanism responsible for the decrease in resistivity during a hold of the material under load. An analysis of the results suggests the presence of another process that can lead to a change in the character of the creep and the structural state of highly distorted systems. This process might be the appearance and development of collective effects in a dislocation ensemble, which in this case would be the predominant mode of plastic deformation. To check this hypothesis we investigated the creep at 77 K of pure niobium that had been deformed by drawing by 90% at 300 and 77 K. It turned out that at $\sigma = 0.9\sigma_B$ ($\sigma > \sigma_{0.2}$) in the transient stage a transition from a logarithmic dependence of the creep deformation to a power law ($\varepsilon \sim t^{1/3}$) occurs.[1] This result also gives us reason to assume that in the case of a highly imperfect structure such manifestations of structural instability as processes of collective motion of dislocations are possible. The development of these processes is accompanied by a lowering of the average density of dislocations.

Thus the observed features of the low-temperature creep and the changes of the resistivity in highly distorted structures of the NT-50 alloy are formed as a result of large plastic deformations at 300 and 77 K, which are due to the joint action of processes of motion of individual dislocations, martensitic transformations, and the development of collective modes of plasticity in the β matrix, the contribution of some process or other to the observed effects being different under different concrete conditions. For example, in the initial stages of creep the mechanisms of deformation due to the structural instability (both phase instability and the collective motion of dislocations) contributes relatively little to the deformation, since otherwise the recovery creep would be observed immediately after application of the load. The realization of a logarithmic law means that in the initial stages the main contribution to the deformation is due to the motion of individual dislocations not coupled into ordered ensembles. In cases of relatively equilibrium structural states the dislocations arise in the process of application of the load, while in highly distorted systems they have already been intro-

duced during the preliminary drawing and are located inside the fragments. However, this mode of plasticity is rapidly exhausted, and at long times of holding under load the processes due to structural instability become the leading contributors, and that leads to the realization of recovery creep and, as a consequence, to a change in the creep law.

---

†Deceased.
*E-mail: volchok@kharkov.org
1)This result will be considered in detail in our next paper.

————

1 E. É. Zasimchuk, *Collective Deformation Processes amd Localization of Deformation* [in Russian], Naukova Dumka, Kiev (1989).
2 V. K. Aksenov, O. I. Volchok, A. V. Mats, and Ya. D. Starodubov, Fiz. Nizk. Temp. **21**, 1246 (1995) [Low Temp. Phys. **21**, 954 (1995)].
3 V. K. Aksenov, O. I. Volchok, V. M. Gorbatenko, V. A. Emlyaninov, M. B. Lazareva, A. V. Mats, V. S. Okovit, Ya. D. Starodubov, O. V. Chernyi, and L. A. Chirkina, Fiz. Nizk. Temp. **20**, 595 (1994) [Low Temp. Phys. **20**, 471 (1994)].
4 O. V. Chernyĭ, Ya. D. Starodubov, O. I. Volchok, and G. E. Storozhilov, ''Method of preparing a niobium–titanium superconductor'' [in Russian], Ukraine Patent No. 42487, Byull. No. 9 (2001).
5 O. I. Volchok, M. B. Lazareva, V. S. Okovit, Ya. D. Starodubov, O. V. Chernyi, and L. A. Chirkina, Fiz. Nizk. Temp. **27**, 482 (2001) [Low Temp. Phys. **27**, 353 (2001)].
6 O. I. Volchok, I. M. Neklyudov, Ya. D. Starodubov, and B. P. Chernyĭ, Metallovedenie i Termicheskaya Obrabotka Metallov, No. 12, 8 (1993).
7 I. A. Gindin, V. P. Lebedev, and Ya. D. Starodubov, *Machines and Devices for Testing of Materials* [in Russian], Metallurgiya, Moscow (1971), p. 18.
8 I. A. Gindin and Ya. D. Starodubov, *Physical Processes of Plastic Deformatoin at Low Temperatures* [in Russian], Naukova Dumka, Kiev (1974), p. 322.
9 N. K. Nechvolod, *Creep of Crystalline Solids at Low Temperature* [in Russian], Vishcha Shkola, Kiev (1980).
10 V. A. Lototskaya, *Low-Temperature Mechanical Properties and the Structural State of Nb–Ti Alloys and Composites Based on Them* [in Russian], Author's Abstract of Candidate's Dissertation, Kharkov (1990).

Translated by Steve Torstveit

ERRATA

Erratum: Fluctuation conductivity and critical currents in YBCO films [Low Temp. Phys. 29, 973 (2003)]

A. L. Solovjov, V. M. Dmitriev, V. N. Svetlov, and V. B. Stepanov
Fiz. Nizk. Temp. **30**, 463 (April 2004)

1. The following phrase should be added to the caption of Fig. 2: For better visualization the values of $j_c(T)$ for sample W62 has been multiplied by 20.
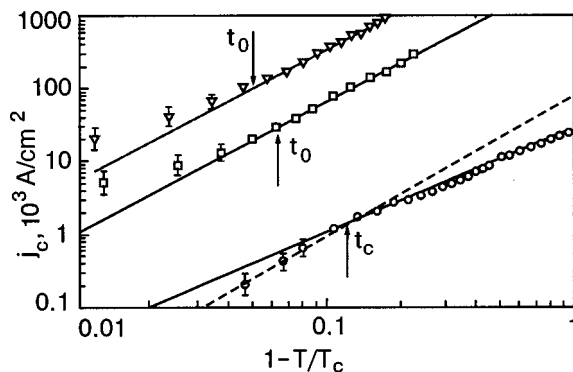
2. Figure 3 should look as follows:

FIG. 3. Temperature dependence of the critical current densities for samples W62 (○), W136 (□), and W154 (▽) in double logarithmic coordinates; the straight lines are plots of the equations $j_c(T) = j_c(0)(1 - T/T_c)^s$ for each sample with the same values of the parameters $j_c(0)$ and s as in Fig. 2; the dashed line is a plot of $j_c(T) \sim t^2$. The arrows indicate the temperatures t_0 for samples W154 and W136 and t_c for sample W62.